Thesis: Florian Leroi (2020) "Investigation of novel fibre laser designs and power-scaling concepts for the development of a continuous-wave green source", University of Southampton, Optoelectronics Research Centre, PhD Thesis, pagination.

UNIVERSITY OF SOUTHAMPTON

FACULTY OF ENGINEERING AND PHYSICAL SCIENCES

OPTOELECTRONICS RESEARCH CENTRE

INVESTIGATION OF NOVEL FIBRE LASER DESIGNS AND POWER-SCALING CONCEPTS FOR THE DEVELOPMENT OF A CONTINUOUS-WAVE GREEN SOURCE

Author:	*Supervisor:*
Florian LEROI	Pr. W. A. CLARKSON
ORCID ID: 0000-0001-6665-4689	

Thesis for the degree of Doctor of Philosophy

September 16, 2020

UNIVERSITY OF SOUTHAMPTON

ABSTRACT

FACULTY OF ENGINEERING AND PHYSICAL SCIENCES

OPTOELECTRONICS RESEARCH CENTRE

Doctor of Philosophy

POWER-SCALING OF A CONTINUOUS-WAVE GREEN SOURCE BASED ON NOVEL FIBRE LASER DESIGNS

By Florian Leroi

A novel method for power scaling continuous-wave ytterbium-doped frequency-doubled fibre lasers is investigated. The limiting effects on output powers and the requirement on polarisation control are discussed. A ring fibre laser configuration using a Faraday mirror without the requirement of polarisation-maintaining fibre is proposed. The requirement for a seed source to prevent self-pulsing in fibre lasers during alignment is presented. It lead to the construction of a 1075.0nm-central-wavelength 85pm-linewidth ASE source with 2.97W output. The fibre feedback was tackled using large bulk end-caps processed in the lab. A first ring fibre laser configuration without a frequency-doubling scheme was built: a wavelength-tuneable linearly-polarised source was obtained with an 32.0W average power over the 1047.1-1085.8nm range, a linewidth inferior to 0.4nm, a 70.2% slope efficiency and a polarisation extinction ratio below 100:1. Injection-locking of a similar cavity was tested with the ASE source. With an 1.86W injected signal, 17.4W were extracted at 1075.0nm. Then, power-scaling of the ring fibre laser pumped by 276W power was studied first without and then with empty enhancement cavity in used for frequency-doubling. Thermal effects, beam distortion, fibre recoupling efficiency reduction and unwanted polarisation rotation were diagnosed and tackled. Hybrid end-caps were produced and improved recoupling efficiencies by 16%. Power instabilities are reported with the investigation of their cause. The nonlinear crystal was placed in the enhancement cavity at last.

Contents

Abstract **vi**

List of Tables **xiii**

List of Figures **xxi**

Author's Declaration **xxiv**

1 Introduction **1**

1.1 Context 1

1.2 Motivation 2

1.3 State of the art 4

1.4 Outline of the thesis 6

Bibliography 8

Acknowledgements **1**

2 Fibre lasers for high-power green generation **13**

2.1 Single-pass and intra-cavity frequency-doubling schemes 13

2.1.1 Nonlinear polarisation 14

2.1.2 Second-harmonic generation and phase-matching 15

2.1.3 Single-pass configuration 18

2.1.4 Intra-cavity SHG and heat deposition in bulk gain media 19

2.2 Ytterbium-doped fibres as a gain medium 22

2.2.1 The waveguide nature of optical fibres 22

2.2.2 Absorption and emission spectra of Yb^{3+}-doped fibres 24

2.2.3 Brightness and pumping of doped double-clad fibres 27

2.2.4 Fibre laser performance 29

2.2.5 Free-space to fibre coupling 30

2.3 Enhancement cavities for frequency-doubling 33

2.3.1 External enhancement cavity 33

2.3.2 Internal enhancement cavity 35

Bibliography 38

3 Narrow-linewidth fiberised amplified spontaneous emission source 43

3.1 Motivation 43

3.1.1 ASE source presentation 44

3.1.2 Uses of a narrow-linewidth ASE source 45

3.2 Design 47

3.2.1 Concept 47

3.2.2 Spectrum-narrowing method 48

3.2.3 Gain stages 49

3.2.4 Final design 50

3.3 Results and discussions 51

3.4 Conclusions and prospects for development 54

Bibliography 55

4 Wavelength-tuneable linearly-polarised ytterbium-doped fibre ring laser 59

4.1 Polarisation control in fibre lasers 59

4.1.1 Birefringence in fibres 60

4.1.2 Faraday mirror approach 61

4.1.3 Spatial hole burning and Faraday mirrors 64

4.2 Experimental set-up 65

4.2.1 Set-up overview 65

4.2.2 Gain module 68

4.2.3 Requirements for large end-caps 71

4.3 Experimental results and discussion 75

4.3.1 Power, efficiency, bandwidth, linewidth 76

4.3.2 M^2-parameter 78

4.3.3 Polarisation purity 80

4.4 Conclusions and prospects for development 82

Bibliography 83

5 Injection-locking of a fibre laser cavity with an all-fibre amplified spontaneous emission source 87

5.1 Concept presentation 88

5.1.1 Injection-locking 88

5.1.2 Injection-seeding 91

5.2 Motivation 92

5.3 Injection-locking of a fibre laser with an ASE source 94

5.4 Optical set-up for the injection-locking of a linearly-polarised fibre laser . . 96

5.5 Results and discussion 98

5.6 Conclusions 106

Bibliography 107

6 Development of a high-power ytterbium-doped fibre laser configuration 109

6.1 The empty triangular ring cavity 109

6.2 High-power handling gain stage 111

6.2.1 Description 111

6.2.2 Tap couplers for characterisation 112

6.2.3 Gain stage performances 113

6.3 Optical nonlinear effects triggered at high-power levels 114

6.3.1 Stimulated Brillouin Scattering 114

6.3.2 Stimulated Raman Scattering 116

6.4 Alignment process 117

6.5 Power distribution and fibre recoupling evaluations 119

6.6 Experimental results: linear cavities 120

6.6.1 Linear cavity with collimated beams 120

6.6.2 Linear cavity with a focussed beam 126

6.7 Experimental results: empty triangular ring cavity 128

6.7.1 Presentation and performances 128

6.7.2 End-capping optimisation 131

6.7.3 Conclusion and discussion 134

Bibliography 135

7 Green generation using internally-enhanced frequency-doubling in a fibre laser 137

7.1 Enhancement cavity introduction 137

7.1.1 The bow-tie geometry 137

7.1.2 Longitudinal mode-matching 139

7.1.3 Impedance matching 141

7.2 LBO crytals for second-harmonic generation 144

7.2.1 Refractive index in isotropic and birefringent crystals 144

7.2.2 Phase-matching in birefringent crystals 146

7.2.3 LBO 149

7.3 Geometry considerations 151

7.3.1 Optimum waist in the nonlinear crystal 152

7.3.2 Waist conversion in the bow-tie cavity 154

7.3.3 Beam radius in triangular ring arm 157

7.4 Experimental results: triangular ring cavity with empty enhancement cavity 157

7.4.1 Introduction 157

7.4.2 Polarisation maintenance 159

7.4.3 Performance of the empty enhancement cavity 164

7.4.4 Power instabilities at high power operation 166

7.5 Configuration for green generation 174

7.6 Conclusion and discussion 179

Bibliography 181

8 Conclusions and future prospects 185

8.1 Summary of thesis 185

8.2 Conclusions and future prospects 187

List of Tables

4.1 Jones matrices of phase retardation, rotation and mirror reflection 63

5.1 Stable solutions of the rate equations for two competing modes at frequencies ω_1 and ω_2 for various self- and cross-saturation coefficient ratios relative to the small-signal gain ratio 105

6.1 List of components for the linear configurations 121

6.2 Configuration V: list of components 127

6.3 Configurations VI and VII: list of components 129

7.1 Ring fibre laser with empty enhancement cavity: list of components (configurations VIII and IX) 159

List of Figures

1.1 Experimental power records for ytterbium-doped fibre lasers for different architectures: (MM) multimode, (SM-DP) single-mode diode-pumped, (SM-TP) single-mode tandem-pumped, (CBC) coherent beam combination [30] . 6

2.1 Harmonic intensity evolution in three different conditions as a function of the normalised propagation direction z/l_{coh} as from [3] 17

2.2 Frequency conversion from a nonlinear crystal placed on a laser output . . . 18

2.3 Intra-cavity frequency conversion schemes 19

2.4 Several common gain medium geometries for thermal handling 21

2.5 Step-index fibre: (left) refractive index profile, (right) ray propagation . . . 23

2.6 (a) Typical energy level diagram of ytterbium ion in silica glass; (b) Typical emission and absorption cross-section in aluminosilicate fibre [15] 25

2.7 Cladding-pumping of a double-clad fibre, the high numerical aperture of the large inner cladding allows the use of low-brightness sources 27

2.8 Double-clad fibre: (left) refractive index profile (right) various symmetry perturbations 28

2.9 Fundamental Gaussian mode diverging from its waist along the propagation axis (left) and transverse distribution (right) 31

2.10 Frequency conversion in an external enhancement cavity 34

2.11 Internal enhancement cavity in a standing-wave fibre laser cavity 36

2.12 Internal enhancement cavity in a ring laser using polarisation-maintaining fibres 37

3.1 Schematic of an ASE signal covering a laser axial modes 44

3.2 Stages of the narrow-linewidth ASE source 47

3.3 For any incident signal on the grating pitch, only a portion around the Bragg wavelength λ_B is reflected 48

3.4 GTWave technology: (left) geometry (right) refractive index profile 50

3.5 ASE source set-up 50

3.6 Spectrum output from (a) SLED after isolator, (b) bandwidth slice #1, (c) bandwidth slice #2, (d) bandwidth slice #3 (linear scale, arbitrary units) . 52

3.7 Preamplifier power output with no feedback and when spliced to a circulator 53

4.1 Typical PANDA fibre geometry 61

4.2 Faraday mirror: 90° polarisation rotation 62

4.3 Fibre coupled to a Faraday mirror: 90° polarisation rotation 62

4.4 Set-up for linearly-polarised wavelength-tuneable ytterbium-doped fibre ring laser and polarisation distribution 66

4.5 Picture of the fibre gain module 69

4.6 Gain module set in a laser configuration 70

4.7 Cladding-mode stripping using a high refractive index gel applied on a bare section of fibre cladding 71

4.8 First round-trip evolution of 1W of incident power on an active fibre coupled to a Faraday mirror considering the Fresnel reflections at the fibre ends . . 72

4.9 Feedback management in fibre with (a) an angle cleave, (b) a coreless end-cap 73

4.10 Beam propagation and feedback distribution in a large bulk end-cap 74

4.11 Front and back views of a 25mm-diameter end-cap spliced to a fibre with a 130µm-diameter cladding 75

4.12 Output power at different emission wavelength 76

4.13 The output spectrum is a narrow-linewidth (0.4nm and bellow) smoothly varying over the bandwidth covered by the laser 77

4.14 Beam radius around the waist position for M^2-parameter measurement . . . 79

4.15 Longitudinal and transverse evolution of a diffraction-limited beam and a beam with a M^2 value of 1.08 79

4.16 Polarisation evolution in the free-space arm in abnormal operation (purple) 81

5.1 Regenerative gain curve for an injected signal at angular frequency ω_{inj} around the free-running angular frequency ω_0 of the slave resonator as from [1] 89

5.2 Locking range and intensity profiles of the free-running oscillation (I_0, ω_0) and the regeneratively amplified signal $(G_{reg}P_{inj}, \omega_{inj})$ as from [1] 90

5.3 Representation of the injected signal in-between the axial modes of the slave oscillator 92

5.4 Overlap of the ASE source emission spectrum with some longitudinal modes of the slave resonator 94

5.5 Position of the slave longitudinal modes shifting relative to the ASE spectrum (ν_{ASE}: ASE central frequency) 95

5.6 Set-up for injection-locking of a fibre laser by a narrow-linewidth ASE source 97

5.7 ASE source on with unpumped slave resonator 98

5.8 Free-running configuration at low (6.5W) and high (40W) pump power . . . 99

5.9 Output spectrum in injection-locking conditions below and above 33W pump power (laser diode output) 100

5.10 Signal outputs as from the RF spectrum analyser 101

5.11 Simulation of a regeneratively-amplified-only signal for an perfectly flat input ASE signal based on experimental values 103

6.1 Empty triangular ring fibre laser showing the location of the internal enhancement cavity 110

6.2 Principal components of the fibre gain module provided by SPI Lasers . . . 111

6.3 Power stability of the spooled fibre (HR-grating/14%-reflection grating) . . 113

6.4 Alignment configurations: (top) ASE source coupling via the tap coupler, (bottom) linear cavity using a partially transmissive mirror on the FSA fibre end 118

6.5 Power at the various locations in the laser resonator around the gain module119

6.6 (top) The linear configuration and (bottom) its intra-cavity power evolution (configurations I to IV) 121

6.7 Performances of Configuration I 122

6.8 Visible and thermal images of (left) BK7 plano-convex lens, (centre) BK7 wedge and (right) fused silica aspheric lens with 79W of 1080-1100nm incident radiation 123

6.9 Comparative performances of linear configurations I, II and III 125

6.10 Performances of Configuration IV 126

6.11 Stable linear arrangements for a free-space coupling from a fibre with a feedback mirror: (left) collimated beam, (right) focussed beam with waist on mirror 126

6.12 Configuration V: linear cavity with a focussed beam 127

6.13 Configurations V: recoupling efficiencies 128

6.14 Empty triangular configuration (configurations VI and VII) 129

6.15 Recoupling efficiencies of the empty triangular configuration before and after end-cap revision (configurations VI and VII) 130

6.16 Intensity profile evolution of (top) the FMA, and (bottom) the FSA fibre outputs and the optical arrangement for measurement 131

6.17 Schematic of the hybrid end-cap (not to scale) 132

6.18 Intensity profile evolution of the fibre output with a hybrid end-cap and the optical arrangement for measurement 133

7.1 Propagation and beam size evolution in a bow-tie cavity 138

7.2 Ring fibre laser configuration with an internal enhancement cavity 139

7.3 Overlap of the ring and bow-tie longitudinal modes with an arbitrary spectrum-narrowing element transmission window (not-to-scale) 140

7.4 Bow-tie notations for impedance-matching calculations 141

7.5 Typical dispersion curve for a transparent substance as from [4] 145

7.6 Refractive index dependence on the polarisation state for three directions of propagations in a uniaxial crystal: (a) along the optic axis, (b) perpendicular to the optic axis, (c) at an angle θ with the optic axis 145

7.7 Directions for type I and type II SHG critical phase-matching visualized by the intersection of the index surfaces for the fundamental and harmonic frequencies in the piezoelectric axes system [8] 147

7.8 Phase mismatch effect on harmonic intensity as from [9] 148

7.9 Dielectric axes for a LBO crystal with a ($\theta 90°, \phi 11.36°$) cut 150

7.10 Temperature tuning curves for type I and type II NCPM in LBO [19] . . . 150

7.11 Theoretical generated green power inside a 15mm-long LBO crystal for various fundamental input powers and beam diameters 153

7.12 Lens system equivalent to the bow-tie cavity 155

7.13 Upper and lower arms lengths as functions of the targeted lower arm waist for a fixed 162μm upper-arm waist and six available concave mirror radii of curvature 156

7.14 Ring fibre laser with empty enhancement cavity: schematic representation (configurations VIII and IX) 158

7.15 Configuration VIII: power distribution at low power above threshold 160

7.16 Mechanical stress points in mirror mounts 162

7.17 Configuration IX: power distribution at low power above threshold 164

7.18 Beam profile of signal (left) transmitted through $M_{FSA,1}$, (middle) rejected by M_{in} and (right) transmitted through $M_{FSA,2}$ 165

7.19 Configuration IX: temporal stability as from the tap coupler low-power port for 14.9W and 112W pump power, below instability threshold 167

7.20 Configuration IX: temporal behaviour as from the tap coupler low-power port at two arbitrarily-chosen times, above instability threshold 168

7.21 First optomechanical arrangement for the alignment of an end-capped fibre with a collimating lens 171

7.22 Robust mounting of the end-capped fibre with the collimating lens 172

7.23 Configuration X: triangular ring fibre laser with internal enhancement cavity for frequency-doubling to the green 175

7.24 Second harmonic transverse profile in a nonlinear crystal pumped by a fundamental beam with a high beam divergence 176

7.25 Configuration X: power distribution at low power above threshold 178

7.26 Configuration X: picture of the FSA in operation 179

Author's Declaration

I, Florian Leroi, declare that this thesis entitled "Power-Scaling of a Continuous-Wave Green Source based on Novel Fibre Laser Designs" and the work presented in it are my own. I confirm that:

- this work was done wholly while in candidature for a research degree at the University of Southampton;
- where any part of this thesis has previously been submitted for a degree or any other qualification at this University or any other institution, this has been clearly stated;
- where I have consulted the published work of others, this is always clearly attributed;
- where I have quoted from the work of others, the source is always given. With the exception of such quotations, this thesis is entirely my own work;
- I have acknowledged all main sources of help;
- where the thesis is based on work done by myself jointly with others, I have made clear exactly what was done by others and what I have contributed myself;
- parts of this work have been published

Signed:

Date: September 16, 2020

Acknowledgements

First and foremost, I would like to thank my supervisor, Pr Andrew Clarkson for embarking me on this fascinating project and sharing his enthusiasm and knowledge everytime I was stuck. I would also like to thank the occasional but particularly valuable help in the lab from Dr Peter Shardlow, and Dr Christophe Codemard too for his advice and assistance.

Also, special mentions should be dedicated to fellow students Dr Antonin Billaud and Dr Stan Vassilev for their help, company and support at the start of this PhD. Should be mentioned my other colleagues, Dr Callum Smith and Dr Robin Uren, Mark Burns, Lars Holmen, and at last Matt Hutchinson and Matt Barber for their company.

Then I would like to express my gratitude to all the other people who were by my side during most of this PhD. Thank you to Omar Abbas for the fascinating stories along with Mari Pappa, Livio Pizzi and Jon Gorecki for their company and support. Thank you to Vinita Mittal and Armen Aghajani for their notable kindness, and thank you to Kyle Bottrill for the endless conversations on this tumultuous modern society. I should also express a special thank to my housemates Joseph Demirtzioglou and César Cívico for the brother-like relationship we developped on Cranbury avenue. My experience in Southampton would have also not been the same if I did not spend the last year and the thesis writing with Sean O'Sullivan and my French gym buddies Bastien Belzunces and Benoit Lemore.

Finally, I would like to thank companies Laser Quantum Ltd for providing nonlinear crystals and SPI Lasers Ltd for their high-power fibre gain modules.

To them and to all the others I could not mention here: thank you.

To the people by my side during this journey

Chapter 1

Introduction

Lasers, and photonics more generally speaking, impact either directly or indirectly our everyday lives, despite suffering from a lack of recognition of their importance among the public at large. They contributed to the technological development of our societies as key enabling technologies over the second half of the twentieth century and continue today with far-reaching future prospects. This project of developing of a high power continuous-wave green fibre source sets in that context.

1.1 Context

Since T. H. Maiman demonstrated the operation of a ruby laser for the first time in 1960 [1] based on the theory of absorption and emission of electromagnetic radiation that Albert Einstein provided in 1917 [2], lasers went through an extraordinary development phase and constitute one of the most omnipresent technologies in this now well engaged 21th century.

The medical and biotechnological fields benefited early on starting with the first destruction of a retinal tumour in 1961 with a giant pulse. The carbon dioxide laser (CO_2 laser) and “Nd:YAG” laser both invented in 1964 found applications respectively in surgery for one, and vision correction and skin resurfacing for the other. ”Q-switching” provided high-energy pulses from 1962 and along with CO_2 lasers found countless applications in the manufacturing industry (aeronautics, automotive) with their abilities to cut, drill, weld, mark, engrave, etc. The electronic industry widely used the high spatial coherence of lasers from the 1970s [3]. Telecommunications vastly benefited from optical fibres from the same decade but it is only in the 1980s with the erbium-doped fibre amplifier that the performances of long distance communications were boosted [4]. Since then, fibre lasers found diverse applications: spectrophotometry, illumination systems, sensing, surgery and dentistry, military and space applications.

This PhD project sets in this long tradition of research with outcomes in industry. Its ambition is the generation of a multiple hundreds watts in the green spectrum from a continuous-wave single-transverse-mode laser source. Its main applications would be in the material processing and biotechnology sectors or for the pumping of other lasers.

1.2 Motivation

Lasers have a number of unique properties compared with other light sources. They have high spatial coherence, which is a measure of the correlation of the wave phase at different locations: a laser beam can be preserved over long distances or can be tightly focussed. They can also have high temporal coherence: a signal phase at any given point is quite predictable and can be controlled. Additionally, the emission spectrum of a laser can range from multiple hundreds of nanometres down to a single-frequency operation. Their wavelength of operation usually covers the spectrum from the ultra-violet to the infrared (but sometimes X-rays and gamma-rays are also included). Lasers can deliver a continuous power signal as well as ultrashort pulses of high energy with an appropriate control over the polarisation state. This project aims at developing one type of laser: a high-power continuous-wave green fibre source.

The optical spectrum covered by designated green lasers goes from 510nm to 570nm wavelength. Most people have once handled a green laser pointer for presentations. They are usually designed for powers below 5mW in accordance with most countries' legislation, but here, couple hundreds watts are targeted. Green lasers can also be found in RGB sources for projection displays and for holography, additive manufacturing, also known as three-dimensional printing [5], interferometry, in bio-instrumentation, Raman spectroscopy for metal oxides, minerals, inorganic materials, the –NH and –OH functional groups, and carbon tube analysis [6] and laser induced breakdown spectroscopy [7]. A major application of high-power green source is optical pumping of other lasers such as the widely-used titanium-sapphire (Ti:sapphire) laser with its useful emission tuning range from 650nm to 1100nm.

In the manufacturing industry, materials such as copper, gold and silicon present high absorption in the green spectrum. On the contrary, well-developed 1-micron laser sources are highly reflected by these materials. For instance, copper absorbs only 5% in the near-infrared against 40% in the green at room temperature. Welding of copper at green wavelength is also more stable with less spatter during the process [8]. Green is therefore more adequate for the micro-welding of conductive materials (thin foil or electrical contacts for instance) and temperature control [9].

Green lasers also find a number of applications in the medical and cosmetic sectors. Visible lasers have a strong absorption in the blood. Green lasers are also used to optically pump dye lasers and Ti:sapphire lasers used for applications such as photodynamic therapy: the interaction of light with cells. Ophthalmology benefits from green lasers for retinal photocoagulation [10].

The gem-diamond industry also uses green lasers despite the transparency of their crystals by using multi-photon absorption through Q-switching. It provides high quality components for eye surgery, diamond anvil cells, LCD scribers, cutting tools and heat spreaders [11].

In the defence and mapping sectors, green is preferred over infrared for the Lidar technology in airborne bathymetric and topo-bathy systems as it can penetrate water [12,13]. Additionally, some companies provide non-lethal responses such as green gun-mounted laser warners [14].

Besides being non-exhaustive, this list covers a wide range of applications and the fields in which green lasers can be used. Amongst them, a high power continuous-wave green laser would be particularly useful for the manufacturing industry and the pumping of Ti:sapphire lasers.

1.3 State of the art

Power scaling of a laser source in the visible and in particular the green can be quite challenging as there is no attractive laser transitions or semiconductor bandgaps in that spectral region. A common approach consists of using the nonlinear properties of some birefringent crystals associated with nonlinear optical processes to convert frequencies from the near-infrared spectrum (where lies ground-breaking power records) to the visible. This section provides the state of the art of what has been achieved with current continuous-wave green lasers, the motivation for a new approach and finally the subject of this project.

Starting with low powers, erbium-doped upconversion lasers can generate a few tens of milliwatts in the green as for example 15mW at 546nm [15] or 75mW at 549nm [16] but these power levels are too limited.

There are a number of gas lasers emitting in the green spectrum. The argon-ion laser can emit at 514.5nm with medical laser products presenting powers up to 15W [17]. Although their beam quality can be excellent, the power efficiency is very poor and the cooling system is very demanding. Helium-neon lasers present a transition at 543.5nm but their powers are limited to a couple of milliwatts. Copper vapour lasers can also emit at 510.6nm but they are pulsed sources.

Overall, there is no adequate semiconductor material to emit in the yellow-green. However, InGaN diodes with a certain design can emit at wavelengths above 500nm although they are difficult to produce. The powers achieved were 5mW at 510-513nm [18], 5mW at 515-518nm for diodes with a confirmed long lifetime [19], 65mW at 520nm [20] and 80mW at 522nm [21]. Also, vertical-external-cavity surface-emitting lasers with a single InGaAs/GaAs layered chip with quantum wells can deliver watts of green power [22, 23]. Complex semiconductor lasers involving a frequency doubling scheme provided higher green powers. For instance, 1.1W was generated at the not-so-common wavelength of 559nm [24]. Also, single-mode outputs were generated at 532nm by intracavity frequency doubling from a single chip of 30W [25] and 64W [26]. One attraction of this technology is that it provides near-diffraction limited beams while the optical pumping can be done with poor quality pump sources. Unfortunately, power scaling of such devices is currently limited by thermal effects.

So far, the highest green levels recorded came from bulk solid-state lasers emitting in the near-infrared and associated with a frequency conversion scheme. Solid-sate lasers encompass lasers whose active medium can either be a crystal or glass which is doped with rare-earth ions or transition metal ions. Bulk media refers to crystals or bulk glass in contrast with optical fibres. Both can be extremely efficient and present power records in the near-infrared. However, power-scaling of these devices is currently limited mostly by the thermal load of their active gain medium. This induces detrimental effects such as thermal lensing and beam quality degradation therefore innovative designs are desired. Accessing the green spectrum is possible through a nonlinear process called second-harmonic generation or frequency-doubling which doubles the frequency from the near-infrared to the visible and can be achieved in certain birefringent crystals.

A prominent technology is the thin-disk laser. As its name suggests, the active medium is a crystal in a large thin-disk shape in contact with a heat sink providing an efficient thermal management. Associated with a nonlinear crystal, it gave tremendous results. In continuous-wave operation, the intra-cavity frequency doubling of an ytterbium-doped-YAG thin-disk laser working at 515nm provided 470W of nearly-single-mode output (25% pump-to-green conversion efficiency) [27]. A comparable configuration provided with 300W of single-mode operation and 403W of nearly single-mode operation (40.7% pump-to-green efficiency at the maximum power). The limitations were attributed to the losses and thermal lensing induced by the numerous optical components in the set-up [28].

A solid-state laser alternative is the fibre laser. An optical fibre is a long axial glass waveguide which can be doped by rare-earth ions. Their high surface-to-volume ratio allows a superior thermal management. Their geometry also provides a near-diffraction-limited beam quality. A study reported a single-mode 532nm continuous-wave operation with a 356W output (single-pass frequency-doubling efficiency of almost 35%) [29]. This study used an ytterbium fibre laser system to deliver 1.06kW at 1064nm.

The Figure 1.1 shows the evolution of the power records achieved by ytterbium-doped fibres over the past decades [30]. The highest multimode outputs achieved so far lay at hundred-kilowatt level while the single-mode fibres are currently limited around 20 kilowatts outputs. However the trends are upward and there is room for further development. Theoretically, it has been evaluated that 36kW of diffraction-limited power can be ex-

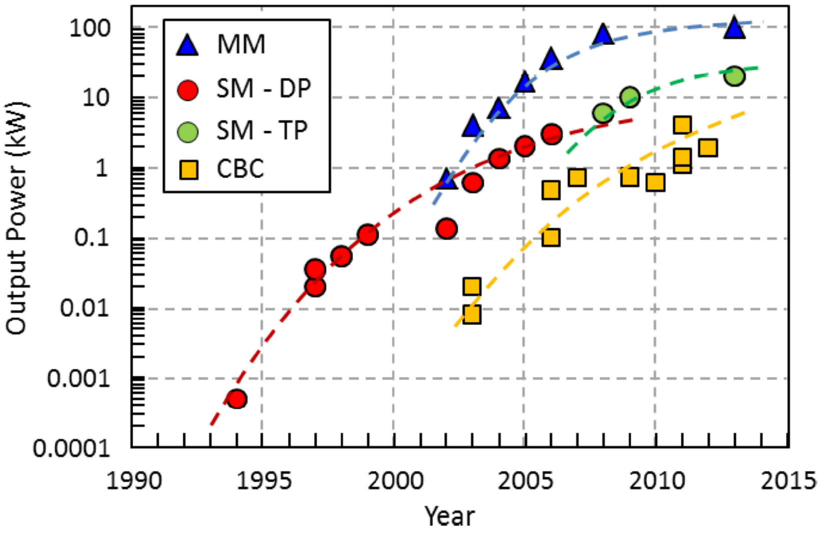

Figure 1.1: Experimental power records for ytterbium-doped fibre lasers for different architectures: (MM) multimode, (SM-DP) single-mode diode-pumped, (SM-TP) single-mode tandem-pumped, (CBC) coherent beam combination [30]

tracted from a fibre laser or amplifier [31]. Another study calculated that single-mode operation could be achieved in ytterbium-doped fibres up to 70kW under certain conditions [32]. These power levels, and the prospects for the future, make fibre lasers ideal for the generation of near-infrared light, and consequently for high-power frequency-doubling in the visible spectrum.

1.4 Outline of the thesis

This thesis is divided into eight chapters including this Chapter 1 which introduced the general context in which the project sets. The motivations for the development of a high-power green laser source were covered and existing technologies, with their performance and pros and cons, were introduced. It appeared that one of the promising techniques combines the high-power near-infrared output of ytterbium-doped fibre lasers with a nonlinear frequency-doubling scheme.

Chapter 2 gives a scientific and technological background on different approaches to achieve efficient frequency-doubling from a near-infrared input. The low frequency conversion of a single-pass through a nonlinear crystal and the thermal limitations of intra-cavity frequency-doubling in bulk solid-state lasers are presented. The thermal management capabilities of optical fibres and the assets of ytterbium-doped fibres are advanced. Then the notion of enhancement cavity for an efficient frequency conversion, and how to implement it in a set-up, is introduced. This leads to the presentation of the targeted experiment: a ring fibre laser with an internal enhancement cavity.

The presentation of the experimental work carried out starts with Chapter 3 with the development of a narrow-linewidth amplified spontaneous emission source at 1075nm. Optical fibres have a tendency to self-pulse during the alignment of laser cavities due to various mechanisms. An external source can be used to saturate the gain of the fibre working in amplification, forbidding these mechanisms. This source was used throughout the PhD. The narrow-linewidth and axial mode-free nature was used to test a form of injection-locking as described in Chapter 5.

Maintaining the polarisation state of light with an optical fibre in the set-up is quite challenging due to the fibre varying birefringence. Rather than using polarisation-maintaining fibres, this PhD thesis proposes to exploit the concept of Faraday mirror. It is introduced in Chapter 4 and implemented in a ring fibre laser configuration. A wavelength-tuneable linearly-polarised ytterbium-doped ring fibre laser is presented and sets as a milestone toward building the targeted green fibre laser.

Power-scaling is also a challenging objective as the behaviour of lasers at low intensities can differ when the pump power increases. Injection-locking was once a popular technique to obtain stable and narrow-linewidth high-power lasers and consisted in injecting a low-power signal with excellent spectral and temporal properties into one or several high-power oscillators. Chapter 5 proposes to test the injection-locking of a linearly-polarised ytterbium-doped ring fibre laser similar to the one from Chapter 4 using the 1075nm narrow-linewidth source developed in Chapter 3. On top of the academic interest relative to such experiment, it can be an interesting technique for wavelength-selection of a complex fibre laser.

Then chapters 6 and 7 present additional milestones in the development of the targeted experiment, namely the internally-enhanced frequency-doubling in a ring fibre laser including a Faraday mirror. Chapter 6 presents the power-scaling of the ring fibre laser working in the near-infrared up to multiple-tens-to-hundred watts and the progress achieved. Chapter 7 exposes the challenges relative to the introduction of the enhancement cavities and the nonlinear crystal.

At last, Chapter 8 provides a summary of the work achieved during this PhD. A conclusion with how this progress had an impact on the green fibre laser project and working with high-power fibre lasers is given.

Bibliography

[1] T. H. Maiman, “Stimulated optical radiation in ruby masers,” *Nature*, vol. 187, pp. 493–494, 08 1960.

[2] A. Einstein, “Zur Quantentheorie der Strahlung,” *Physikalische Zeitschrift*, vol. 18, 1917.

[3] M. Rose, “A history of the laser: A trip through the light fantastic,” *Photonics Spectra*, May 2010.

[4] R. Mears, L. Reekie, I. Jauncey, and D. Payne, “Low-noise erbium-doped fibre amplifier operating at 1.54µm,” *Electronics Letters*, vol. 23, pp. 1026 – 1028, 02 1987.

[5] H. Lee, C. H. J. Lim, M. J. Low, N. Tham, V. M. Murukeshan, and Y.-J. Kim, “Lasers in additive manufacturing: A review,” *International Journal of Precision Engineering and Manufacturing-Green Technology*, vol. 4, no. 3, pp. 307–322, Jul 2017. [Online]. Available: https://doi.org/10.1007/s40684-017-0037-7

[6] P. Zhou, “Choosing the most suitable laser wavelength for your raman,” http://bwtek.com/wp-content/uploads/2015/07/raman-laser-selection-application-note.pdf, 2015, B&W Tek, Inc.

[7] N. Elsherbiny and O. A. Nassef, “Wavelength dependence of laser induced breakdown spectroscopy (LIBS) on questioned document investigation,” *Science & Justice*, vol. 55, no. 4, pp. 254 – 263, 2015. [Online]. Available: http://www.sciencedirect.com/science/article/pii/S1355030615000118

[8] E.-M. Dold, E. Kaiser, K. Klausmann, S. Pricking, S. Zaske, and R. Brockmann, "High-performance welding of copper with green multi-kw continuous-wave disk lasers," 2019. [Online]. Available: https://doi.org/10.1117/12.2509925

[9] G. Shannon, "Green lasers: the key to high volume micro welding of conductive parts," http://info.amadamiyachi.com/blog/bid/168807/Green-Lasers-the-Key-to-High-Volume-Micro-Welding-of-Conductive-Parts, January 2013, Amada Miyachi, Inc.

[10] J.-T. Lin, "Progress of medical lasers: Fundamentals and applications," *Medical Devices and Diagnostic Engineering*, vol. 1, no. 2, pp. 36 – 41, 2016. [Online]. Available: https://www.oatext.com/Progress-of-medical-lasers-Fundamentals-and-Applications.php

[11] D. Wyszyński, J. Gawlik, and M. Janusz, "Application of DPSS Nd:YAG (532nm) laser for precise machining of diamond," *Innovations in management and production engineering*, 01 2013.

[12] A. Nayegandhi, "Green waveform lidar in topo-bathy mapping – principles and applications," https://www.ngs.noaa.gov/corbin/class_description/Nayegandhi_green_lidar.pdf, 2011, U.S. Department of the Interior U.S. Geological Survey.

[13] N. Corti, S. Baier, J. Geist, and T. Schneider, "Evaluation of green-lidar data for mapping extent, density and height of aquatic reed beds at lake chiemsee, bavaria—germany," *Remote Sensing*, vol. 9, p. 1308, 12 2017.

[14] "Glow: Green light optical warner," Brochure, 2010. [Online]. Available: https://www.thalesgroup.com/sites/default/files/database/d7/asset/document/GLOW.pdf

[15] T. J. Whitley, C. A. Millar, R. Wyatt, M. C. Brierley, and D. Szebesta, "Upconversion pumped green lasing in erbium doped fluorozirconate fibre," *Electronics Letters*, vol. 27, no. 20, pp. 1785–1786, Sep. 1991.

[16] S.-T. Lin, C.-L. Chen, H.-X. Tsao, T.-Y. Tsai, C.-L. Wang, H.-C. Su, C.-M. Huang, Y.-W. Jhang, and C. Hu, "A green up-conversion laser with erbium-doped LiLuF$_4$ crystal," in *16th Opto-Electronics and Communications Conference*, July 2011, pp. 655–656.

[17] H. J. Sumit Kumar Gupta and N. Sharma, "Study and applications of laser light," *Research Journal of Optics and Photonics*, vol. 2, no. 2, June 2018.

[18] T. Miyoshi, S. Masui, T. Okada, T. Yanamoto, T. Kozaki, S.-i. Nagahama, and T. Mukai, "510–515 nm InGaN-based green laser diodes on c-plane GaN substrate," *Applied Physics Express*, vol. 2, 06 2009.

[19] T. Miyoshi, S. Masui, T. Okada, T. Yanamoto, T. Kozaki, S. Nagahama, and T. Mukai, "InGaN-based 518 and 488 nm laser diodes on c-plane GaN substrate," *physica status solidi (a)*, vol. 207, pp. 1389 – 1392, 06 2010.

[20] J. Raring, M. C. Schmidt, C. Poblenz, B. Li, Y.-C. Chang, M. J. Mondry, Y.-D. Lin, M. Krames, R. Craig, J. Speck, S. Denbaars, and S. Nakamura, "High-performance blue and green laser diodes based on nonpolar/semipolar bulk GaN substrates," *Proceedings of SPIE - The International Society for Optical Engineering*, vol. 8039, 02 2011.

[21] S. Lutgen, D. Dini, I. Pietzonka, S. Tautz, A. Breidenassel, A. Lell, A. Avramescu, C. Eichler, T. Wurm, J. Müller, G. Bruederl, and A. Gomez-Iglesias, "Recent results of blue and green InGaN laser diodes for laser projection," *Proceedings of SPIE - The International Society for Optical Engineering*, vol. 7953, 02 2011.

[22] M. Arrigoni, B. Morioka, and A. Lepert, "Optically pumped semiconductor lasers: Green OPSLs poised to enter scientific pump-laser market," *Laser Focus World*, 2009. [Online]. Available: https://www.laserfocusworld.com

[23] M. Guina, A. Rantamäki, and A. Härkönen, "Optically pumped VECSELs: review of technology and progress," *Journal of Physics D Applied Physics*, vol. 50, p. 383001, Sep. 2017.

[24] S. Ranta, M. Tavast, T. Leinonen, R. Epstein, and M. Guina, "Narrow linewidth 1118/559 nm VECSEL based on strain compensated GaInAs/GaAs quantum-wells for laser cooling of Mg-ions," *Opt. Mater. Express*, vol. 2, no. 8, pp. 1011–1019, Aug 2012. [Online]. Available: http://www.osapublishing.org/ome/abstract.cfm?URI=ome-2-8-1011

[25] J. D. Berger, D. W. Anthon, A. Caprara, J. Chilla, S. V. Govorkov, A. Lepert, W. Mefferd, Q.-Z. Shu, and L. Spinelli, "20 watt CW TEM_{00} intracavity doubled

optically pumped semiconductor laser at 532 nm," *Proc. SPIE,*, vol. 8242, pp. 4–, 02 2012.

[26] J. Chilla, Q.-Z. Shu, H. Zhou, E. Weiss, M. Reed, and L. Spinelli, "Recent advances in optically pumped semiconductor lasers," *Proc. SPIE*, vol. 6451, 02 2007.

[27] T. Gottwald, V. Kuhn, S.-S. Schad, C. Stolzenburg, and A. Killi, "Recent developments in high power thin disk lasers at TRUMPF laser," pp. 8898 – 8898 – 7, 2013. [Online]. Available: https://doi.org/10.1117/12.2028656

[28] S. Piehler, T. Dietrich, M. Rumpel, T. Graf, and M. A. Ahmed, "Highly efficient 400W near-fundamental-mode green thin-disk laser," *Opt. Lett.*, vol. 41, no. 1, pp. 171–174, Jan 2016. [Online]. Available: http://ol.osa.org/abstract.cfm?URI=ol-41-1-171

[29] V. Gapontsev, A. Avdokhin, P. Kadwani, I. Samartsev, N. Platonov, and R. Yagodkin, "SM green fiber laser operating in CW and QCW regimes and producing over 550W of average output power," *Proceedings of SPIE - The International Society for Optical Engineering*, vol. 8964, 01 2014.

[30] M. Zervas and C. Codemard, "High power fiber lasers: A review," *Selected Topics in Quantum Electronics, IEEE Journal of*, vol. 20, pp. 1–23, 09 2014.

[31] J. W. Dawson, M. J. Messerly, R. J. Beach, M. Y. Shverdin, E. A. Stappaerts, A. K. Sridharan, P. H. Pax, J. E. Heebner, C. W. Siders, and C. Barty, "Analysis of the scalability of diffraction-limited fiber lasers and amplifiers to high average power," *Opt. Express*, vol. 16, no. 17, pp. 13 240–13 266, Aug 2008. [Online]. Available: http://www.opticsexpress.org/abstract.cfm?URI=oe-16-17-13240

[32] J. Zhu, P. Zhou, Y. Ma, X. Xu, and Z. Liu, "Power scaling analysis of tandem-pumped Yb-doped fiber lasers and amplifiers," *Opt. Express*, vol. 19, no. 19, pp. 18 645–18 654, Sep 2011. [Online]. Available: http://www.opticsexpress.org/abstract.cfm?URI=oe-19-19-18645

Chapter 2

Fibre lasers for high-power green generation

The goal of the research project this PhD sets in is the development of a high-power green fibre laser. This background chapter describes different laser cavity designs targeting efficient second-harmonic generation. Alongside, knowledge about free-space solid-state lasers, optical fibres and setting fibres in free-space set-ups is provided to the understanding of the design evolution. During this description, some of the many challenges this PhD have to deal with are raised.

2.1 Single-pass and intra-cavity frequency-doubling schemes

Because some parts of the optical spectrum are difficult to reach with traditional lasers, nonlinear optics can be used to convert some wavelengths from well-developed lasers to wavelengths of interest. Amongst nonlinear processes figures frequency-doubling, also called second-harmonic generation. This process can convert photons from the 1.02-1.14µm near-infrared spectrum to photons with half the wavelength i.e. in the green bandwidth (∼510-570nm). However this process has a low efficiency and laser set-up design is essential.

2.1.1 Nonlinear polarisation

When light encounters a dielectric medium such as a crystal its charges form a dipole moment. This polarisation of the medium $\overrightarrow{\mathcal{P}}$ propagates together with the electric field $\overrightarrow{E}$ of the light. In first instance, the response of the medium is given by:

$$\overrightarrow{\mathcal{P}} = \epsilon_0 \chi \overrightarrow{E} \tag{2.1}$$

where ϵ_0 the permittivity of free space and χ the susceptibility of the material. In return, the polarised medium generates an electric field at the same frequency as the incident electric field as according to the solution of the Maxwell's equations. This behaviour of the medium in response to light is called linear and is representative of reality to a certain extent. Indeed, the medium also exhibits a so-called nonlinear response whose effects are particularly noticeable at high intensity.

The nonlinear response finds its origin in the higher-order components of the susceptibility that are triggered at high optical intensity. The susceptibility is no longer a scalar and the polarisation of the medium becomes:

$$\overrightarrow{\mathcal{P}} = \underbrace{\epsilon_0 \chi^{(1)} \overrightarrow{E}}_{\text{linear polarisation}\,\overrightarrow{\mathcal{P}^{L}}} + \underbrace{\epsilon_0 \chi^{(2)} : \overrightarrow{E} \otimes \overrightarrow{E} + \epsilon_0 \chi^{(3)} \vdots \overrightarrow{E} \otimes \overrightarrow{E} \otimes \overrightarrow{E} + \ldots}_{\text{nonlinear polarisation}\,\overrightarrow{\mathcal{P}^{NL}}} \tag{2.2}$$

where the components of susceptibility $\chi^{(1)}$ characterise the first order linear polarisation $\overrightarrow{\mathcal{P}^{L}}$, $\chi^{(2)}$ the second-order and $\chi^{(3)}$ the third-order nonlinearities. The equation of propagation obtained from the Maxwell's equations is [1]:

$$\nabla^2 \overrightarrow{E} + \frac{\epsilon_r}{c} \frac{\partial^2 \overrightarrow{E}}{\partial t^2} = \mu_0 \frac{\partial^2 \overrightarrow{\mathcal{P}^{NL}}}{\partial t^2} \tag{2.3}$$

where ϵ_r is the relative permittivity and c the speed of light in vacuum, μ_0 is the vacuum permeability and $\overrightarrow{\mathcal{P}^{NL}}$ the nonlinear components of the polarisation. This right-hand part of the equation characterises the acceleration of the charges. They are at the origin of the emission of an electric field at different frequencies.

Second-harmonic generation (SHG), also known as frequency-doubling, is a second-order nonlinear process and happens in media presenting a $\chi^{(2)}$ susceptibility. This can only occur in media where the inversion symmetry is broken, as in noncentrosymmetric crystals (crystals that do not display inversion symmetry). Therefore liquids, gases and amorphous solids such as glass or crystals with inversion symmetry are not suitable for frequency-doubling, and this include classical glass fibres [1].

However, $\chi^{(3)}$ third-order nonlinear processes can happen in both centrosymmetric and noncentrosymmetric media. They are at the origin of processes such as Brillouin and Raman scatterings which can be detrimental effects in optical fibres. As third-order nonlinear processes, they have a much higher stimulation threshold.

2.1.2 Second-harmonic generation and phase-matching

Second harmonic generation is a particular case of sum-frequency generation process. These processes involve three photons and preserve the energy and momentum so that:

$$\omega_1 + \omega_2 = \omega_3 \tag{2.4}$$

$$\overrightarrow{k_1} + \overrightarrow{k_2} = \overrightarrow{k_3} \tag{2.5}$$

where ω_1 and ω_2 are the angular frequencies of respectively the two incident waves on a nonlinear crystal and ω_3 the sum-frequency generated wave. For $i = \{1, 2, 3\}$, $\overrightarrow{k_i}$ is the respective wavevector with $k_i = ||\overrightarrow{k_i}|| = \omega_i n_i / c$ and n_i is the refractive index experienced by each wave propagating in the direction $\overrightarrow{u_i}$.

In the context of second-harmonic generation, the two incident signals have the same frequency $\omega = \omega_1 = \omega_2$ and can originate from a single fundamental wave, and the generated wave frequency is $\omega_3 = 2\omega$. In this project, there are such that ω is in the near-infrared and 2ω is in the green.

Resolving the equation of propagation for these parameters can be quite challenging, notably because of the $\chi^{(2)}$ susceptibility second-order component which is a 3x9-tensor with 27 coefficients. Symmetries in a crystal that will not be developed here can simplify its expression. Given fixed propagation and polarisation directions, a scalar effective susceptibility $\chi^{(2)}_{\mathit{eff}}$ can be defined. In the literature, it is common to find equations using the nonlinear coupling coefficient $d_{\mathit{eff}} = \chi^{(2)}_{\mathit{eff}} / 2$ instead.

The planar wave is a solution of the equation of propagation. In the case where all three waves are collinear and propagating along the z axis, the electric field is given by:

$$\overrightarrow{E_i}(z,t) = A_i(z)\, e^{j(k_i z - \omega_i t)}\, \overrightarrow{u_i} \tag{2.6}$$

where $A_i(z)$ is the complex amplitude of the electric field, and the associated intensity $I_i(z)$ is provided by:

$$I_i(z) = 2n_i\epsilon_0 |A_i(z).A_i^*(z)| \tag{2.7}$$

The resolution of the equation of propagation in the undepleted pump approximation gives the intensity of the radiated frequency-doubled wave, also called the second harmonic, as [2]:

$$I_3(z) = \frac{2\omega^2 d_{\mathit{eff}}^2}{n_1 n_2 n_3 \epsilon_0 c^3}\, I_1^2(0)\, z^2\, \mathrm{sinc}^2\left(\frac{\Delta k z}{2}\right) \tag{2.8}$$

where $\mathrm{sinc}(x) = \sin(x)/x$, and in the case where $I_1(0) = I_2(0)$ are the intensity of the fundamental wave as incident at $z = 0$ on the crystal input face. Δk is known as the phase mismatch between the nonlinear polarisation and the radiated electric field in the propagation direction. It is defined as:

$$\Delta k = k_1 + k_2 - k_3 \tag{2.9}$$

Depending on the value of Δk, the SHG process presents different behaviours.

For a phase mismatch $\Delta k = 0$, all the harmonics are generated at the same frequency and the radiated wave intensity increases exponentially with the travelled distance z: $I_3(z) \propto z^2$. This is the perfect phase-matching where the transfer of energy between the nonlinear polarisation and the radiated wave is the most efficient. It can be achieved in certain birefringent crystals.

For a $\Delta k \neq 0$ mismatch, the transfer of energy from the nonlinear polarisation to the harmonic follows a sinusoidal function: $I_3(z) \propto \sin^2(\Delta k\, z/2)$. The harmonics are generated at different frequencies and eventually gives this succession of constructive and destructive interferences. It has a half period $l_{coh} = \pi/\Delta k$ known as the coherent buildup length, or coherence length, over which the interferences are constructive.

Plots of the second-harmonic intensity in these two conditions are represented in Figure 2.1. One could argue that outside the phase-matching condition the crystal could be

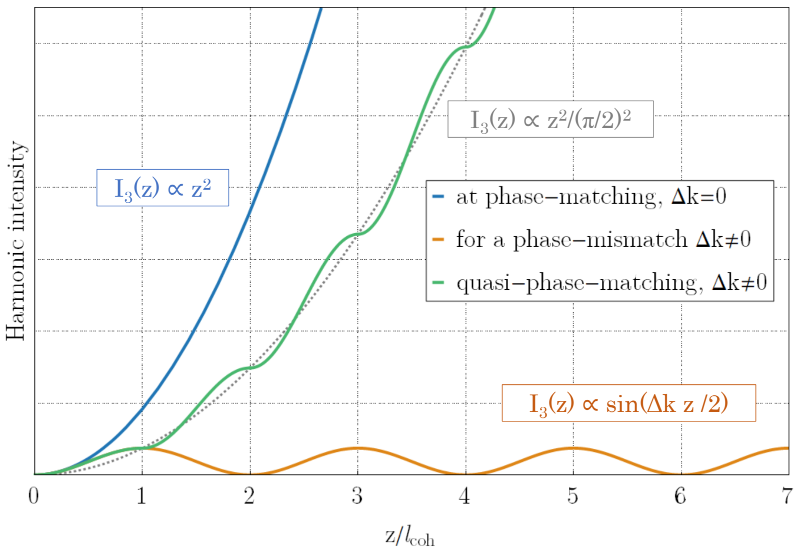

Figure 2.1: Harmonic intensity evolution in three different conditions as a function of the normalised propagation direction z/l_{coh} as from [3]

cut over one coherence length l_{coh}. Unfortunately this usually corresponds to only a few micrometers and a low frequency-conversion efficiency [4].

Nonetheless, frequency-doubling can be achieved without matching the phase velocities in nonlinear structures with a periodic variation of the sign of the nonlinear susceptibility, and therefore a sequence of constructive interferences. This is quasi-phase-matching [5]. It can be achieved with periodic poling [6].

The output intensity for quasi-phase-matching is also represented in Figure 2.1 with the same parameters as previously including the phase mismatch. The overall trend is also exponential with distance and follows a trend [7]: $I_3(z) \propto z^2/(\pi/2)^2$. Another asset of quasi-phase-matching is that the effective nonlinear coefficient d_{eff} value is no longer limited to the phase-matching conditions of work and therefore its value can be higher (tens of pm/V versus several pm/V).

Finally, these equations are valid if the input intensity is little depleted. For high conversion efficiencies, the exact amplitude expressions are [7]:

$$|A_1(z)| = \frac{|A_1(0)|}{\cosh\left(\frac{2\omega d_{eff}}{c\sqrt{n_1 n_2 n_3}}\, z\, |A_1(0)|\right)} \tag{2.10}$$

$$|A_3(z)| = |A_1(0)| \tanh\left(\frac{2\omega d_{eff}}{c\sqrt{n_1 n_2 n_3}}\, z\, |A_1(0)|\right) \tag{2.11}$$

2.1.3 Single-pass configuration

The most straightforward technique to generate green from SHG consists in placing a nonlinear crystal directly on the output of a the near-infrared source. This is the single-pass configuration represented on Figure 2.2 and reported in the introduction chapter from which 356W of power were generated at 532nm from a 1064nm ytterbium-doped fibre [8].

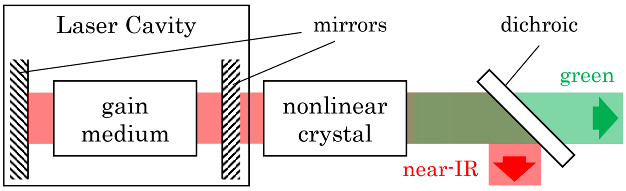

Figure 2.2: Frequency conversion from a nonlinear crystal placed on a laser output

The immediate limitation in continuous-wave operation is the frequency doubling efficiency. In the undepleted pump approximation, for a phase-matched crystal of length l_{cr}, it is defined as:

$$\eta_{SHG} = \frac{I_3(l_{cr})}{I_1(0)} = \frac{2\omega^2 d_{eff}^2 l_{cr}^2}{n_1 n_2 n_3 \epsilon_0 c^3}\, I_1(0) \tag{2.12}$$

The factor of the fundamental wave intensity $I(\omega, 0)$ is usually very small and the only way to achieve a high conversion efficiency η_{SHG} is to work at high optical intensities. In a single-pass configuration, a considerable amount of power is lost despite the crystal being fed with a high input power. The 356W green power as obtained from a 1kW input were laying a conversion efficiency of $\sim$35%.

Periodically-poled crystals used for quasi-phase-matching can theoretically increase the efficiency since their d_{eff} coefficient is higher. However such crystals are difficult to process, expensive, usually designed for one specific operation at a specific wavelength and limited in size. Moreover, photorefractive damage is often a limitation to the power-scaling, notably in frequently-used nonlinear crystal lithium niobate [9]. For these reasons, quasi-phase-matching is ruled out in first instance and working in the phase-matching condition is privileged.

The other way to increase the conversion efficiency of a frequency-doubling scheme in a nonlinear crystal is either increasing the incident power on the crystal or multiple-passing the crystal to achieve a higher overall efficiency.

2.1.4 Intra-cavity SHG and heat deposition in bulk gain media

Rather than placing the nonlinear crystal on the output of the near-infrared laser source it can be put inside the resonator where the second-harmonic generation process benefits from higher circulating power. This intra-cavity configuration, represented on Figure 2.3, proved itself multiple times with the generation of watts and tens-of-watts of visible power with bulk gain media i.e. either doped crystals or doped glasses. This is notably what was achieved in the two studies reported in introduction with the thin-disk laser approach [10, 11]. The generated 300W of green corresponds to just above 30% of pump-to-green efficiency (and therefore a higher near-infrared-to-green efficiency).

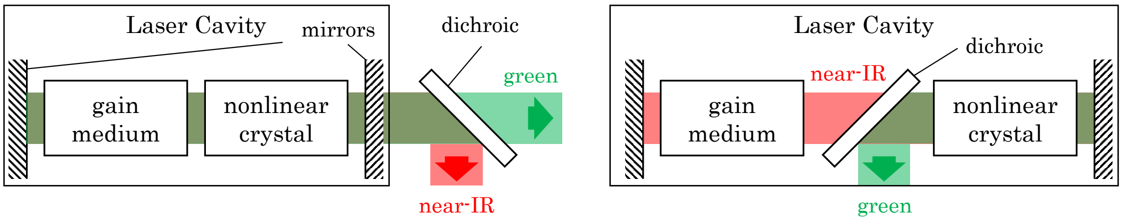

Figure 2.3: Intra-cavity frequency conversion schemes

In terms of power-scaling, this configuration suffers from the thermal load in various optical components of a set-up and in particular in the gain medium. They are particularly subject to their high quantum defect. It is the difference of energy between the laser transition and the pumping transition $\Delta\mathcal{E}_{QD} = (h\nu)_{pump} - (h\nu)_{laser}$ lost through non-radiative emission which is inevitable. This optical energy is transmitted to phonons whose vibration heats up the gain medium.

Also, parasitic spectroscopic processes can occur in certain gain media and contribute to the temperature increase. Energy-transfer up-conversion occurs when a photon emitted at the lasing wavelength is reabsorbed by an excited ion from the upper manifold to higher level of energy, and then non-radiatively decays. Cross-relaxation is a transfer of energy from an excited ion to an ion from the ground levels so that they both end up in an intermediate level, and then non-radiatively decay. These processes are likely to occur in media with a high concentration of active ions and clusters of active ions. As its name implies, excited state absorption is the absorption of a photon at the pump or lasing wavelength by an ion in the excited state and is also followed by a susbsequent non-radiative re-emission. It is more probable in transition-metal-doped crystals than it is in rare-earth-doped crystals. These processes are known to decrease a laser efficiency and contribute to heating due to the non-radiative decays.

The heating of the gain medium occurs along the beam path and a gradient of temperature arises between the propagation axis and the outer surface. Therefore a refractive index difference along with a differential mechanical expansion occurs as well. This induces thermal lensing which covers three mechanisms: stress-induced lensing, lensing relative to the gradient of refractive index, and bulging of the end faces of the crystals. Thermal lensing induces a wave front curvature, either positive or negative, and a distortion of the beam [12]. Ultimately, thermal loading can lead to the fracture of the gain medium or its melting whether it is a crystal or a glass host.

In order to avoid the effects of strong thermal loading, heat-sinking strategies are implemented and Figure 2.4 presents some common geometries.

The laser rod geometry can either be end-pumped or pumped side-way and the heat can be extracted from its lateral surface. The end-faces set in the resonator while the lateral side is thermally connected to a heat-sink. This geometry allows the use of high-power diode stacks. The advantage of end-pumping is the good spatial overlap between the pump and the laser modes. To a certain extent, the cylindrical symmetry provides a relatively cylindrical temperature distribution. The thermal lensing can be partially compensated in a laser cavity using lenses, curved mirrors or the shaping of the end-faces by polishing. However some thermal lensing remains inhomogeneous with strong aberrations in the pumping beam wings and unevenly distributed along the rod length. It is possible to work with elongated rods (e.g. single crystal fibres) or composite rods

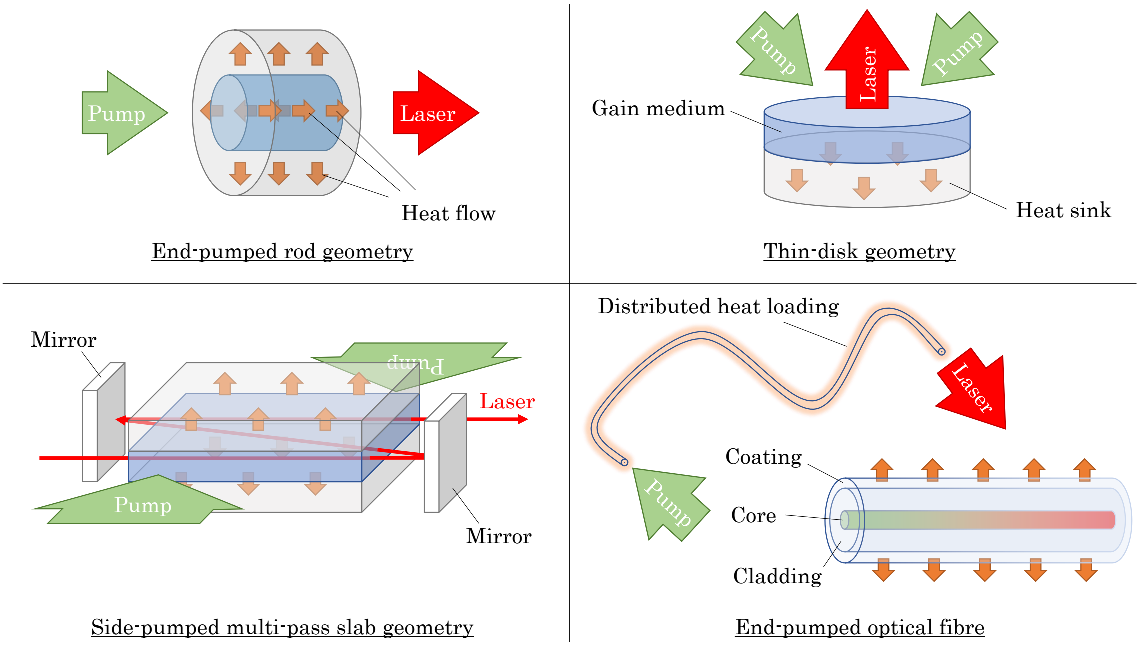

Figure 2.4: Several common gain medium geometries for thermal handling

whose doping concentration is respectively locally lower or distributed in-homogeneously along its length. Nonetheless, the rod geometry notably suffers from a poor output beam quality in the kilowatt regime.

The slab geometry offers a large surface-to-volume cooling ratio for bulk gain medium. They are cut in a thin block shape where the laser beam can propagate along the two orthogonal long directions and, in the case of edge-pumping, the third direction is thermally connected to a heat-sink. The side-pumping allows the use of low phase-front quality diode bars without requirement for dichroic optics to separate the pump and lasers modes, however it provides a poor overlap between them. Strategies like zig-zag path or multi-pass configuration can overcome this limitation. However, the slab geometry has a strong thermal lensing in the heat-flow direction. The zig-zag strategy proposes to average out its effects and involves total internal reflection on the cooled faces but this requires no contact with a metallic heat-sink for instance. With multi-pass configurations with a folded beam path, the doping level of the pumped ions can be reduced, which decreases the absorption coefficient, the temperature gradient and therefore thermal lensing. It can provide a combination of high efficiency, high beam quality and high power [13]. Yet, the power levels and output beam quality are lower than the ones provided by thin-disk geometries and optical fibres.

The thin-disk geometry is a large thin cylinder where one flat face is actively cooled down while the pump and laser modes are coupled in and out from the other face. The thickness of the gain medium is considerably smaller than the beam sizes and its low absorption is compensated with multiple double-passes through. The thinness ensures an efficient heat-sinking and therefore a weak thermal lensing. It also has a high fracture limit. However, its power-scaling suffers from complicated pumping architectures, degraded beam quality, and requires efficient high-reflection and anti-reflection coatings for respectively the back and the front faces.

Rare-earth-doped fibres are the one alternative that is gaining more and more interest over the years as they can notably deliver near diffraction-limited outputs at very high powers with an excellent efficiency. They are usually composed of a core where a signal can be guided by a surrounding cladding over long distances. This core can be doped with rare-earth elements and their concentration can be spread over its length, distributing the thermal loading. Additionally, heat-sinking is particularly efficient due to their high surface-to-volume ratio preventing notably the damage of the coating. Also, the thermally-induced refractive index gradient has a limited impact on the beam quality, especially with step-index fibres with a small core as required for single-mode operation.

2.2 Ytterbium-doped fibres as a gain medium

Rare-earth-doped fibres are an attractive alternative to bulk gain media regarding heat management. The double-clad structure allows them to be pumped by low-brightness diodes and emit near diffraction-limited outputs.

2.2.1 The waveguide nature of optical fibres

Optical fibres exploit the principle of total internal reflection of light to guide a signal with theoretically no losses. From a simple ray optics approach, the Snell-Descartes laws give the existence of a range of angle for which light is completely reflected at the boundary between media with different refractive indices. The total reflection occurs when light is incident from the medium of higher index.

Step-index fibres (see Figure 2.5) exploit this total reflection principle to conduct light in a cylindrical core surrounded by a cladding with a lower index. Any ray propagating in the core at an angle superior to the critical angle θ_c experiences a total internal reflection throughout the fibre.

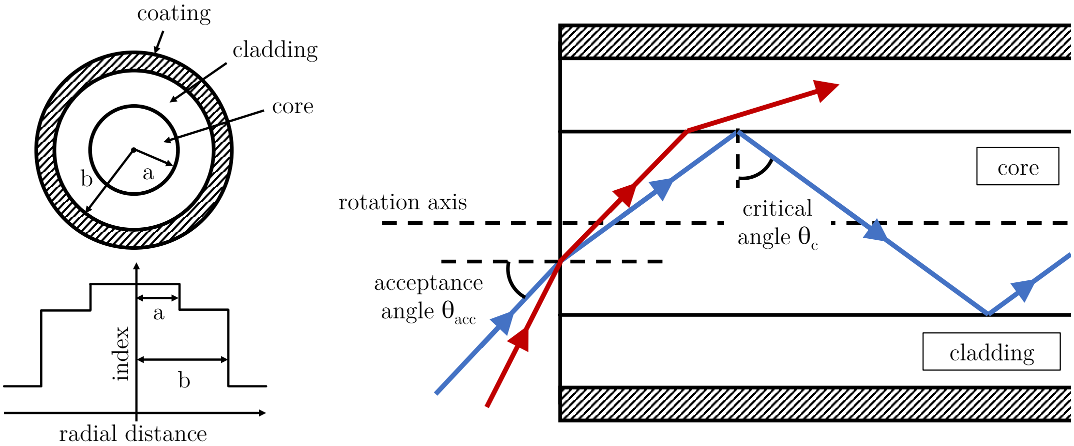

Figure 2.5: Step-index fibre: (left) refractive index profile, (right) ray propagation

To the critical angle within the fibre corresponds an external acceptance angle θ_{acc}. Only the light incident on the fibre within an cone delimited by the acceptance angle can be successfully coupled in and propagate through the fibre. The numerical aperture (NA), defined as $NA = n\sin(\theta_{acc})$ with n the refractive index of the medium where the fibre sets, is a common tool to characterise this angle. The NA can be expressed as:

$$NA = \sqrt{n_{core}^2 - n_{clad}^2} \tag{2.13}$$

where n_{core} and n_{clad} are the refractive indices of respectively the core and the cladding. A fibre with a low NA will only accept laser beams with a small divergence whereas high NA fibres have a wider acceptance.

Silica glass has a refractive index of approximately 1.44 in the near-infrared [14] but this value can be altered using a number of dopant ions for either an increase (e.g. germanosilicate, phosphosilicate and aluminosilicate) or a decrease (e.g. fluorine and boron oxide) of this value.

The core of the fibre can also be doped with rare-earth ions so that this section can work as a gain medium. Fibres can then be designed with a low concentration of rare-earth ions distributed over a long length. The thermal loading associated with quantum defect and parasitic spectroscopic processes is distributed over that length and the high surface-to-volume ratio becomes an asset for thermal handling.

Among the rare-earth dopants figures ytterbium ions. The ytterbium-doped fibres can emit at wavelegnths over a large spectrum around 1.1µm. Second-harmonic generation in the green can be achieved from certain wavelengths of that spectrum.

2.2.2 Absorption and emission spectra of Yb^{3+}-doped fibres

Ytterbium is the chemical element from the rare-earth metals of the lanthanide series which emits around 1.1µm in silica fibres with the highest efficiencies in comparison to any other rare-earth-doped fibres.

The electronic configuration of ytterbium ions, noted Yb^{3+}, present a partially filled $4f$ shell. Its energy is distributed between two levels noted $^2F_{7/2}$ (lower level) and $^2F_{5/2}$ (upper level). Due to the Stark effect, each level is split into manifolds of sublevels. In a crystal host, these sublevels tend to be discrete and distributed whereas in a glass host they are relatively broad and overlapping. Consequently, the emission and the absorption spectra are continuous and relatively broad. Given its electronic state distribution, ytterbium-doped fibre are often considered as quasi-three level lasers.

Figure 2.6(a) provides with typical working wavelengths for absorption and emission from the bottom upper and lower manifolds. The exact distribution depends on the glass composition and the ytterbium ions concentration [15]. Cross-sections quantify the likelihood of the transitions and are represented for an ytterbium-doped fibre on Figure 2.6(b). The absorption cross-section spectrum presents notably a broad peak at 910nm and an even greater but narrower peak at 976nm. The existence of high-power narrow-linewidth commercially-available laser diodes at the latter wavelength allows an efficient pumping of such fibres [16]. The emission cross-section spectrum presents relatively high values from 1030nm and beyond so that ytterbium-doped fibres are suitable for emission at these wavelengths. In its early development, it was reported that a single-mode ytterbium-doped fibre

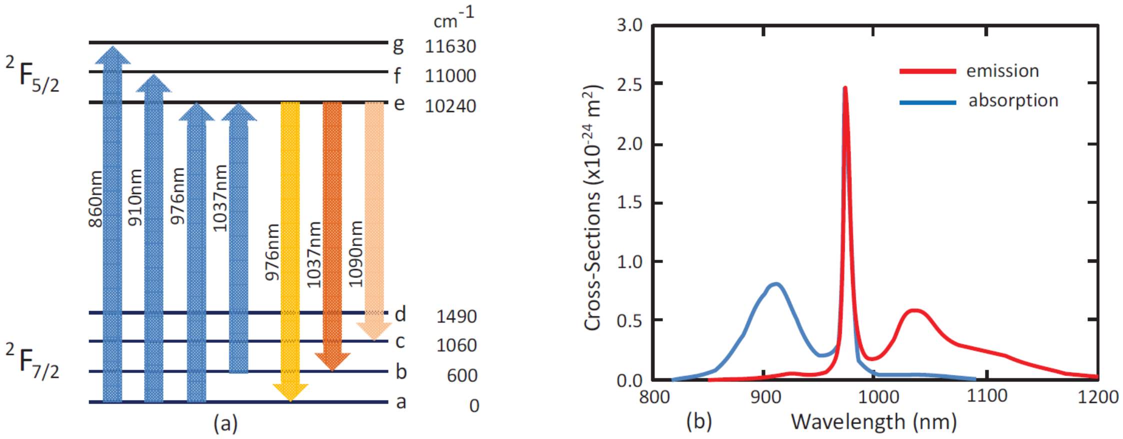

Figure 2.6: (a) Typical energy level diagram of ytterbium ion in silica glass; (b) Typical emission and absorption cross-section in aluminosilicate fibre [15]

was continuously and smoothly tuned over a 1010-1162nm spectrum with output power around 10mW [17]. Since then power-scaling has been tremendous (as reported in Chapter 1).

The cross-sections are related to the optical gain of a fibre at a position z along its length. The gain coefficient $g(\lambda, z)$ (in m^{-1}) is given by [18]:

$$g(\lambda, z) = \Gamma\left[\sigma_{em}(\lambda)N_{up}(z) - \sigma_{abs}(\lambda)N_{gr}(z)\right] \tag{2.14}$$

where $\sigma_{abs}(\lambda)$ and $\sigma_{em}(\lambda)$ are respectively the emission and absorption cross-sections, $N_{gr}(z)$ and $N_{up}(z)$ are respectively the ground-state and the upper-level atoms population, and Γ is the overlap between the beam and the dopant ($\Gamma \sim 1$ for the signal and $\Gamma \simeq A_{core}/A_{clad}$ the ratio of cladding to core areas for the pump signal). The gain coefficient can either be positive for a emitted signal and negative at the pump wavelength. It is a function of distance as population inversion varies with pump intensity. The net power gain G over a length l of fibre is given by:

$$G(\lambda) = \exp\left(\int_0^l g(z, \lambda)\,\mathrm{d}z - \alpha_{prop}\,l\right) \tag{2.15}$$

where α_{prop} is the propagation loss coefficient.

The gain of fibres can be significantly high. For a quasi-three levels system optically pumped at wavelength $\lambda_p = c/\nu_p$ for a length of fibre long enough to absorb a pump power $P_{p,abs}$, the small-signal gain, or unsaturated gain, of a signal at wavelength λ_l becomes [19]:

$$G_0(\lambda_l) = \exp\left[\frac{\big(\sigma_{abs}(\lambda_l) + \sigma_{em}(\lambda_l)\big)\tau_f\eta_q}{A_{core}h\nu_p}P_{p,abs}(l) - \underbrace{N_{tot}\sigma_{abs}(\lambda_l)\,l}_{\substack{\text{re-absorption}\\ \text{loss } L_{reabs}}} - \underbrace{\alpha_{prop}(\lambda_l)\,l}_{\substack{\text{propagation}\\ \text{loss } L_{prop}}}\right] \tag{2.16}$$

where τ_f is the fluorescence lifetime of the upper level, η_q is the pumping quantum efficiency (the fraction of absorbed pump photons that leads to excited ions in the upper laser level), N_{tot} is the total population of the ground and upper manifolds. A_{core} is the doped-section area where the laser mode is absorbed and re-emitted i.e the core area. These parameters are intrinsic to the fibre constituents and design.

The contributions to the propagation loss L_{prop} are various. There is an intrinsic absorption of the light by the glass itself. There is an extrinsic absorption from -OH hydroxide ions from water introduced during manufacturing and from dopants either used for refractive index variation of laser amplification. However if the propagation losses was just below 20dB/km [20] in the early development of fibres in the 70s, nowadays it can be as low as 0.142dB/km [21]. In fibre assemblies where portions of fibres are spliced together, losses can occur at the splice location due to angular, longitudinal and lateral misalignments, and core-size mismatch. However, overall, these losses can be kept very low too.

This gain expression takes into account the re-absorption in the doped core L_{reabs}. Pumping a long fibre certainly ensures a higher absorption of the pump light, however it also means a re-absorption of the emitted signal and consequent re-emission at higher wavelength. Therefore the lowest wavelengths promised by the emission cross-section curve are only possible for short fibre lengths.

Ytterbium-doped fibres are therefore versatile laser sources as they can emit on a broad spectrum. They also have a large emission bandwidth allowing wavelength tuneability in a laser set-up. One other major advantage of fibres is that they can be pumped by low brightness sources and still deliver high-quality laser beams. This is notably true in single-transverse-mode operation which is intended in this project.

2.2.3 Brightness and pumping of doped double-clad fibres

This project proposes to work in single-mode operation which means that the fibre core can only support a single transverse mode around 1.1µm wavelength which is true for core diameters of the order of ∼10µm (depending on the numerical aperture of the fibre). Coupling light in such a confined area in order to pump the doped ions require pump sources with a high-beam quality or high brightness.

For a non-diffraction-limited beam the brightness (or radiance) of a laser source can be defined as [22]:

$$Brightness = \frac{Power}{Area \times Solid\text{-}Angle} = \frac{P_{output}}{M_x^2 M_y^2 \lambda^2} \tag{2.17}$$

where M_x^2 and M_y^2 are the M^2-parameters in the transverse directions of the laser source (the M^2-parameter characterises the deviation from the ideal theoretical beam shape, M$^2 = 1$ for an ideal beam) emitting a power P_{output} at wavelength λ.

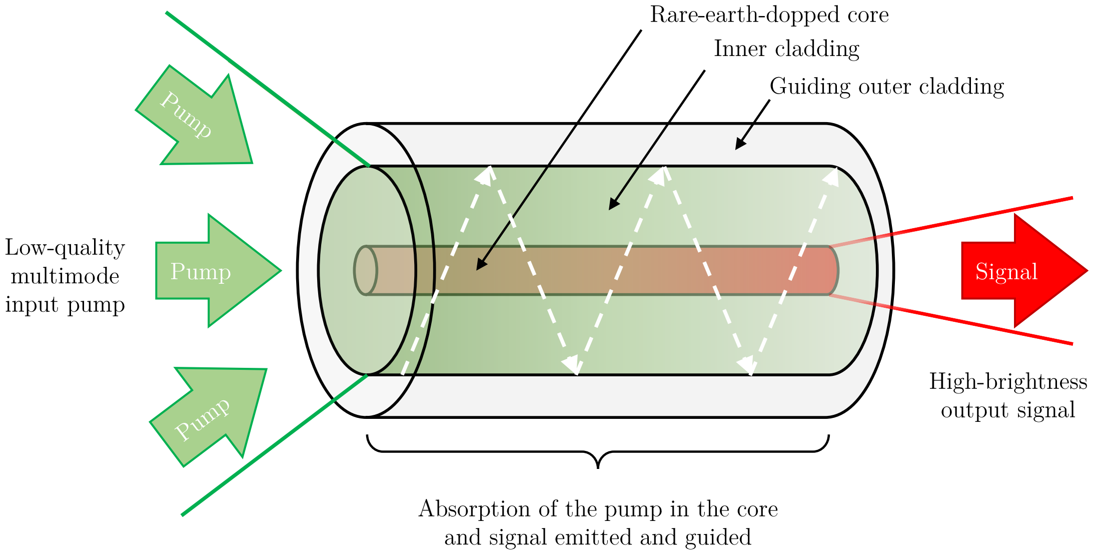

Figure 2.7: Cladding-pumping of a double-clad fibre, the high numerical aperture of the large inner cladding allows the use of low-brightness sources

Unfortunately in the case of high-power diodes, the brightness value is limited by a number of imperfections: high asymmetry of beam radii ($w_x \neq w_y$), high asymmetry of the beam quality ($M_x^2 \neq M_y^2 \neq 1$), large beam-divergence and astigmatism. However the high-power asset of these low-brightness laser diodes can be used given some pumping strategies.

A common solution is cladding-pumping in double-clad fibres as represented on Figure 2.7. Double-clad fibres are composed of a small core (that can be single-mode) where light is guided by a large inner cladding with a slightly lower refractive index. Additionally, the inner cladding is also surrounded by an outer low-index cladding and can support high-order modes. The typical refractive index profile is given on Figure 2.8. The small core contains the rare-earth ions and light from low-brightness laser diodes is coupled in the inner cladding. As this pump light propagates, it gets eventually absorbed by the ions in the core. However, in a perfectly symmetrical circular geometry, modes in the inner cladding can travel without encountering the core with a poor absorption as a result. Different strategies are therefore used to break the symmetry.

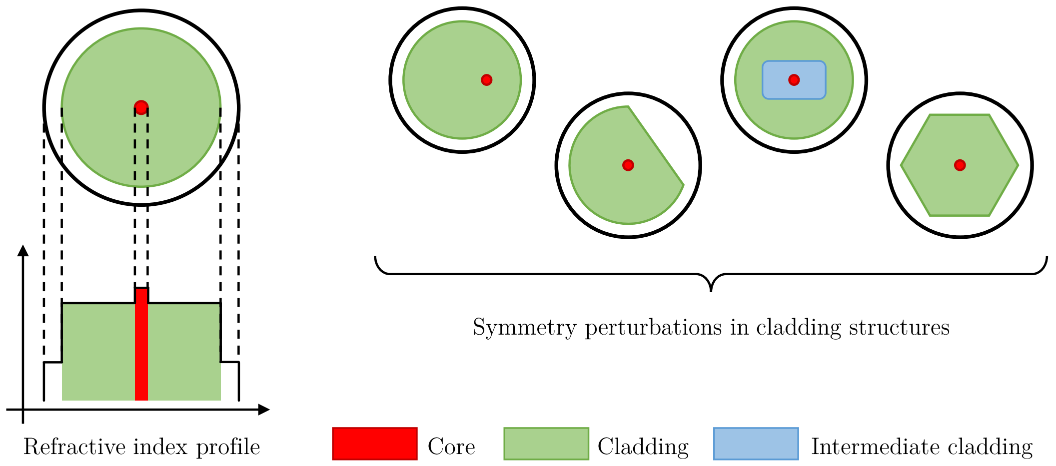

Figure 2.8: Double-clad fibre: (left) refractive index profile (right) various symmetry perturbations

End-pumping is one of the most common cladding-pumping techniques: pump light can either be coupled from free-space to the fibre (hybrid end-pumping) or fibre-combined and delivered by a multi-mode fibre (all-fibre end-pumping). Another popular pumping technique is all-fibre side-pumping: the pump light is coupled in the cladding at different locations in the fibre.

With a high-power pump source, one drawback of hybrid pumping is the necessity to align finely the free-space optics for the pump delivery. Another downside is the special care to avoid back-reflections from the fibre ends. All-fibre techniques are more attractive for an all-fibre set-up [15]. All-fibre pumping was chosen for the different gain modules developed in this project. One type of gain module involved end-pumping using a multimode-to-single-mode pump combiner. Another type of gain module involved side-pumping using the GTWave technology.

Double-clad fibres have the advantage to deliver near diffraction-limited beams from low-brightness sources. Associated with their thermal handling capabilities, they are serious competitors to bulk gain media whose phase-front is largely affected by any heating in comparison.

2.2.4 Fibre laser performance

As a gain medium is optically pumped, it generates both spontaneous and stimulated emissions until the inversion of population condition is met and stimulated emission becomes greater than spontaneous emission. When the gain medium is placed inside a resonator, the gain increases until it equates the round-trip cavity losses $L_{r.t.}$ and output coupler transmission $T_{o.c.}$:

$$G_0(1 - L_{r.t.})(1 - T_{o.c.}) = 1 \tag{2.18}$$

for a laser cavity where the fibre is single-pass (e.g. in ring oscillators) with small-signal gain G_0. Equation (2.16) provides G_0 for an ytterbium-doped fibre as a quasi-three-level system. From the previous equation, with previous notations, the pump absorption threshold $P_{p,th}$ can be deducted:

$$P_{p,th} = \frac{A_{core} h\nu_p}{\tau_f \eta_q \big[\sigma_{abs}(\lambda_l) + \sigma_{em}(\lambda_l)\big]} \Big[-\ln(1 - T_{o.c.}) - \ln(1 - L_{r.t.}) + L_{reabs} + L_{prop} \Big] \tag{2.19}$$

From this threshold power, the laser cavity generates a relatively linear output relative to the pump power P_{pump}:

$$P_{laser} \simeq \eta_{laser}(P_{pump} - P_{p,th}) \tag{2.20}$$

with η_{laser} the slope efficiency given by:

$$\eta_{laser} = \left(\frac{T_{o.c.}}{T_{o.c.} + L_{r.t.}\sqrt{\dfrac{1 - T_{o.c.}}{1 - L_{r.t.}}}} \right) \frac{\nu_l}{\nu_p} \eta_q \eta_{abs} \tag{2.21}$$

$$\approx \quad \frac{T_{o.c.}}{T_{o.c.} + L_{r.t.}} \frac{\nu_l}{\nu_p} \eta_q \eta_{abs} \qquad \text{providing} \qquad (T_{o.c.} + L_{r.t.}) \ll 1 \tag{2.22}$$

where η_{abs} is the fraction of incident pump light absorbed in the doped area. It is dependent of the doping, the fibre design and the pumping strategies.

Working with a high output coupler transmission means a higher efficiency. However it also means a higher pump threshold. Nonetheless, the pump threshold of ytterbium-doped fibres is usually relatively low. For instance, $P_{p,th}(T_{o.c.}{=}90\%) = 0.18\text{W}$ and $P_{p,th}(T_{o.c.}{=}15\%) = 13\text{mW}$ for a 10µm-diameter-core fibre pumped at 976nm as the fibres used in this thesis (supposed negligible losses, $\eta_q = 1$, $\tau_f = 1\text{ms}$, $\sigma_{abs}(\lambda_l) = 10^{-27}\text{m}^2$ and $\sigma_{em}(\lambda_l) = 2.10^{-25}\text{m}^2$. Therefore a high transmission provides overall a strong power extraction. Finally, high losses impacts negatively both the laser efficiency and the pump threshold.

As a matter of comparison, in bulk solid-state lasers the threshold pump power is strongly dependent on the size of the laser mode and pump beam and in particular how tightly the pump beam can be focussed. In a cladding-pumped fibre, the small ratio of core-to-cladding areas ensures a smaller threshold value despite fibre gain media having a lower emission cross-section.

2.2.5 Free-space to fibre coupling

In a step-index fibre, the transverse modes can be approximated with the linearly polarised modes (LP modes). A fibre is single-mode when it only supports the first order mode, the LP_{01} mode. A common tool to evaluate the number of modes a fibre can support is the V-number defined as:

$$V = \frac{2\pi}{\lambda} \rho_{core} NA \tag{2.23}$$

where ρ_{core} is the fibre core radius. For $V < 2.405$, the fibre is considered single-mode. This tool highlights that there are upper limits on the core diameter and numerical aperture for single-mode operation.

The fundamental mode in a free-space set-up is the TEM$_{00}$ mode. In a medium of refractive index n, it is propagating along the z axis in a (x, y, z) axes system, with $r^2 = x^2 + y^2$, and is given by [23]:

$$E(r,z) = E_0 \frac{w_0}{w(z)} \exp\left[-i\left(kz + \phi(z)\right) - r^2\left(\frac{1}{w^2(z)} + i\frac{k}{2R(z)}\right)\right] \tag{2.24}$$

where E_0 is the amplitude, $k = 2\pi n/\lambda$ the wavevector, $\phi(z) = \arctan(z/z_0)$ a propagation dependent phase, w_0 and $w(z)$ characterise the radius of the beam, $R(z) = z + z_0^2/z$ the radius of curvature of the beam, with z_0 the Rayleigh range.

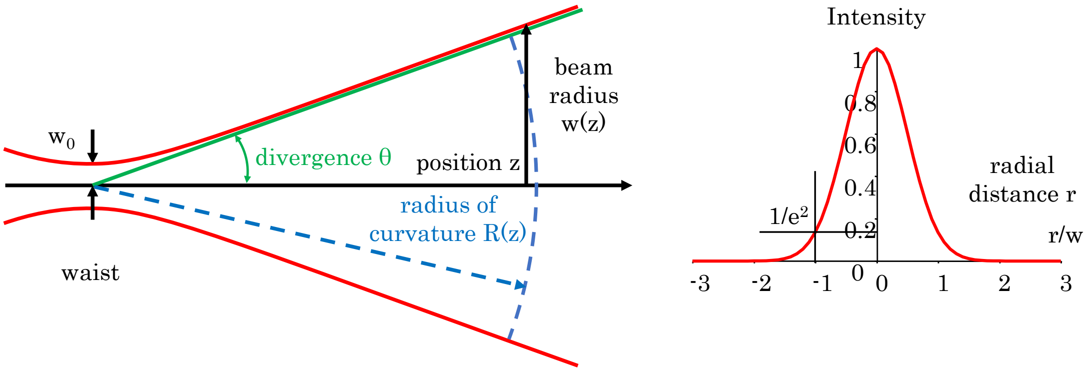

Figure 2.9: Fundamental Gaussian mode diverging from its waist along the propagation axis (left) and transverse distribution (right)

The beam profile along the propagation axis is given in Figure 2.9. The beam expands from a minimum waist of radius w_0 and the radius at any given point from that waist is given by:

$$w(z) = w_0\sqrt{1 + \left(\frac{z}{z_0}\right)^2} \quad ; \quad z_0 = \frac{\pi w_0^2 n}{\lambda} \tag{2.25}$$

where the Rayleigh range z_0 is defined as the distance over which the beam radius is increased by $\sqrt{2}$. The diameter of the beam is often defined as twice the radius $w(z)$ and about 86% of the power lies within this diameter as represented on the transverse intensity distribution in Figure 2.9 which follows the equation:

$$I(r,z) = |E(r,z).E^*(r,z)| = I_0(z)\exp\left(-\frac{2r^2}{w^2(z)}\right) \tag{2.26}$$

where $I_0(z)$ is the maximum intensity at that position z.

The divergence θ of a beam in the far field is given by:

$$\tan(\theta) = \frac{w(z)}{z} \tag{2.27}$$

where z is the distance from waist. For a small waist radius w_0 the Rayleigh range is short and the beam divergence is strong.

This project worked with single-mode fibres with NA∼0.1 and approximately 10µm-diameter cores. A focussed free-space beam with a waist diameter of 10µm presents a divergence of ∼0.07, close to the fibre NA. Coupling light from free-space to a fibre can therefore be challenging. It can be limited because the incident beam is not totally single-mode, the focussing lens is not aberration-free, or the fibre has a linear and angular misalignmement [24]. These limitations in the fibre coupling efficiencies contribute to the round-trip losses of a fibre laser. However, since fibre lasers are usually characterised by a high slope efficiency and a low power threshold, these losses are not necessarily a cause of concern for the laser operation.

Another contribution to the limitation of the fibre coupling efficiency is the 4% Fresnel reflection at the air-silica interface. This Fresnel reflection is particularly unwanted because they are also at the origin of counter-propagating beams and multi-resonators issues. There are a couple of techniques to reduce such reflection such as applying an anti-reflection coating to the fibre end. It is also possible to circumvent the effects of the reflection with an angle-cleave or a coreless fibre end-cap. However their performances are limited, they are impractical, or not suitable for high-power operations. An alternative proposed in this project is the splicing of large bulk end-caps with anti-reflection coatings. It associates the feedback reduction of coreless-fibre end-caps with the performances of bulk optics coatings. Large end-caps were developed and used during this PhD and their evolution reflects in the development of this thesis.

In conclusion, ytterbium-doped fibres are efficient laser sources. They can be pumped with low-brightness diodes and emit near diffraction-limited outputs. Their continuous emission cross-section gives access to a wide range of wavelength and, combined with second-harmonic generation, the whole green spectrum can be covered.

2.3 Enhancement cavities for frequency-doubling

As introduced at the beginning of this chapter, second-harmonic generation is only efficient when pumped at high power. A popular technique to achieve an efficient frequency-doubling is to employ a so-called enhancement cavity. Their implementation in a laser set-up requires some considerations developed in this section.

2.3.1 External enhancement cavity

An enhancement cavity is nothing more than a resonator which concentrates light from an incident signal so that the circulating power inside is much higher than its input. Its principle is close to the principle of a Fabry-Pérot etalon. Placing a nonlinear crystal in benefits to the frequency-doubling efficiency.

A Fabry-Pérot etalon is composed of two mirrors with a low transmission coefficient. Longitudinal, or axial, modes that are resonant in the etalon, contribute to constructive interferences and are transmitted whereas all the other modes contributes to destructive interference and are reflected by the input mirror. As light is "trapped" temporarily in the etalon, the intensity is locally much higher compared to the input and output. The enhancement cavity is based on the same principle and is design with the nonlinear crystal placed in and the second-harmonic process benefits from a much higher power level.

A popular geometry for the enhancement cavity is the bow-tie cavity. It is composed of four mirrors and can be design with two partially transmissive ones acting as input and output couplers. Since second-harmonic generation is the conversion of a wavelength from the near-infrared to the visible, an efficient process translates into a reduction of near-infrared power. Therefore a bow-tie can be designed with only one partially transmissive mirror acting as an input coupler and the nonlinear crystal acts as an output coupler. This configuration is represented in Figure 2.10.

When a signal is incident on the enhancement cavity, given that it is resonating, the condition for which no power is rejected by the input coupler is called the impedance-matching. This condition specifies that if the input coupler transmission is equal to the total of the losses of the cavity, including the output coupler transmission and the frequency-conversion

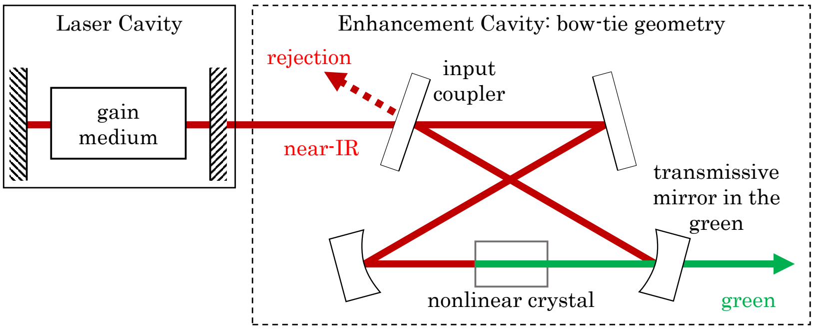

Figure 2.10: Frequency conversion in an external enhancement cavity

efficiency, then the incident signal is entirely coupled in and no circulating power is coupled out from the input mirror.

Finally, to the longitudinal mode-matching condition and the impedance-matching condition previously described comes the spatial mode-matching: can only be coupled in and resonate transverse modes that repeat themselves after a round-trip in the cavity.

The bow-tie design is composed of two arms: one arm aligned with the input signal and one arm offset where the green signal is generated. Of the four mirrors of the cavity, two are curved so that the beam radius is converted to match the requirement on the beam size for an efficient second-harmonic generation (high intensity, low divergence).

Placing the enhancement cavity on a single-frequency laser output as on Figure 2.10 is a common technique to achieve efficient second-harmonic generation. It was successfully accomplished to generate 170W of continuous-wave single-transverse-mode green power [25]. However, this technique requires the overlapping of the laser single-frequency output with one of the enhancement cavity longitudinal modes. Their relative position in the frequency spectrum varies with cavity lengths, themselves subject to variations: vibrations of the optical set-up, temperature-induced dilatation and contraction of the optical components.

This longitudinal mode-matching requires an active stabilisation to be successful. A technique consists in adjusting the enhancement cavity length using a piezo actuator on the back of one of its mirrors. The position of the mirror is adjusted according to the amount of power rejected by the input coupler. This technique proved to be successful, however, it is rather complex and also requires an electronic feedback loop. Moreover, this configuration is not suitable for a laser linewidth covering multiple longitudinal modes of the enhancement cavity as the mode-matching condition cannot be met.

Single-frequency fibre lasers suffer from a low power threshold to third-order nonlinear processes (related to the $\chi^{(3)}$ susceptibility component in Equation 2.2) known as stimulated Brillouin scattering (SBS) and stimulated Ramand scattering (SRS). These processes generate counter-propagating waves with a frequency shift and highly limit the performance of the fibre laser, including the maximum output power. Working with multiple longitudinal modes increases the SBS and SRS thresholds. However, these modes do not necessarily fulfil the mode-matching condition required for an efficient enhancement cavity coupling.

Indeed, the width and the separation between the longitudinal modes of the fibre laser and the enhancement cavity are very different as illustrated by the free spectral range (FSR) $\Delta\nu_{FSR}$ defined as:

$$\Delta\nu_{FSR} = \frac{c}{l_{r.t.}n} \tag{2.28}$$

where $l_{r.t}$ is the round-trip length of the cavity and n the refractive index inside. The bottom part of this expression becomes $\sum\limits_i l_i n_i$ for cavities with portions of media of refractive indices n_i over lengths l_i. Because of the difference of cavity lengths between the bow-tie cavity (∼1m) and the fibre laser (∼10m). The longitudinal mode-matching condition cannot be met.

This lead to consider placing the enhancement cavity not outside but inside the fibre laser cavity.

2.3.2 Internal enhancement cavity

By placing the enhancement cavity with the nonlinear crystal inside the fibre laser, only the longitudinal modes that are resonant in both the fibre laser and the enhancement cavity can circulate. Therefore the mode-matching condition is supposedly met at any time. The Advance Solid-State Sources group at the Optoelectronics Research Centre this PhD was carried out within had started exploring various versions of this last configuration with a fibre laser.

In first instance, the enhancement cavity was placed inside a linear fibre laser configuration.

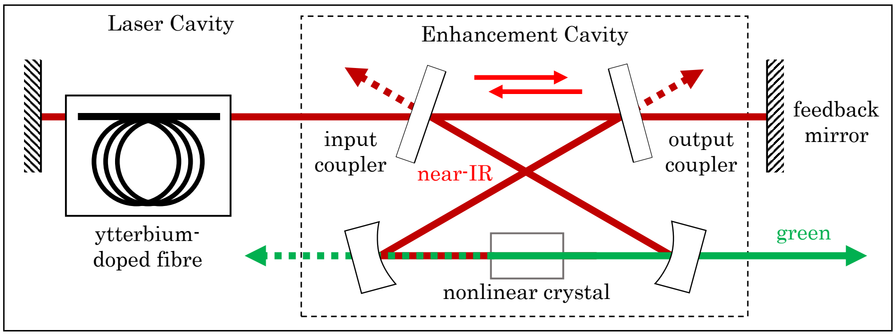

Figure 2.11: Internal enhancement cavity in a standing-wave fibre laser cavity

The bow-tie resonator was composed of an input and an output couplers aligned in one of the free-space feedback arm of the fibre laser resonator. Light generated by the fibre was coupled in and out of the enhancement cavity to meet a feedback mirror before being recoupled back in and out the enhancement cavity (see Figure 2.11). This provided ∼13W of single-mode output and 15W of nearly-single-mode output [26,27]. The major drawback of this configuration was that the enhancement cavity was designed to transmit very little power. After a double-pass after reflection on the feedback mirror, too little feedback was provided to the fibre.

From this observation, it appeared more adequate to put the enhancement cavity in a ring configuration as it would largely decrease the fibre laser round-trip loss. An internally-enhanced ring fibre laser was implemented as represented in Figure 2.12. An isolator was required to ensure the unidirectionality. Green outputs up to 17.4W were achieved in single-spatial-mode operation [28].

This reported configuration used polarisation-maintaining fibres (PM-fibres). Second-harmonic generation is a polarisation dependent process and optical fibres have a natural birefringence. This birefringence fluctuates with time and affects the polarisation state of the circulating signal in the ring. PM-fibres are efficient at maintaining a linear polarisation state over their length but they are expensive, requires other fiberised components to be polarisation-maintained and impractical to use.

For the targeted power levels of this PhD project, the gain modules available were built with non-PM ytterbium-doped fibres. A strategy to tackle the fibre birefringence uses

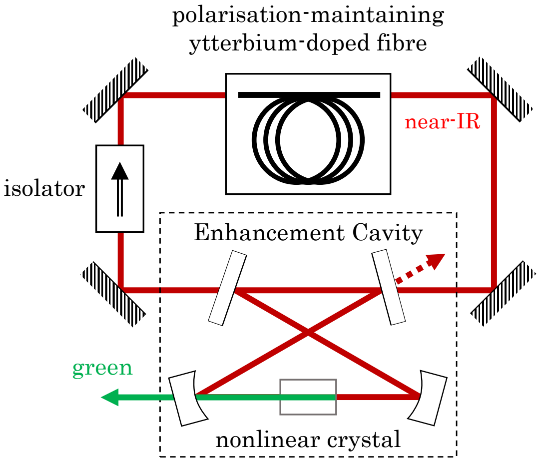

Figure 2.12: Internal enhancement cavity in a ring laser using polarisation-maintaining fibres

a Faraday mirror which stabilises the polarisation state. A double-pass through a fibre coupled to a Faraday rotator achieves a 90° rotation of any polarisation state, regardless of the fibre birefringence. The targeted experiment of this project consisted in having the enhancement cavity inside a ring fibre laser containing a Faraday mirror without the requirement for PM-fibres.

If the linear configuration and the ring configuration were proofs of concepts by successfully generating ~10-20W of single-mode green outputs, the reasons of the limitation of their power-scaling were not all identified. The implementation of the targeted set-up was therefore done step by step. Chapter 4 presents a version of the ring laser without the enhancement cavity working in the tens-of-watts regime. Chapter 6 and 7 present further power-scaling up to the ~200W pump power regime. The implementation of the enhancement cavity is not presented before Chapter 7.

Such configuration is rather complex and its alignment can be quite challenging. When a fibre is optically pumped but does not set in a laser cavity, as this is the case during alignment, it is particularly prone to self-pulsing due to the lack of feedback. The self-pulsing mechanism is unclear but the effects are the generation of high-energy pulses at the nanosecond scale which usually lead to the deterioration of the fibre. A way to prevent self-pulsing consists in ensuring that the ytterbium fibre works as an amplifier during the alignment procedure. This partially lead to the construction of the laser source presented in Chapter 3 which acted as a seed for amplification.

The seed source developed in Chapter 3 was notably designed as an amplified spontaneous emission (ASE) source with the goal of testing injection-locking of the ring fibre configuration without the enhancement cavity as presented in Chapter 5. Injection-locking forces high power resonators to generate a stable frequency output.

Bibliography

[1] R. W. Boyd, “Chapter 1 - The Nonlinear Optical Susceptibility,” in *Nonlinear Optics (Third Edition)*, third edition ed., R. W. Boyd, Ed. Burlington: Academic Press, 2008, pp. 1 – 67. [Online]. Available: http://www.sciencedirect.com/science/article/pii/B9780123694706000010

[2] ——, “Chapter 2 - Wave-Equation Description of Nonlinear Optical Interactions,” in *Nonlinear Optics (Third Edition)*, third edition ed., R. W. Boyd, Ed. Burlington: Academic Press, 2008, pp. 69 – 133. [Online]. Available: http://www.sciencedirect.com/science/article/pii/B9780123694706000022

[3] M. M. Fejer, G. A. Magel, D. H. Jundt, and R. L. Byer, “Quasi-phase-matched second harmonic generation: tuning and tolerances,” *IEEE Journal of Quantum Electronics*, vol. 28, no. 11, pp. 2631–2654, 1992.

[4] F. Hache, in *Optique Non Linéaire*, E. S. CNRS Editions, Ed., 2016.

[5] D. S. Hum and M. M. Fejer, “Quasi-phasematching,” *Comptes Rendus Physique*, vol. 8, no. 2, pp. 180 – 198, 2007, recent advances in crystal optics. [Online]. Available: http://www.sciencedirect.com/science/article/pii/S1631070506002349

[6] P. A. Franken and J. F. Ward, “Optical harmonics and nonlinear phenomena,” *Rev. Mod. Phys.*, vol. 35, pp. 23–39, Jan 1963. [Online]. Available: https://link.aps.org/doi/10.1103/RevModPhys.35.23

[7] I. Zaquine and N. Dubreuil, “Lecture notes in Second Harmonic Generation,” http://paristech.institutoptique.fr/site.php?id=26, November 2018, online; accessed 23 November 2018.

[8] V. Gapontsev, A. Avdokhin, P. Kadwani, I. Samartsev, N. Platonov, and R. Yagodkin, “SM green fiber laser operating in CW and QCW regimes and producing over 550W of average output power,” *Proceedings of SPIE - The International Society for Optical Engineering*, vol. 8964, 01 2014.

[9] J. Villarroel, J. Carnicero, F. Luedtke, M. Carrascosa, A. G.-C. nes, J. M. Cabrera, A. Alcazar, and B. Ramiro, “Analysis of photorefractive optical damage in lithium niobate: application to planar waveguides,” *Opt. Express*, vol. 18, no. 20, pp. 20 852–20 861, Sep 2010. [Online]. Available: http://www.opticsexpress.org/abstract.cfm?URI=oe-18-20-20852

[10] T. Gottwald, V. Kuhn, S.-S. Schad, C. Stolzenburg, and A. Killi, “Recent developments in high power thin disk lasers at trumpf laser,” pp. 8898 – 8898 – 7, 2013. [Online]. Available: https://doi.org/10.1117/12.2028656

[11] S. Piehler, T. Dietrich, M. Rumpel, T. Graf, and M. A. Ahmed, “Highly efficient 400W near-fundamental-mode green thin-disk laser,” *Opt. Lett.*, vol. 41, no. 1, pp. 171–174, Jan 2016. [Online]. Available: http://ol.osa.org/abstract.cfm?URI=ol-41-1-171

[12] V. Ashoori, M. Shayganmanesh, and S. A. Radmard, “Chapter 12 - Heat Generation and Removal in Solid State Lasers,” in *An Overview of Heat Transfer Phenomena*, S. N. Kazil, Ed. IntechOpen, 2012, pp. 341–376. [Online]. Available: http://dx.doi.org/10.5772/2623

[13] A. Dergachev, J. Flint, Y. Isyanova, B. Pati, E. Slobodtchikov, K. F. Wall, and P. F. Moulton, “Review of multipass slab laser systems,” *Selected Topics in Quantum Electronics, IEEE Journal of*, vol. 13, pp. 647 – 660, 06 2007.

[14] I. H. Malitson, “Interspecimen comparison of the refractive index of fused silica,” *J. Opt. Soc. Am.*, vol. 55, no. 10, pp. 1205–1209, Oct 1965. [Online]. Available: http://www.osapublishing.org/abstract.cfm?URI=josa-55-10-1205

[15] M. Zervas, “High power ytterbium-doped fiber lasers - fundamentals and applications,” *International Journal of Modern Physics B*, vol. 28, 04 2014.

[16] M. Hemenway, Z. Chen, M. Kanskar, W. Urbanek, D. Dawson, L. Bao, M. DeFranza, M. DeVito, K. Fortier, R. Martinsen, and K. Welch, “976nm high brightness

fiber-coupled laser modules for ytterbium fiber laser pumping," 2019. [Online]. Available: https://doi.org/10.1117/12.2513911

[17] D. Hanna, R. Percival, I. Perry, R. Smart, P. Suni, and A. Tropper, "An ytterbium-doped monomode fibre laser: broadly tunable operation from 1.010um to 1.162um and three-level operation at 974nm," *Journal of Modern Optics*, vol. 37, no. 4, pp. 517–525, April 1990. [Online]. Available: https://eprints.soton.ac.uk/78631/

[18] M. Ilchi-Ghazaani and P. Parvin, *Gain Saturation in Optical Fiber Laser Amplifiers*, 03 2016, pp. 297–320.

[19] H. M. Pask, R. J. Carman, D. C. Hanna, A. C. Tropper, C. J. Mackechnie, P. R. Barber, and J. M. Dawes, "Ytterbium-doped silica fiber lasers: versatile sources for the 1-1.2um region," *IEEE Journal of Selected Topics in Quantum Electronics*, vol. 1, no. 1, pp. 2–13, April 1995.

[20] D. B. Keck and A. R. Tynes, "Spectral response of low-loss optical waveguides," *Appl. Opt.*, vol. 11, no. 7, pp. 1502–1506, Jul 1972. [Online]. Available: http://ao.osa.org/abstract.cfm?URI=ao-11-7-1502

[21] Y. Tamura, H. Sakuma, Y. Yamamoto, and T. Hasegawa, "Ultra-low loss silica core fiber for long haul transmission," in *Conference on Lasers and Electro-Optics.* Optical Society of America, 2018, p. SF2K.3. [Online]. Available: http://www.osapublishing.org/abstract.cfm?URI=CLEO_SI-2018-SF2K.3

[22] P. Shukla, J. Lawrence, and Y. Zhang, "Understanding laser beam brightness: A review and new prospective in material processing," *Optics & Laser Technology*, vol. 75, pp. 40 – 51, 2015. [Online]. Available: http://www.sciencedirect.com/science/article/pii/S0030399215001656

[23] H. Kogelnik and T. Li, "Laser beams and resonators," *Appl. Opt.*, vol. 5, no. 10, pp. 1550–1567, Oct 1966. [Online]. Available: http://ao.osa.org/abstract.cfm?URI=ao-5-10-1550

[24] R. E. Wagner and W. J. Tomlinson, "Coupling efficiency of optics in single-mode fiber components," *Appl. Opt.*, vol. 21, no. 15, pp. 2671–2688, Aug 1982. [Online]. Available: http://ao.osa.org/abstract.cfm?URI=ao-21-15-2671

[25] Y. Grapov, V. Gapontsev, and A. Avdokhin, “New generation of high power green fiber laser,” in *15th International Conference on Laser Optics*, June 2012.

[26] R. Cieslak, “Power scaling of novel fibre sources,” Ph.D. dissertation, University of Southampton - Optoelectronics Research Centre, 2012.

[27] R. Cieslak and W. A. Clarkson, “Internal resonantly enhanced frequency doubling of continuous-wave fiber lasers,” *Opt. Lett.*, vol. 36, no. 10, pp. 1896–1898, May 2011. [Online]. Available: http://ol.osa.org/abstract.cfm?URI=ol-36-10-1896

[28] S. K. Vassilev, “Power scaling of novel frequency doubled continuous-wave fibre lasers,” Ph.D. dissertation, University of Southampton - Optoelectronics Research Centre, 2017.

Chapter 3

Narrow-linewidth fiberised amplified spontaneous emission source

This chapter presents the motivation, development and performance of the narrow-linewidth amplified spontaneous emission source developed in this project. The development of such source comes from two requirements: the need of an ASE source for the alignment of fibre lasers to prevent self-pulsing, and the need of a narrow-linewidth ASE source for the investigation of injection-locking of a fibre laser.

3.1 Motivation

This section presents amplified spontaneous emission (ASE), and sources based on that principle and their applications.

3.1.1 ASE source presentation

When a laser gain medium is progressively pumped, spontaneous emission can be followed by stimulated emission of that same radiation when the population inversion is met. This is the amplified spontaneous emission. The ASE spectrum is usually broad (although not as broad as the spontaneous emission spectrum) and the signal has therefore low temporal coherence. On the contrary, the spatial coherence can be high and as good as from a laser source. In particular, ASE from rare-earth doped fibres can deliver near perfect spatial coherence.

The ASE spectrum does not present longitudinal modes since it can be produced outside a resonator. However on the contrary, ASE is present in laser cavities. As the gain medium is pumped, ASE occurs and achieves population inversion until the lasing threshold is met. The cavity then amplifies laser oscillations but parasitic ASE can still occur. It is detrimental since it increases the pumping threshold and reduces the maximum attainable gain.

A major attraction of an ASE source lies in its spectral coverage. A laser spectrum is a composition of longitudinal modes with respective linewidths. On the contrary, an ASE spectrum is an uninterrupted continuous broadband signal. Thus, an ASE spectrum can cover the modes of a laser cavity as represented in Figure 3.1.

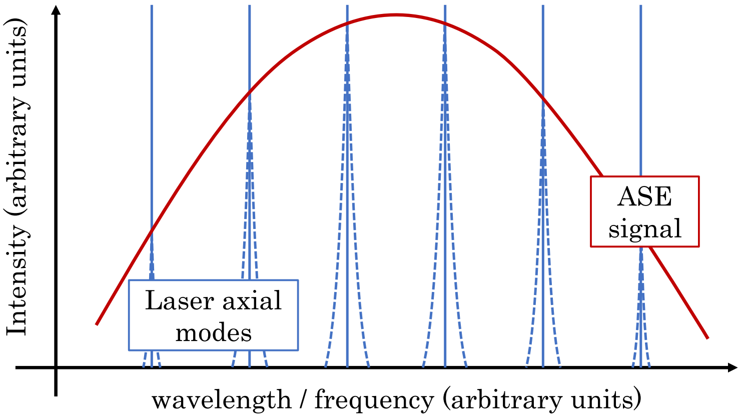

Figure 3.1: Schematic of an ASE signal covering a laser axial modes

There are two main types of ASE source. Superluminescent diodes (SLED) are compact and have an attractive price but they are particularly sensitive to feedback (leading to parasitic lasing and eventually damage). Doped fibres can be used as ASE sources, they can deliver high powers as well as good beam quality.

3.1.2 Uses of a narrow-linewidth ASE source

The requirement for a narrow-linewidth ASE source comes from the way injection-locking was attempted as presented in Chapter 5. An ASE source is also a useful way to prevent self-pulsing in fibres during alignment. This section also presents additional applications of such sources.

With their properties, different from standard lasers, ASE sources (also known as superluminescent sources) find a number of applications in optical coherence tomography [1,2], telecommunications with device characterisation [3], gyroscopes [4,5], interferometry [6], and fibre-optic sensors for the measurement of temperature, strain or pressure [7] to cite but a few [8].

Narrow-linewidth ASE sources have a number of interests. In the context of laser guide stars, a 20pm(5.3GHz)-linewidth 589nm ASE output (wavelength of the D_2 sodium line) was reported [9] as a solution to the power limitation with the current technologies [10]. Also, a high power thulium-based ASE source tuneable from 1940nm to 2010nm with a 364W 1.9nm-linewidth signal at 1980nm was generated in the prospect of laser material processing and metrology [11].

The alignment of free-space laser set-ups where the gain medium is a fibre can be challenging. Once aligned, mirrors or components providing feedback define the resonator. During the alignment, the laser cavity is open and feedback is not provided. Theoretically, a pumped fibre in an open set-up should generate an ASE signal. However in practice this is only true at very low power levels which can be too weak to be used for alignment. As the pump power is increased, parasitic lasing can occur from residual feedback sources such as imperfections and splices. Ultimately it can trigger so-called self-pulsing phenomena.

Self-pulsing expresses itself through the generation of pulses of energy at the nanosecond time-scale. There are multiple theories about its origin ranging from Q-switching, reabsorption in weakly-pumped or unpumped sections of fibres, ion-pairing, stimulated Brillouin scattering, distributed Rayleigh scattering and other nonlinear effects [12]. Self-pulsing is often met in the absence of feedback to the active fibre and when the fibre is run close to laser threshold. If the origin of self-pulsing is unclear, it appeared that stimulated Brillouin scattering contributes to the amplification of the pulses to the point of creating damage points in the fibre and ultimately leading to its fracture.

In the context of this PhD, a number of fibre gain stages were lost to self-pulsing during the alignment of laser configurations. Reassembling a fibre gain stage requires time and also money as active fibres are expensive.

Preventing self-pulsing during laser alignment can be done via saturation of the gain by an external laser source. The fibre works as an amplifier of the input signal rather than generating an unwanted ASE signal that could trigger self-pulsing mechanisms. The fibre can therefore be pumped at higher power levels and the amplified signal can, in practice, be used for alignment.

An advantage of an ASE source for gain saturation is its continuous spectrum covering all the modes of any given cavity. During the alignment of a complex laser with internal cavities (e.g. an internal enhancement cavity) the power transmitted by a closed cavity should remain constant. On the contrary, the transmission of an input with longitudinal modes would be subject to the fluctuations of the internal cavity length. The constant power levels makes alignment easier.

Finally, an attentive reader could point out that optical fibres do not require an external ASE source to saturate their gain since the flat cleaves of the fibre ends provide a 4% Fresnel reflections which is enough feedback for laser oscillations. However in this project, strategies were implemented to eliminate this feedback and it is therefore essential to saturate the gain with an external source during alignment to prevent self-pulsing.

3.2 Design

This section presents the design of the narrow-linewidth ASE source. It is based on the fibre amplification of the fibre-coupled output of an SLED with spectrum-narrowing elements.

3.2.1 Concept

The followed strategy to generate a watt-level narrow linewidth ASE source is based on the spectrum-narrowing of the ASE output from an SLED through a number of bandwidth-slicing and amplification stages summarised in Figure 3.2.

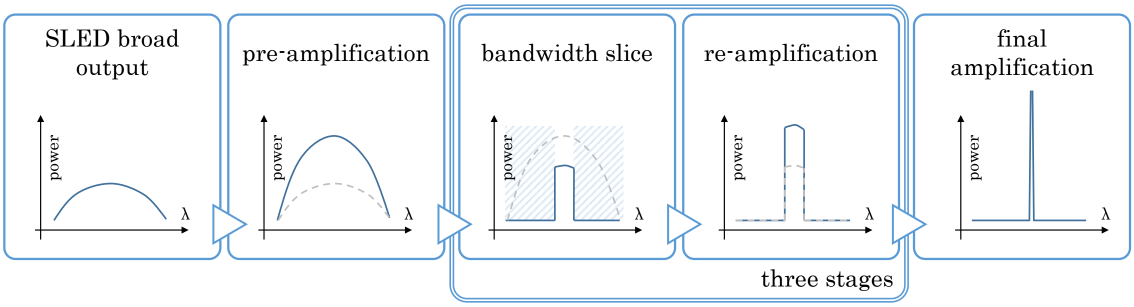

Figure 3.2: Stages of the narrow-linewidth ASE source

The initial ASE signal is provided by a commercially available SLED. Such sources have limited output powers around 10-100mW [8,13] and 300-350mW [14]. This average power is distributed over the entire emission bandwidth which can be of several tens of nanometres. A direct narrow-linewidth extraction from this output would be too low in power and at the noise level. It is preferable to narrow the bandwidth in several steps with amplifier stages in-between every bandwidth slice. This way, the reamplified signal also remains well-above the noise level. The amplification was carried out using ytterbium-doped fibre amplifiers.

The emission wavelength of interest for this project is 1075nm as this is where the gain of the fibre module used in chapter 6 and 7 is the highest. The target linewidth was initially 10-20GHz (39-77pm) for the purpose of injection-locking of Chapter 5. This linewidth is supposedly narrow enough to ensure a high power density and therefore a successful injection-locking.

3.2.2 Spectrum-narrowing method

Fibre Bragg gratings (FBG) were chosen to narrow the bandwidth of the broad ASE signal. A FBG is a periodic perturbation of the refractive index in a fibre core. It can be achieved via exposure of the core to an intense optical interference pattern [15]. The periodic index variation induces a coherent scattering at certain wavelengths. It can be compared to the dielectric coating of a bulk mirror. The spacing Λ of the interference pattern determines the centre wavelength of the portion of signal reflected by the grating known as the Bragg wavelength λ_B and is related via the relation:

$$\lambda_B = 2n_{eff}\Lambda \tag{3.1}$$

where n_{eff} is the effective refractive index of the considered mode of propagation. This is represented in Figure 3.3.

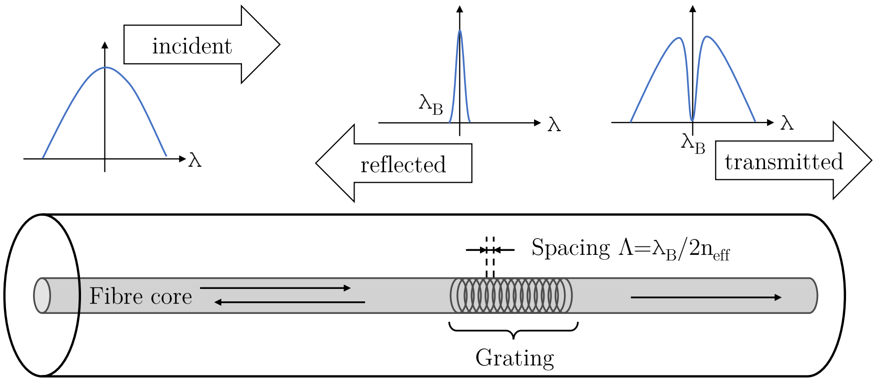

Figure 3.3: For any incident signal on the grating pitch, only a portion around the Bragg wavelength λ_B is reflected

A grating is written in a fibre when the refractive index is varied periodically. It is achieved using the interference pattern of two UV beams and the photosensitive properties of the exposed material. Depending on the exposure the bandwidth of the reflection grating can be adjusted: a long saturated exposure will broaden the reflection spectrum from a sine function or Gaussian shape to a reflection window with steep edges. The reflection bandwidth and the reflection coefficient also depend on the length over which the grating is written. These properties make FBGs valuable for wavelength selection, especially in all-fibre set-ups.

Three FBGs were used in this experiment. The two broadest were produced in-house within the Optoelectronics Research Centre with bandwidths of 0.9 and 0.3nm. Their respective Bragg wavelengths were 1074.0 and 1074.5nm below the 1075nm target. These FBGs were set on translation stages: pulling the fibre increases the periodic pattern length and induces a central reflection wavelength shift according to Equation (3.1). As a rough guide, for silica glass with a refractive index value of 1.45, the periodic index variation has an approximate 371nm spacing. A wavelength-shift of 1nm is achieved for a spacing-variation of 0.3nm. Regarding the third FBG, it was manufactured by a private company with a 1075.26nm central wavelength and a 0.09nm bandwidth. The 3 gratings were written in Hi1060 fibres.

3.2.3 Gain stages

A considerable amount of power is lost after every bandwidth reduction, gain stages were implemented to amplify signals.

Every amplification stage is composed of double-clad ytterbium-doped fibre (YDF) pumped by a 976nm laser diode in a co-propagating configuration. The YDF is side-pumped using GTWave fibres (see Figure 3.4). With this technology, first introduced by SPI Lasers [16], one or multiple multimode pump fibres are in physical contact with the YDF inner cladding in a guiding low-index polymer outer cladding. As pump light propagates it gets coupled in the YDF and eventually absorbed by the doped core. Residual pump light can remain in the pump fibre(s). This technology has proved itself up to the kilowatts regime [17–19].

The maximum gain of the YDF is obtained at 1075nm for approximately 20 meters of fibre. The active fibre was spooled on a metallic rounded rectangle connected to a large metallic plate for efficient heat extraction even though at the power levels of operations (couple watts of maximum pumping) the heat generated remained small. The rounded rectangular shape the fibre is spooled to ensures a macrobending of the fibre. This suppresses higher-order modes and the symmetry-breaking can contribute to a higher absorption efficiency. This design provides fair space management. The unabsorbed power remaining in the

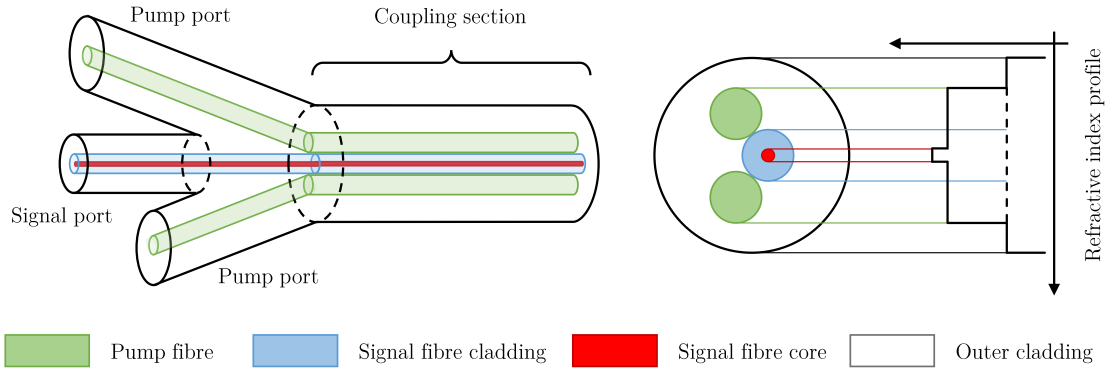

Figure 3.4: GTWave technology: (left) geometry (right) refractive index profile

pump fibre was coupled out to free-space to a beam stop on the bench.

3.2.4 Final design

The final set-up is represented in Figure 3.2. An SLED generates a multi-tens-of-nanometers broad ASE signal around 1080nm. An isolator is spliced to its output since SLEDs are particularly sensitive to feedback due to their high optical gain. The signal is first preamplified before being sent to a bandwidth slice stage and a reamplification stage three times.

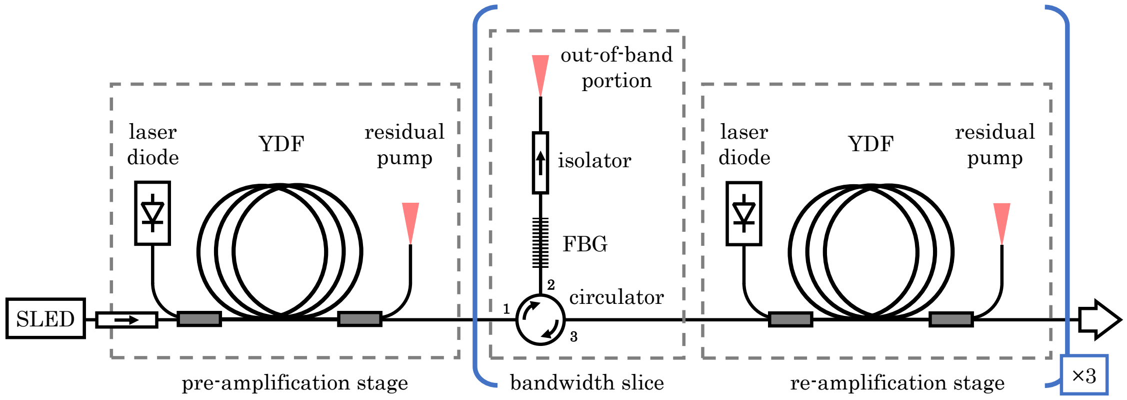

Figure 3.5: ASE source set-up

Every bandwidth-slicing stage is composed of a 3-port isolator, an FBG and an isolator. With the circulator, light can be transmitted from port 1 to port 2 and from port 2 to port 3 only. Port 1 is the input port, the FBG is connected to port 2, and port 3 is the output port.

As the input signal is incident on port 1, it gets coupled out from port 2 toward the FBG. The FBG works in reflection: the in-band portion is reflected back to port 2 and coupled out from port 3 whereas the out-of-band portion is fed to an isolator and free-space coupled out before being dumped.

The isolator role in the bandwidth-slicing stage is feedback suppression. In the presence of feedback from, for instance, the 4% Fresnel reflections of a perpendicular flat cleave, this out-of-band portion would be fed back to the port 2 of the circulator. The output signal from port 3 would be the superposition of the in-band signal with residual out-of-band portion on its side. These wings would constitute a type of optical noise. Off-the-self isolators (with ∼20dB isolation and better) were available in the lab for this feedback suppression but less costly ways could have been implemented.

After every bandwidth slice, the signal goes through a single-pass reamplification stage. Feedback in these stages would be particularly detrimental for two reasons. First, it would trigger laser oscillations and generate longitudinal modes, and the ASE nature of the signal would be lost. Secondly, these stages are high-gain: any feedback could generate signals beyond the power-handling of the fiberised components. Ultimately, it can lead to the generation of high-energy pulses which can destroy the whole set-up. Apart from the last reamplification stage, every active fibre is bounded on both ends by either an isolator or a circulator.

The isolation properties of the available circulators and isolators was limited by their power-handling. Because of their heat management capabilities and the risk of feedback, no isolator was placed on these ASE source output after the last reamplification stage in order to generate higher powers.

3.3 Results and discussions

The spectra at different locations of the set-up are reported in Figure 3.6. The SLED generates a broad 35nm-FWHM 1090nm-centered output. This signal bandwidth is consecutively reduced to 0.74nm, 0.20nm and finally 85pm centered at 1074.97nm.

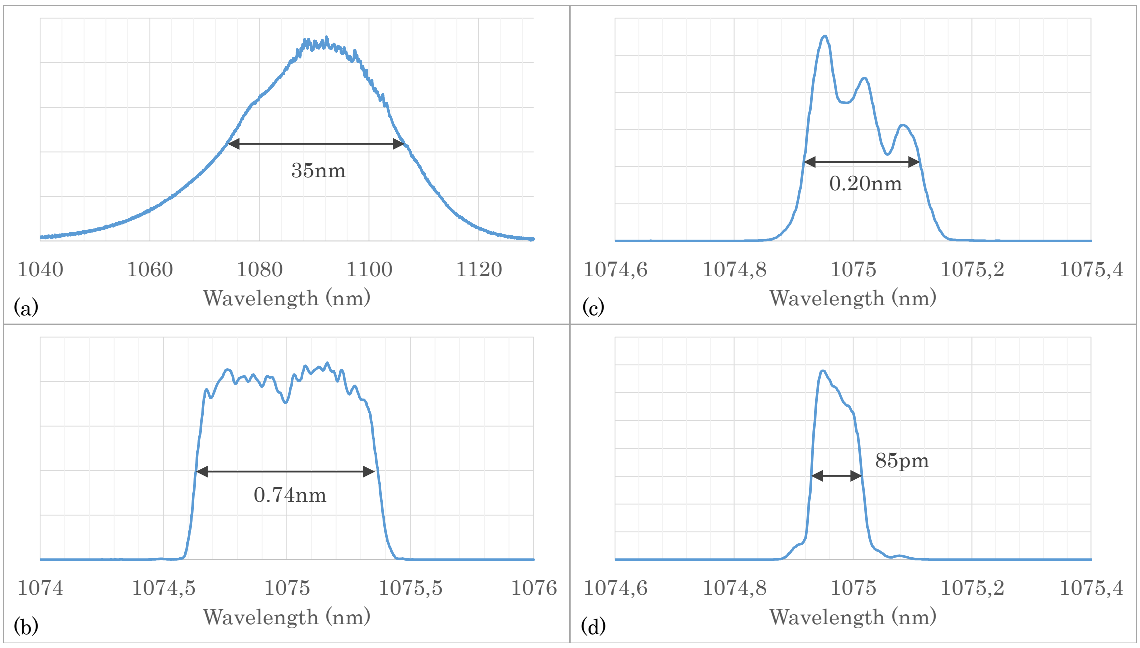

Figure 3.6: Spectrum output from (a) SLED after isolator, (b) bandwidth slice #1, (c) bandwidth slice #2, (d) bandwidth slice #3 (linear scale, arbitrary units)

The SLED output spectrum is measured after the isolator preventing any feedback. The source was run at maximum drive current and therefore with the highest gain: feedback would have led to its destruction. The SLED output spectrum is continuous but not smooth, with ripples between approximately 1080 and 1105nm, and is centred around 1090nm instead of the 1080nm centre wavelength specification.

At low drive current, the SLED could be run without isolator and the output was smooth without ripples. The isolator was design for a 1064nm centre wavelength and a ±30nm wavelength range. Its insertion loss was wavelength dependant with 1.34dB at 1064nm and 0.89dB at 1090nm. Longer wavelengths underwent a lower insertion loss hence a spectrum centred around 1090nm rather than 1080nm. The wavelength-dependance could also explain the noise-type feature.

The first bandwidth slice was done at 1075nm in what appears to be a smooth portion of the ASE output. Nonetheless, the output after slicing still present ripples. They might originate from the wavelength dependence of the circulator transmission. The fact that an

ASE source is essentially a noise source (amplification of spontaneous emission) can also contribute to this roughen spectrum. On the bright side, the first bandwidth slice offers a neat cut between the in-band and out-of-band portions of the FBG with no power left on the side.

The spectrum output from the second bandwidth slice also presents features but different from the noise-type ones previously reported. They can legitimately be attributed to the quality of the FBG reflection itself. All these features are not detrimental as the final narrow-linewidth spectrum obtained after the third bandwidth slice has a regular shape and was considered satisfying.

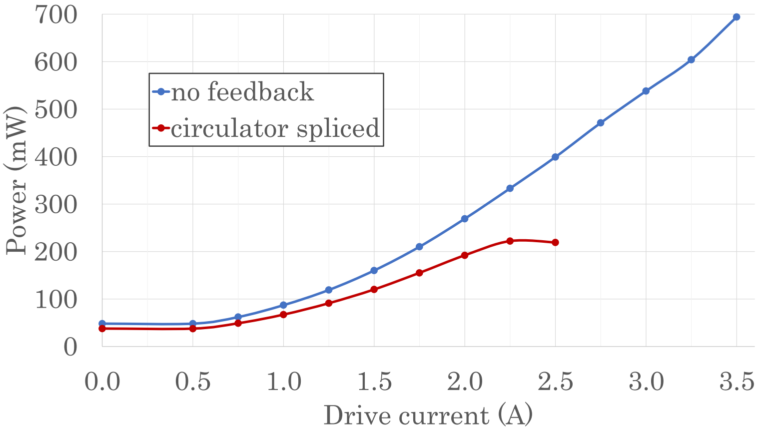

Figure 3.7: Preamplifier power output with no feedback and when spliced to a circulator

Power-wise, the SLED delivered 102mW (after isolation) amplified up to 192mW by the preamplifier stage, the maximum power that could be extracted. Figure 3.7 gives its amplification curve for two conditions: with a feedback-suppression element (a large bulk anti-reflection-coated end-cap on the fibre output end) and with a circulator spliced (power measured as off port 2). With no feedback the signal was amplified linearly whereas with the circulator the power stopped increasing from a certain drive current and started to roll-off and drop.

What is the origin of this roll-off and drop? Possibly, the circulator following the preamplification stage eventually provided feedback and laser oscillations were triggered, generating signals in both direction. The backward portion would be lost and would explain the downfall trend. However according to specifications, it has a 300mW power-handling in continuous-wave operation and a 55dB return loss (~1µW feedback for 300mW incident power). The return loss is too great to sustain laser oscillations.

Another explanation could be thermal beam distortion. Despite the specified 300mW power-handling value given by the manufacturer, the lack of exit port for the rejected light induces a temperature increase of the whole device which eventually distort the beam direction [20]. Portion of the deviated beam would not be transmitted by the circulator. This explanation is reinforced by the fact that the downfall trend was not only function of the pump power but also varying with time with a few seconds time-scale. Heat-sinking the circulators and isolator could therefore be useful to perhaps attain output powers closer to 300mW.

Similar behaviour was also observed in the subsequent reamplification stages but with power outputs around 200-250mW. For each stage, the drive current was chosen in the linear portion of the curve but far enough from roll-over.

The two first reamplification gain values were $G_{reamp\#1} \sim G_{reamp\#2} \sim 60$. A feedback-suppression element was put on the third reamplification stage output so that this whole ASE source delivered 2.97W with a last reamplification gain $G_{reamp\#3} = 60.6$.

3.4 Conclusions and prospects for development

A 2.97W 85pm-bandwidth 1074.97nm-centred all-fibre ASE source was developed. It is based on the spectrum-narrowing of a SLED output using FBGs, and reamplification stages using ytterbium-doped fibres.

An alternative to the SLED as the original ASE source would be using an ytterbium-doped fibre [21, 22]. One end of the fibre generating the ASE signal could be spliced to a fibre loop mirror while the other end would require a feedback-suppression strategy. This requirement is similar to what is done inside a SLED structure: one of the active layer face is reflective whereas the output face has an anti-reflection coating.

In terms of further reducing the spectrum linewidth, this experiment would require an additional bandwidth slice with a narrower FBG but this experiment used the narrowest commercially-available ones at a reasonable price, at this wavelength. In order to reach a bandwidth lower than 85pm, the use of a Fabry-Pérot cavity can be considered.

In terms of power-scaling, the final reamplification stage can be redesigned to amplify the powers at least to the few-tens-of-watts level. However if one considers putting an isolator on the output, this isolator must be able to handle the aimed power levels. The power-scaling would also require to thermally contact the amplification stages to heat sinks.

Finally, the set-up can be redesigned with exclusively polarisation-maintaining components in order to deliver a linearly-polarised output. This was not done in the first place since the costs associated are higher.

Back to the context of this PhD project, this ASE source was frequently used for the alignment of complex laser cavities. At times it received unfortunate feedback from laser experiments. The final gain stage would blow up and the adjacent circulator would take the hit. It is essential to protect this source from feedback. The last reamplification stage being unprotected, it would require a walls-level protection such as a fibre-to-free-space or simply a free-space isolator as they can usually handle this sort of powers.

Still for this PhD project, this ASE source was also used for the injection-locking experiment of Chapter 5.

Bibliography

[1] I. Trifanov, P. Caldas, L. Neagu, R. Romero, M. O. Berendt, J. A. R. Salcedo, A. G. Podoleanu, and A. B. Lobo Ribeiro, “Combined neodymium-ytterbium-doped ASE fiber-optic source for optical coherence tomography applications,” *IEEE Photonics Technology Letters*, vol. 23, no. 1, pp. 21–23, Jan 2011.

[2] A. A. Ferin, A. B. Rulkov, J. C. Travers, S. V. Popov, and J. R. Taylor, “Broadband, low intensity noise source for optical coherence tomography at 1.8μm,” in *2007 Conference on Lasers and Electro-Optics (CLEO)*, May 2007, pp. 1–2.

[3] X. Wang, H. Ming, and W. Huang, "Band selective ASE source for dual-band DWDM device characterization and metro networks," *Proceedings of SPIE - The International Society for Optical Engineering*, vol. 6019, 11 2005.

[4] P. Nageswara Rao and S. K Shrivastava, "1.3mW 1550nm Er-doped super fluorescent fiber source for missile fiber optics gyroscope," *JOURNAL OF ADVANCES IN PHYSICS*, vol. 5, pp. 993–1000, 10 2014.

[5] B. Cadier, S. Ferrand, J.-J. Bonnefois, E. Pinsard, A. Laurent, T. Robin, C. Moluçon, and M. Boutillier, "Radiation resistant erbium doped fiber for ASE source and fiber gyroscope application," 11 2017, p. 106.

[6] O. Sasaki, Y. Ikeada, and T. Suzuki, "Superluminescent diode interferometer using sinusoidal phase modulation for step-profile measurement," *Appl. Opt.*, vol. 37, no. 22, pp. 5126–5131, Aug 1998. [Online]. Available: http://ao.osa.org/abstract.cfm?URI=ao-37-22-5126

[7] S. W. Harun, M. Yasin, H. Rahman, H. Arof, and H. Ahmad, *Fiber Optic Temperature Sensors*, 02 2012.

[8] M. Rossetti, J. Napierala, N. Matuschek, U. Achatz, M. Duelk, C. Vélez, A. Castiglia, N. Grandjean, J. Dorsaz, and E. Feltin, "Superluminescent light emitting diodes: the best out of two worlds," 2012. [Online]. Available: https://doi.org/10.1117/12.912759

[9] X. Chen, Y. Lu, H. Hu, L. Tong, L. Zhang, Y. Yu, J. Wang, H. Ren, and L. Xu, "Narrow-linewidth, quasi-continuous-wave ASE source based on a multiple-pass Nd:YAG zigzag slab amplifier configuration," *Opt. Express*, vol. 26, no. 5, pp. 5602–5608, Mar 2018. [Online]. Available: http://www.opticsexpress.org/abstract.cfm?URI=oe-26-5-5602

[10] J.-P. Pique and S. Farinotti, "Efficient modeless laser for a mesospheric sodium laser guide star," *J. Opt. Soc. Am. B*, vol. 20, no. 10, pp. 2093–2101, Oct 2003. [Online]. Available: http://josab.osa.org/abstract.cfm?URI=josab-20-10-2093

[11] J. Liu, H. Shi, C. Liu, and P. Wang, "Widely-tunable high-power narrow-linewidth thulium-doped all-fiber superfluorescent source," in *CLEO: 2015*. Optical Society of America, 2015, p. JTh2A.98. [Online]. Available: http://www.osapublishing.org/abstract.cfm?URI=CLEO_SI-2015-JTh2A.98

[12] B. Upadhyaya, "Self-pulsing dynamics in Yb-doped fiber lasers," in *Fiber Laser*. IntechOpen, 03 2016, ch. 1, pp. 1–20.

[13] A. Chamorovskiy, "Insight into superluminescent diodes," *Science Omega Review Europe*, p. 28, 08 2013.

[14] Innolume GmbH, "300mW SLD at 1060 nm," https://www.innolume.com/news/n_141031.htm, October 2014.

[15] K. O. Hill and G. Meltz, "Fiber bragg grating technology fundamentals and overview," *Journal of Lightwave Technology*, vol. 15, no. 8, pp. 1263–1276, Aug 1997.

[16] A. B. Grudinin, D. N. Payne, P. W. Turner, L. J. A. Nilsson, M. N. Zervas, M. Ibsen, and M. K. Durkin, "Multi-fibre arrangement for high power fibre lasers and amplifiers," May 22 2007, uS Patent 7,221,822.

[17] H. Zimer, M. Kozak, A. Liem, F. Flohrer, F. Doerfel, P. Riedel, S. Linke, R. Horley, F. Ghiringhelli, S. Desmoulins, M. Zervas, J. Kirchhof, S. Unger, S. Jetschke, T. Peschel, and T. Schreiber, "Fibers and fiber-optic components for high-power fiber lasers," 2011. [Online]. Available: https://doi.org/10.1117/12.879622

[18] H. Zhan, Q. Liu, Y. Wang, W. Ke, L. Ni, X. Wang, K. Peng, C. Gao, Y. Li, H. Lin, J. Wang, F. Jing, and A. Lin, "5kW GTWave fiber amplifier directly pumped by commercial 976nm laser diodes," *Opt. Express*, vol. 24, no. 24, pp. 27 087–27 095, Nov 2016. [Online]. Available: http://www.opticsexpress.org/abstract.cfm?URI=oe-24-24-27087

[19] H. Zhan, K. Peng, Y. Wang, X. Wang, L. Ni, S. Liu, Y. Li, J. Yu, L. Jiang, J. Wang, F. Jing, and A. Lin, "6kW GTWave fiber amplifier," in *Asia Communications and Photonics Conference*. Optical Society of America, 2017, p. M1A.3. [Online]. Available: http://www.osapublishing.org/abstract.cfm?URI=ACPC-2017-M1A.3

[20] F. W. Quelle, "Thermal distortion of diffraction-limited optical elements," *Appl. Opt.*, vol. 5, no. 4, pp. 633–637, Apr 1966. [Online]. Available: http://ao.osa.org/abstract.cfm?URI=ao-5-4-633

[21] P. Ma, R. Tao, X. Wang, P. Zhou, and Z. Liu, "High-power narrow-band and polarization-maintained all fiber superfluorescent source," *IEEE Photonics Technology Letters*, vol. 27, no. 8, pp. 879–882, April 2015.

[22] O. Schmidt, M. Rekas, C. Wirth, J. Rothhardt, S. Rhein, A. Kliner, M. Strecker, T. Schreiber, J. Limpert, R. Eberhardt, and A. Tünnermann, "High power narrow-band fiber-based ase source," *Opt. Express*, vol. 19, no. 5, pp. 4421–4427, Feb 2011. [Online]. Available: http://www.opticsexpress.org/abstract.cfm?URI=oe-19-5-4421

Chapter 4

Wavelength-tuneable linearly-polarised ytterbium-doped fibre ring laser

This chapter presents a ring fibre laser configuration delivering a few tens-of-watts power in the near-infrared regime. It proposes to test the control of the polarisation state using a Faraday mirror whose concept is introduced. This laser design sets as a milestone toward building an efficient green fibre laser.

4.1 Polarisation control in fibre lasers

Polarisation control is essential in the context of frequency-doubling in a nonlinear crystal. The birefringence of optical fibres make polarisation maintenance rather difficult and the Faraday mirror approach appears to offer an attractive solution.

4.1.1 Birefringence in fibres

The denomination 'single-mode' attributed to a fibre can be misleading as it refers only to the spatial mode i.e. the transverse distribution of the electric field. However, a single-mode signal can support different polarisation states. A single-mode cavity presents two resonant polarisation states which are the polarisation eigenmodes. Preserving the polarisation state in optical fibres is complicated because of their birefringence.

Birefringence is a property of some anisotropic materials where the refractive index varies with the direction of propagation and the electric field direction. In the first instance, optical fibres should theoretically be isotropic as they are made of amorphous silica glass. However in practice, the symmetry of the cylindrical geometry of the fibre core is broken and varies locally all along its length, plus the core is under mechanical stress. Fibres are overall anisotropic.

In first instance, the fibre presents a linear birefringence: the core presents two orthogonal fast and slow axes with separate refractive index values. A linear polarisation parallel to one of these axes remains linear however if it sets at an angle between them, it experiences a phase retardation, similarly to a waveplate. The birefringence strength and the direction of the fast and slow axes is different for any section of a considered fibre so that over the total length, an overall phase retardation exists as the sum of all these sections. Unfortunately, the birefringence is subject to temperature and stress variations in the fibre and the overall retardation varies accordingly. It is therefore difficult to maintain a polarisation state in a fibre [1].

In the first instance, the phase retardation can be readjusted using half and quarter waveplates. Another option consists in adding a counteracting birefringence via bending [2] or twisting [3] of the fibre. However since the birefringence varies with time, these strategies should be associated with an active feedback loop, adding complexity and increasing costs.

The fibre birefringence can also be tackled with polarisation-maintaining (PM) fibres. They are designed to introduce a large birefringence with well-defined fast and slow axes by, for example, putting the fibre core under stress. A popular geometry is the PANDA fibre where stress rods are present on both sides of the core as presented on Figure 4.1. Unfortunately, these fibres are expensive due to a more complex manufacturing process.

Additionally, in practice, any other fiberised component also needs to be polarisation-maintaining, increasingly rapidly the costs. Also, the splicing of PM-fibres requires a continuity of the fast and slow axes and therefore a splicer that can handle angular adjustment. Putting fibre end-caps can also be challenging due to the difference of thermal expansion of the stress rods relative to the core and cladding. Finally, the stress rods are scattering sources and reduces the performances of cladding-pumped fibres.

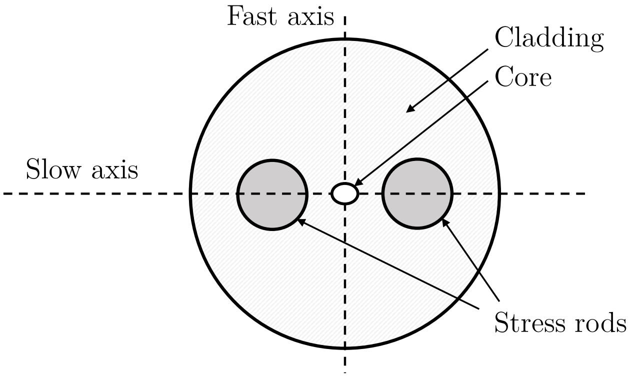

Figure 4.1: Typical PANDA fibre geometry

PM-fibres were previously considered for the design of the green fibre laser. They were implemented in the research group this PhD took place, however for the reasons mentioned above, and due to the lack of available high-power PM-fibre gain stage, another strategy was considered that does not require PM-fibres: the Faraday mirror approach.

4.1.2 Faraday mirror approach

Faraday rotators achieve a 45° rotation of the polarisation. When associated to a mirror returning the light the Faraday rotator, it forms a Faraday mirror as represented in Figure 4.2. A double-pass through a Faraday mirror rotates any polarisation state by 90°.

Now considering a single-pass through a fibre, as previously described, it can be assimilated to a waveplate with fast and slow axes whose position relative to an horizontal direction x and a vertical direction y vary. Any incident electric field $\overrightarrow{E}$ with components $\overrightarrow{E_x}$ and $\overrightarrow{E_y}$ in both directions most probably comes out elliptical. After double-passing the Faraday rotator, this signal is rotated so that the two components are switched. On a second

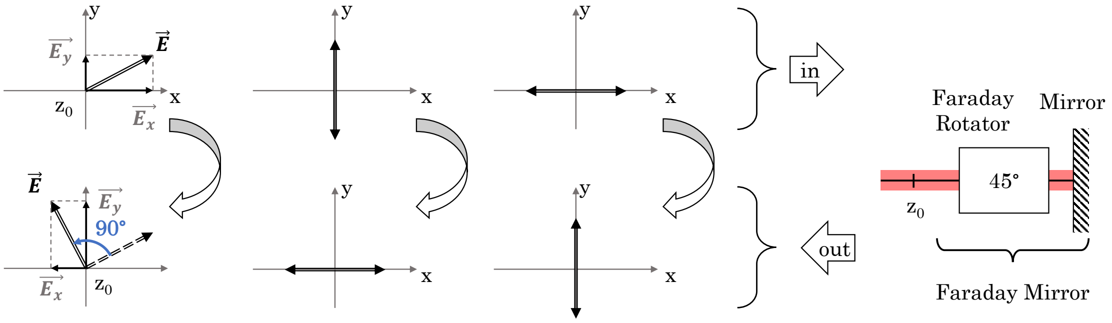

Figure 4.2: Faraday mirror: 90° polarisation rotation

pass through the fibre, the phase retardation applies again but this time on the switched electric field components. The polarisation output from the fibre is therefore 90° rotated in comparison with the input polarisation.

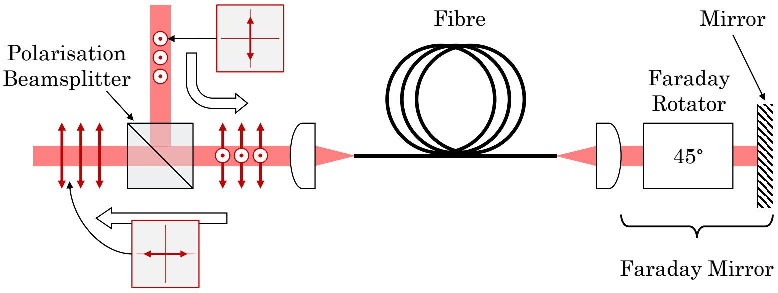

Figure 4.3: Fibre coupled to a Faraday mirror: 90° polarisation rotation

In summary, a signal double-passing a fibre coupled to a Faraday mirror experiences a 90° rotation of its polarisation. The effects of the phase retardation induced by the first pass through the fibre are unravelled by the phase retardation on the second pass thanks to the 90° polarisation rotation of the Faraday mirror. In practice, a linear horizontal polarisation is returned vertical and vice-versa as illustrated in Figure 4.3.

The general plane wave equation of a signal propagating along the z axis in a $(\overrightarrow{u_x}, \overrightarrow{u_y}, \overrightarrow{u_z})$ Euclidean space is given by:

$$\overrightarrow{E}(z,t) = E_{0x}\cos(\omega t - kz + \phi_x)\overrightarrow{u_x} + E_{0y}\cos(\omega t - kz + \phi_y)\overrightarrow{u_y} \tag{4.1}$$

where ω is the angular frequency, k the wavenumber, E_{0x} and E_{0y} the amplitudes and ϕ_x and ϕ_y the initial phases in the x and y directions respectively. In the Jones formalism [4], the electric field is written as:

$$\begin{pmatrix} E_x(t) \\ E_y(t) \end{pmatrix} = \begin{pmatrix} E_{0x}\, e^{i(\omega t - kz + \phi_x)} \\ E_{0y}\, e^{i(\omega t - kz + \phi_y)} \end{pmatrix} = V_J \,.\, e^{i(\omega t - kz)} \tag{4.2}$$

with the Jones vector V_J which characterises the polarisation state at a given point:

$$V_J = \begin{pmatrix} V_x \\ V_y \end{pmatrix} = \begin{pmatrix} E_{0x}\, e^{i\phi_x} \\ E_{0y}\, e^{i\phi_y} \end{pmatrix} \tag{4.3}$$

Optical systems are often described by a Jones Matrix M_J. For an input vector V_{in} on that optical system corresponds an output vector V_{out} given by:

$$V_{out} = M_J \,.\, V_{in} \tag{4.4}$$

Table 4.1 gives the components of the Jones matrices of relevance here. The fibre phase retardation is defined as $\psi = 2\pi/\lambda\,(n_f - n_s)\, l_{fib}$ with n_f and n_s the refractive indices relative respectively to the fast and slow axes and a fibre length l_{fib}. The Jones matrix expression for an arbitrary birefringent material is rather complex. In first instance, this description considers a linear birefringence as expressed in [5].

Rayleigh scattering is considered negligible and so are Brillouin and Raman scatterings in first instance (see Chapter 6 for stimulated Brillouin and Raman scatterings).

Fibre birefringence (linear phase retardation ψ)	M_{fib}	$\begin{pmatrix} e^{i\frac{\psi}{2}} & 0 \\ 0 & e^{-i\frac{\psi}{2}} \end{pmatrix}$
Rotator (rotation angle θ)	$R_{rot}(\theta)$	$\begin{pmatrix} \cos\theta & -\sin\theta \\ \sin\theta & \cos\theta \end{pmatrix}$
Mirror reflection	M_{mir}	$\begin{pmatrix} -1 & 0 \\ 0 & 1 \end{pmatrix}$

Table 4.1: Jones matrices of phase retardation, rotation and mirror reflection

The round-trip matrix is given by:

$$M_{round\text{-}trip} = M_{fib}.R_{rot}(-45^\circ).M_{mir}.R_{rot}(45^\circ).M_{fib} \tag{4.5}$$

For $V_{in} = \begin{pmatrix} V_x \\ V_y \end{pmatrix}$, the output after round-trip is $V_{out} \equiv \begin{pmatrix} V_y \\ V_x \end{pmatrix}$ where the components are switched. Therefore a linear vertical polarised input $\begin{pmatrix} 0 \\ 1 \end{pmatrix}$ returns a linear horizontal polarised output $\begin{pmatrix} 1 \\ 0 \end{pmatrix}$ and vice-versa. Similarly, a left-hand circular polarisation $\frac{\sqrt{2}}{2}\begin{pmatrix} 1 \\ +i \end{pmatrix}$ returns a right-hand circular polarisation $\frac{\sqrt{2}}{2}\begin{pmatrix} 1 \\ -i \end{pmatrix}$.

In summary, the polarisation state variation induced by the birefringence of fibres can be compensated when the fibre is coupled to a Faraday mirror. An linear input polarisation returns linear with a 90°-rotation. An input circular polarisation comes back circular with an inverted handedness. This configuration therefore allows to use non-PM fibres while keeping control over the polarisation state. This scheme is applied to various experiments in this PhD project.

4.1.3 Spatial hole burning and Faraday mirrors

Several authors reported about how Faraday mirrors could or could not tackle spatial hole burning. This section provides clarification on that matter.

Considering an optical fibre with a mirror on one end, a single-frequency narrow-bandwidth signal double-passing the fibre interferes with itself. It results in a standing-wave pattern with a periodic distribution of portions of low gain (nodes) and high gain (anti-nodes). The gain is saturated in the anti-nodes. As a result, maintaining a high laser efficiency or achieving a narrow-bandwidth or single-mode emission can become challenging. Yet, spatial hole burning can be used to stabilise the single-frequency operation of a saturable absorber such as optical fibres [6].

Considering an anisotropic gain medium associated with a Faraday mirror. An input linear polarisation returns rotated by 90° and there is therefore no interference between the two orthogonal signals. Now considering a birefringent gain medium coupled to a Faraday mirror, a first description showed that, at any point, forward and backward polarisations are orthogonal and therefore spatial hole burning should not occur [7].

A complementary study highlighted that surely the two waves travelling in opposite direction were orthogonal but everywhere the polarisation is not linear, the waves are interfering. As the polarisation state is mostly elliptical along the fibre length, it has horizontal and vertical components which interact with the components of the 90°-rotated polarisation returning on the way back [8].

For this reason, spatial hole burning should be expected in a fibre coupled to a Faraday mirror. Although, in the following experiment, the laser runs on a large number of longitudinal modes. Each mode has its own standing-wave pattern due to dispersion (different phase velocity for each mode) with nodes and anti-nodes distributions. The sum of all these overlapping modes averages out the gain distribution along the fibre length. The gain should be uniform and strong spatial hole burning should not occur.

4.2 Experimental set-up

This experiment proposes a wavelength-tuneable linearly-polarised fibre laser configuration using a standard ytterbium-doped fibre as a gain medium and coupled to a Faraday mirror.

Using an active fibre coupled to a Faraday mirror as an amplifier is not new and was successfully achieved early on during the development of erbium-doped fibre amplifiers [9, 10]. Also, a linearly-polarised wavelength-tuneable erbium-doped fibre laser was also reported [11]. However these were achieved in the tens-of-milliwatts to the 1W regime.

4.2.1 Set-up overview

The proposed optical set-up for this experiment is given in Figure 4.4. The gain medium is a diode-pumped ytterbium-doped fibre gain module working in a double-pass configuration. On one end, the beam is collimated by an aspheric lens toward the Faraday mirror: this is the Faraday mirror arm (FMA). On the other end, a similar aspheric lens collimates the beam to a thin-film polariser (TFP) which opens a ring: this is the free-space arm (FSA).

A technique to select the polarisation in a laser cavity consists in placing a polariser in the resonator which favours the propagation of one preferential polarisation state over the others. As only the modes with the highest gain can successfully resonate, all the polarisation states experiencing a strong round-trip loss are excluded. For instance, a polariser working in transmission would allow the propagation of the *p*-polarisation at the expense of the *s*-polarisation, and vice-versa when working in reflection.

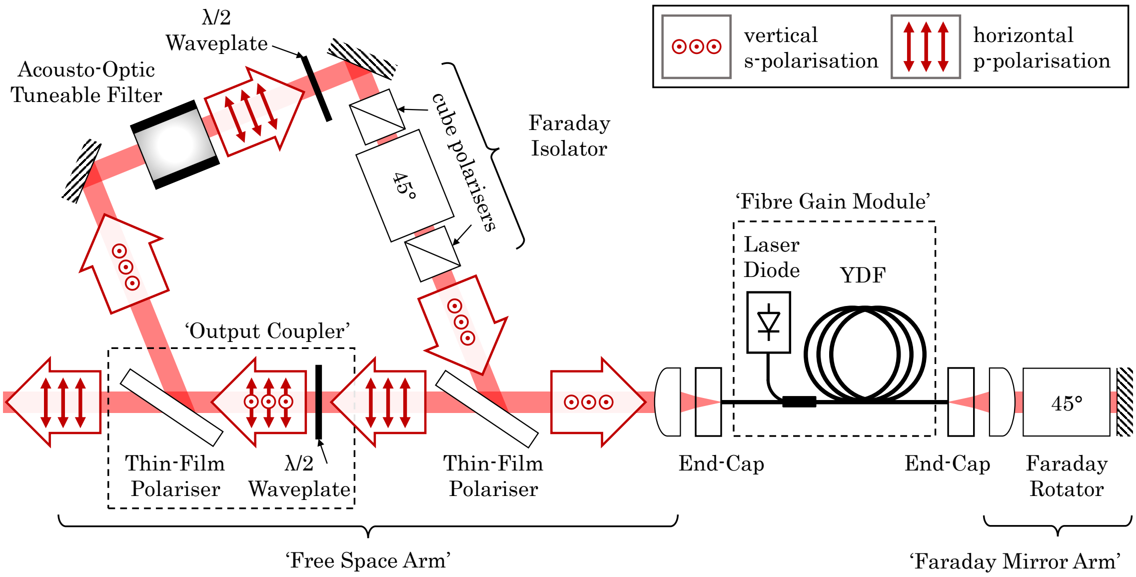

Figure 4.4: Set-up for linearly-polarised wavelength-tuneable ytterbium-doped fibre ring laser and polarisation distribution

In this experiment, the ring is unidirectional thanks to the combination of a thin-film polariser set at Brewster's angle (56°) with a Faraday isolator. Any horizontal polarisation against the optic bench output from the fibre in the FSA is transmitted by the polariser and can achieve a round-trip in the ring without polarisation loss. After completion of the loop, the polarisation comes back vertical on the polariser and is reflected toward the fibre. Meanwhile, the vertical polarisation input to the fibre coupled to the Faraday mirror is returned horizontal.

The Faraday isolator is composed of a Faraday rotator which rotates a linear polarisation by 45°. It has input and output cube polarisers which only allows one linear polarisation to go forward and beam out any polarisation state on the way backward. This ensures the unidirectionality.

The output coupler is composed of a half-waveplate and an additional thin-film polariser placed afterwards. Half-waveplate phase retardation rotates the polarisation without affecting its linear nature. The degree of rotation depends on the angle between the axes of the plate and the electric field direction. The horizontal component of the tilted polarisation is output from the laser by the thin-film polariser while the vertical component continues its propagation in the ring. These two optics constitute an output coupler whose transmission coefficient can be tuned with the angle of the half waveplate axes.

Ytterbium-doped fibres can emit over a broad spectrum. A wavelength-selective element was introduced to select the wavelength of operation. An acousto-optic tuneable filter (AOTF) is placed inside the feedback part of the ring, after the output coupler. It is a type of acousto-optic modulator which are composed of a transparent and birefringent crystal or glass whose refractive index can be tuned via the application of an external radio-frequency signal. Depending on the frequency and intensity of the applied electric field, the AOTF diffracts a portion of light at a specific wavelength with a given linewidth. In this experiment, the diffracted signal is rotated by 90°: an additional half-waveplate is used to readjust the polarisation orientation in accordance with the Faraday isolator transmission.

It should be noted that as this experiment is set, there is a limited amount of optics in the FSA on the path from the fibre to the output coupler. This is where the power is supposedly the highest. The position of components with a non-negligible transmission loss like the AOTF and the Faraday isolator is essential. The application of the Rigrod analysis [12], which gives the distribution of power in a laser configuration, would suggest to place these pieces where the power is the smallest so that their transmission loss have a minimum impact on the laser performances.

Indeed, for an output power $P_{o.c.}$ from the output coupler with a transmission $T_{o.c.}$, and a random optic with a non-negligible power loss P_{loss} and transmission T_{loss}, the ratios of extracted power over the power lost depending on the position of the lossy optics are:

$$\left.\frac{P_{o.c.}}{P_{loss}}\right|_{before} = \frac{T_{o.c.}T_{loss}}{1-T_{loss}} \tag{4.6}$$

$$\left.\frac{P_{o.c.}}{P_{loss}}\right|_{after} = \frac{T_{o.c.}}{(1-T_{out})(1-T_{loss})} \tag{4.7}$$

where subscript *before* corresponds to an optic placed before the output coupler and subscript *after* refer to an optic placed after, as it is done in this experiment. For $T_{o.c.} = 90\%$ and $T_{loss} = 95\%$ for example, $P_{o.c.}/P_{loss}|_{before} = 17.1$ and $P_{o.c.}/P_{loss}|_{after} = 180$. The ratio when the transmission optic is placed before the output coupler is small in comparison to the ratio when it is placed after, even though its transmission value is high (95% in this example). This example highlights how the extracted power is dependent on the position of lossy optics with respect to the output coupler.

The application of the Rigrod analysis also gives an idea of the single-pass gain G of the gain module. Its expression is obtained from the calculation of the power evolution in the set-up. Above laser threshold, the gain is clamped and, at any location on the laser path, the power should repeat itself after round-trip in the cavity. The gain therefore is:

$$G^2 = \frac{1}{(1 - T_{o.c.})T_{loss}\eta_c^2 T_{FR}^2} \tag{4.8}$$

For a transmission coefficient $T_{loss} = 95\%$ representative of the AOTF and the Faraday isolator together, an output coupler transmission $T_{o.c.} = 90\%$, a fibre recoupling efficiency $\eta_c = 75\%$, a Faraday rotator transmission $T_{FR} = 99\%$, the single-pass gain is $G = 4.4$.

The output coupler transmission is wanted high to maximise the power extracted from the cavity. At first glance this means very low feedback to the fibre. On top of this the fibre recoupling efficiencies also provides a strong loss contribution. One could suggest that it would be difficult for a laser to operate in such configuration. However, active fibre can achieve significant gain levels as high as the one calculated here to counterbalance the losses.

4.2.2 Gain module

The ytterbium-doped fibre used in this experiment is a single-mode large-core double-clad fibre. The core NA is 0.075 and the core diameter is 11µm providing a V-number around 1080nm-wavelength below but close to the single-mode limit of 2.405. The inner cladding is 130µm-diameter and octagonally-shaped to break the cylindrical symmetry.

The fibre is spooled on a plate with round edges. On these bent sections, the fibre geometry is altered. For the cladding section, this contributes to additional symmetry breaking and improves absorption. Any residual higher-order modes in the core is coupled out on that bent section. Also, the plate is thermally connected to a larger water-cooled plate which acts as a heat sink, as can be seen on the photography of Figure 4.5.

The ytterbium-doped fibre is pumped by a 60W-class 975nm multimode fibre-coupled laser diode. It is spliced to one of the two pump ports of a (2+1) multimode combiner. The laser diode is screwed to the bottom side of the large cooling plate.

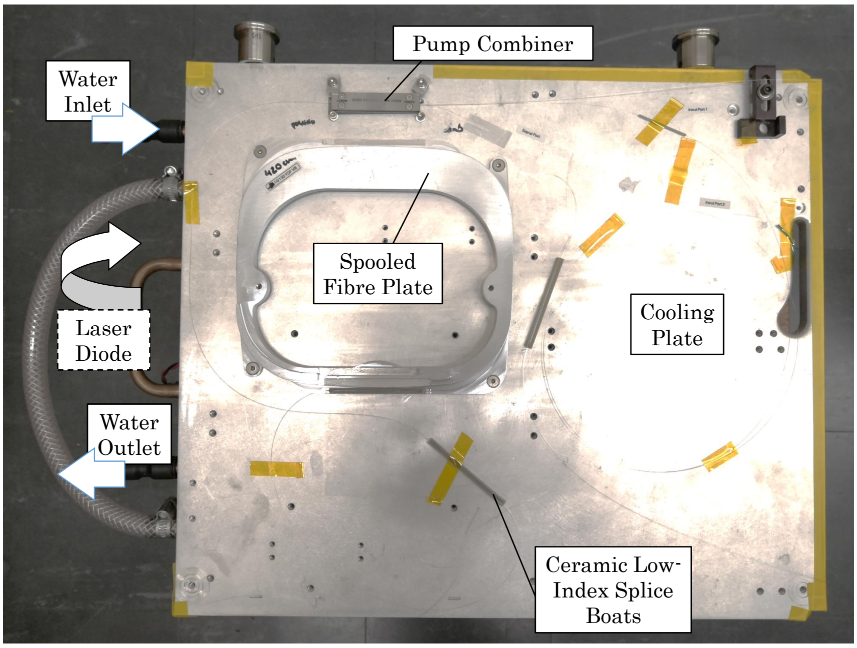

Figure 4.5: Picture of the fibre gain module

As this gain module handles multiple tens of watts of optical power, appropriate attention to the fibre splices must be taken for operation without damage or failure. Between the laser diode fibre and the multimode pump port of the combiner, a splice protector sleeve was applied for mechanical robustness. Its refractive index is lower than of the fibre multimode core and acts as a guide for any portion of uncoupled signal due to splice imperfections. Additionally, the splices at the termination of the active fibre were set in ceramic splice boats containing a low-index polymer and thermally-connected to the cooling plate. Such guiding technique allows to conduct light with minimum heating resulting from interface irregularities and scattered light absorption at the splice point. For instance, it is possible to bear only a ~12°C temperature increase at the splice point of a cylindrical pump fibre with a doped octagonally-shaped fibre of both 400µm diameter crossed by 520W pump power [13].

A preliminary attenuation cutback was carried out over an initial 2.14m of unspooled fibre. The absorption coefficient α_{abs} was evaluated following the equation:

$$\alpha_{abs}\, l = 10 \log \left(\frac{P_{in}}{P_{out}} \right) \tag{4.9}$$

where P_{in} is the laser diode power injected in the cladding of the ytterbium-doped fibre and P_{out} is the transmitted pump power after a length l of fibre. The resulting absorption coefficient was evaluated at 1.6dB/m. A length of 4.2m of fibre was spooled. From this experimental value, it was calculated that it would achieve 79% of pump absorption. It is fine but a higher value is expected as the fibre is coiled and should ensure a higher absorption efficiency.

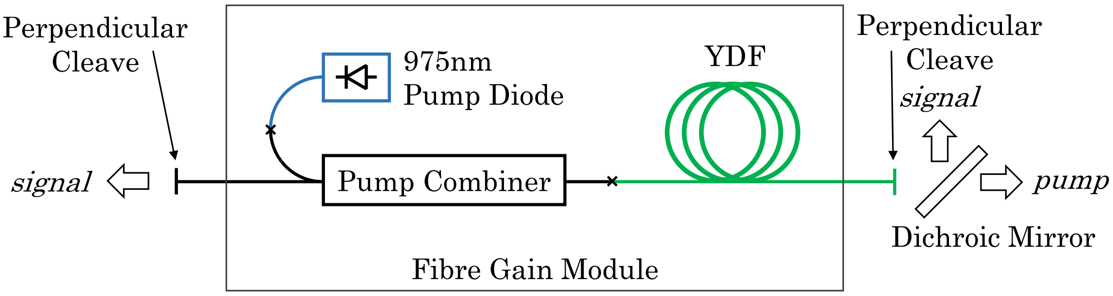

Figure 4.6: Gain module set in a laser configuration

In order to evaluate the performances of the gain module running in a laser configuration, both fibre ends were flat-cleaved to provide a ~4% Fresnel reflection as represented on Figure 4.6. A dichroic mirror was used to separate the pump wave from the 1.0-1.1µm signal.

In total, 39.0W of signal power were generated from both ends and 4.9W of unabsorbed pump power was coupled out. The launched power through the pump combiner was 48.1W giving a pump absorption efficiency $\eta_{abs} = 89.8\%$ and 2.4dB/m. The ratio of total signal power generated to the launched pump power was 81.1%. The ratio of total signal power to the absorbed pump power was 90.3%. This value is higher than what was measured with the attenuation cutback. This is mostly due to the fact that the fibre was spooled on a plate and the bending improved the absorption. A longer length of fibre could also improve the absorption however it would also induce more re-absorption losses which would counterbalance the benefits.

There was residual light in the cladding which was composed mostly of unabsorbed pump power but also a little bit of signal light coupled out from the core (due to an imperfect splice joint or bending for instance). In a larger free-space experiment, this residual light requires to be discarded. One cladding-mode stripping technique consists in applying a medium of identical refractive index, or at least higher refractive index, against a portion of cladding to guide the light out.

When processing a fibre cleave, the protective polymer coating of the end portion of the fibre is stripped and a high-index gel can be applied. Unfortunately, it turned out that at high power levels, the gel would eventually heat and induce thermal dilatation or expansion of the fibre end and misalign the laser. Instead, the gel can be applied on a stripped portion of cladding anywhere away from the fibre end as represented on Figure 4.7. Additional bending of the fibre over that section can improve the cladding-mode stripping efficiency. An alternative to high-index gel is the application of a graphite or copper sheet. The sheet adhesive material in contact with the cladding achieves the mode-stripping and the graphite or copper acts as a heat-sink by absorbing the optical power. Graphite sheets applied on bent polymer-coating-stripped sections of fibres were used on both ends of the gain module for this chapter experiment.

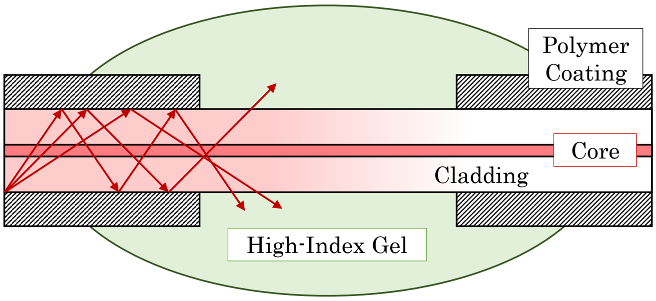

Figure 4.7: Cladding-mode stripping using a high refractive index gel applied on a bare section of fibre cladding

In conclusion, this all-fibre end-pumped gain module showed good absorption performances in a laser configuration. The fact that a feedback as low as the perpendicular cleaves 4%-reflection is sufficient for a laser operation highlights the requirement for strategies to reduce feedback and avoid multi-resonator effects.

4.2.3 Requirements for large end-caps

The 4% Fresnel reflections at the air-glass interface of a fibre has a number of implications. The standard techniques to tackle unwanted reflections are presented along with the procedure for splicing large bulk end-caps.

First and foremost, the Fresnel reflections from a flat cleave can be detrimental when the fibre is amplifying a signal: the 4% reflection that is not coupled out from a fibre is re-amplified and consequently the power can build up. In the context of the experiment presented in this chapter, the 4% portion that is not coupled in the FMA does not undergo a 90° polarisation rotation and neither does its amplified signal. Then secondly, the Fresnel reflections can be responsible for multi-resonators effects such as gain reduction. And lastly, they constitute an undesired 4% loss.

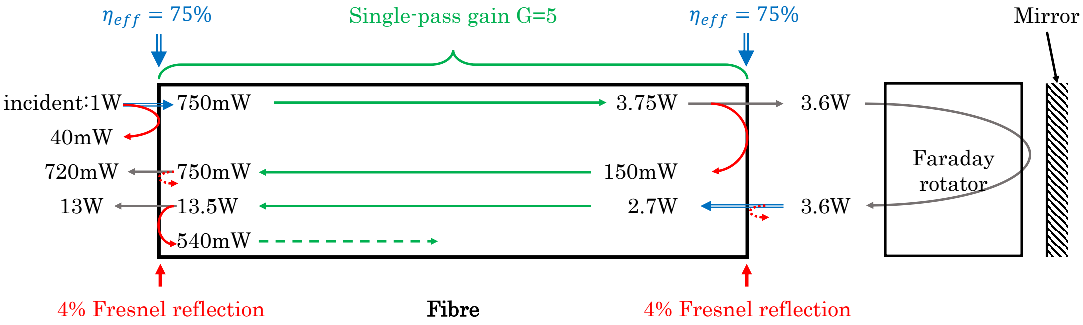

Figure 4.8: First round-trip evolution of 1W of incident power on an active fibre coupled to a Faraday mirror considering the Fresnel reflections at the fibre ends

As a rough guide, an active fibre with a single-pass gain $G = 5$ is considered in a double-pass configuration and the feedback is provided by a Faraday mirror with a 100% transmission. The fibre coupling efficiencies are $\eta_c = 75\%$. Figure 4.8 gives the power distribution according to the first few 4% Fresnel reflections for 1W of incident power on the fibre.

The portion of coupled light which double-passes only the fibre returns with 750mW power on the fibre input face. The portion of coupled light which double-passes both the fibre and the Faraday rotator returns with 13.5W power on the fibre input face. In terms of polarisation state, all 13.5W have undergone a 90° rotation whereas the rotated portion of the 750mW is subject to the birefringence of the fibre. In terms of power level, the returning 13.5W also experience a 4% reflection so that 540mW are reflected at the fibre end. This power is considerable in comparison to the initial incident 1W.

In this configuration, the power can build up in the fibre and lead to damage while a considerable portion of power never double-passes the Faraday mirror and is only subject to the varying phase retardation of the fibre.

Some manufacturers propose fibres with anti-reflection coatings at their ends whose reflection coefficient values are around 0.1% and 0.5% [14–16]. However they are expensive and can present defects introduced during coating deposition, affecting the output beam phase-front quality.

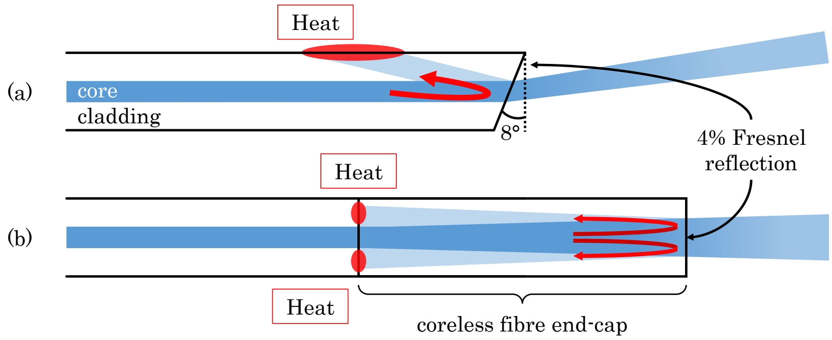

Figure 4.9: Feedback management in fibre with (a) an angle cleave, (b) a coreless end-cap

A strategy to eliminate feedback that has been applied since the early development of fibres [17] is to cleave the fibre end at an angle big enough so that the internal back-reflection is not contained in the core but in the cladding (see Figure 4.9(a)). The optimum angle depends on the fibre design but 8° is a common value. However, the output beam from such termination comes out at an angle and slightly elliptical. This can complicate the alignment. Additionally, at high power, the power reflected in the cladding is absorbed by the polymer coating. Consequently, the fibre is subject to thermal expansion or shrinkage over that end section which misaligns the output beam.

Another popular technique consists in splicing a length of coreless fibre to the fibre end known as an end-cap. The core light is entirely transmitted in that glass section since there is no significant refractive index change. The 4% Fresnel reflection ultimately occurs at the end-cap tip and provides feedback to the fibre. However, as the beam expands on this round-trip in the end-cap, only the central portion of the expanded beam is coupled back in the core, reducing considerably the effective feedback (see Figure 4.9(b)). One drawback is that the remaining uncoupled ring of light is absorbed at the splice section, potentially heats up and induces misalignment.

It is obvious that a long end-cap means a wider beam expansion, and therefore a lower effective feedback in the fibre core. However the length is limited by the clipping of the expanding beam on the outer diameter of the end-cap. For instance, for a 10µm-diameter core (NA=0.075) and 130µm-diameter cladding (values extracted from a single-mode fibre used in this project), and a coreless end-cap of similar diameter, the maximum length before clipping after round-trip in the end-cap is 475µm.

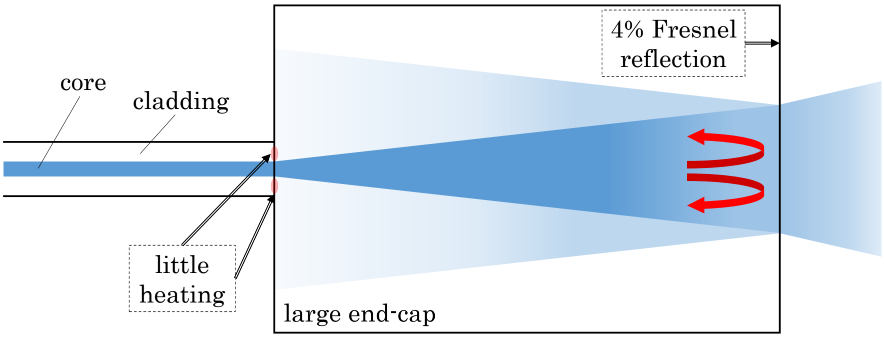

Figure 4.10: Beam propagation and feedback distribution in a large bulk end-cap

Large end-caps with lengths and diameters of the millimetre scale get rid of the clipping issue (see Figure 4.10). It is closer to the dimensions of a glass rod. The effective feedback is dramatically reduced and two additional advantages arise. First, it is possible to have a high-quality anti-reflection coating on the output surface. This eliminates feedback issues and also improves the transmission. Secondly, it is easier to handle the mechanical stability and the thermal loading of a large bulk end-cap than of an angle-cleave or a coreless end-cap.

There are commercially available devices that can achieve the splicing of large end-cap onto fibres but they can be expensive and constraining in terms of dimensions of the end-cap. An optical set-up was developed within the Advanced Solid-State Sources group at the Optoelectronics Research Centre over the course of this PhD project. Improvement of the splicing process was carried out by the different research members as requirements arose. This improvement increment reflects in the quality of end-caps in this PhD thesis.

The common techniques for fibre splicing, or fibre fusion, involve filament fusion, arc-discharge, hydrogen flame and CO_2 laser [18]. The optical device developed is based on the heating of the large end-cap using a CO_2 laser whose 10.6µm-wavelength radiation is absorbed by silica glass. At some point of the splicing process, the fibre is pushed against the glass near the melting temperature and heat is transferred via conduction. The fibre is then spliced.

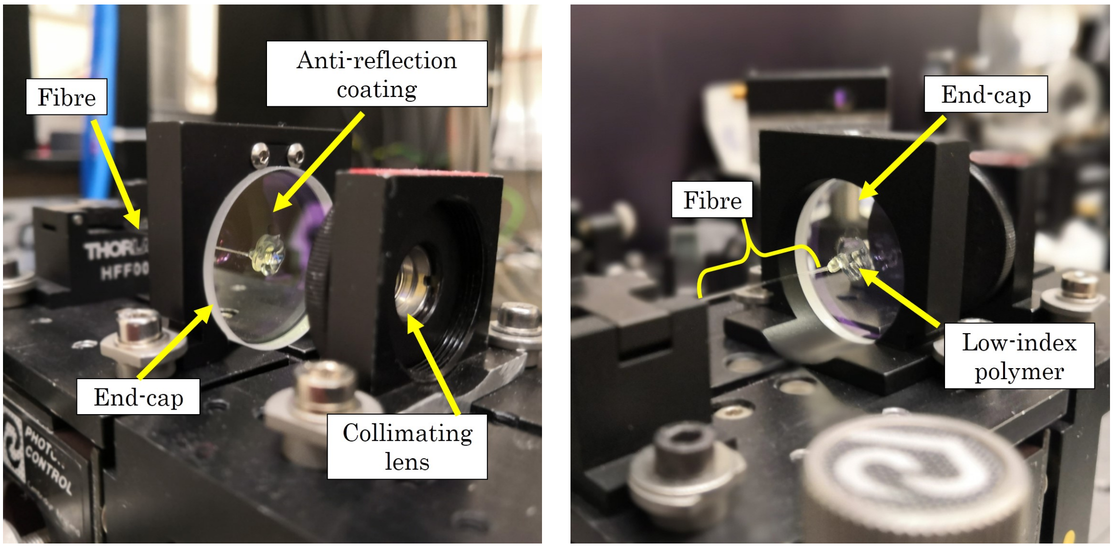

Figure 4.11: Front and back views of a 25mm-diameter end-cap spliced to a fibre with a 130µm-diameter cladding

The end-caps used in this experiment were originally 25mm-diameter 5mm-thick UV-fused-silica broadband mirrors with anti-reflection coatings with 0.2% reflectivity at 1060nm and <0.04% at 1100nm. One window face was polished to remove the anti-reflection coating and allow splicing. The spliced fibre was double-clad single-mode with a 130µm-diameter cladding. Figure 4.11 is a picture of the end-cap. A UV-curable low-index polymer used in-house for fibre coating (PC-373-AP) was deposited at the splice region to provide mechanical robustness.

4.3 Experimental results and discussion

This section provides the results from the implementation of the targeted set-up of Figure 4.4 using the gain stage and the end-caps previously introduced.

4.3.1 Power, efficiency, bandwidth, linewidth

The laser delivered an average 32.0W over an optical spectrum ranging from 1047.1 to 1085.8nm with a maximum value of 32.7W at 1057.3nm as reported in Figure 4.12. The slope efficiency with respect to the laser diode output, the combined pump power and the absorbed pump power were respectively 64%, 68% and 70%.

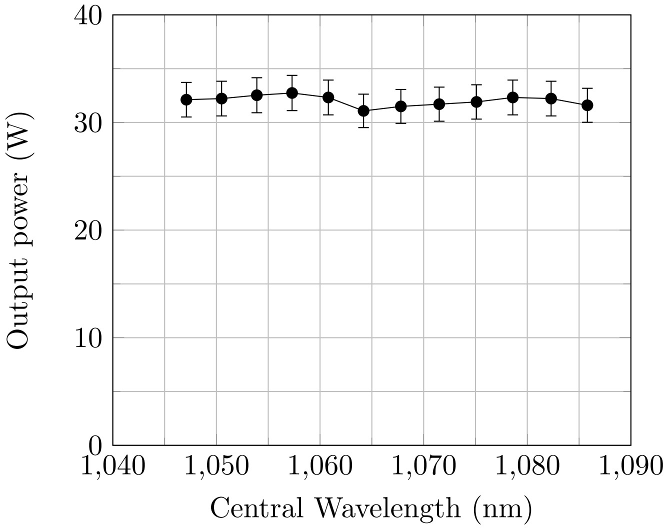

Figure 4.12: Output power at different emission wavelength

The output coupler transmission was set at its highest possible value for a maximum slope efficiency η_{laser} according to Equation (2.22). This was achieved for a $\mathrm{T}_{\mathrm{o.c.}} = 97.1\%$ (as measured at 1075nm). Above this value the power fed back in the ring part of the FSA arm was too low and the laser was unstable.

The 68% ratio of laser power to the combined pump power can be compared to the theoretical slope efficiency. For a 975nm pump wavelength, a 1075nm laser signal, a pump absorption $\eta_{abs} = 89.8\%$, a pumping quantum efficiency $\eta_q = 1$, and a round-trip loss $L_{r.t.} = T_{loss}\eta_c^2$ with the total transmission losses of the optics working in transmission $T_{loss} = 95\%$ and $\eta_c = 75\%$ the fibre recoupling efficiencies, the slope efficiency is $\eta_{laser} = 53\%$. The experimental slope efficiency exceeded the theoretical one. This can be due to an overestimation of the losses in the set-up: 68% slope efficiency can be obtained for a 19% round-trip loss.

For an average output power of 32.0W, the output coupler (the thin-film polariser) reflected 0.96W of vertical polarisation in the ring. According to its specifications, the AOTF transmission is superior to 95%. Together with the Faraday isolator, their transmission can be approximated to 95% (the Faraday isolator beamed out less than 20mW on the way forward) so that the incident power on the fibre is 0.91W. Assuming that the entire output from the fibre is horizontally polarised, its power output is 33.0W. The single-pass gain G_{exp} can be deducted from $G_{exp}^2 \eta_c^2 = 33.0/0.91$ and was $G_{exp} = 8.0$.

The spectrum covered ranged from 1047.1nm to 1085.8nm. Beyond these values, the output power starts to fall off. Eventually the laser would get unstable and the fibre would self-pulse. Over this bandwidth, the output spectrum is a narrow-linewidth signal with a FWHM of 0.4nm and below. Figure 4.13 gives the spectrum as measured by a single-mode fibre connected to an optical spectrum analyser.

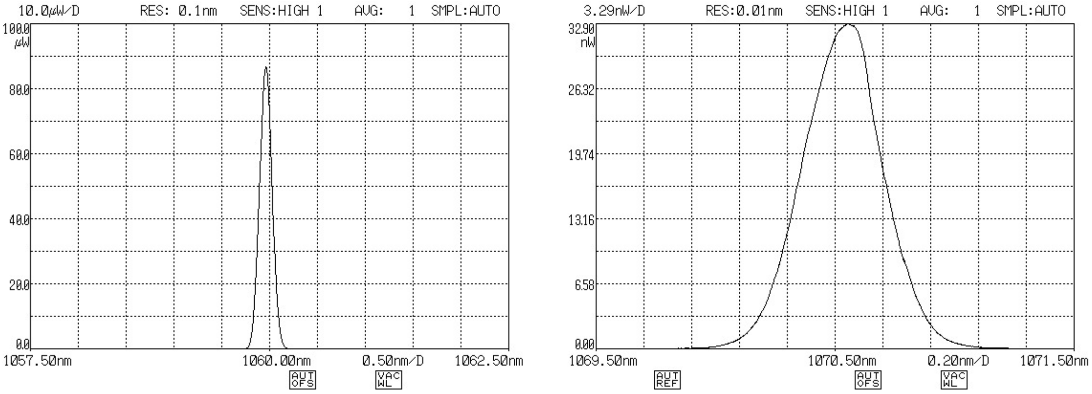

(a) Example of output spectrum near 1060nm central wavelength (0.50nm per division)

(b) FWHM=0.4nm at 1070.6nm central wavelength (0.20nm per division)

Figure 4.13: The output spectrum is a narrow-linewidth (0.4nm and bellow) smoothly varying over the bandwidth covered by the laser

The AOTF resolution (FWHM) is 2nm and below according to the specifications (at 1650nm, with the AOTF wavelength range being 1100-2200nm). Obtaining linewidths of 0.4nm and below indicates that the fibre laser emitted at wavelengths within the AOTF transmission window where the gain was the highest.

Outside the 1047.1nm-1085.8nm spectrum covered by the laser, the power falls off until the fibre self-pulses. This comes from the fact that as the AOTF transmission window is tuned outside that range, the fibre preferentially lases at wavelengths which have a much higher gain outside that window. These wavelengths experience a strong round-trip loss because of the AOTF. Eventually, the fibre stops receiving enough feedback and self-pulsing mechanisms are triggered.

4.3.2 M^2-parameter

In practice, the transverse profile of a laser beam can differ from the ideal Gaussian description as a result of imperfections in the phase-front. Additionally, a beam can appear identical to the fundamental TEM$_{00}$ mode (or any other mode) when it is actually the sum of higher-order modes. The M^2-parameter (sometimes called beam quality factor, or beam propagation factor) is a common tool to evaluate how close a practical beam is compared with the theoretical TEM$_{00}$ mode [19].

For a practical beam of waist w_0 from which the radius $w(z)$ expands, the M^2-parameter is integrated in the Rayleigh range z_0 definition:

$$w(z) = w_0\sqrt{1+\left(\frac{z}{z_0}\right)^2} \quad ; \quad z_0 = \frac{\pi w_0^2 n}{M^2\lambda} \tag{4.10}$$

where λ is the wavelength and n the refractive index of the medium of propagation. In practice the beam can deviate from a perfect Gaussian mode differently depending on the transverse direction so that a M_x^2 and a M_y^2 can be defined.

For any arbitrary beam: $M_{x/y}^2 \geq 1$. For a perfect superposition of the experimental beam with the theoretical TEM$_{00}$ mode: $M_{x/y}^2 = 1$. The beam is then considered diffraction-limited: the quality of the beam is ideal and it can be focussed down to the theoretical minimum.

In the far-field, along the propagation axis (several Rayleigh range away from the waist), an approximation of the M^2-parameter can be calculated from the divergence with:

$$\tan\theta = \frac{beam\,radius}{distance\,from\,waist} = \frac{M^2\lambda}{\pi w_0 n} \tag{4.11}$$

A 30.0cm-focal-length plano-convex lens was placed on the collimated laser output to focus the beam down to a waist and extract the M^2-parameter from the divergence. The beam radius was measured before and after the waist and is reported in Figure 4.14. Following the previous equation, the beam divergence gave $M^2 \sim 1.08$ in two arbitrary orthogonal transverse directions ($M_x^2 \approx M_y^2$), in the near-field and far-field.

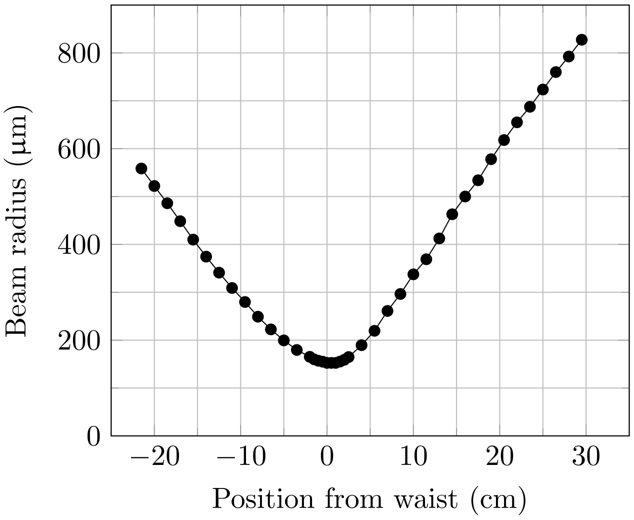

Figure 4.14: Beam radius around the waist position for M^2-parameter measurement

What is the impact of this M^2 value on the phase-front and in terms of power distribution? The 30cm-focal-length lens focussed the output beam down to approximately 150µm radius at waist. In the case where the beam is ideal, i.e. $M^2 = 1$, the circulating collimated beam in the FSA has a beam radius of 701µm. With $M^2 = 1.08$ it is 754µm (at 1075nm). These radii are illustrated in 4.15.

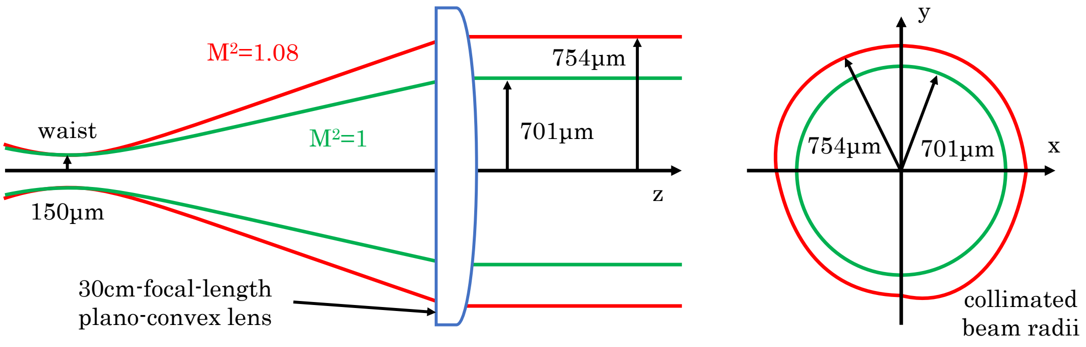

Figure 4.15: Longitudinal and transverse evolution of a diffraction-limited beam and a beam with a M^2 value of 1.08

The power P transmitted through an aperture of radius r_{ap} is defined and given by:

$$P(r_{ap}) = \int_0^{r_{ap}} I(r) 2\pi r \mathrm{d}r = P_{tot} \left[1 - \exp\left(-\frac{2r_{ap}^2}{w^2} \right) \right] \quad \text{where} \quad P_{tot} = \int_0^{\infty} I(r) 2\pi r \mathrm{d}r \tag{4.12}$$

Now considering $r_{ap} = 701\mu$m, 86.5% of the perfect $M^2 = 1$ beam with a 701µm waist would be transmitted whereas 82.3% would be for the $M^2 = 1.08$ beam with a 754µm waist. If, for instance, one considers that only the power circulating in the set-up within that aperture contributes effectively to the laser operation, then the imperfect $M^2 = 1.08$ beam constitutes a 4.9% loss contribution. This value is rather small but not negligible.

As light is emitted from the fibre in the FSA, its path crosses an aspheric lens, two thin-film polarisers and a waveplate which together should note affect the beam quality much. Therefore, the M^2 value is an indication of the quality of the end-cap splice. Considering the power distribution between the experimental beam and an hypothetical ideal beam, the end-caps quality could be improved. This is done in Chapter 6.

4.3.3 Polarisation purity

Evaluating the polarisation purity at different locations provides with some information.

The polarisation extinction ratio (PER) of the output beam was measured using a half-waveplate and a cube polariser. PER $<$ 1000:1 at 1054nm and 1075nm. This result is as good as one would expect from an output coupler composed of a thin-film polariser and indicates the efficiency of the 90° polarisation rotation achieved by the fibre coupled to the Faraday mirror. The overall performance of the laser with its 70.2% slope efficiency relative to the absorbed pump power indicates that a priori the 90° rotation was achieved successfully.

Calculating the PER of the fibre output in the FSA arm provides a more precise evaluation of the 90° rotation. The expected fibre output is a linear horizontal polarisation and any unrotated polarisation should be vertical. The vertical component should be reflected by the TFP towards the Faraday isolator and then beamed off by its input cube polariser as represented in Figure 4.16. The PER can then be defined as the ratio of this beamed-off vertical polarisation to the total incident power on the TFP. It was ~100:1 and is

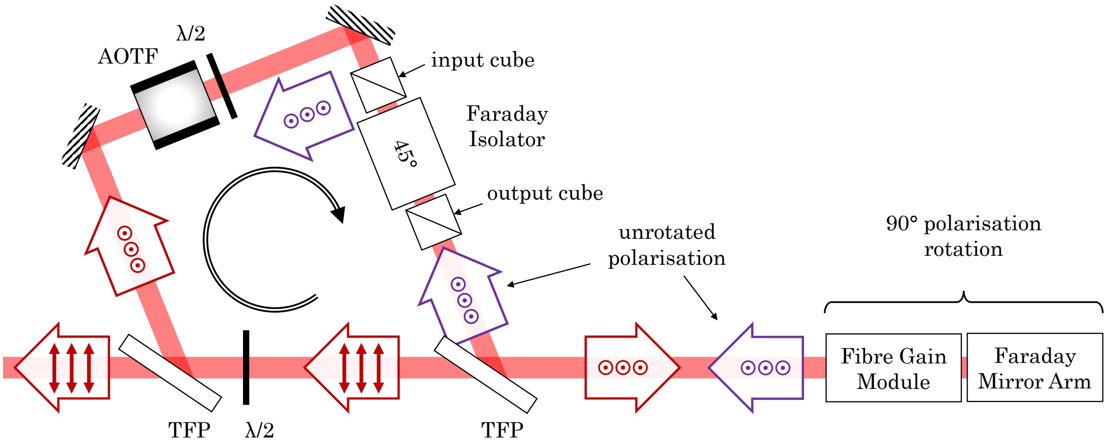

Figure 4.16: Polarisation evolution in the free-space arm in abnormal operation (purple)

considered satisfactory.

Finally, the PER performances of the two thin-film polarisers can also explain the limitation in terms of spectrum coverage.

According to their specifications, from ∼1040nm and below, the horizontal polarisation gets progressively reflected. Power reflected by the first TFP should be beamed out by the Faraday isolator. Power reflected by the output coupler (second TFP met) would not be diffracted by the AOTF and would be lost. In both cases, the contribution to the loop and the feedback to the fibre is reduced and could explain the self-pulsing behaviour.

From ∼1070nm and above, part of the vertical polarisation gets gradually transmitted. If now considering that the Faraday isolator polarisers can also transmit the wrong polarisation, then the ring laser would start to allow a counter-propagating beam with consequences such as laser efficiency reduction and pulses associated with no strong polarisation selection.

4.4 Conclusions and prospects for development

A wavelength-tuneable linearly-polarised ytterbium-doped fibre ring laser was reported with a 70.2% efficiency relative to the absorbed pump. The spectrum covered ranged from 1047.1nm to 1085.8nm with an average power of 32.0W and a FWHM of 0.4nm and less. The output beam is single-mode as according to the $M^2 \sim 1.08$ value.

The laser output beam has excellent polarisation purity. Also the PER of the signal output from the fibre in the FSA of ~100:1 indicates that the 90°-polarisation-rotation by the double-pass through a fibre coupled to a Faraday mirror is achieved in the multi-tens of watts regime. This constitutes an example of linearly-polarised fibre laser which does not require polarisation-maintaining fibre.

One of the prospect for development is power-scaling. One of the limitation could be thermal lensing resulting from heating in bulk optics such as the rotating materials (primarily in the Faraday rotator but also in the isolator), the polarisers and the birefringent material of the AOTF (only in the case of strong feedback in the ring part). The use of anti-reflection end-caps on the fibre ends should prevent parasitic lasing at higher powers in first instance.

This experiment proves the polarisation control of an ytterbium-doped fibre laser resonator using a Faraday mirror. The concept can be extended to other rare-earth-doped fibre lasers given the availability of Faraday rotators at the corresponding emission bandwidths.

Finally, this experiment sets as a milestone in the development of a green fibre laser source. Indeed, it opens the possibility of putting an enhancement cavity containing a nonlinear crystal inside the ring part of the free-space arm to frequency-double the near-infrared signal.

This work was presented at a conference: F. Leroi, P. C. Shardlow, and W. A. Clarkson, "Wavelength-tuneable linearly-polarised ytterbium-doped fibre ring laser," in *8th EPS-QEOD Europhoton Conference*, 02-07 September 2018, presentation WeA1.3

Bibliography

[1] G. Agrawal, "Chapter 1 - Introduction," in *Nonlinear Fiber Optics (Third Edition)*, third edition ed., ser. Optics and Photonics, G. Agrawal, Ed. Academic Press, 2001, pp. 1 – 25.

[2] R. Ulrich, S. C. Rashleigh, and W. Eickhoff, "Bending-induced birefringence in single-mode fibers," *Opt. Lett.*, vol. 5, no. 6, pp. 273–275, Jun 1980. [Online]. Available: http://ol.osa.org/abstract.cfm?URI=ol-5-6-273

[3] R. Ulrich and A. Simon, "Polarization optics of twisted single-mode fibers," *Appl. Opt.*, vol. 18, no. 13, pp. 2241–2251, Jul 1979. [Online]. Available: http://ao.osa.org/abstract.cfm?URI=ao-18-13-2241

[4] R. C. Jones, "A new calculus for the treatment of optical systems I. Description and discussion of the calculus," *J. Opt. Soc. Am.*, vol. 31, no. 7, pp. 488–493, Jul 1941. [Online]. Available: http://www.osapublishing.org/abstract.cfm?URI=josa-31-7-488

[5] T. R. Woliński, "Polarization in optical fibers," *Acta Physica Polonica*, vol. 95, no. 5, pp. 749–760, 1999.

[6] R. Paschotta, J. Nilsson, L. Reekie, A. C. Trooper, and D. C. Hanna, "Single-frequency ytterbium-doped fiber laser stabilized by spatial hole burning," *Opt. Lett.*, vol. 22, no. 1, pp. 40–42, Jan 1997. [Online]. Available: http://ol.osa.org/abstract.cfm?URI=ol-22-1-40

[7] M. Martinelli, "A universal compensator for polarization changes induced by birefringence on a retracing beam," *Optics Communications*, vol. 72, no. 6, pp. 341 – 344, 1989. [Online]. Available: http://www.sciencedirect.com/science/article/pii/0030401889904367

[8] D. S. Glassner and R. D. Esman, "Spatial hole burning in erbium fiber lasers using Faraday rotator mirrors," in *Proceedings of Optical Fiber Communication Conference (*, Feb 1997, pp. 66–67.

[9] F. Hakimi, E. S. Kintzer, and R. S. Bondurant, "High-power single-polarization edfa with wavelength-multiplexed pumps," in *Technical Digest. Summaries of Papers Pre-*

sented at the Conference on Lasers and Electro-Optics. Conference Edition. 1998 Technical Digest Series, Vol.6 (IEEE Cat. No.98CH36178), May 1998, pp. 287–288.

[10] T. M. Yarnall, T. G. Ulmer, N. W. Spellmeyer, and D. O. Caplan, "Single-polarization cladding-pumped optical amplifier without polarization-maintaining gain fiber," *IEEE Photonics Technology Letters*, vol. 21, no. 18, pp. 1326–1328, Sep. 2009.

[11] I. N. Duling and R. D. Esman, "Single-polarisation fibre amplifier," *Electronics Letters*, vol. 28, no. 12, pp. 1126–1128, June 1992.

[12] W. W. Rigrod, "Saturation effects in high-gain lasers," *Journal of Applied Physics*, vol. 36, no. 8, pp. 2487–2490, 1965. [Online]. Available: https://doi.org/10.1063/1.1714517

[13] M.-A. Lapointe, S. Chatigny, M. Piché, M. Cain-Skaff, and J.-N. Maran, "Thermal effects in high-power CW fiber lasers," in *Fiber Lasers VI: Technology, Systems, and Applications*, D. V. Gapontsev, D. A. Kliner, J. W. Dawson, and K. Tankala, Eds., vol. 7195, International Society for Optics and Photonics. SPIE, 2009, pp. 430 – 440. [Online]. Available: https://doi.org/10.1117/12.809021

[14] SQS Vláknová optika a.s., "Components with antireflection coating," Catalog Sheet, March 2015. [Online]. Available: https://www.sqs-fiberoptics.com/images/pdf-soubory/antireflection-coating.pdf

[15] Laser Components GmbH, "AR coating for optical fibers," Data Sheet, May 2013. [Online]. Available: https://www.lasercomponents.com/fileadmin/user_upload/home/Datasheets/lcw/ar_coating_opt_fiber-e.pdf

[16] Thorlabs, Inc., "Single mode patch cables: AR coated," Catalog, p. 1009. [Online]. Available: http://pdf.directindustry.fr/pdf-en/thorlabs/fiber/36188-362511.html

[17] C. J. Koester and E. Snitzer, "Amplification in a fiber laser," *Appl. Opt.*, vol. 3, no. 10, pp. 1182–1186, Oct 1964. [Online]. Available: http://ao.osa.org/abstract.cfm?URI=ao-3-10-1182

[18] B. S. Wang and J. Faustino, "Latest advances on fused fiber components for power scaling of fiber lasers," pp. 9359 – 9359 – 6, 2015. [Online]. Available: https://doi.org/10.1117/12.2081752

[19] A. E. Siegman, "How to (maybe) measure laser beam quality," in *DPSS (Diode Pumped Solid State) Lasers: Applications and Issues.* Optical Society of America, 1998, p. MQ1. [Online]. Available: http://www.osapublishing.org/abstract.cfm?URI=DLAI-1998-MQ1

Chapter 5

Injection-locking of a fibre laser cavity with an all-fibre amplified spontaneous emission source

This chapter presents an attempt to achieve the injection-locking of a fibre laser by an ASE seed source. Injection-locking can be presented as a technique where the laser operating wavelength can be monitored by an external source. The green fibre laser configuration could benefit from injection-locking as it would allow to remove the spectrum-narrowing element of the cavity. The round-trip cavity loss would be reduced and the operating wavelength linewidth tightened and no longer limited but the spectrum-narrowing element performances.

Additionally, the experiment presented in this chapter proposes the injection-locking of a ring fibre laser containing a Faraday mirror i.e with a maintained polarisation. Injection-locking requires longitudinal mode-matching between the laser and the external source. A successful injection-locking with an ASE source would circumvent that requirement.

5.1 Concept presentation

Injection-locking and injection-seeding are techniques which have proved to be useful to generate high-power narrow-linewidth low-noise signals from high power lasers with poor bandwidth and strong noise. It involves the use of a stable low-power master oscillator with a narrow-linewidth or running in single-frequency operation with a less well-behaving high-power slave oscillator. It constitutes an alternative to master oscillator power amplifiers which can also achieve such amplification but suffer from intrinsic amplifier noise.

Injection-locking can provide single-frequency outputs, narrow linewidths and frequency stability. Also, the injection-locking of several slave oscillators by a single master oscillator can synchronise their phase and frequency.

There are some uncertainties regarding the proper use of the term injection locking, often mistaken with injection seeding. According to the literature, these two techniques differ from the longitudinal modes overlap between the master and the slave resonators, and also the conditions of amplifications.

5.1.1 Injection-locking

The following presents the "true injection-locking" as described notably by a number of authors [1–3]. In practice, injection-locking has been mostly applied to continuous-wave lasers.

A self-sustained high-power laser oscillator is considered free-running at an angular frequency $\omega_0 = 2\pi\nu_0$ with power P_0. This is the maximum power that can be extracted from that laser as the gain is the highest at this frequency (given notably the gain medium, the internal losses and the output coupling). This is the slave resonator.

A much lower-power self-sustained oscillator is also considered, external to the previous one, and free-running at angular frequency $\omega_{inj} = 2\pi\nu_{inj}$ close to ω_0 and producing an output power $P_{inj} \ll P_0$. This is the master resonator.

Now in the case where the low-power signal from the master resonator is coupled in the high-power slave resonator, it will experience a regenerative amplification. The amplification gain G_{reg} from input to output is a function of the angular frequency $\omega \neq \omega_0$ around its central value ω_0 given by:

$$G_{reg}(\omega) = \frac{\gamma_e^2}{(\omega - \omega_0)^2} \tag{5.1}$$

where γ_e is the energy decay rate which is a function of the input/output coupler coefficient and the transit time for one round-trip inside the cavity. This gain distribution is represented in Figure 5.1.

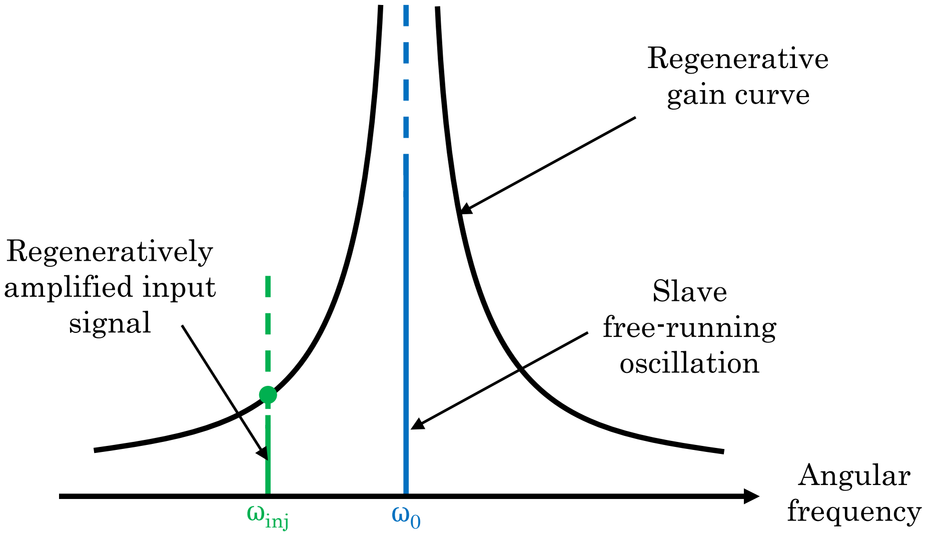

Figure 5.1: Regenerative gain curve for an injected signal at angular frequency ω_{inj} around the free-running angular frequency ω_0 of the slave resonator as from [1]

For frequencies ω_{inj} considerably far from ω_0, the slave resonator delivers two signals: a weakly regeneratively amplified signal of power $G_{reg}(\omega_{inj})P_{inj}$ at frequency ω_{inj} and a strong and barely affected high-power signal $\sim P_0$ at ω_0. However, as frequency ω_{inj} is tuned closer to the slave-resonator free-running frequency ω_0, the regenerative amplification gets stronger following Equation (5.1) and the power is transferred from one signal to the other. Both signals extract their intensity from the same laser medium.

As frequency ω_{inj} gets closer to ω_0, there comes a point where the amplified signal is just strong enough to saturate the laser gain so that the free-running oscillation is no longer generated and all the power is transferred to the one of pulsation ω_{inj}: this is injection locking. The slave resonator is "locked" on operating at the master frequency. Figure 5.2

gives the intensity evolution for the two signals as a function of the separation between the two frequencies.

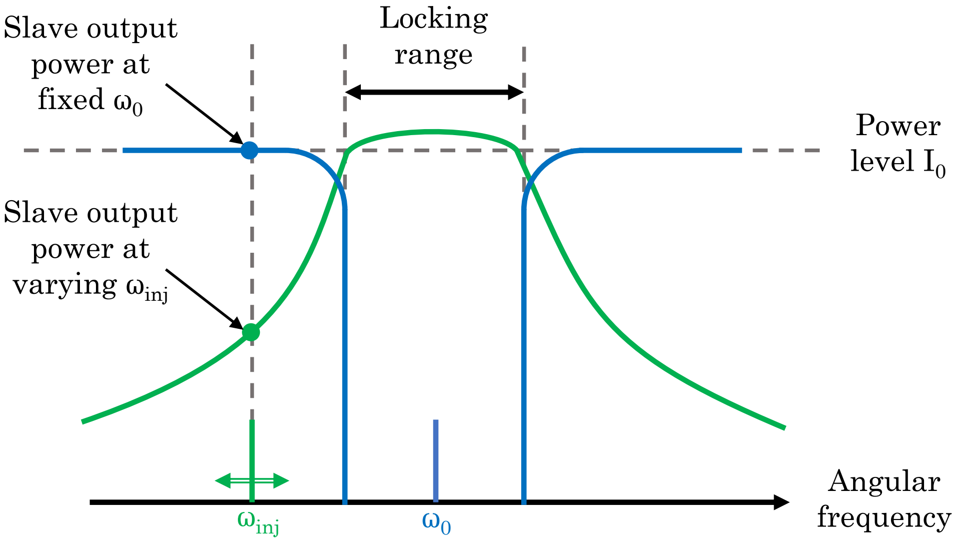

Figure 5.2: Locking range and intensity profiles of the free-running oscillation (I_0, ω_0) and the regeneratively amplified signal $(G_{reg}P_{inj}, \omega_{inj})$ as from [1]

The narrow bandwidth around ω_0 over which injection-locking occurs is called the injection locking range. Over that range, the unique output at frequency ω_{inj} has an approximately constant intensity equal to P_0, the slave resonator free-running power. It is defined as:

$$\Delta\omega_{lock} = 2|\omega_{inj} - \omega_0| \qquad \text{for} \qquad G_{reg}(\omega_{inj})P_{inj} = P_0 \tag{5.2}$$

For an injected steady-state signal from the master oscillator, the locking range $\Delta\omega_{lock}$ centred at ω_0 is given by:

$$\Delta\omega_{lock} = \frac{2\,T_{o.c.}\,c}{l_{r.t.}}\sqrt{\frac{P_{inj}}{P_0}} \tag{5.3}$$

where $T_{o.c.}$ is the output coupler transmission and $l_{r.t.}$ the effective length over which light does a round-trip in the cavity. It is given by the Adler equation applied to laser resonators. The Adler equation characterises any type of locked resonators whether it is from laser physics, electronics, mechanics or any other resonator [4].

The locking range can be expressed as:

$$\Delta\omega_{lock} = \Delta\omega_{0FSR}\frac{T_{o.c.}}{\pi}\sqrt{\frac{P_{inj}}{P_0}} \tag{5.4}$$

where $\Delta\omega_{0FSR}$ is the free spectral range of the slave resonator. As the output coupler transmission is by definition less than unity and injection-locking considers $P_{inj} \ll P_0$, then $\Delta\omega_{lock} \ll \Delta\omega_{0FSR}$. Therefore the locking range covers a small bandwidth around ω_0 away from the next adjacent longitudinal modes.

From the description of "true injection-locking" reported here, a slave resonator is considered injection-locked by a master resonator at the condition that the master frequency is within a certain locking-range. Also, the injection-locking mechanism is the saturation of the slave gain medium by the regeneratively amplified signal which overtakes the free-running oscillation. The conditions for injection-seeding are slightly different.

5.1.2 Injection-seeding

The following presents "injection-seeding" as presented by a number of authors for which it applies mostly to pulsed lasers or optical parametric oscillators [5–7].

With injection-seeding, the master oscillator generates a single-frequency signal at one of the longitudinal mode of the slave resonator. This "seed" is delivered to the slave resonator during its turn-on period. As the pulse is generated, both the seed and spontaneous emission are regeneratively amplified. At some point of the amplification, the injected signal eventually saturates the gain and prevents the slave oscillator from generating any other longitudinal mode.

In this situation, the seed provides the initial conditions on the spatial and spectral modes from which the pulses build up. Injection-seeding is ensured as long as enough power from the injected signal overlaps with one of the longitudinal modes of the slave resonator as represented on Figure 5.3. In fact, the injected signal frequency is often too far off the locking range considered for injection-locking, and its power is also too low to saturate the gain. As the energy of the pulses increases, the injected signal no longer has an influence besides having provided the initial conditions.

As injection seeding is often referred to the injection of a pulsed high-power oscillator in the literature, it is also sometimes called "pulsed injection locking".

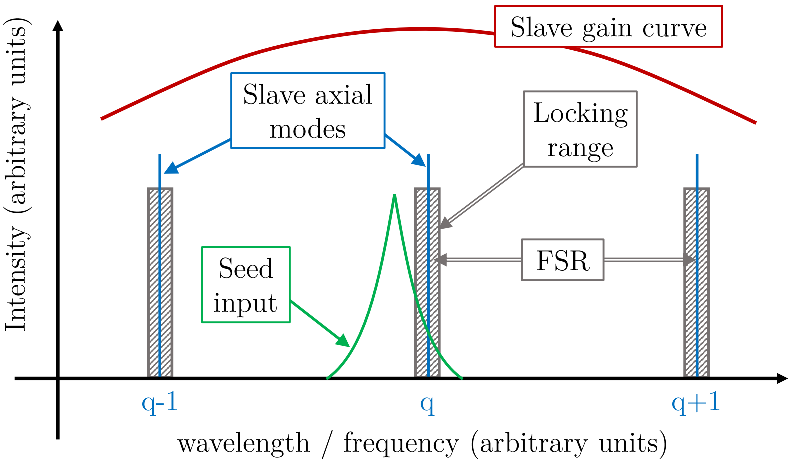

Figure 5.3: Representation of the injected signal in-between the axial modes of the slave oscillator

5.2 Motivation

The interest of injection-locking and injection-seeding is that a high-power ouput can be generated with the higher-quality properties of a low-power single-frequency laser. This presents a number of advantages.

One of the major attractions is the control of the spectral properties by the master laser. As it is running at low powers, it does not face the same issues encountered with higher-power lasers such as spatial hole-burning, pump non-uniformities, and thermally-induced lensing and birefringence. The master laser output can therefore have a narrow linewidth or be single-frequency.

Wavelength control in high-power lasers require spectrum-narrowing elements which can be insufficiently efficient or subject to optical damage. In free-space solid-state lasers they can be gratings, dichroic mirrors, birefringent filters or etalons. Additionally, the losses these components introduce in the intracavity circulating power can be detrimental to the laser efficiency and limit the output power. Injection-locking can be used in association with a spectrum-narrowing element to further reduce the emission bandwidth of the slave resonator. It can also be used to remove completely the spectrum-narrowing element inside the high-power laser cavity depending on the laser gain distribution [7].

Injection-locking and injection-seeding were successfully achieved with a number of laser types. The first reported injection-locking was achieved with helium-neon lasers [8] while the first injection-seeding immediately followed with a ruby laser [9]. Nd:YAG lasers have been subject to development too with recently 101W generated in a slave resonator with a 2W injection from a master oscillator [10]. Finally, CO_2 lasers [11] and laser diodes [12] have been extensively studied for injection-locking.

Another popular way to achieve high-power generation consists in amplifying the output of a low-power laser with good performances with a succession of amplifiers or "amplifier chain". It is known as a master oscillator power amplifier or MOPA. They can require a number of amplifiers which all individually add some noise. Although, alternatively, their number can be reduced by adopting a multi-pass configuration. In addition to this, it is sometimes required to add optics (e.g. isolators or band-pass filters) between the gain stages increasing complexity and overall costs. The main downside is the amplifier noise. Quantum noise is intrinsic to a laser amplifier and leads to phase noise i.e. the broadening of the output linewidth [13].

Besides the noise issues and the complications related to the number of amplification stages and optical components, one popular type of MOPA is the master oscillator fibre amplifier (MOFA) where the amplification is carried out by active fibres. Since the emission bandwidth of fibre lasers can be extensive, and therefore so can the amplification bandwidth, it provides a wide tuning range. MOFA can also deliver near-diffraction limited output.

Last but not least, injection-locking is particularly interesting when it comes to synchronising the output of several high-power lasers. The signal from a single master oscillator can be distributed over different slave resonators. The consequent high-power outputs can eventually be combined.

The experiment of this chapter proposes to attempt the injection-locking (or injection-seeding depending on the view) of a fibre laser set in a free-space cavity which hopefully can ally the advantages of injection-locking with optical fibres performances.

5.3 Injection-locking of a fibre laser with an ASE source

The proposed experiment is the injection-locking of a fibre laser by an ASE source as a master oscillator. The slave fibre laser contains a Faraday mirror.

In the previous descriptions, both master and slave lasers are resonators and successful injection-locking is possible if there is an overlap of both cavities modes. However, the positions of the longitudinal modes in the frequency spectrum are subject to variations mainly due to vibrations and thermal variations. A common technique to ensure longitudinal mode-matching is to employ active stabilisation. The power generated from the slave resonator is supposedly the highest when the modes overlap. Therefore a photodiode placed on the set-up output can indicate whether the mode-matching condition is met. A piezo-actuator can be placed on the back of the mirror of the slave resonator and, associated to a feedback loop with the photodiode, can adjust accordingly the cavity length to maintain the mode-matching. This obviously adds complexity to the set-up.

The following experiment considers replacing the master laser with an ASE source to overcome the mode-matching complications since an ASE output is continuously distributed over its entire emission spectrum. If the ASE bandwidth is larger than the slave resonator free spectral range then it is ensured that it always covers at least one slave mode as represented on Figure 5.4.

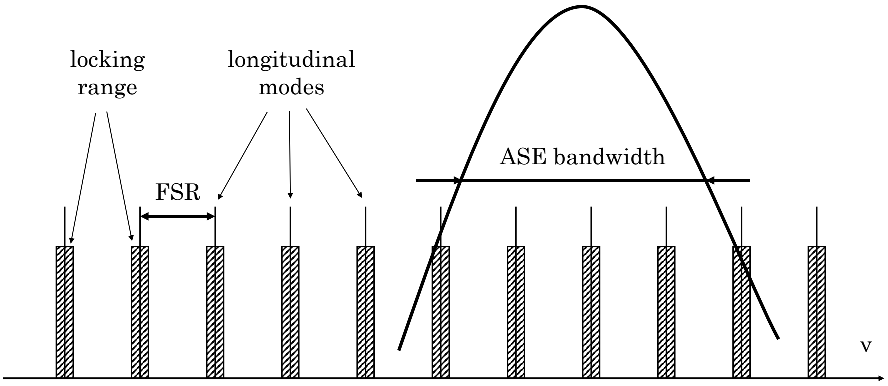

Figure 5.4: Overlap of the ASE source emission spectrum with some longitudinal modes of the slave resonator

As introduced previously, in the injection-locking condition, the slave resonator lases at the master frequency within a locking-range. With an ASE spectrum with a linewidth covering one locking range, the lasing is expected where the gain is the highest within that range. However, the overlap of the ASE linewidth with the locking range is hard to maintain as the slave resonator modes position always move due to temperature variations and vibrations as represented on Figure 5.5. There would be situation where the ASE signal does not cover longitudinal modes. It would require active cavity-length stabilisation.

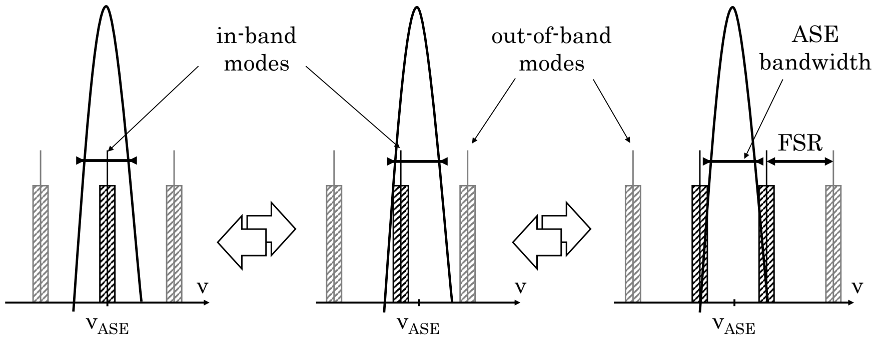

Figure 5.5: Position of the slave longitudinal modes shifting relative to the ASE spectrum (ν_{ASE}: ASE central frequency)

With an ASE spectrum covering several modes as represented on Figure 5.4, without gain consideration, regenerative amplification should be expected in the out-of-locking-range portions and lasing should occur within the locking range. The assumption is that the amplification gain within any locking range should be higher than the regenerative amplification gain so that it saturates the gain medium and only lasing is allowed. With optical fibres, the gain is relatively homogeneously broadened so that modes have a more or less equal gain coefficient.

The term injection-locking might not be appropriately used here as the master oscillator does not deliver a single mode which matches one of the slave resonator modes. Injection-seeding as described previously is equally not a suitable denomination: the master oscillator does not provide only initial conditions. Injection-seeding can certainly occur as long as a portion of the injected signal covers one axial mode of the slave resonator. For this experiment and the following, the term injection-locking will be used yet the term seed laser for the ASE source will be used over master oscillator.

Being able to injection-lock resonators with an ASE source could be useful in the case where active stabilisation with a piezo-actuator becomes challenging. A recent study reported the injection-locking of a multi-core ytterbium-doped phosphate fibre by a single-frequency 1030nm laser diode [14]. All the 19 cores of the 5.6cm-long fibre were successfully injection-locked. However, in the case where the fibre is several meters long, will the lengths of each individual core remain sufficiently close to ensure a constant superposition of their longitudinal modes? This is where, if proved successful, using an ASE source as master oscillator could become valuable.

5.4 Optical set-up for the injection-locking of a linearly-polarised fibre laser

The elected optical set-up, given on Figure 5.6, is similar to the wavelength-tuneable linearly-polarised ytterbium-doped fibre ring laser set-up and uses the same fibre gain module (the one developed in previous chapter).

On the Faraday mirror arm (FMA), a collimating lens delivers a beam to the Faraday mirror composed of a Faraday rotator and a high-reflection mirror. On the free-space arm (FSA), another lens collimates the beam directing it towards a thin-film polariser set at Brewster's angle (56°). Linear horizontal polarisation is transmitted whereas vertical polarisation is reflected and beamed out by a Faraday isolator. The ring portion differs with only one input-output coupler, a 70%-transmission mirror, and a high-reflection mirror to close the loop. The horizontal polarisation is transmitted through the Faraday isolator and undergoes a 45° rotation. Follows a half-waveplate which rotates the polarisation by an additional 45° so that the incident polarisation on the polariser is linear and vertical, and the signal is fed back to the fibre. Finally, there is no spectrum-narrowing element.

The ASE seed signal is coupled in this slave resonator through the 70%-transmission dichroic mirror in the direction of the high-reflection mirror. The same mirror also acts as an output coupler for the fibre laser. This input-output coupler is set at an angle so that no output signal is directed toward the ASE source. Also, the signal coming from the mirror is purely the sum of the partial reflection of the seed on the input coupler and the slave output.

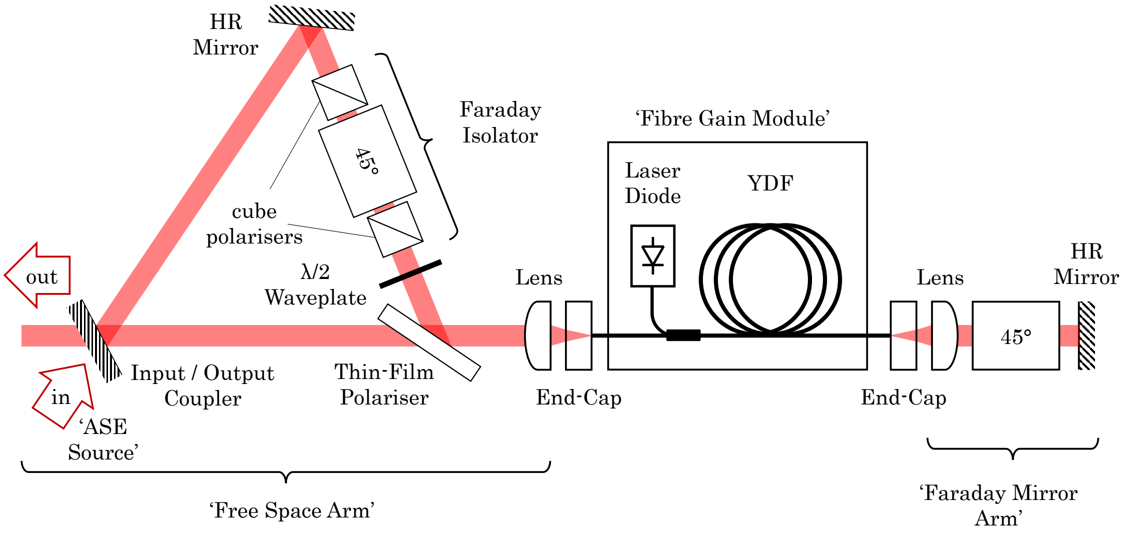

Figure 5.6: Set-up for injection-locking of a fibre laser by a narrow-linewidth ASE source

The seed is the 1075nm narrow-linewidth ASE source developed in Chapter 3. It is a fibre source whose polarisation is variable and subject to temperature and mechanical perturbations. However these variations are slow and half and quarter waveplates were used to provide a horizontal polarisation that can be resonant in the laser cavity. The pick-off signal from the Faraday isolator input cube polariser is essentially the portion of input vertical polarisation from the ASE source. A photodiode was used to monitor this unwanted signal and waveplates were angled to keep it at a minimum.

The fibre gain module was composed of 420cm of active fibre and, with the passive sections of fibre used for convenience, was approximately 500cm long. The round-trip length in the free-space sections was approximately 1m. Consequently the slave resonator free spectral range was $\Delta\nu_{FSR} \simeq 36$MHz. The ASE spectrum had a full-width at half maximum of 85pm or $\Delta\nu_{FWHM} = 22.1$GHz. Therefore the ASE source should cover approximately 600 longitudinal modes of the slave resonator.

This set-up was run under three conditions: with only the ASE seed turned on, with only the fibre laser pumped (free-running configuration) and with both master and slave turned on (supposed injection-locking condition). The denomination 'output signal' used in the following designates the signal incoming from the input-output coupler in any of the three working conditions (i.e. whether the slave resonator is seeded or not, pumped or not). In the injection-locking condition, it is notably the sum of the reflected portion of the ASE seed and the signal output from the slave resonator.

5.5 Results and discussion

The ASE source delivered 2.88W that were incident on the input coupler. With the slave resonator unpumped, 1.86W were coupled in and 176mW further beamed out by the input cube polariser of the Faraday isolator. After a single-pass through the fibre, 1.073W were measured in the FMA. 449mW were measured after a double-pass through the fibre and the Faraday mirror after the TFP in the FSA. According to the previous chapter, the gain module has a single-pass absorption of 2.4dB/m and the fibre recoupling efficiencies on its both ends were evaluated at ∼75%. Figure 5.7 is the output spectrum. As expected, it was a simple narrow peak at 1075nm like the ASE source spectrum is (see Figure 3.6).

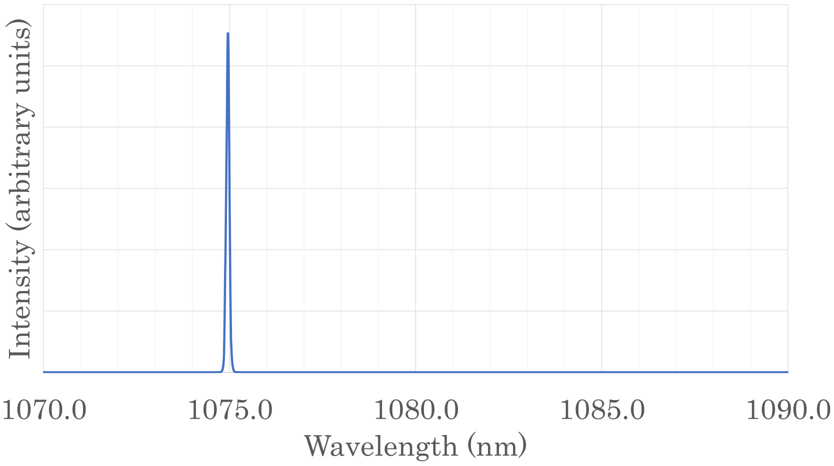

Figure 5.7: ASE source on with unpumped slave resonator

With the ASE seed source deactivated, the slave resonator could free-run and generate up to 25.9W of output for a laser diode pumping at 51.4W. Figure 5.8 gives the output spectrum at two arbitrary pump powers: around 6.5W (above threshold) and 40W (well above threshold). Over the power range covered by the pump diode, the number of peaks and their positions would vary. These variations were also observed over time. Nevertheless, the output spectrum was observed remaining in the 1070-1090nm range.

This corresponds to wavelengths expected from the fibre gain stage with the optics working in transmission over that range.

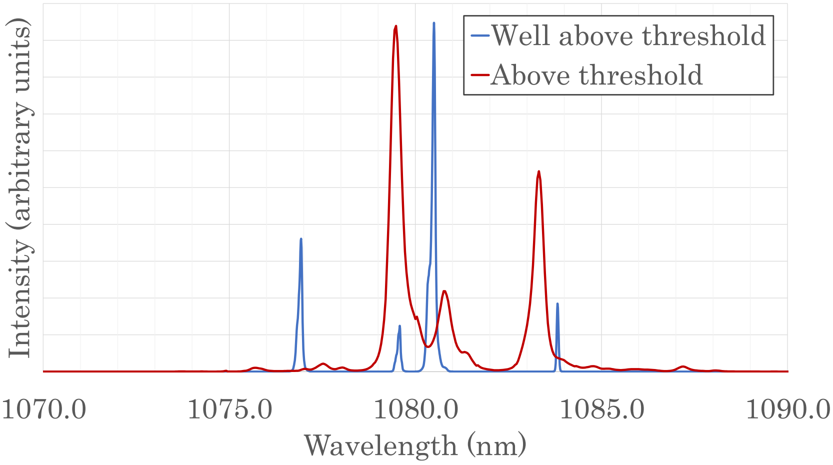

Figure 5.8: Free-running configuration at low (6.5W) and high (40W) pump power

There is no or very little power at 1075nm in the free-running configuration. If injection-locking occurs in the supposed injection-locking conditions, one should expect the power from all the longitudinal modes in the 1070-1090nm bandwidth of the free-running configuration to be transferred to one or several modes of the 85pm-bandwidth 1075nm.

The whole set-up was run in the injection-locking conditions with 2.88W of incident ASE power. Up to approximately 33W of pump power (17.4W output signal), the output signal was a peak at 1075nm and the injection-locking appears successfully achieved. Above the 33W pump power, additional signals at 1084 and 1088nm started to emerge as reported in Figure 5.9.

In what appears to be successful injection-locking, two mechanisms could have actually occurred: either the ASE signal underwent a regenerative amplification or it actually locked certain longitudinal modes of the slave resonator. In the case of proper injection-locking, an observation of the 1075nm peak with a higher spectral resolution should exhibit one or several lines corresponding to signals within the longitudinal modes locking range. In the case of regenerative amplification, the spectrum covering several longitudinal modes should be continuous, with power distributed within the locking range and also between the modes.

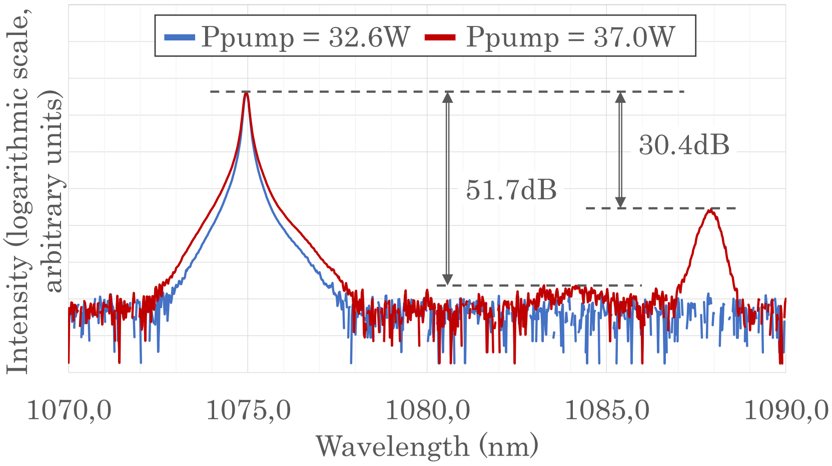

Figure 5.9: Output spectrum in injection-locking conditions below and above 33W pump power (laser diode output)

The previous spectra were provided by an optical spectrum analyser (OSA) whose maximum resolution is 0.015nm. This resolution is too poor to separate two longitudinal modes from the slave resonator as the free spectral range is evaluated around 36MHz. This OSA takes an optical signal as an input and processes it with a combination of reflective diffraction gratings, optical sensor and motorised alignment optics. The resolution is ultimately limited by the signal processing in the optical domain.

An alternative is the use of a radio-frequency (RF) spectrum analyser which uses ultra-fast photodiodes to directly measure an optical input and proceed to an electronic signal processing. In short, the signal processing consists in converting a time-domain measurement (the photodiode fast acquisition) into a frequency-domain measurement via a Fourier transform, and eventually scan these frequencies with internally generated frequencies. The RF spectrum analyser can give access to better resolution than an OSA.

Figure 5.10 is the frequency spectrum as provided by the RF spectrum analyser in the three running conditions i.e. ASE seed operating only, the free-running laser and the injection-locking condition. The intensity axis is given in decibel-milliwatts (dBm), a power unit referenced to one milliwatt. A number of observations can be made. Before that, it should be noted that the downward trend clearly apparent in all three spectra can be attributed to the frequency response of the available photodiode.

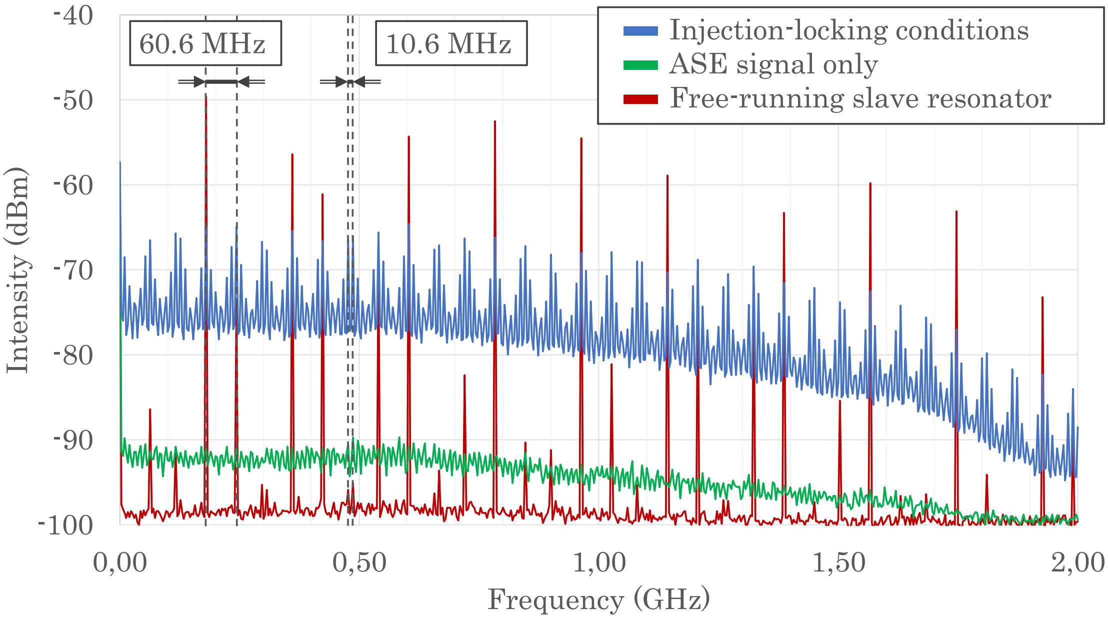

Figure 5.10: Signal outputs as from the RF spectrum analyser

First and foremost, the free-running laser is a succession of peaks with a free spectral range of 60.6MHz. According to Equation 2.28, it corresponds to a free-space resonator of 4.9m round-trip length or a 3.4m-long all-fibre cavity which is not too far from the previous evaluation. Not all of the peaks reported here have the same intensity and this is attributed to mode competition. The zero level is approximately around -100dBm.

Now regarding the ASE signal, this is a rather continuous spectrum above the noise floor at -100Bm however it presents a number of small oscillations. In fact, these oscillations are quite periodic with a 10.6MHz separation. One could assume that the seed does not provide a proper ASE signal and laser oscillations occurred somewhere in the master source. However if this 10.6MHz separation was the free spectral range of a resonator, it would correspond to the round-trip cavity length of a $\sim$19m-long fibre. This value does correspond to the length of the different ASE-source fibre amplifier stages of $\sim$20m. However, if laser oscillations would have occurred in these stages, the fibre cavity round-trip length would be doubled and the free-spectral range value would be around half 10.6MHz. Therefore these oscillations cannot be attributed to a lasing effect in the ASE source.

The explanation to these oscillations could come from the original signal generated by the SLED, the initial component of the ASE source (see Chapter 3). The SLED is an ASE source itself, there is no control over its emission spectrum other than the gain bandwidth of its gain medium. Therefore it can be seen as a noise source with random fluctuations. Over tens-of-nanometre bandwidth the spectrum appears smooth and continuous but locally, at the megahertz scale, such fluctuations could appear.

In the supposed injection-locking conditions, several clear features appear on the signal output. First, the general offset from the noise floor at -100dBm seems to be an homogeneous amplification of the ASE signal. It can therefore be associated with regenerative amplification. Secondly, above that offset, the signal presents fast oscillations at 10.6MHz which is the same period as for the ASE signal. Thirdly then, another periodical pattern in the shape of an envelope presents a succession of maxima with a periodicity of 60.6MHz. The maxima overlap with the positions of the free-running longitudinal modes of the slave resonator.

From this RF spectrum, set aside the 10.6MHz fast oscillations, it clearly appears that regenerative amplification occurred partially, if not totally. The envelope maxima overlapping with the slave resonator longitudinal modes in free-running operation suggests that there might be an injection-locking contribution.

To get a clearer picture, the theoretical output was computed supposing only regenerative amplification occurred in the laser cavity. Following formulas from [1], the ratio of output power P_{out} relative to the externally input power P_{inj} is given by :

$$\left.\frac{P_{out}}{P_{inj}}\right|_{reg}(\omega) = \left| \left(\frac{r_{cp} - g_{reg}(\omega)}{1 - r_{cp}\, g_{reg}(\omega)}\right) \cdot \left(\frac{r_{cp} - g_{reg}(\omega)}{1 - r_{cp}\, g_{reg}(\omega)}\right)^{*} \right| \tag{5.5}$$

with $r_{cp}^2 = R_{cp}$ the input-output-coupler reflection power coefficient and the round-trip gain $g_{reg}(\omega)$ relative to the electric field amplitude given by:

$$g_{reg}(\omega) = g_{tot}.e^{-i\frac{\omega}{c}l_{cav}} \tag{5.6}$$

where l_{cav} is the cavity optical path length and $G_{tot} = g_{tot}^2$ is the total round-trip power gain inside the laser cavity. These coefficients include the fibre gain, the reflectivity of internal mirrors other than the input-output coupler, and all the sources of loss (propagation loss, absorption, scattering of optics). Above lasing threshold, the round-trip gain is such that $G_{tot}.R_{cp} = 1$.

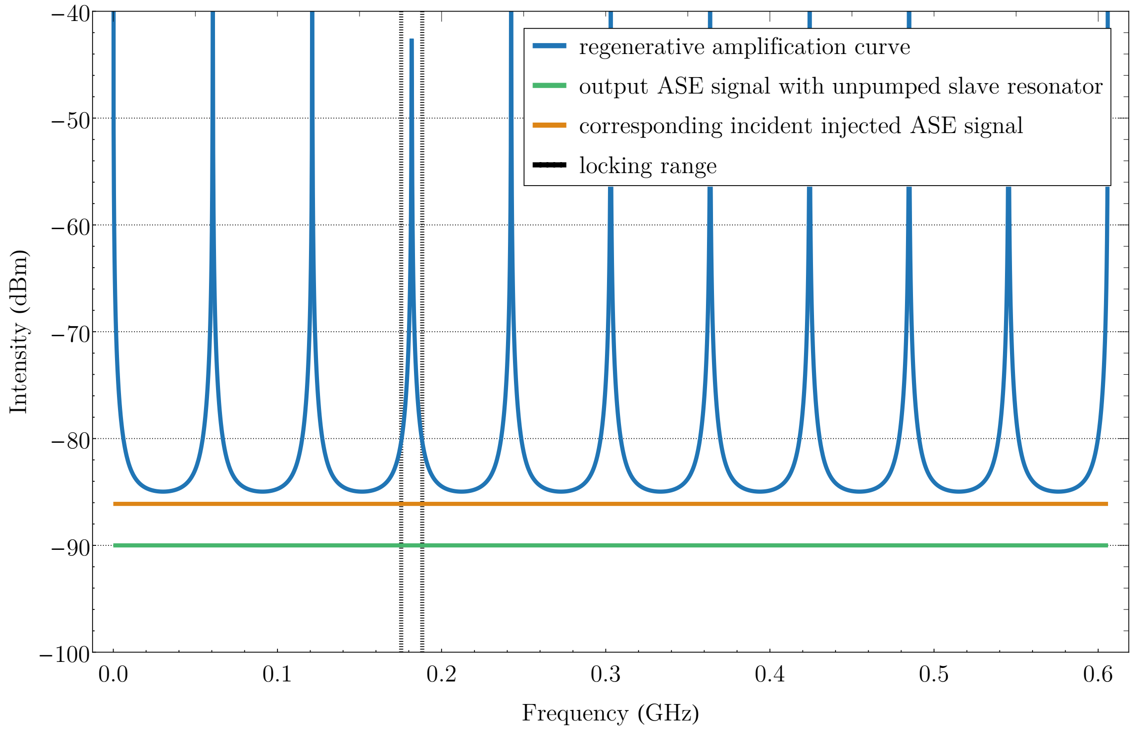

Figure 5.11: Simulation of a regeneratively-amplified-only signal for an perfectly flat input ASE signal based on experimental values

Figure 5.11 is a plot of Equation (5.5) at the dBm scale. In the condition where the slave resonator is unpumped and the ASE source switched on, the mirror reflectivity was evaluated at $R_{cp} = 35\%$ and the RF analyser returned an output of approximately -90dBm, which corresponds to an incident injected power of -86dBm. For the record, $P_{\text{dBm}} = 10\log(P_{\text{W}}/1\text{mW})$. l_{cav} is obtained from the experimental 60.6MHz free spectral range. The theoretical locking range is also plotted and is rather large due to the large ratio of injected power to the free-running power for this measurement.

It clearly appears that the general offset of power and the envelope observed in the experimental results find their origin in regenerative amplification. The curves may not perfectly overlap but this is attributed to the number of calculation approximations and the repeatability quality of the RF spectrum analyser photodiode measurements.

This simulation reinforces the idea that injection-locking did not occur in these conditions of operation. The initial assumption of this whole experiment was that the injection-locking process would be favoured over regenerative amplification. Apparently, the gain for regenerative amplification was overall greater.

In this context of sole regenerative amplification, the 10.6MHz periodical peaks could find their origin from mode competition within the 60.6MHz-frequency envelope. The input ASE 10.6MHz periodical maxima were amplified at the expense of the other frequencies within that envelope.

From these observations, regenerative amplification is the only process involved in this experiment. Nonetheless, could there be conditions of operation and specific laser designs for which injection-locking would be favoured over regenerative amplification? After all, the injection-locking gain around the slave resonator longitudinal mode frequency is locally higher than the regenerative gain outside the locking range. This goes down to mode competition.

Considering two signals of angular frequencies ω_1 and ω_2 from a completely homogeneous atomic transition, with a perfect spatial overlap and respective circulating powers $P_{circ,1}$ and $P_{circ,2}$ in a laser resonator, the gain saturation g_m for each signal in an homogeneous gain medium is [1]:

$$\left\{ \begin{aligned} g_m(\omega_1) &= \frac{g_0(\omega_1)}{1 + \kappa_{11} P_{circ,1} + \kappa_{12} P_{circ,2}} \\ g_m(\omega_2) &= \frac{g_0(\omega_2)}{1 + \kappa_{22} P_{circ,2} + \kappa_{21} P_{circ,1}} \end{aligned} \right. \tag{5.7}$$

with g_0 being the small-signal gain. The self-saturation coefficients κ_{11} and κ_{22} represent the saturation of the gain by the signal itself. The cross-saturation coefficients κ_{12} characterises the gain saturation of the signal at frequency ω_1 by the signal at frequency ω_2, and vice-versa for κ_{21}. These four coefficients are dependent on the saturation power of the gain medium and the spectral overlap between the two modes.

The rate equations are then given by:

$$\left\{ \begin{aligned} \frac{dP_{circ,1}}{dt} &= g_m(\omega_1) P_{circ,1} \\ \frac{dP_{circ,2}}{dt} &= g_m(\omega_2) P_{circ,2} \end{aligned} \right. \tag{5.8}$$

The resolution of these equations in the steady-state regime and in the small-perturbation regime highlights different modes of operation depending on the coefficients values. They are reported in Table 5.1.

$\dfrac{g_0(\omega_1)}{g_0(\omega_2)}$	$> \dfrac{\kappa_{21}}{\kappa_{22}}$	$< \dfrac{\kappa_{21}}{\kappa_{22}}$
$< \dfrac{\kappa_{11}}{\kappa_{21}}$	one dual-mode solution weak coupling	one single-mode solution ω_2 signal favoured
$> \dfrac{\kappa_{11}}{\kappa_{21}}$	one single-mode solution ω_1 signal favoured	two single-mode solutions strong coupling

Table 5.1: Stable solutions of the rate equations for two competing modes at frequencies ω_1 and ω_2 for various self- and cross-saturation coefficient ratios relative to the small-signal gain ratio

Four modes of operation are possible. In the one single-mode operation where either ω_1 or ω_2 is favoured, only one signal experiences an amplification and extracts power from the gain medium. The dual-mode solution is characterised by a simultaneous amplification of both modes which both share the same gain medium. This happens when the coupling between the two modes is weak. On the contrary, when the coupling is strong, two single-mode solutions exist but not simultaneously. In this last case, the ratio of circulating power $P_{circ,1}/P_{circ,2}$ at any given time sets the one of the two favoured modes which solely extracts power from the gain medium. This $P_{circ,1}/P_{circ,2}$ ratio can be an initial condition of operation or a perturbation from a steady-state operation.

Back to the context of injection-locking, may again ω_{inj} and ω_0 be the angular frequencies of respectively an injected single-frequency signal and the nearest corresponding slave resonator longitudinal mode. In the case where the injected frequency ω_{inj} is outside the locking range, the regenerative gain enters a competition with the free-running gain, both frequencies coexist, both signal extract their power from the gain medium, the ω_0 free-running oscillation gain is slightly diminished, this is the dual-mode regime. However, for ω_{inj} within the locking range, the injected frequency ω_{inj} is favoured over the free-running frequency ω_0 whose circulating power drops down to zero. This is a single-mode operation.

Now, what should be expected in the context of an ASE input covering both the locking range and the external wings? The calculations become significantly more complicated. A possible direction of investigation would be to rewrite equations (5.7) not considering two individual frequencies but integrating frequencies over the in-band and out-of-band portions of the locking range. It would lead to a redefinition of the small-signal gains and self- and cross-saturation coefficients. Their resolutions would determine whether or not there is a range of conditions of operation where the injection-locking process wins over regenerative amplification.

5.6 Conclusions

Strictly speaking, injection-locking is the seeding of a high-power slave oscillator by a low-power master oscillator. However, this chapter presented an attempt to achieve injection-locking of a fibre laser with a narrow-linewidth ASE source.

The ASE seed source generated 2.88W at 1075nm with a 85pm FWHM. The slave resonator was an ytterbium-doped fibre laser which could free-run up to 25.9W of output with peaks between 1070 and 1090nm with varying positions and intensities. With 1.86W of seed power coupled in, the slave resonator lased strictly at 1075nm up to 17.4W output power. For higher pump power, the slave resonator would present a additional signals at longer wavelengths.

With an injection-locking configuration, two behaviours can be expected depending on the master resonator operating frequency relative to the slave resonator longitudinal mode locking range: either regenerative amplification or "proper" injection-locking. A closer look at the 1075nm signal in the injection-locking conditions bellow 17.4W output indicated that regenerative amplification did occur and it is unclear whether injection-locking partially did as well.

The assumption initially made when designing this experiment was that regenerative amplification would be taken over by injection-locking using an ASE source but this experiment did not confirm it. A direction for further development would be to provide a proper gain competition analysis opposing the regenerative amplification gain outside the locking range to the free-running gain value within that locking range. This analysis would highlight whether or not, depending notably on the input-output coupler reflection coefficient and the ratio of injected power to the resonator free-running power, it is possible to achieve injection-locking from an ASE source.

Nevertheless, this set-up did achieve a form of amplification at the seed source wavelength.

In that context, the set-up could be easily rearranged to work as a double-pass amplifier by removing the input-output coupler and return an amplified output without any of the oscillations observed. In fact, this arrangement was also tested in the lab and one should be cautious about isolation and feedback to the seed source. Of course, the main interest of the double-pass configuration through a fibre and Faraday mirror is the polarisation maintenance without the requirement for polarisation-maintaining fibres.

In conclusion, injection-locking as a saturation of a gain within a locking-range of the ring fibre laser by the ASE source was not achieved. However, this configuration did manage to extract up to 17.4W of 1075nm signal with the 85pm FWHM linewidth of the 2.88W input ASE source without the requirement for any spectrum-narrowing element. An interesting experiment would be the use of an ASE source with a narrower linewidth, covering only a few slave longitudinal modes.

In the context of the green fibre laser project, the efficiency of the frequency doubling process is notably dependent on the signal linewidth of the nonlinear crystal input. Currently, the wavelength selection is done with spectrum-narrowing elements set inside the fibre cavity which favour certain wavelengths of operation over others. Discarding such component and selecting the frequency of operation and its linewidth from an external seed source using injection-locking could be interesting for a single-frequency operation. Potential longitudinal modes need to be shared by the enhancement cavity as well.

Bibliography

[1] A. E. Siegman, *Lasers.* University Science Books, 1986.

[2] C. J. Buczek, R. J. Freiberg, and M. L. Skolnick, “Laser injection locking,” *Proceedings of the IEEE*, vol. 61, no. 10, pp. 1411–1431, Oct 1973.

[3] C. L. Tang and H. Statz, “Phase locking of laser oscillators by injected signal,” *Journal of Applied Physics*, vol. 38, no. 1, pp. 323–324, 1967. [Online]. Available: https://doi.org/10.1063/1.1708974

[4] R. Adler, “A study of locking phenomena in oscillators,” *Proceedings of the IRE*, vol. 34, no. 6, pp. 351–357, June 1946.

[5] W. Koechner, *Solid-state laser engineering*, 6th ed. Springer, 2006, vol. Springer series in optical sciences.

[6] Y. Park, G. Giuliani, and R. Byer, "Single axial mode operation of a Q-switched Nd:YAG oscillator by injection seeding," *IEEE Journal of Quantum Electronics*, vol. 20, no. 2, pp. 117–125, February 1984.

[7] N. P. Barnes and J. C. Barnes, "Injection seeding. I. theory," *IEEE Journal of Quantum Electronics*, vol. 29, no. 10, pp. 2670–2683, Oct 1993.

[8] H. L. Stover and W. H. Steier, "Locking of laser oscillators by light injection," *Applied Physics Letters*, vol. 8, no. 4, pp. 91–93, 1966. [Online]. Available: https://doi.org/10.1063/1.1754502

[9] A. N. Bondarenko, K. G. Folin, V. A. Smirmov, and V. V. Antsiferov, "Generation induced in a Q-switch ruby laser by an extemal signal," *JETP Letters*, vol. 6, pp. 178–180, 1967. [Online]. Available: http://www.jetpletters.ac.ru/ps/1670/index.shtml

[10] K. Takeno, T. Ozeki, S. Moriwaki, and N. Mio, "100 W, single-frequency operation of an injection-locked Nd:YAG laser," *Opt. Lett.*, vol. 30, no. 16, pp. 2110–2112, Aug 2005. [Online]. Available: http://ol.osa.org/abstract.cfm?URI=ol-30-16-2110

[11] D. M. Tratt, A. K. Kar, and R. G. Harrison, *Injection-Locked Single Mode TEA CO_2 Lasers: Some Recent Measurements and Innovations.* Boston, MA: Springer US, 1985, pp. 343–353. [Online]. Available: https://doi.org/10.1007/978-1-4757-6187-0_23

[12] J. Troger, P. . Nicati, L. Thevenaz, and P. A. Robert, "Novel measurement scheme for injection-locking experiments," *IEEE Journal of Quantum Electronics*, vol. 35, no. 1, pp. 32–38, 1999.

[13] C. M. Caves, "Quantum limits on noise in linear amplifiers," *Phys. Rev. D*, vol. 26, pp. 1817–1839, Oct 1982. [Online]. Available: https://link.aps.org/doi/10.1103/PhysRevD.26.1817

[14] V. Demir, M. Akbulut, D. Nguyen, Y. Kaneda, M. Neifeld, and N. Peyghambarian, "Injection-locked, single frequency, multi-core yb-doped phosphate fiber laser," *Scientific Reports*, vol. 9, no. 1, Dec. 2019.

Chapter 6

Development of a high-power ytterbium-doped fibre laser configuration

The wavelength-tuneable linearly-polarised ytterbium-doped fibre ring laser developed in Chapter 4 showed that the ring fibre laser with a Faraday mirror works in the few tens of watts regime. This new chapter investigates power-scaling of a novel ring fibre laser: the "triangular ring configuration". This is in this configuration that the enhancement cavity will later on be placed. This chapter begins by investigating the power scaling of certain linear configurations built in the lab as a precursor to the construction of the triangular ring. The triangular configuration is then considered.

6.1 The empty triangular ring cavity

The triangular ring cavity is a ring configuration that can welcome the enhancement cavity which has a bow-tie geometry. The bow-tie geometry takes a waist as an input and converts it to another waist with a smaller radius. Considerations relative to the size of these waists are presented in Chapter 7. The empty triangular configuration is presented in Figure 6.1 and the empty section with the waist is where the enhancement cavity will be placed. It has the asset of being compact and using relatively few optics.

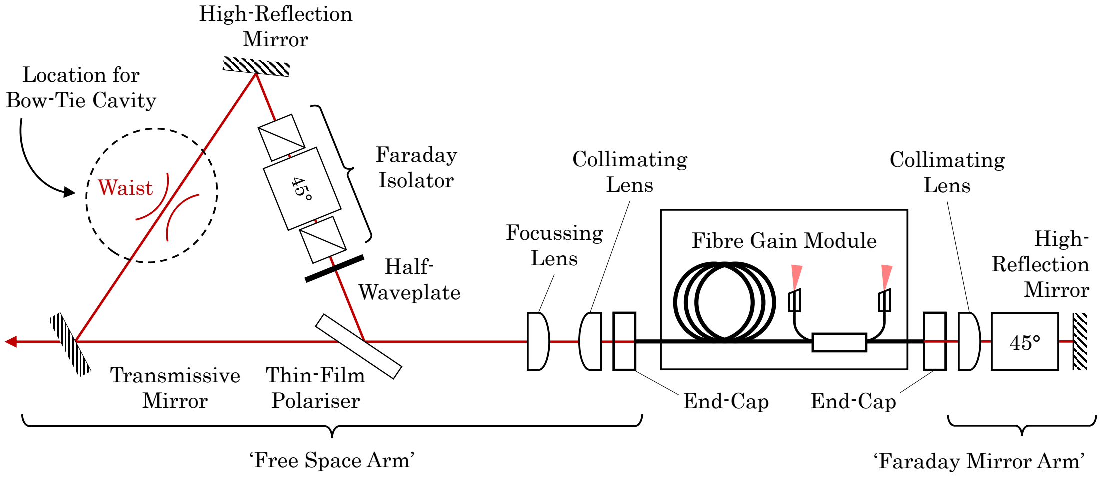

Figure 6.1: Empty triangular ring fibre laser showing the location of the internal enhancement cavity

The triangular ring cavity is very similar to Chapter 5 configuration. A fibre gain stage generates a near-infrared radiation and works in a double-pass configuration with on one end a Faraday mirror (Faraday mirror arm FMA) and on the other end a unidirectional triangular ring (free-space arm FSA). The difference lies in the presence of a focussing optic on the FSA fibre output which generates a waist in the middle of that optical path of that arm.

The triangle also incorporates polarisation selection achieved with the aid of a thin-film polariser working as a beam-splitter, and a Faraday isolator associated with a half-waveplate which also ensure the unidirectionality of propagation. The polarisation distribution is the same as in the experiments of the previous chapters: the fibre generates an horizontal polarisation which is coupled in the triangle and is returned vertical. The fibre coupled to the Faraday rotator achieve a 90° polarisation rotation.

This original shape was also notably chosen because it has a limited amount of lenses: the focussing lens also acts as the re-collimating lens due to the symmetry. One less transmission optic also means less aberrations in the phase-front.

Frequency-doubling can be seen as a source of loss as the 1060-1080nm signal circulating in the ring is converted to the green. In the empty triangle, a partially transmissive mirror simulates this loss. It also provides an output coupler to the set-up, role that the enhancement cavity will further take. This design was not built straight away: linear configurations were first implemented and their power-scaling raised challenges.

6.2 High-power handling gain stage

The high-power fibre gain stage was provided by SPI Lasers and differs in some respects from the gain stage used in the two previous chapters.

6.2.1 Description

The gain stage is composed of 17 meters of spooled GTwave ytterbium-doped fibre pumped on both ends by two 950nm 140W-class laser diodes. On one end of the active fibre a 10%-transmission 2x2 tap coupler is spliced. Angled physical contact (APC) connectors are spliced to its tap ports. High-power handling cladding-mode strippers are placed to remove cladding light at various strategic locations. The tap coupler side is intended to be connected to the Faraday mirror arm. The gain module is represented in Figure 6.2.

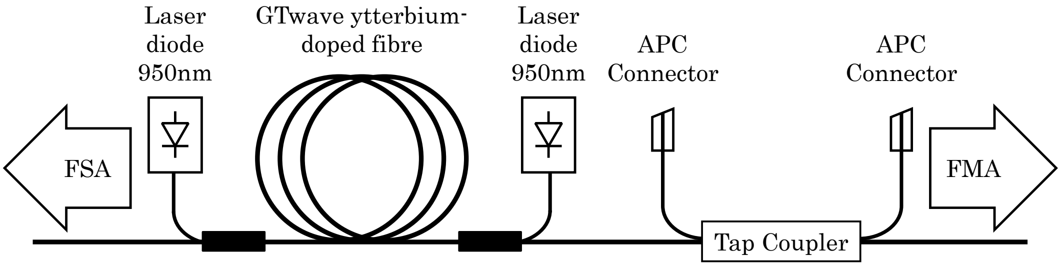

Figure 6.2: Principal components of the fibre gain module provided by SPI Lasers

Fibres in APC connectors set in a ceramic ferrule with an angle-cleave termination. The angle-cleave ensures negligible feedback and the ferule allows mechanical stability however these terminations can degrade in the multiple-watts/ten-watts and above regime and then provide feedback.

The laser diodes, the fibre spool and all the components are thermally connected to a large water-cooled plate. The fibre spool sets in a heat-conductive material. The plate was cooled to around ∼20°.

6.2.2 Tap couplers for characterisation

In a tap coupler, the core of two or more fibres are set so close that light can be partially coupled from one fibre to the other. The value of this coupling, or transmission, is defined amongst others by the distance between the cores and the lengths over which they are tightly adjacent. The 2x2 tap coupler can be seen as followed: power propagates through a main fibre and an adjacent tap fibre takes a 10% pick-off in either direction of propagation. Inversely, 10% of any input from a tap port is coupled to the main port. Light is directly coupled from one core to the other. This differs from a multimode pump combiner where light is launched in one or multiple multimode fibre ports and coupled in the cladding of a single-mode fibre. This tap coupler in this location has a number of attractions.

During any laser configuration alignment, the cavity is open and the active fibre is prone to self-pulsing. The injection of an external source via one of the tap ports can saturate the gain and, as a consequence, the gain module acts as an amplifier. The 1075nm ASE source developed in Chapter 3 was used for this purpose. In point of fact, the 1075nm central wavelength was initially chosen because it is in the region of highest gain of this module.

Also during alignment, the tap coupler can be used to attest the level of feedback to the gain module: they provide a pick-off sampling the circulating power. Photodiodes connected to an electronic amplifier and an oscilloscope were used at the APC tap port outputs to provide a fast feedback evaluation. These photodiodes were also used to detect the onset of any self-pulsing behaviour.

Finally the 10%-pick-off in both directions helps evaluating the fibre recoupling efficiency on both ends of the module. For instance, on the FMA, the tap provides the powers both coming out and returning to the fibre end while the laser is still running. The principle applies on the FSA too given that the fibre gain can be evaluated.

6.2.3 Gain stage performances

The following data was provided by SPI Lasers.

The combined 950nm output of the two laser diodes was 276W at the maximum drive current of 12A. The performance of the spooled ytterbium-doped fibre were evaluated in a linear configuration without the tap coupler. One end of the spool was spliced to a highly reflective fibre Bragg grating with a 99.9% reflection coefficient and the other end was spliced to a 14%-reflection grating acting as an output coupler. The reflection wavelength was centered at 1072.5nm. The signal-to-pump slope efficiency is 78.7%. A little more than 220W were generated.

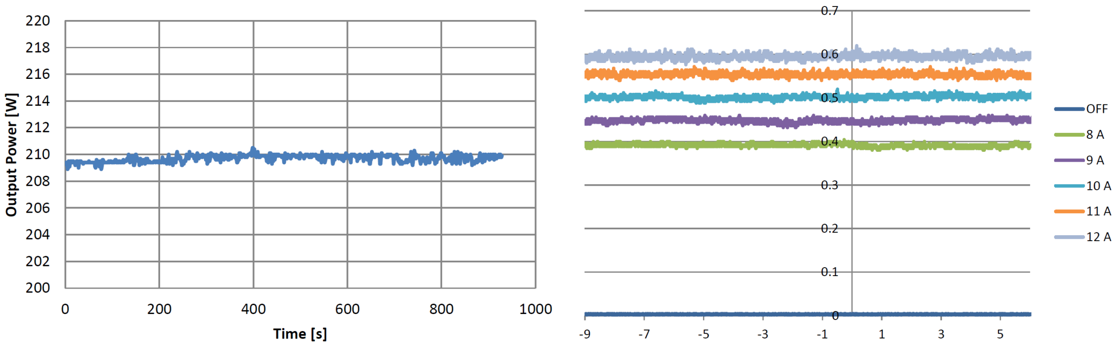

(a) 10min-long stability measurement from thermal power meter

(b) 10s-long stability measurement from photodiode

Figure 6.3: Power stability of the spooled fibre (HR-grating/14%-reflection grating)

The output power stability was given as measured by a thermal power meter over 10min in Figure 7.7(a) and by a photodiode during 10s for various diode drive currents in Figure 7.7(b). The output power is overall stable. The fast detection indicates rapid fluctuations of typically 3-4% around the average value. The slow detection highlights negligible moderate long-term variations. The fibre spool as a stand-alone laser can be considered as stable.

6.3 Optical nonlinear effects triggered at high-power levels

At high optical intensities, third-order nonlinearities can be triggered in the glass core of optical fibres. Their particular confined geometry, which is an asset to maintain a single-mode operation, turns to a disadvantage for mechanisms like stimulated Brillouin and Raman scattering.

6.3.1 Stimulated Brillouin Scattering

With spontaneous Brillouin scattering, a photon from an input optical wave (frequency ν_{input}) is converted into an acoustic phonon contributing to the vibration of the crystal and a scattered photon down-shifted in frequency. The scattered photons form the Stokes wave (frequency ν_{Stokes}) which can propagate in optical fibres in either the forward direction, which is weak and negligible, or the backward direction.

From a certain power threshold, the phonons affect the medium's density to the point of generating an acoustic wave via electrostriction. It results in a periodic modulation of the refractive index and the generation of a Bragg grating which constitutes an additional contribution to the backscattering of the input signal. The back-reflected light experiences a gain and extracts its power from the incident wave. This is known as stimulated Brillouin scattering (SBS). SBS in fibres can result in the generation of pulses fluctuating stochastically with a time-scale of 5-10ns. At high power, SBS can lead to the destruction of the fibre turned into "white powder".

An approximation of the Brillouin frequency-shift defined as $\nu_B = \nu_{input} - \nu_{Stokes}$ is given by the equivalent frequency in the backward direction [1]:

$$\nu_B \simeq 2v_{ac}\frac{\nu_{input}n_{eff}}{c} \tag{6.1}$$

where n_{eff} is the effective refractive index, c is the speed of light in vacuum and v_{ac} is the acoustic velocity or speed of sound in the medium of interest. The Brillouin gain spectrum $g_B(\nu)$ has a Lorentzian shape whose FWHM $\Delta\nu_B$ is inversely proportional to the phonon lifetime τ_B with $\Delta\nu_B = 1/(2\pi\tau_B)$. The Brillouin gain is maximal at ν_B and is provided by [2]:

$$g_B(\nu_B) = \frac{\pi n^7 p_{12}^2}{c\lambda_{input}^2 \rho v_{ac} \Delta\nu_B} \tag{6.2}$$

where p_{12} is the longitudinal elasto-optic coefficient of the medium of propagation.

The critical power P_{crit} is defined as the power below which SBS can be considered negligible or in other words it is the power from which the effects of SBS become significant. The convention follows the experimental approximation [3]:

$$P_{crit} \simeq \frac{21 A_{eff}}{g_B(\nu_B) l_{eff}} \tag{6.3}$$

where A_{eff} is the effective cross sectional area, $l_{eff} = [1 - \exp(-\alpha l_{fibre})]/\alpha$ is the effective length of the gain fibre of length l_{fibre} and propagation loss α.

These parameters were evaluated for an 1075nm-wavelength input signal in a silica glass fibre of 10µm-diameter core with 17m of active section and with $n_{eff} \sim 0.45$, $p_{12} = 0.252$ and $T_B \sim 10$ns. The acoustic velocity was evaluated for a volumetric deformation (longitudinal wave) so that $v_{ac} = \sqrt{E_{Young}(1 - \nu_{Poisson})/\rho(1 + \nu_{Poisson})(1 - \nu_{Poisson})} = 5.9\text{km.s}^{-1}$ (Young's modulus $E_{Young} = 71.7$GPa, Poisson's ratio $\nu_{Poisson} = 0.17$, density $\rho = 2.203\text{g.cm}^{-3}$).

The Brillouin frequency shift is $\nu_B = 16.0$GHz and has a linewidth of $\Delta\nu_B = 15.9$MHz. In the wavelength spectrum, the Brillouin shift is 61.5pm and the Brillouin gain has a 0.061pm linewidth which, in practice, are too small to be evaluated with standard optical spectral analysers. The gain peak is $g_B(\nu_B) = 5.4.10^{-11}\text{m.W}^{-1}$ and the critical power $P_{crit} = 3.06$W. This SBS threshold value is considerably low in comparison with the few hundreds of watts the SPI gain stage can generate. However, in the case of large input linewidth $\Delta\nu_{input}$, the SBS power threshold expression is proportional to the ratio between the input and the Stokes wave linewidths [1]:

$$P_{crit} \simeq \frac{21 A_{eff}}{g_B(\nu_B) l_{eff}} \left(1 + \frac{\Delta\nu_{input}}{\Delta\nu_B}\right) \tag{6.4}$$

and this increases significantly the critical power. For instance, with a signal as narrow as $\Delta\lambda_{input} = 0.1$nm i.e $\Delta\nu_{input} = 26.0$GHz, the critical power value is increased by 1630 and is approximately 5.0kW.

It is also possible to approach the critical power as relative to a unique frequency. For a laser cavity operating on different longitudinal mode, the power is distributed over these modes so that the overall critical power increases. The empty triangular cavity has a round-trip length of approximately 40m so that its free spectral range is 5.2MHz. A circulating signal of 0.1nm linewidth, i.e. 26GHz, would cover approximately 5000 longitudinal modes. It gives a critical power of 15.3kW.

The fibre gain module is pumped by two 140W-class laser diodes. This is small in comparison to these rough estimations of the critical power and therefore SBS should not be encountered.

6.3.2 Stimulated Raman Scattering

With spontaneous Raman scattering, an input photon into a Raman active medium (frequency ν_{input}) is also converted into an optical phonon associated with the vibration or the rotation of a molecule (frequency ν_R) and a photon of lower frequency $\nu_{Stokes} = \nu_{input} - \nu_R$. With the Raman process, if the medium of propagation is in an excited state, an additional anti-Stokes wave with a higher frequency $\nu_{anti-Stokes} = \nu_{input} + \nu_R$ than the incident photon can also be generated but it is not thermodynamically favoured.

Now considering a Raman active medium where in addition to the input wave at frequency ν_{input} a probe beam at frequency ν_{probe} is also incident, if their difference of frequency matches one of the vibrational modes of the molecules of the medium, the probe signal will experience a Raman amplification at the expense of the input wave. The latter acts as a pump to the stimulated Raman scattering (SRS) process.

Silica glass has a noncrystalline structure and therefore the vibration modes are numerous and overlapping. Therefore the SRS gain $g_R(\nu)$ spectrum over which the probe signal can be amplified is relatively wide. For a fibre with an input wavelength of 1µm, this gain is as broad as 40THz (133nm) with a large peak around 13THz (43nm) [4].

In the context of this project, there is no additional probe signal. However, spontaneous Raman scattering can generate a signal at any frequency ν_{Stokes} within the gain spectrum of stimulated Raman scattering which can in return behave as a probe signal. Consequently it gets amplified via SRS and the critical power P_{crit} from which this process is appreciable is approximately [3]:

$$P_{crit} \simeq \frac{16A_{eff}}{g_R(\nu)l_{eff}} \tag{6.5}$$

where A_{eff} and l_{eff} definitions are the same as for SBS. This expression is valid for forward SRS whereas backward SRS has a higher power threshold and is therefore usually not encountered. This expression is to compare with the SBS critical power of Equation (6.3): they differ from their approximation coefficient (16 for SRS whereas 21 for SBS) and their gain coefficient value. The Raman gain spectrum is maximal around 13THz with a value of $g_R \sim 1.10^{-13}$m.W^{-1} smaller by two orders of magnitude than the previously calculated SBS value $g_B(\nu_B) = 5.4.10^{-11}$m.W^{-1}. Therefore SBS effects should be observed before SRS effects.

In conclusion, SBS and SRS are two detrimental processes to the operation of a fibre laser at high power. The main detrimental effect of SBS is the generation of high-energy pulses. In the case of SRS, a portion of the 1060-1080m signal is shifted by a couple tens of nanometers and represents a loss.

6.4 Alignment process

As introduced in Chapter 3, fibre gain modules are particularly prone to self-pulsing when they are run near laser threshold with a lack of optical feedback. The consequences are the generation of high-energy pulses which damage the fibre. The gain module then needs to be rebuilt. This requires time and the replacement of the active fibre if not all the fiberised components.

Running the gain module at low pump power below threshold in an open cavity only provides ASE outputs up to approximately 100mW at best on both ends. This is sometimes enough to align cavities with very few optics but not for some of the following complex configurations. Two strategies were consequently followed to avoid self-pulsing as shown in Figure 6.4.

The first strategy consisted in using the ASE source developed in Chapter 3 to saturate the fibre gain via its coupling through the 10%-transmission tap coupler. Once pumped the gain module preferentially works as an amplifier of the ASE signal in the open cavity.

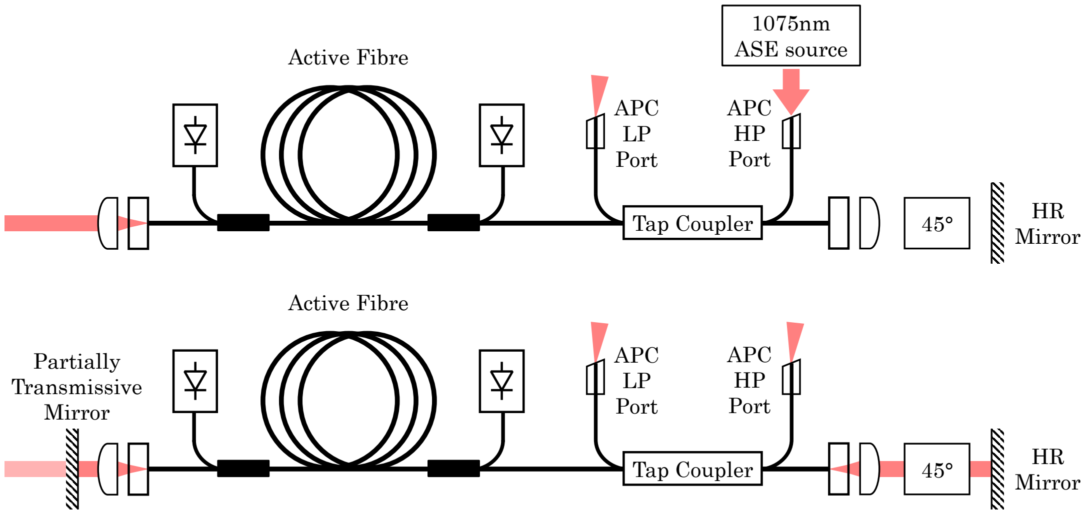

Figure 6.4: Alignment configurations: (top) ASE source coupling via the tap coupler, (bottom) linear cavity using a partially transmissive mirror on the FSA fibre end

The tap coupler ports were denominated high-power (HP port) and low-power (LP port) as in a double-pass configuration, the power coming from the active fibre toward the tap coupler is inherently greater than the one doing a round-trip in the Faraday mirror arm due to the fibre recoupling efficiency. The ASE source output was coupled to the HP port in the direction of the active portion of fibre of the gain stage.

The second strategy did not involve the ASE source but consisted in setting the gain module in a linear cavity with the Faraday rotator and a HR mirror on the FMA end and a partially transmissive mirror on the FSA end. Greater power can be extracted from the gain module.

In practice, self-pulsing occurred a few times during the development process and the gain module was successively damaged. High-power pulses are generated at every output including the tap ports. As the ASE source final amplification stage is high gain and not optically isolated, any feedback could lead to its failure if not its damage. For this reason, the linear cavity strategy was sometimes privileged over the ASE source coupling strategy.

6.5 Power distribution and fibre recoupling evaluations

This section provides the evaluation of the circulating powers and the fibre recoupling efficiencies. They are calculated from the power pick-offs from partially transmissive mirrors and the tap coupler. The denominations defined here are used throughout this chapter and the following one.

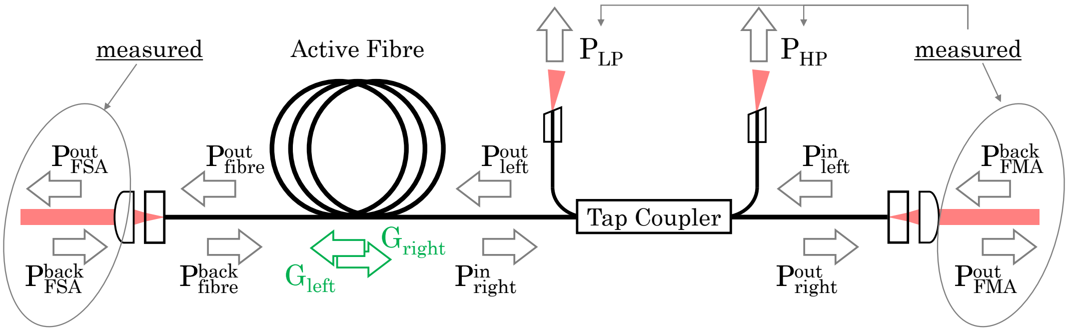

Figure 6.5: Power at the various locations in the laser resonator around the gain module

On both FSA and FMA ends of the gain module, it is assumed that the output powers, respectively P^{out}_{FSA} and P^{out}_{FMA}, and incident powers, respectively P^{back}_{FSA} and P^{back}_{FMA}, can be measured.

The low-power and high-power tap coupler power outputs, respectively P_{LP} and P_{HP}, provides the circulating power in and out the component either on the left-hand side, respectively P^{in}_{left} and P^{out}_{left}, or the right-hand side, respectively P^{in}_{right} and P^{out}_{right} (see Figure 6.5). For a tap coupler transmission T_{tap}, their values are given by:

$$P^{in}_{right} = \frac{P_{HP}}{T_{tap}} \qquad P^{out}_{right} = \left(\frac{1}{T_{tap}} - 1\right) P_{HP} \tag{6.6}$$

$$P^{in}_{left} = \frac{P_{LP}}{T_{tap}} \qquad P^{out}_{left} = \left(\frac{1}{T_{tap}} - 1\right) P_{LP} \tag{6.7}$$

The active fibre has single-pass gains G_{left} and G_{right} in respectively the left and right directions given by:

$$P^{out}_{fibre} = G_{left} \,.\, P^{out}_{left} \tag{6.8}$$

$$P^{in}_{right} = G_{right} \,.\, P^{back}_{fibre} \tag{6.9}$$

where P^{out}_{fibre} and P^{back}_{right} are the powers in the FSA fibre end in respectively the outward and returning directions. It is assumed that the gain module stands in a resonator and the single-pass gain is equal in both directions. Its value is noted G and considering $P^{out}_{FSA} = P^{out}_{fibre}$ it is given by:

$$P^{out}_{FSA} = G.P^{out}_{left} = G.\left(\frac{1}{T_{tap}} - 1\right) P_{LP} \tag{6.10}$$

As the gain module is optically pumped, the fibre gain increases up to a threshold value where the round-trip losses are compensated. The gain is then clamped to a certain value representative of the losses of the laser configuration.

Finally, the fibre recoupling efficiencies in the free-space arm and the Faraday mirror arm, respectively $\eta_c(FSA)$ and $\eta_c(FMA)$, are given by:

$$\eta_c(FMA) = \frac{P^{in}_{left}}{P^{back}_{FMA}} = \frac{P_{LP}}{T_{tap}\,.\,P^{back}_{FMA}} \tag{6.11}$$

$$\eta_c(FSA) = \frac{P^{back}_{fibre}}{P^{back}_{FSA}} = \frac{P_{HP}}{G\,.\,T_{tap}\,.\,P^{back}_{FSA}} \tag{6.12}$$

In conclusion, the different power pick-offs give access to the power distribution, the fibre single-pass gain and the fibre recoupling efficiencies at both ends of the module. This knowledge helped identifying the sources of failure.

6.6 Experimental results: linear cavities

6.6.1 Linear cavity with collimated beams

The starting point was a linear standing-wave resonator: the fibre gain module sits between two mirrors as represented on Figure 6.6. The FMA feedback mirror $\mathrm{M_{FMA}}$ has a 1.4% transmission and provides a power pick-off whereas the FSA feedback mirror $\mathrm{M_{FSA}}$ act as an output coupler with a 70% transmission. Aspheric lenses collimate the fibre outputs at both ends. The set-up was tested with the Faraday rotator in or out of the FMA.

Figure 6.6 also shows a (not-to-scale) representation of the power evolution in the two counter-propagating directions (the fibre recoupling losses are not represented for simplification). Mirror $\mathrm{M_{FMA}}$ transmission is so low that the fibre works essentially as a

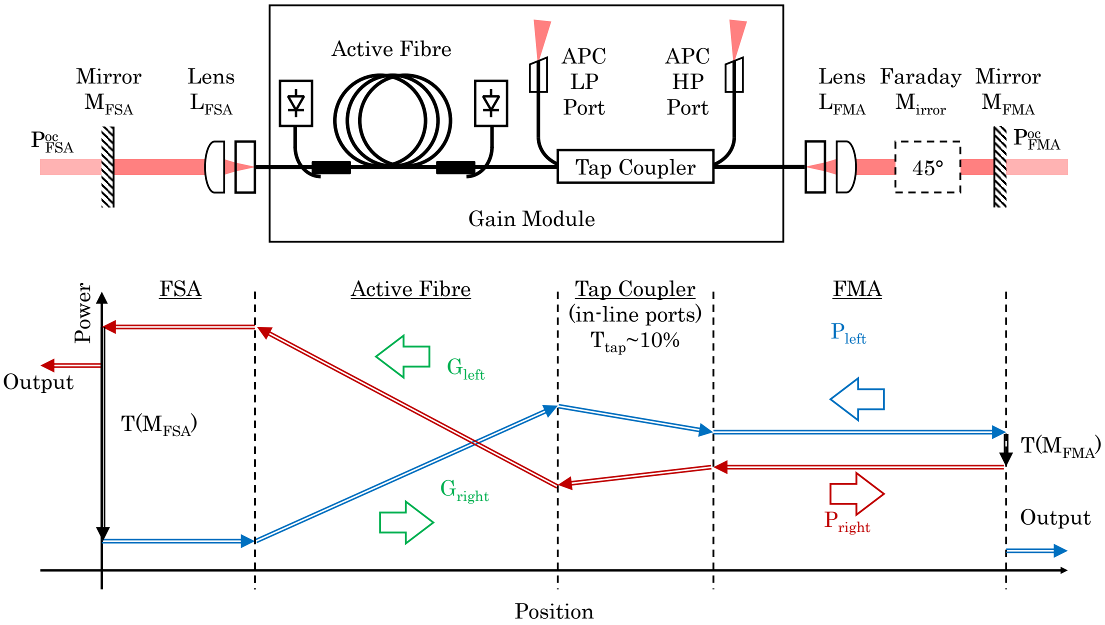

Figure 6.6: (top) The linear configuration and (bottom) its intra-cavity power evolution (configurations I to IV)

double-pass amplifier and the power level is the highest in the FSA. The tap coupler is sensitive to its circulating power and is therefore placed on the FMA side of the gain module where the power is lower.

	Configuration	I	II	III	IV
FSA	M_{FSA}	M70SH	M70FS	M70FS	M70FS
	L_{FSA}	LTH15	LTH15	LAS15	LAS15
FMA	L_{FMA}	LTH18	LTH18	LAS15	LAS15
	Faraday Rotator	out	out	out	FR1
	M_{FMA}	M95FS	M95FS	M95FS	M95FS

Table 6.1: List of components for the linear configurations

This linear configuration was tested with four sets of components as reported in Table 6.1 and referenced in Appendix A with their relevant characteristics. All the components were designed to work at 1060-1080nm or over a wider range.

Figure 6.7 gives the performances of the laser in Configuration I built with off-the-shelf components. The power from the FSA output coupler P^{oc}_{FSA} is relatively linear with a 48% slope efficiency up to 138W pump power. It is in good agreement with the theoretical slope efficiency $\eta_{laser} = 44\%$ calculated from Equation (2.22) (round-trip loss $L_{r.t.} = \eta_c^2 T(M_{FMA}) = 55\%$ with a fibre recoupling efficiency $\eta_c = 75\%$, absorption efficiency $\eta_{abs} = 90\%$ and pumping quantum efficiency $\eta_q = 1$). However above 138W pump power, the laser gets unstable. There is more going on and this is where a closer look at the fibre recoupling and the fibre gain is necessary.

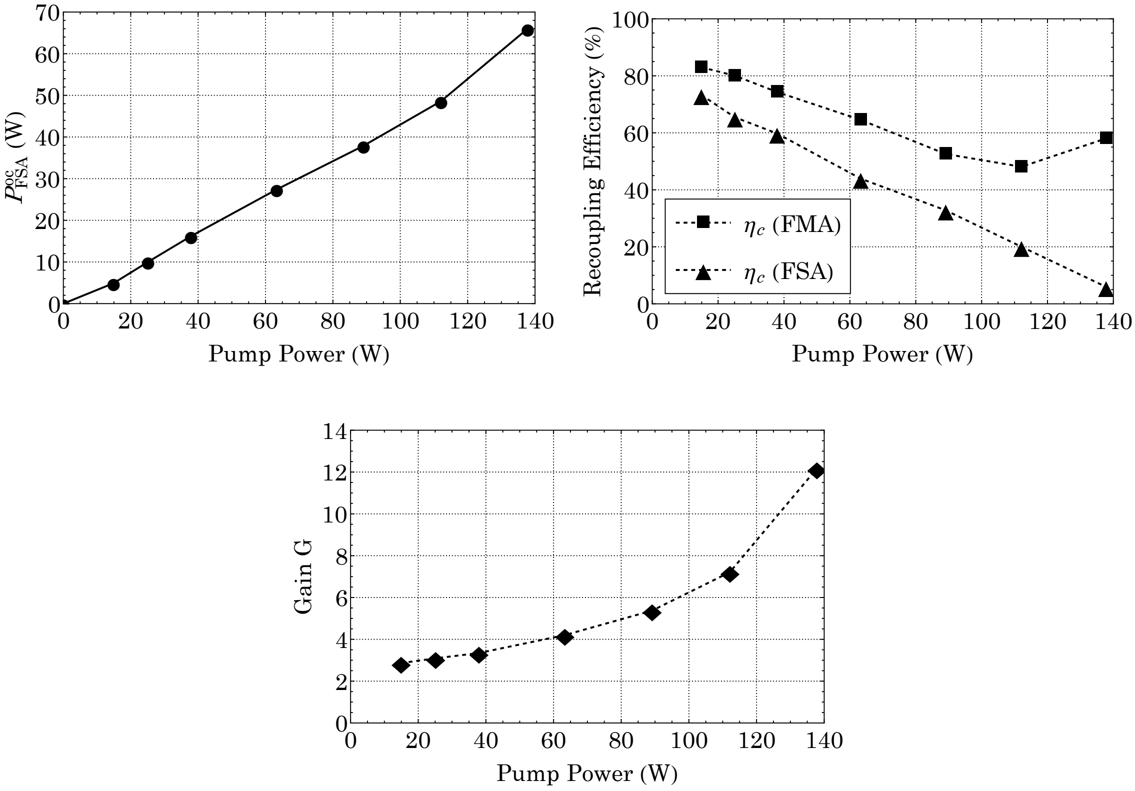

Figure 6.7: Performances of Configuration I

The fibre recoupling efficiencies went from $\eta_c(FSA) = 57.0\%$ and $\eta_c(FMA) = 83.0\%$ at low pump power (14.9W) down to $\eta_c(FSA) = 4.6\%$ and $\eta_c(FMA) = 58.0\%$ at higher power (138W). As the pump power was increased the FSA arm recoupling efficiency eventually dropped to values that were too low to provide enough feedback to the fibre, which started self-pulsing.

The single-pass gain increased from 2.86 (at 14.9W pump power) up to 12.2 (at 138W pump power). The fact that above laser threshold the gain value increases indicates that the losses of the system increased as well. This is in good agreement with the reduction of the fibre recoupling efficiency reductions with power. The active fibre compensated with a higher gain until it was too high and triggered self-pulsing mechanisms.

What is the origin of the reduction in recoupling efficiencies and where did the power go? A thermography camera was used to detect the infrared radiation from heat sources. At high power operation, a number of heat points with elevated temperature were recorded with a room temperature at 21°C.

First, the aspheric lenses were heating up: +15°C for L_{FMA}, +24°C for L_{FSA} (and +10°C for the mount it was glued to). Also, cladding-mode strippers located on both ends of the gain module, just before the end-caps, observed +10°C and +18°C variations on respectively the FMA and FSA sides. It appears that as the lenses were heating up, thermal lensing and the introduction of optical aberrations altered the phase-front quality, its focussing ability and its alignment. Consequently, it appears that a large portion of the light returning to the fibre was coupled in the cladding.

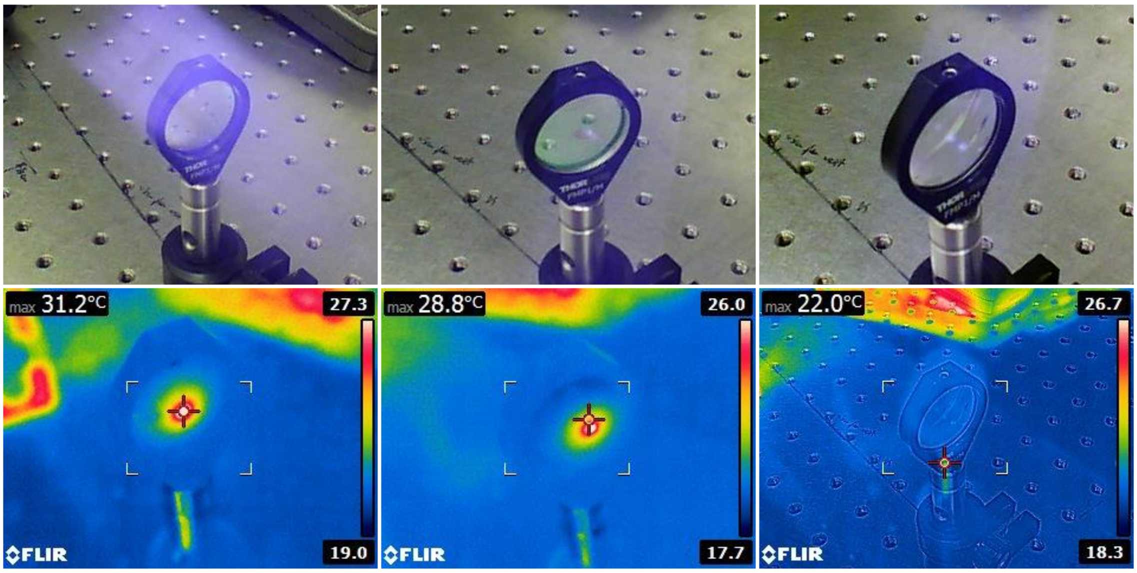

Figure 6.8: Visible and thermal images of (left) BK7 plano-convex lens, (centre) BK7 wedge and (right) fused silica aspheric lens with 79W of 1080-1100nm incident radiation

Secondly, a +40°C variation was observed on the output coupler $\mathrm{M_{FSA}}$ contributing to additional thermal lensing whereas pick-off mirror $\mathrm{M_{FMA}}$ did not heat up. This explains the asymmetry between the two arms recoupling efficiencies and the stronger downward trend of the FSA one.

The heating from the lenses and the mirror can be due to the absorption of the near-infrared radiation either by the substrate or the coatings. Several off-the-shelf test optics working in transmission with different substrates were crossed by a 79W of continuous-wave 1080-1100nm radiation and observed with the thermal camera. Three of them are reported in Figure 6.8. Optics whose substrate was BK7, H-LaK54 (lenses LTH15 and LTH18) and D-ZK3 heated up by approximately +10°C. This variation was not expected from optics designed at these wavelengths. However, fused silica substrates did not heat up which is notably the material of end-caps and mirror $\mathrm{M_{FMA}}$. The latter became the substrate of choice for the replacement optics.

Mirror $\mathrm{M_{FSA}}$ was replaced with a mirror with the same transmission (70%) and provided Configuration II. The aspheric lenses were changed between configurations II and III. Figure 6.9 gives the power output P^{oc}_{FSA} and the recoupling efficiencies after substitution of the optics.

Replacing the output coupler in the FSA in Configuration II was enough to keep the recoupling efficiency constant with a mean value of $\eta_c(FSA) \sim 66.8\%$. The gain module ran up to approximately 160W pump power before experiencing a power roll-over. The single-pass gain went from 2.71 at 14.9W pump power to 4.35 at 210W pump power, considerably lower than the Configuration I 12.2 value at 138W pump power.

The recoupling efficiencies obtained from replacing the aspheric lenses in Configuration III were relatively constant over the power range covered (up to 210W pump power) with average values of $\eta_c(FSA) \sim 58.3\%$ and $\eta_c(FMA) \sim 64.8\%$. However, in comparison to recoupling efficiencies with previous lenses at low power operation, these values are lower. There is a trade-off here. Lenses LTH15 and LTH18 appear better at preserving a good beam phase-front quality than fused silica lens LAS15. However, lens LAS15 has a fused silica substrate and does not absorb nor heat up at high power.

Finally, Configuration IV introduces a Faraday rotator FR1 in the FMA with the same

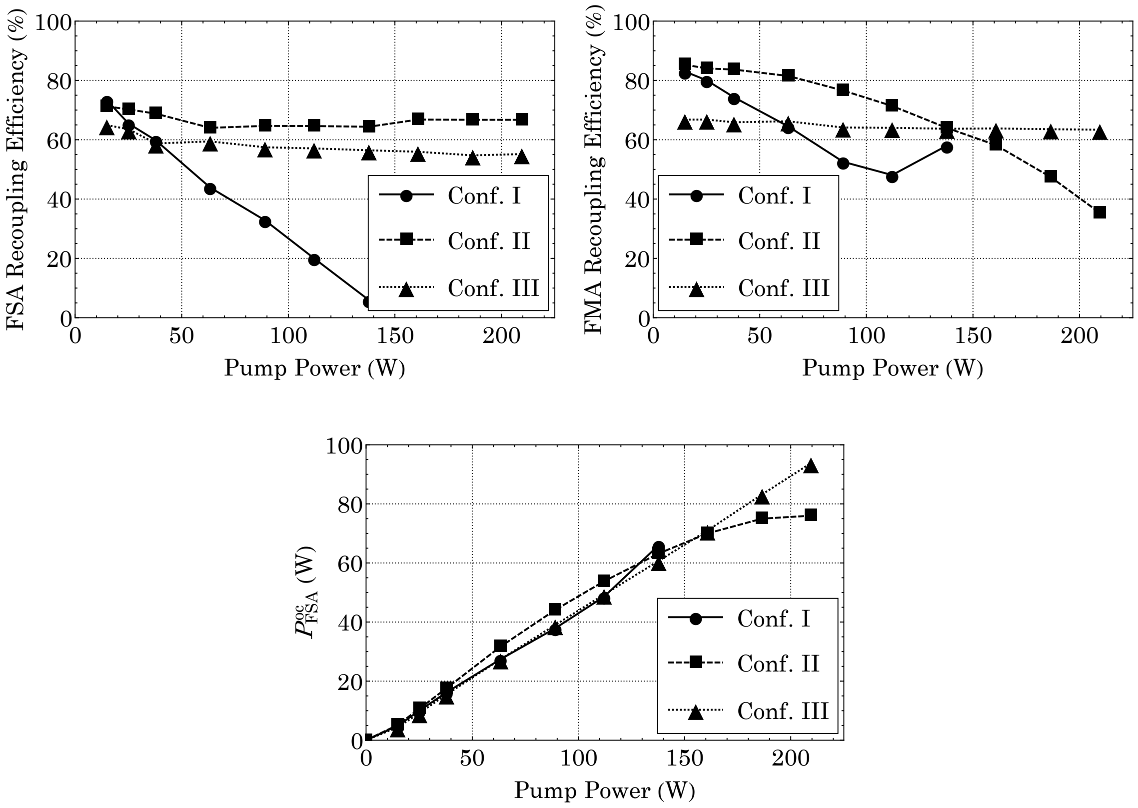

Figure 6.9: Comparative performances of linear configurations I, II and III

set of components as in Configuration III. Figure 6.10 provides the recoupling efficiencies of both arms. The FSA one is barely affected by the power-scaling however the FMA one decreases. This can be attributed to thermal lensing in the Faraday rotator.

Ideally, replacing the rotator material with a crystal of lower absorption is the best option. Alternatively, the thermally induced defocussing can be tackled by actually aligning the laser in the high power regime. However this is not ideal and does not address the phase-front quality degradation. It was reported in the literature that for a rod-shaped rotating crystal whose symmetry axis is along the beam path, the lensing effect can be compensated by either the use of a spherical lens or a curved mirror, or a spherical grinding of the rod face [5]. A Faraday rotator with a higher quality rotator material was not immediately available at this stage of development and the FR1 was kept in the following configurations.

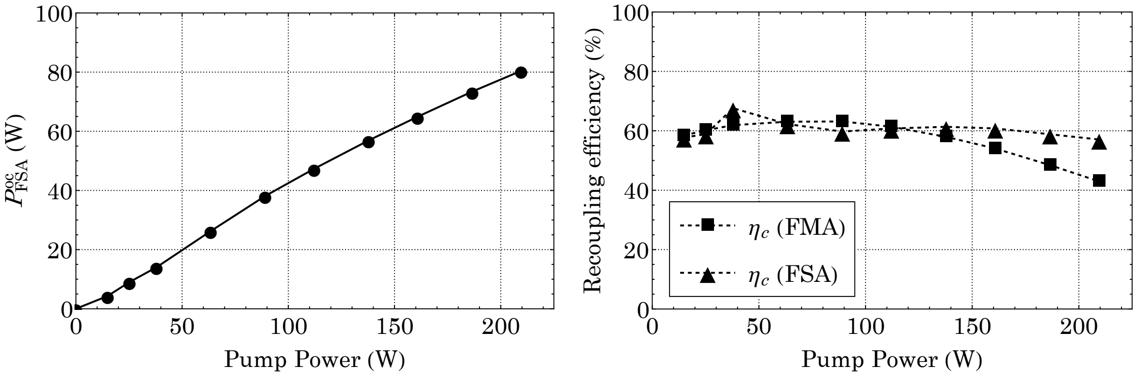

Figure 6.10: Performances of Configuration IV

6.6.2 Linear cavity with a focussed beam

In the previous configurations, lenses collimate the fibre outputs so that in each arm the transverse mode maintains its size and can be recoupled down to the fibre core after round-trip. Another stable reproduction of the fundamental Gaussian mode after round-trip can be achieved if a beam waist is generated in the middle of the feedback arm. For instance, the fibre output lens can focus the beam on the feedback mirror face and this constitutes a stable configuration. These two options are represented on Figure 6.11.

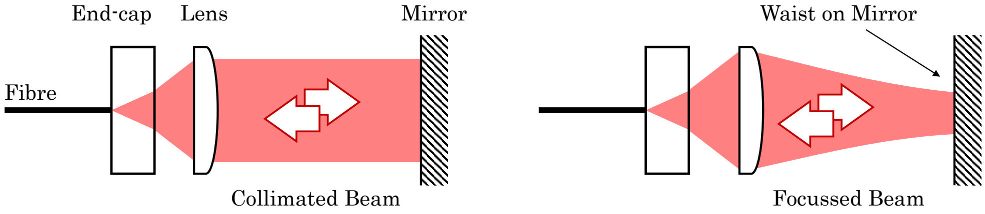

Figure 6.11: Stable linear arrangements for a free-space coupling from a fibre with a feedback mirror: (left) collimated beam, (right) focussed beam with waist on mirror

Configuration V, represented in Figure 6.12, simulates the waist intended to be in the upper arm of the enhancement cavity but in a linear configuration. In the FSA, a first aspheric lens $L_{\mathrm{FSA,C}}$ collimates the output beam from the fibre followed by a plano-convex focussing lens $L_{\mathrm{FSA,F}}$ of 500mm focal length. The waist is generated on the 70%-transmission mirror $M_{\mathrm{FSA,2}}$ still acting as an output coupler. In-between a highly-reflective mirror $M_{\mathrm{FSA,1}}$ is placed at the angle required for the upcoming triangular ring configuration. The other components are the same as in Configuration IV. See Table 6.2.

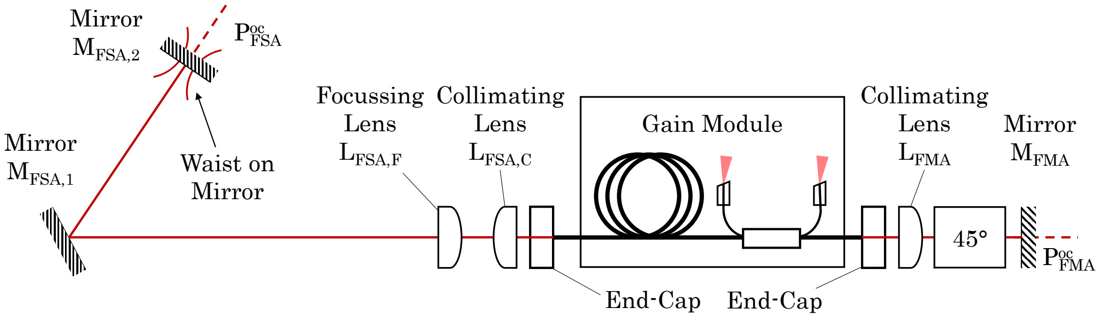

Figure 6.12: Configuration V: linear cavity with a focussed beam

	Configuration	V
FSA	L_{FSA}	LAS15
	L_{FSA}	LTH500
	$M_{FSA,1}$	HR mirror
	$M_{FSA,2}$	LAS15
FMA	L_{FMA}	LAS15
	Faraday Rotator	FR1
	M_{FMA}	M95FS

Table 6.2: Configuration V: list of components

The focussing lens $L_{FSA,F}$ was set on a translation stage to position precisely the waist on mirror $M_{FSA,2}$. Once set, this should also be the optimum waist position for a triangular ring configuration. Configuration V recoupling efficiencies are given in Figure 6.13. The trends and values are similar to the previous configuration and no new sources of failure were identified.

In conclusion, the gain module was tested in a linear configuration and thermal effects originating from bulk optics were detected, impacting the fibre recoupling efficiencies. It was showed that commercial glasses BK7, H-LaK54 and D-ZK3 were heating up when working in transmission or reflection in the multiple tens of watts regime at 1080-1100nm wavelength as well as the Faraday rotator crystal. A temperature increase of approximately 10°C is sufficient to induce thermal lensing and aberrations which are detrimental to

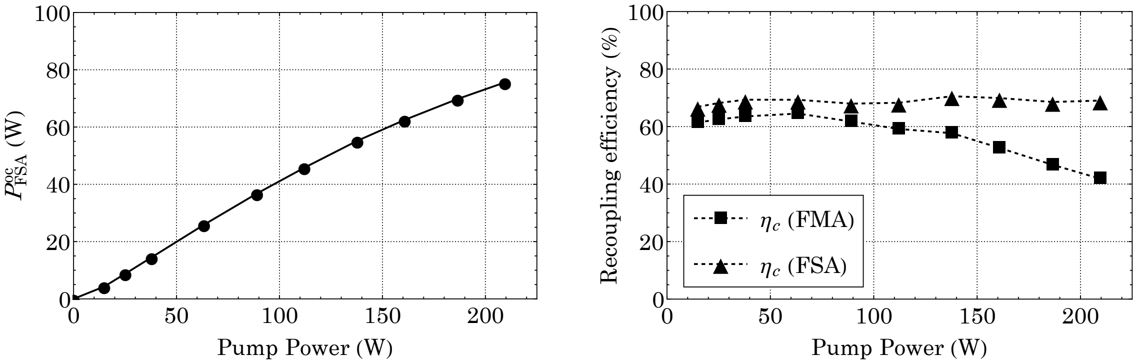

Figure 6.13: Configurations V: recoupling efficiencies

the fibre recoupling efficiencies and therefore the operation of the laser at high-power. Optics with a fused silica substrate yielded no temperature variation and good recoupling efficiencies were observed using them. Also, the performances of a linear configuration simulating an upper-arm waist were comparable to a linear configuration with collimated beams in both arms and can be used as a base to compare the performances of the triangular ring cavity.

6.7 Experimental results: empty triangular ring cavity

6.7.1 Presentation and performances

A schematic of the empty triangular configuration is given in Figure 6.14. The FMA remains unchanged and is composed of a collimating lens $\mathrm{L_{FMA}}$, a Faraday rotator and a feedback mirror $\mathrm{M_{FMA}}$. The FSA is composed of a collimating lens $\mathrm{L_{FSA,C}}$ and a focussing lens $\mathrm{L_{FSA.F}}$ on the fibre output. A thin-film polariser opens the ring in the triangular shape and then a first mirror $\mathrm{M_{FSA,1}}$ in the trajectory of the allowed circulating polarisation together with a second mirror $\mathrm{M_{FSA,2}}$ close the loop. The waist is generated between these two mirrors. A Faraday isolator and a half-waveplate designed for operation at 1064nm are placed before the thin-film polariser in the returning loop to ensure respectively the unidirectionality of propagation and the required polarisation rotation for re-injection in the fibre gain stage.

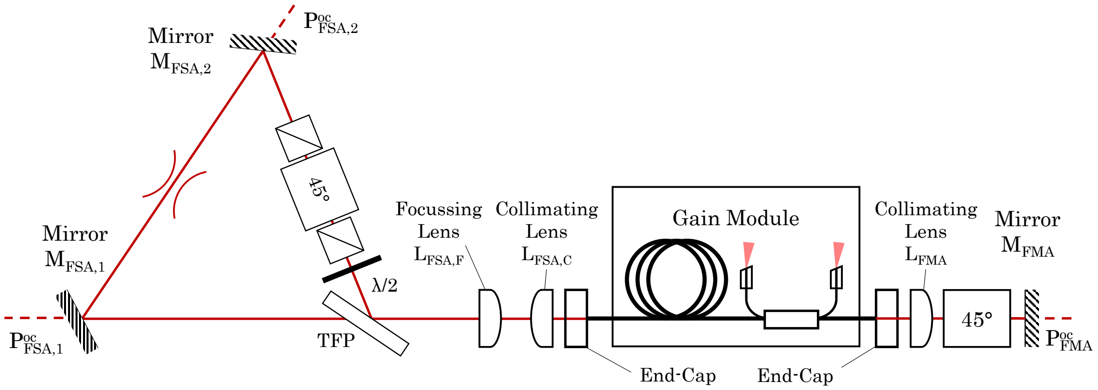

Figure 6.14: Empty triangular configuration (configurations VI and VII)

The empty triangular configuration was tested in Configuration VI with the components referenced in Table 6.3. It uses the ones of Configuration V with a few additions. Mirror $M_{FSA,2}$ has a 80% transmission and acts as the FSA output coupler. Mirror $M_{FSA,1}$ has a 96.4% reflection and provides a pick-off. The Faraday isolator is placed after the FSA output coupler and is therefore crossed by little power so that no strong thermal lensing is expected.

	Configuration	VI	VII
FSA	$L_{FSA,C}$	LAS15	LAS15
	$L_{FSA,F}$	LTH500	LTH500
	$M_{FSA,1}$	M70FS	M70FS
	$M_{FSA,2}$	M95FS	M95FS
	TFP	TFPNP	TFPNP
FMA	L_{FMA}	LAS15	LAS15
	Faraday Rotator	FR1	FR1
	M_{FMA}	M95FS	M95FS
	End-Caps	Bulk	Hybrid

Table 6.3: Configurations VI and VII: list of components

The recoupling efficiencies in both arms are reported in Figure 6.15. In the FMA, there was a slow decrease with power due to thermal lensing in the Faraday rotator. However, in the FSA it was overall constant but experienced a considerable reduction in comparison with Configuration V with an average η_c(FSA) = 49.5%. The fact that this value is steady with pump power rules out the hypothesis of thermal lensing in any of the newly introduced components (Faraday isolator, wave-plate and thin-film polariser) even though the thin-film polariser TFPNP substrate is BK7 and the Faraday isolator rotating material is identical to Faraday rotator FR1 one.

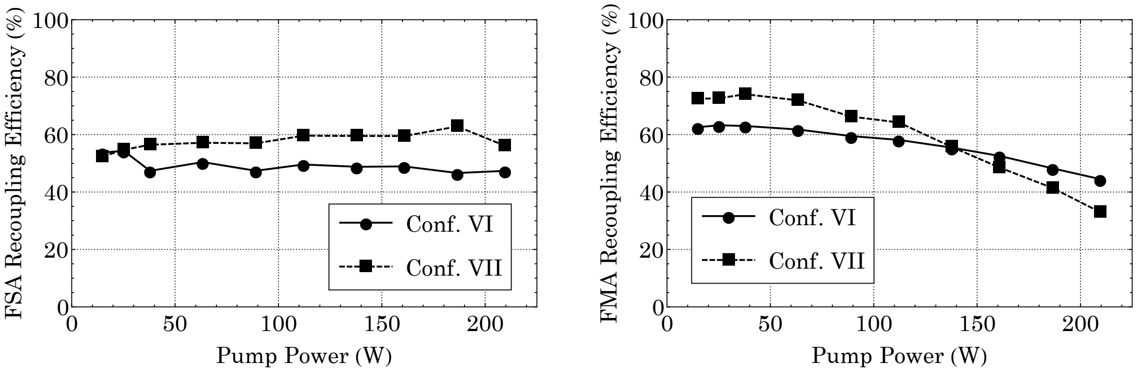

Figure 6.15: Recoupling efficiencies of the empty triangular configuration before and after end-cap revision (configurations VI and VII)

A reasonable assumption to this recoupling efficiency diminution would be an alteration of the phase-front quality variation due to these newly introduced optics. This can be caused by imperfect surfaces and coatings or aberrations intrinsic to the optic's design. The phase-front quality straight out of the two fibre ends of the gain module were evaluated. In the ideal scenario, as the fibre is single-mode, one should observe a circular symmetric fundamental Gaussian mode.

Figure 6.16 gives a schematic of the phase-front evaluation set-up and the resulting beam profiles for both fibre ends. Each fibre output was collimated with a 15mm-focal-length aspheric lens (LAS15). A pick-off from the fibre output was provided by a wedge placed on the beam path and fed to a fixed-position camera. The Rayleigh range of the output of a 10μm-diameter fibre core collimated by a 15mm-focal-length lens around 1080nm is ∼3m. The camera was placed at a fixed position at approximately this distance away from the fibre end. The separation between the fibre termination and the lens was tuned so that the camera records an intensity profile before the waist (near-field), at waist and after the waist (far-field). The beam radius did change but for clarity they appear identical on the figure.

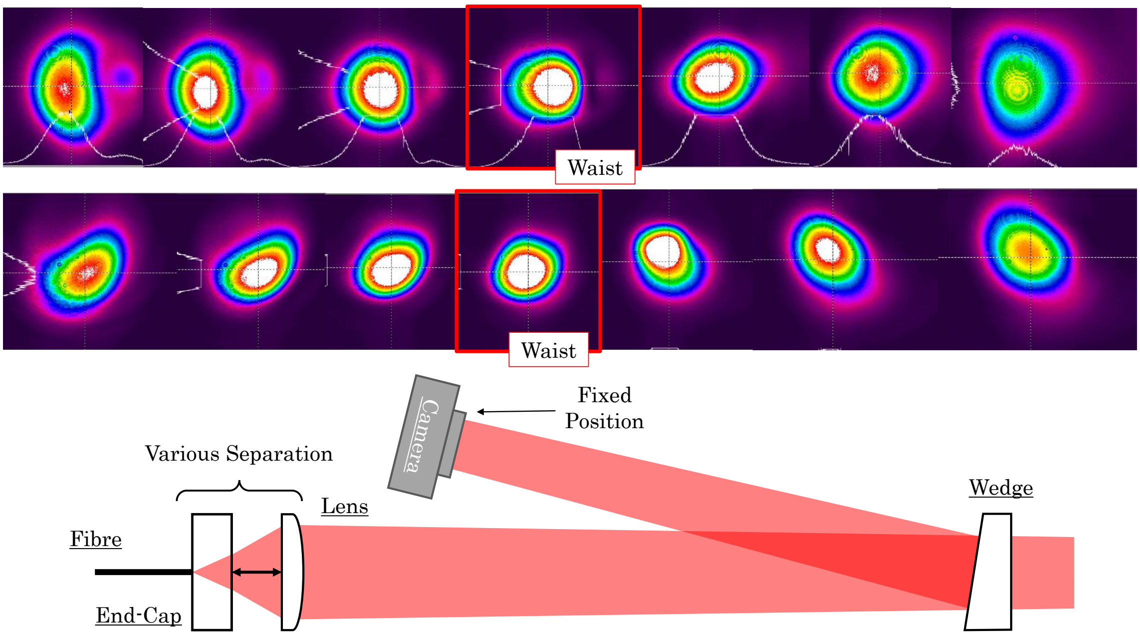

Figure 6.16: Intensity profile evolution of (top) the FMA, and (bottom) the FSA fibre outputs and the optical arrangement for measurement

For both arms, the phase-front at waist is not a symmetrical fundamental Gaussian mode and presents some features. In the near-field and far-field these features expands and give a bean shape to the beam. It appears from this immediate qualitative observation that such a beam would hardly reproduce after a round-trip in each feedback arm.

The FSA large bulk end-cap was a 12.7mm-diameter and 3mm-thick fused-silica window produced in-house. The FMA end-cap was 1mm-diameter and 4mm-length and provided by SPI Lasers. Both had an anti-reflection coating at 1micron on there outer surface. Their output phase-front quality is comparable and could be improved.

6.7.2 End-capping optimisation

As introduced in Chapter 4, the research group this PhD took place within started to develop a fibre end-capping set-up. It is under constant development and progressively improved by the members of the group as the requirements on the end-cap quality varied or increased.

To the understanding of this end-capping process, some of the main steps of the procedure can be outlined. The large end-cap is a bulk optic, in this case a fused-silica optical window with an AR-coating on one side, whose non-coated side is heated up with a CO_2 laser 10.6μm radiation. A flat-cleaved fibre is approached and put in contact with the bulk optic surface. As the heat is transferred to the fibre for a short duration the fibre gets eventually fused to the bulk optic. During this critical phase, it is common that the core symmetry is lost at the splice point and that the core diameter increases inhomogeneously with an impact on the output phase-front quality. In principle, parameters such as the CO_2 laser radiation intensity, the push strength of the fibre against the bulk optic, or the heating duration during the various phases could be optimised to maintain the fibre core geometry at the splice point. A proposed alternative is the hybrid end-cap.

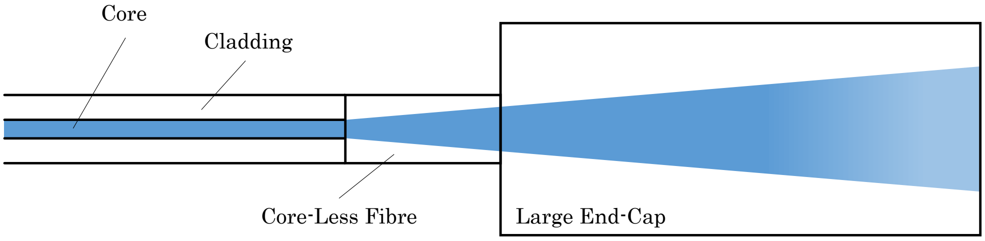

Figure 6.17: Schematic of the hybrid end-cap (not to scale)

Hybrid end-caps, as defined in this thesis, are the combination of a traditional end-cap of approximately the diameter of a fibre (or core-less fibre) with a large bulk optic as represented on Figure 6.17. The end-capping process is composed of a fibre-to-fibre splice between the fibre of interest and the core-less fibre and a consecutive end-capping splice between the core-less fibre and the bulk optic following the previously described process. This strategy takes advantage of the splicing quality of the now well-developed commercially-available fibre splicers to ensure that the fibre core geometry is not or barely altered at the splice point. The requirements on the core-less fibre to bulk optic splice reduce to ensuring a parallel splice to limit astigmatism.

Two hybrid end-caps were produced with 130μm-diameter core-less fibre sections of 365 and 255μm length, within the clipping limit. Figure 6.18 gives the phase-front of one of them. The camera arrangement was changed to a 4f system (or telescope): the fibre output is collimated by the 15mm-focal-length LAS15 aspheric lens and a 300mm-focal-length plano-convex lens focussed the beam down to a waist. The camera was moved on both sides of the waist.

A direct observation is qualitative: the phase-front is much better preserved for this hybrid end-cap than for bulk end-caps. However it still presents some features in the near-field (close to the plano-convex lens) and in the far field (approximately two focal lengths away from the plano-convex lens). Moreover, rotating each lens separately without touching the rest of the alignment does not affect the phase-front profile. Therefore the features cannot be attributed to any astigmatism induced by these optics and come from the end-cap itself.

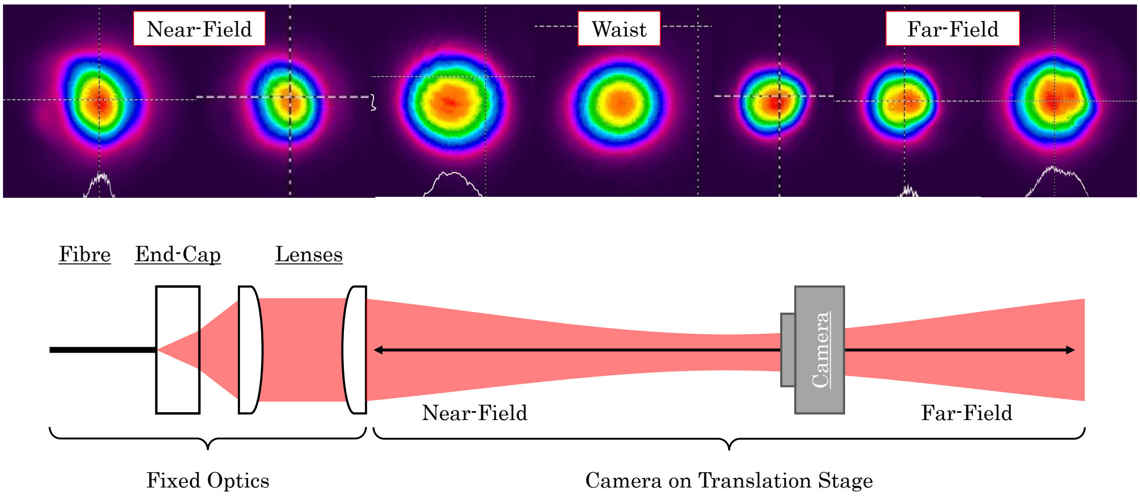

Figure 6.18: Intensity profile evolution of the fibre output with a hybrid end-cap and the optical arrangement for measurement

An inhomogeneous fibre-to-fibre splice can be responsible for these features. This can be due to an imperfect flat cleave before splice, and also the splicer fusing performances but to a low extent. Also, it may be worth considering that since the core-less fibre length is only $\sim$300µm, the fibre-to-fibre splice point is still very close to the bulk optic during the end-capping process. The high temperature can be the cause of dopants diffusion and resulting beam distortion.

Phosphorus, fluorine and germanium dopants can be diffused in silica fibres. From the literature, GeO_2-doped silica fibres of $\sim$10µm-diameter core and $\sim$130µm-diameter cladding placed in furnaces presented considerable diffusion profiles. For instance a 5h-long heating at 1400°C resulted in a increase of the mode-field diameter of the fibres by 2.5 [6]. However the heating time during the in-house end-capping process is of the order of the minute. Nevertheless, the splicing temperature of fused silica is around 2000°C and a simulation of the end-capping of a 700µm-diameter fibre in contact with a bulk optic heated up to this temperature showed a gradient of temperature along the fibre of 220°C every 560µm length [7]. Therefore the fibre-to-fibre splice point is also at a temperature close to 2000°C and this might be sufficient for a core dopant diffusion.

These hybrids end-caps were implemented in Configuration VI and provided Configuration VII. The fibre recoupling efficiencies are also presented in Figure 6.15. The FSA recoupling efficiency increased from an average 49.5% to an average 57.5%. At low pump power, the FMA recoupling efficiency increased from 62.6% to 72.4%. However at high power it would also drop due to thermal lensing in the Faraday rotator.

The hybrid end-caps provided a 16.3% improvement of the recoupling efficiency in the FSA on average and a 16.1% improvement in the FMA at low powers. Further optimisation in the end-capping process may yield further beam quality improvements.

6.7.3 Conclusion and discussion

From the linear cavity with a focussed beam to the empty triangular configuration after end-cap optimisation, the fibre recoupling efficiencies went from 68.8% to 57.5% in the FSA, and from 62.5% to 72.4% at low power in the FMA. The single-pass fibre amplification gain ranged from 2.66 at low pump power (14.9W) up to 3.84 at high pump power (210W).

The recoupling performance of the FSA is not perfect but reasonable. Chapter 4 experiment highlighted this configuration can actually work with very little power returning from the FSA to the fibre. This is due to the high gain capabilities of ytterbium-doped fibres. However, the FSA is meant to house the enhancement cavity which is designed to have a low transmission coefficient (see Chapter 7). This reduces considerably the feedback to the fibre and consequently inversely increases the fibre gain value. A too-high gain could trigger undesired and detrimental effects and it is primordial to maintain a reasonably good fibre recoupling efficiency.

No multi-resonators effects from the fibre standing in the free-space cavity such as wrong polarisation distribution were observed thanks to the end-caps. Hybrid end-caps showed their superiority in terms of phase-front quality and recoupling efficiency in comparison with bulk end-caps (whether the latter was provided from an external company or developed in the lab).

At this stage of development, no nonlinear effects were detected. SBS would have expressed itself in the shape of counter-propagating beams with unwanted polarisation with pulses of 5-10ns periodicity. As SRS power threshold is higher than the SBS one it was supposed it would not occur neither and no signals at unusual wavelengths were observed on an optical spectrum analyser.

Finally, the FSA polarisation output was not reported here as previous experiments showed it should have excellent polarisation extinction ratios. However, polarisation becomes a matter of concern when the enhancement cavity is implemented as developed in Chapter 7.

Bibliography

[1] A. Kobyakov, M. Sauer, and D. Chowdhury, "Stimulated Brillouin scattering in optical fibers," *Adv. Opt. Photon.*, vol. 2, no. 1, pp. 1–59, Mar 2010. [Online]. Available: http://aop.osa.org/abstract.cfm?URI=aop-2-1-1

[2] G. Agrawal, "Chapter 9 - Stimulated Brillouin Scattering," in *Nonlinear Fiber Optics (Third Edition)*, third edition ed., ser. Optics and Photonics, G. Agrawal, Ed. Academic Press, 2001, pp. 355–388.

[3] R. G. Smith, "Optical power handling capacity of low loss optical fibers as determined by stimulated Raman and Brillouin scattering," *Appl. Opt.*, vol. 11, no. 11, pp. 2489–2494, Nov 1972. [Online]. Available: http://ao.osa.org/abstract.cfm?URI=ao-11-11-2489

[4] G. Agrawal, “Chapter 8 - Stimulated Raman Scattering,” in *Nonlinear Fiber Optics (Third Edition)*, third edition ed., ser. Optics and Photonics, G. Agrawal, Ed. Academic Press, 2001, pp. 298–354.

[5] W. Koechner, “Thermal lensing in a nd:yag laser rod,” *Appl. Opt.*, vol. 9, no. 11, pp. 2548–2553, Nov 1970. [Online]. Available: http://ao.osa.org/abstract.cfm?URI=ao-9-11-2548

[6] K. Shiraishi, Y. Aizawa, and S. Kawakami, “Beam expanding fiber using thermal diffusion of the dopant,” *Journal of Lightwave Technology*, vol. 8, no. 8, pp. 1151–1161, Aug 1990.

[7] S. Böhme, E. Beckert, R. Eberhardt, and A. Tuennermann, “Laser splicing of end caps: process requirements in high power laser applications,” 02 2009.

Chapter 7

Green generation using internally-enhanced frequency-doubling in a fibre laser

This chapter follows the implementation of the triangular ring fibre laser by including an internal enhancement cavity for frequency-doubling with maintenance of a linear polarisation using a Faraday mirror. The theoretical considerations to bear in mind when introducing the enhancement cavity with the nonlinear crystal are given along with design considerations. Experimental results regarding the implementation of the enhancement cavity first without and then with the nonlinear crystal are given. The chapter finishes with a discussion and prospects for development.

7.1 Enhancement cavity introduction

7.1.1 The bow-tie geometry

The bow-tie cavity, represented on Figure 7.1, is composed of two partially-transmissive flat mirrors acting as input and output couplers and two highly-reflective (HR) curved mirrors, at 1060-1080nm. The upper arm between the two flat mirrors is collinear with the beam propagating in the overall ring laser set-up given on Figure 7.2 and the nonlinear crystal sits in the lower arm.

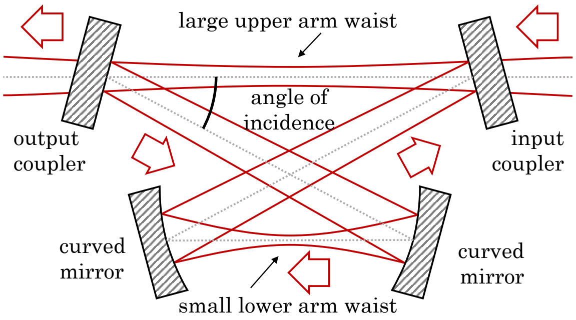

Figure 7.1: Propagation and beam size evolution in a bow-tie cavity

In this experiment, the bow-tie is designed to contain a waist in the middle of both arms. The nonlinear crystal is located in the lower arm. Its waist is chosen for optimal second harmonic generation therefore with a small beam radius for high intensity (and efficient SHG) but a low divergence to be within the crystal acceptance angle. Its size is significantly smaller than the waist generated in by the triangle in the upper arm. The waist size conversion depends on the arms lengths and the curved mirrors radii of curvature. They must be chosen so that the upper arm waist overlep with the triangle waist. This is the spatial mode-matching.

An empty bow-tie cavity works essentially like a Fabry-Pérot etalon: input longitudinal modes that are resonant contribute to constructive interferences, are coupled in the four-mirror cavity and transmitted via an output coupler whereas non-resonating modes contribute to destructive interferences and are rejected. The enhancement cavity is located within the ring fibre laser: only modes that are resonant in both cavities experience a high gain and circulate. An assumption here is that enhancement cavity incident signal should be coupled in i.e. the longitudinal mode-matching condition is met at any time.

Placing a nonlinear crystal in constitutes a source of optical loss for the 1060-1080nm signal. Given that the mode-matching condition is met, the input and output couplers transmission coefficients can be chosen in accordance to this loss so that all the power can be coupled in with no rejected light from the input coupler. This is the impedance-matching condition.

The enhancement cavity could be designed as a cavity with two parallel flat mirrors. It would mean less optics, no astigmatism induced by the curved mirrors, a more compact set-up with a better mechanical stability. However, the bow-tie has an number of advantages. It gives access to small waists which cannot be generated in the triangle due to their large divergence. The lower arm waist can be tuned which provides more flexibility on the triangular arm design. The green output position is offset from the ring laser beam axis. The input mirror is set at an angle so that residual back-reflected light is off-axis and does not constitute an undesired feedback. Finally, astigmatism relative to the use of curved mirrors can be considerably reduced by working at a small angle.

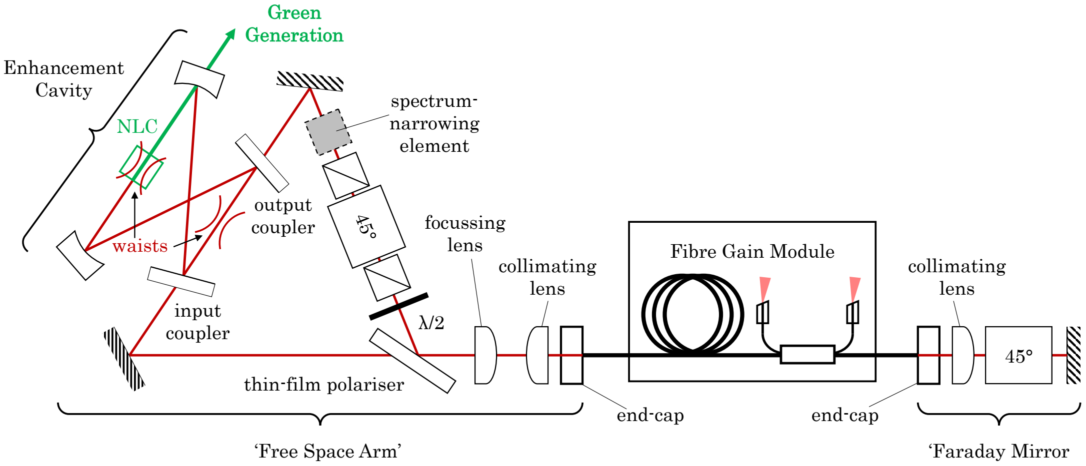

Figure 7.2: Ring fibre laser configuration with an internal enhancement cavity

The targeted set-up represented on Figure 7.2 is the previous chapter last triangular ring configuration with the addition of the enhancement cavity. A spectrum-narrowing element is also included in the ring to select the circulating wavelength and its bandwidth. A narrow bandwidth keeps the lasing spectrum within the second-harmonic generation phase-matching bandwidth.

7.1.2 Longitudinal mode-matching

The longitudinal mode-matching condition is the condition for which the only allowed longitudinal modes are the ones resonating in both cavities.

The unfolded bow-tie is ~1m long and its FSR is $\Delta\nu_{FSR}^{bow\text{-}tie} \simeq 300\text{MHz}$ whereas the whole ring fibre laser is ∼40m long and $\Delta\nu_{FSR}^{ring} \simeq 5.2$MHz. This means that between two adjacent bow-tie modes there are approximately 58 ring modes. This is represented in Figure 7.3 (not to scale).

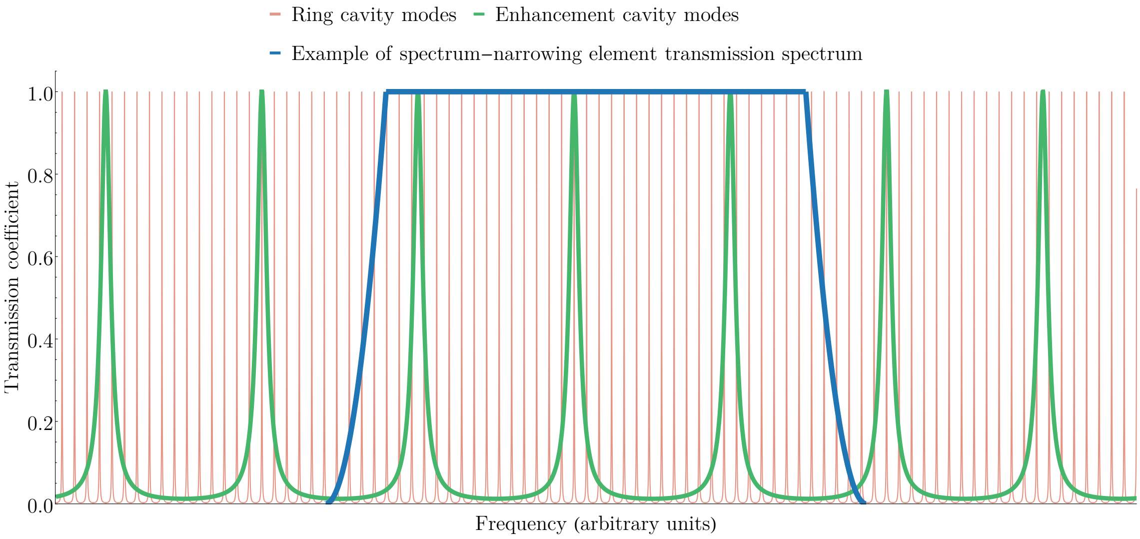

Figure 7.3: Overlap of the ring and bow-tie longitudinal modes with an arbitrary spectrum-narrowing element transmission window (not-to-scale)

The enhancement cavity acts as a filter: only the ring modes within the bow-tie mode linewidth are transmitted. In practice, at all time, this condition should be met.

The SHG efficiency is dependent on whether the signal is within a certain wavelength phase-matching bandwidth. A spectrum-narrowing element was used to select the wavelength of operation and its bandwidth over the broad emission spectrum of the ring fibre laser. It is also represented in the Figure 7.3.

The introduction of the enhancement cavity reduces the number of ring resonator modes and therefore the SBS critical power too. A rough evaluation can be done using the numbers obtained in the previous chapter. For a spectrum-narrowing element with a 0.1nm linewidth (26GHz) and a bow-tie longitudinal-mode linewidth approximately equal to a tenth of the free spectral range, the number of modes allowed is 500. For a 3.06W critical power per mode, the overall set-up critical power is approximately 1.5kW. This value is well above what is expected in the fibre.

7.1.3 Impedance matching

This section present the calculations which back up the impedance-matching considerations i.e. the entire coupling of a signal in the enhancement with no reflection on the input coupler. The following description follows the theory of Ashkin, Boyd and Dziedzic [1].

For every signal of electric field E, its intensity is $I = |E^{*}.\,E|$ and its power is $P = I.\,S$ where $S = \pi w^2/2$ for a Gaussian beam of radius w. The input and output couplers have a power reflection $R_{in/out} = r^2_{in/out}$ and power transmission $T_{in/out} = t^2_{in/out} = 1 - R_{in/out}$. The curved mirrors are highly reflective.

A wave E_{inc} is incident on the input mirror. The circulating signal inside the bow-tie is characterised by the waves $E_{circ,1}$ and $E_{circ,2}$ defined respectively as departing from and incident on the input coupler. The rejected electric field E_{rej} is defined as the sum of the reflection of the incident wave E_{inc} with the portion of circulating signal $E_{circ,2}$ transmitted through the input coupler. Finally the signal transmitted through the upper arm via the output coupler is noted E_{tr} (see Figure 7.4).

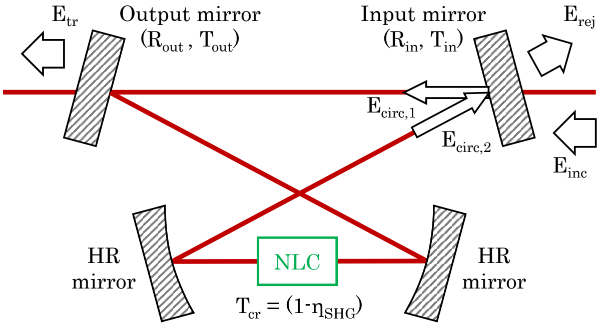

Figure 7.4: Bow-tie notations for impedance-matching calculations

As the single-pass conversion efficiency η_{SHG} is low, the transmission coefficient through the nonlinear crystal is defined as $T_{cr} = t^2_{cr} = 1 - \eta_{SHG}$ and is close to unity.

For lossless cavity, a reflectance parameter r_m characterising the round-trip amplitude variation is defined as:

$$r_m = r_{in} r_{out} t_{cr} \tag{7.1}$$

The phase-shift for a cavity round-trip is ϕ_{rt} and for the upper arm section ϕ_{up}. An electric field doing a round-trip in the cavity experiences an amplitude and phase variation $r_m e^{i\phi_{rt}}$.

Bearing in mind that the transmission through a dielectric mirror presents a $\pi/2$-phase-shift $\exp(i\pi/2) = i$ following the formalism from [2], the circulating electric fields expressed as the sum of the waves after every single roundtrip is:

$$\begin{aligned} E_{circ,1} &= i\,t_{in}E_{inc} + i\,t_{in}E_{inc}\left(r_m e^{i\phi_{rt}}\right) + i\,t_{in}E_{inc}\left(r_m e^{i\phi_{rt}}\right)^2 + \ldots \\ &= i\,t_{in}E_{inc}\sum_{n=0}^{\infty}\left(r_m e^{i\phi_{rt}}\right)^n \\ &= \frac{i\,t_{in}}{1 - r_m e^{i\phi_{rt}}}E_{inc} \end{aligned} \tag{7.2}$$

$$E_{circ,2} = \frac{i\,t_{in}t_{cr}r_{out}e^{i\phi_{rt}}}{1 - r_m e^{i\phi_{rt}}}E_{inc} \tag{7.3}$$

The power circulating in the enhancement cavity relative to the incident power is:

$$\frac{P_{circ,1}}{P_{inc}} = \frac{|E_{circ,1}.E^*_{circ,1}|}{|E_{inc}.E^*_{inc}|} = \frac{t_{in}^2}{(1 - r_m)^2 + 4r_m\sin^2(\phi_{rt}/2)} \tag{7.4}$$

The transmitted and rejected electric fields are:

$$E_{tr} = it_{out}E_{circ,1} = \frac{-t_{in}t_{out}e^{i\phi_{up}}}{1 - r_m e^{i\phi_{rt}}}E_{inc} \tag{7.5}$$

$$E_{rej} = r_{in}E_{inc} + it_{in}E_{circ,2} = \frac{r_{in} - (r_m/r_{in})\,e^{i\phi_{rt}}}{1 - r_m e^{i\phi_{rt}}} \tag{7.6}$$

From these equations, the cavity transmission coefficient $T_{cav}(\phi_{rt})$, expressed as the ratio of the transmitted power P_{tr} over the rejected power P_{rej}, can be deducted:

$$T_{cav}(\phi_{rt}) = \frac{P_{tr}}{P_{inc}} = \frac{t_{in}^2 t_{out}^2}{(1 - r_m)^2 + 4r_m\sin^2(\phi_{rt}/2)} \tag{7.7}$$

$$\frac{P_{rej}}{P_{inc}} = \frac{(r_{in} - r_m/r_{in})^2 + 4r_m\sin^2(\phi_{rt}/2)}{(1 - r_m)^2 + 4r_m\sin^2(\phi_{rt}/2)} \tag{7.8}$$

This gives the cavity transmission from the input coupler to the output coupler $T_{cav}(\phi_{rt})$ which has the form of a traditional Fabry-Pérot etalon transmission. Its maximum value $T_{cav|res}$ is accessible at resonance i.e. where the round-trip phase-shift is a integer number of times 2π. These expressions become:

$$T_{cav|res} = \left.\frac{P_{tr}}{P_{inc}}\right|_{res} = \frac{t_{in}^2 t_{out}^2}{(1-r_m)^2} \tag{7.9}$$

$$\left.\frac{P_{rej}}{P_{inc}}\right|_{res} = \frac{(r_{in} - r_m/r_{in})^2}{(1-r_m)^2} \tag{7.10}$$

The transmitted power is maximum and the rejected power null for:

$$\textbf{impedance-matching condition (general form) :}\ r_{in} = r_m/r_{in} \tag{7.11}$$

This is the impedance-matching: all the incident power is coupled in the cavity and either contributes to the second-harmonic generation or is transmitted through the output coupler. The theory from Ashkin, Boyd and Dziedzic reported that any significant deviation from the optimum impedance-matching condition would still ensure a good frequency-doubling efficiency. However, they mentioned it is better to be over-coupled ($r_{in} < r_m/r_{in}$) than under-coupled.

With the previous definition of the reflectance parameter where the cavity is assumed without loss, this becomes:

impedance-matching condition (lossless cavity) :

$$R_{in} = R_{out}\,(1 - \eta_{SHG}) \tag{7.12}$$

Now considering losses, for a crystal with a single-pass loss L_{cr} including the internal absorption and the reflection and scattering of the surfaces, the crystal transmission becomes $T_{cr} = 1 - \eta_{SHG} - L_{cr}$. With non-perfectly highly-reflective curved mirrors of reflection $R_{HR} \neq 1$, the reflectance parameter becomes $r_m = r_{in}\, r_{out}\, r_{HR}^2\, t_{cr}$ and the impedance-matching condition becomes:

impedance-matching condition (including losses) :

$$R_{in} = R_{out} R_{HR}^2\,(1 - \eta_{SHG} - L_{cr}) \tag{7.13}$$

These impedance-matching conditions highlight that the input coupler reflectivity (or transmission depending on the view) compensates for all the loss sources in the cavity. In this regard, the frequency conversion in the nonlinear crystal and the transmission through the output coupler are considered as losses.

7.2 LBO crytals for second-harmonic generation

The choice of crystals for second-harmonic generation is rather limited and this is due to the requirements on the phase-matching condition. Only birefringent crystals allow reasonable frequency-doubling efficiencies. LBO is a crystal of choice for conversion from 1060-1080nm to the green.

As introduced in Chapter 2, from the phase-mismatch definition from equation (2.9), the phase-matching condition $\Delta k = 0$ can be rewritten as :

$$\textbf{SHG phase-matching condition} : n_1(\omega_1 = \omega) + n_2(\omega_2 = \omega) = 2n_3(\omega_3 = 2\omega) \quad (7.14)$$

This condition is not trivial as it can be achieved in a limited amount of materials.

7.2.1 Refractive index in isotropic and birefringent crystals

With isotropic crystals, the refractive index is identical in every direction. It is subject to chromatic dispersion following the empirical Sellmeier equation [3] whom a general plot is given on Figure 7.5 over different parts of the optical spectrum. The downward sections of the curve correspond to a so-called normal dispersion whereas the upward dashed lines correspond to anomalous dispersion.

In an isotropic medium, the phase-matching condition reduces to $n(\omega) = n(2\omega)$. This condition can only be achieved if the fundamental input and the harmonic belong separately to normal and anomalous parts. This is known as anomalous-dispersion phase-matched second harmonic generation [5]. There is a very limited number of materials which can achieve this and at very specific wavelengths. Isotropic media are usually not suitable for SHG at high-power operation.

With anisotropic crystals, the refractive index remains subject to chromatic dispersion but also varies with the crystal orientation and the polarisation state of light. There are called

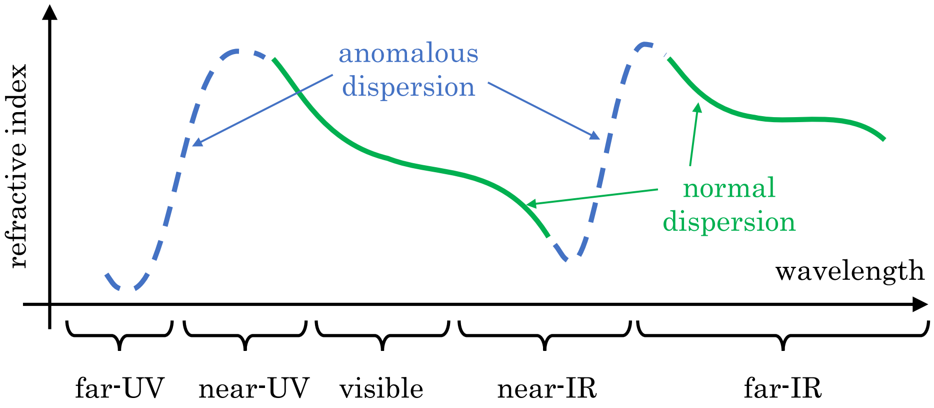

Figure 7.5: Typical dispersion curve for a transparent substance as from [4]

birefringent crystals and two classes are defined: the uniaxial and the biaxial classes.

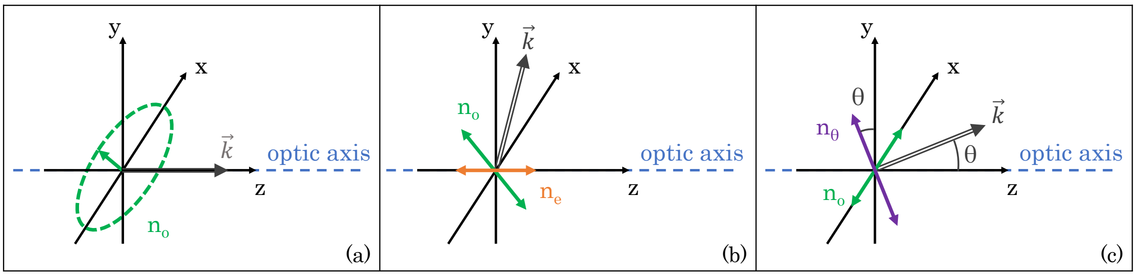

Figure 7.6: Refractive index dependence on the polarisation state for three directions of propagations in a uniaxial crystal: (a) along the optic axis, (b) perpendicular to the optic axis, (c) at an angle θ with the optic axis

Uniaxial crystals present a so-called optic axis. Any wave propagating along the optic axis (wavevector $\overrightarrow{k}$ collinear to that axis) experience an ordinary refractive index n_o as if there was virtually no birefringence (see Figure 7.6(a)). Any signal with a linear polarisation along the optic axis experiences an extraordinary index n_e. For any signal propagating perpendicular to the optic axis, there is a set of two orthogonal linear polarisations experiencing respectively indices n_o and n_e (Figure 7.6(b)). And for a wave propagating at an angle θ against the optic axis, there is a set of two orthogonal polarisations experiencing respectively an index n_o and n_θ (Figure 7.6(c)) defined as [6]:

$$\frac{1}{n_\theta^2} = \frac{\cos^2\theta}{n_o^2} + \frac{\sin^2\theta}{n_e^2} \tag{7.15}$$

The same principle applies to biaxial crystals where not one but two optic axes are defined. The refractive index value is a complex mixture of three indices of reference n_x, n_y and n_z defined according to axes in the piezoelectric system.

Thanks to these properties, a wave propagating at an angle (θ, φ) in the piezoelectric system (relative to the crystal, not to the lab) can present a set of two perpendicular polarisation states experiencing two refractive indices $n^-(\theta, \varphi)$ and $n^+(\theta, \varphi)$ defined so that $n^- < n^+$. These indices describe sheets that do not overlap. Now, considering that the indices n_x, n_y and n_z still follow respective Sellmeier equations, there are ranges of angles (θ, φ) where n^- and n^+ sheets meet for frequencies ω and 2ω. These intersections provide the phase-matching condition.

7.2.2 Phase-matching in birefringent crystals

Depending on the direction of propagation (θ, φ), the frequency ω of the two interacting waves and the frequency 2ω of its second harmonic and their respective polarisation state, two phase-matching conditions were defined [7].

Type I phase-matching corresponds to the situation where the two interacting waves have the same polarisation state which is perpendicular to the second-harmonic polarisation. It is achieved at an angle (θ, φ) for:

$$\textbf{Type I} \quad : \quad n_1^-(\omega) + n_2^-(\omega) = 2n_3^+(2\omega) \tag{7.16}$$

With type II, the two interacting waves are orthogonal in polarisation and the phase-matching condition is obtained at angles (θ, φ) where:

$$\textbf{Type II} \quad : \quad n_1^-(\omega) + n_2^+(\omega) = 2n_3^+(2\omega) \tag{7.17}$$

Certain birefringent crystals provide a range of angles (θ, φ) where type I and type II phase-matching can be achieved. These angles expressions are quite complicated but they can be represented in the piezoelectric system: Figure 7.7 gives examples for a uniaxial and a biaxial crystals. Over that range, there is an optimum angle (θ_m, φ_m) for which the nonlinear coupling coefficient d_{eff} is the highest.

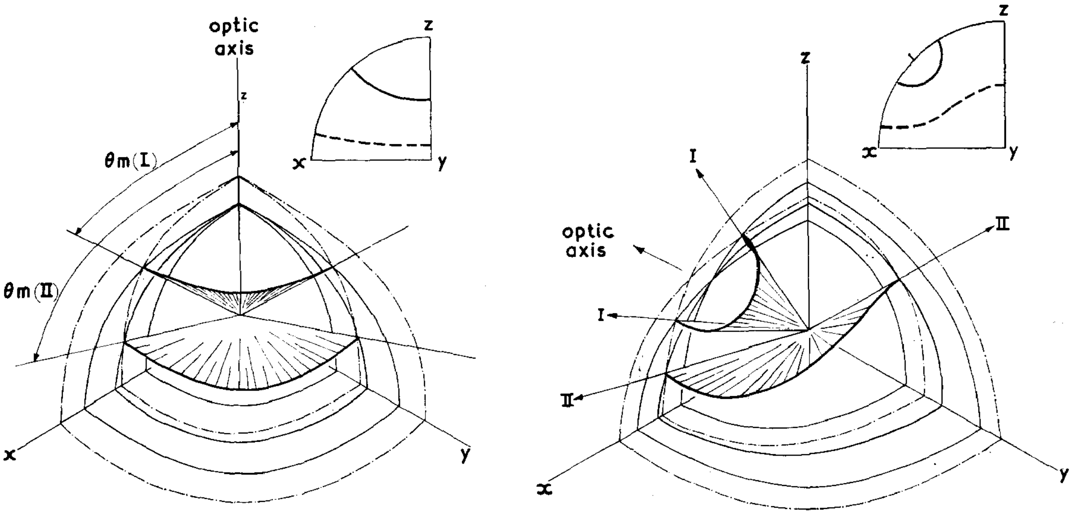

(a) A positive uniaxial crystal

(b) A positive biaxial crystal

Figure 7.7: Directions for type I and type II SHG critical phase-matching visualized by the intersection of the index surfaces for the fundamental and harmonic frequencies in the piezoelectric axes system [8]

This way to achieve phase-matching is called angular or birefringent phase-matching. It is sometimes called critical phase-matching as any deviation from the optimum alignment rapidly leads to a drop in frequency-conversion efficiency. With deviation, the phase mismatch Δk rapidly drifts away from the phase-matching condition $\Delta k = 0$. Figure 7.8 is a the plot of the phase-mismatch-dependent part of the second-harmonic intensity $\mathrm{sinc}^2(\Delta kz/2)$ as from Equation (2.8). Its square cardinal sine function highlights this phenomena.

Via the refractive indices, the phase-mismatch is also a function of the direction of propagation through the crystal (θ, φ) and the frequency of operation ω. A phase-matching width as a function of these parameters around the phase-matching condition can be defined as the full-width at half-maximum of the cardinal sine function. The angular phase-matching width is usually of the order of 10mrad for 1.0cm-long nonlinear crystals. The "critical" denomination comes from this tight tolerance on the angle. The wavelength phase-matching width is however a few tens of nanometers. In certain conditions it can be as wide as 1.0µm [10]. For instance, the acceptance angle of a KTP crystal ($KTiOPO_4$) operating at 1064nm was reported of the order of $\sim 1°$ in any direction. The correspond-

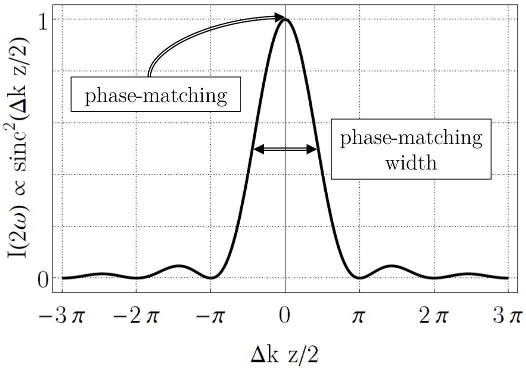

Figure 7.8: Phase mismatch effect on harmonic intensity as from [9]

ing wavelength acceptance was 23nm [11]. The tolerance on the wavelength usually comes second after the angular tolerance.

Non-critical phase-matching (NCPM) opposes critical phase-matching. It consists in achieving phase-matching along the axes of the crystal in the (x, y, z) piezoelectric system rather than at the optimum angle (θ_m, φ_m) of angular phase-matching. Mathematically, NCPM is achieved when the n^+ and n^- indices take values of the n_x, n_y, n_z indices.

At any given temperature, for instance room temperature, NCPM can only be achieved at discreet wavelengths. For some crystals, the refractive indices can be tuned with temperature so that NCPM can be achieved over a range of wavelengths. This is notably the case for lithium niobate ($LiNbO_3$) [12]. It is naturally birefringent and also a pyroelectric material: a temperature variation induces a rearrangement of the atomic structure providing a spontaneous polarisation [13].

One of the major assets of NCPM is avoiding walk-off. With critical phase-matching, the direction of energy transport (characterised by the Poynting vector) and the direction of propagation (given by the wavevector $\overrightarrow{k}$) are slightly different. This walk-off limits the interaction length between the fundamental and the second harmonic waves. NCPM means working along the crystalaxes and this eliminates walk-off considerations.

Because of the tight tolerance on phase-matching angles and frequency-doubling efficiency diminution associated with spatial walk-off, it is often better to work in NCPM conditions.

7.2.3 LBO

KTP crystal is frequently used for the frequency-doubling of the 1064nm Nd:YAG radiation in the green. However, a number of borates presenting a high nonlinearity such as lithium triborate LBO (LiB_3O_5) and barium borate BBO (BaB_2O_4) can be used for green generation [14]. A LBO crystal was used in this chapter experiment. It was provided by Laser Quantum Ltd.

LBO crystals have a couple attractions. It is very low loss with a low residual absorption and is therefore adequate for enhancement cavities. Also, LBO has a wide transparency range (typically from ∼160nm to ∼2600nm) and a high damage threshold. Additionally, it has wide angular, spectral and temperature phase-matching acceptances.

LBO is an orthorhombic non-centrosymmetrical crystal (space group $Pna2$ and point group $mm2$). It is a negative biaxial crystal. The dielectric axes x and y are parallel to the crystallographic axes a and c.

The provided crystal had a 2.5×2.5×15 mm^3 cuboid shape and was cut so that its long axis matches the ($\theta = 90°$, $\varphi = 11.36°$) angles in the piezoelectric system (see Figure 7.9). Type I phase-matching is achieved for crystals working at $\theta = 90°$ angle. The phase-matching angle φ_m depends on the wavelength of operation. With this crystal cut, critical phase-matching around 1060-1080nm can be achieved for a perpendicular incidence.

Indeed, the first paper published on an LBO crystal reported that type I phase-matching can be achieved at angle $\theta = 90°$ and varying angle φ depending on the wavelength of operation. This study reported that at 1064nm operation, the phase-matching angle is $\varphi_m = 10.73°$ [15]. Other studies on LBO crystals reported experimental internal angles of 11.4° at 1064nm [16], 10.7° at 1079nm [17] and 10.6° at 1079.6nm [18].

However, the φ-angle acceptances reported were as low as 95mrad in a 6mm-long crystal [15], 8.54mrad.cm in a 5×5×2mm^3 crystal with a (100)×(010)×(001) cut [17] and 4.2mrad.cm in a 3.9×6.0×4.0mm^3 crystal corresponding to a 1.0° external angle. As a matter of comparison, the θ-angle acceptance is much broader with an angle of 7.4° (31.3mrad.cm) [16].

LBO is also a crystal of choice for NCPM as it has a wide temperature-tuning range.

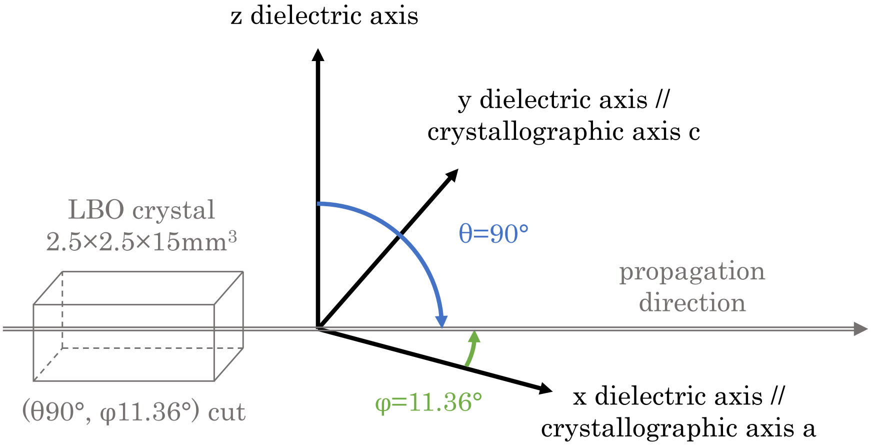

Figure 7.9: Dielectric axes for a LBO crystal with a $(\theta 90°, \phi 11.36°)$ cut

It can be used to provide outputs from the UV to the near infrared with temperatures ranging from -40 to 270°C [19]. Type I NCPM is achieved at $(\theta = 90°, \varphi = 0°)$ angles.

A theoretical and experimental study reported the temperature-tuning curves for type I and type II NCPM carried out from 0.95 to 1.60µm (Figure 7.10). At 1064nm, type I NCPM can be achieved at 112°C. Incidentally, NCPM occurs at room temperature at the discreet wavelengths of 1.21µm and 1.42µm [19].

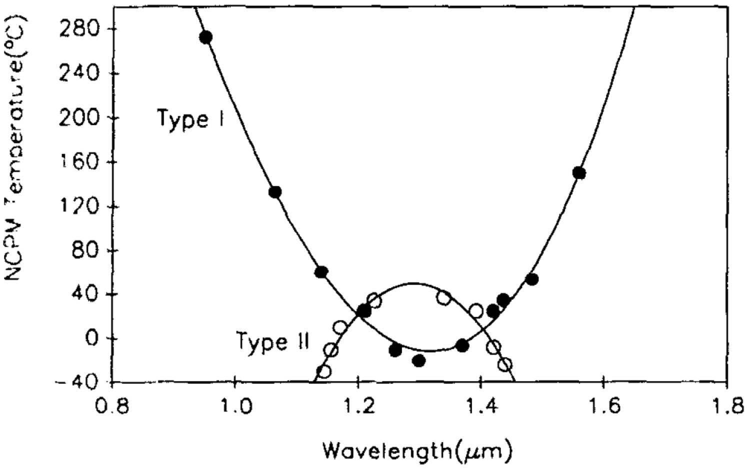

Figure 7.10: Temperature tuning curves for type I and type II NCPM in LBO [19]

NCPM at 1079.6nm was achieved at 135°C with a temperature acceptance exceeding 8°C in a 59mm-long crystal. This acceptance was far greater than the temperature gradient observed in their nonlinear crystal [18]. The NCPM at 1064nm was reported at 148°C with a 10.1°C acceptance (or 3.9°C.cm). This increased the φ-angle acceptance to 9.1° (71.9mrad.cm$^{1/2}$) and the θ-angle acceptance to 6.6° (99.1 mrad.cm$^{1/2}$) [16].

Also in LBO, type I angular phase-matching has a 10% higher efficiency than type II but suffers from a stronger walk-off (type II 3/5 smaller than type I) but with NCPM this consideration is no longer an issue. Another advantage of NCPM is that at $\theta = 90°$, the effective nonlinear coefficient expressed as $d_{eff} = d_{32}\cos(\varphi)$ (SHG coefficient $d_{32} \sim$ 1pm/V) is higher at $\varphi = 0°$ [17].

The LBO crystal was mounted in thermal contact with a Peltier heater associated with a thermoelectric temperature controller. The rotation around the φ-axis was perpendicular to the optical bench.

Nonlinear crystals are sometimes cut at Brewster angle to avoid the Fresnel reflections. Their losses would be detrimental to the frequency-doubling efficiency. However, the Brewster angle is wavelength dependent and a cut for optimum transmission at 1060-1080nm yields a considerable reflection loss in the green. Also, a Brewster cut adds complexity to the cavity design and the crystal mounting. The LBO crystal used in this chapter experiment has, alternatively, anti-reflection coatings on both surfaces. They are designed at the green wavelength and near 1060-1080nm with reflection coefficients R_{cr}(532nm) = 0.027% and R_{cr}(1064nm) = 0.022%.

7.3 Geometry considerations

The triangular set-up geometry introduces a number of constraints. This section presents the considerations on the beam radius. The calculations were done using the ABCD matrices formalism [20].

7.3.1 Optimum waist in the nonlinear crystal

The optimum waist size in the nonlinear crystal constrains the rest of the set-up dimensions.

Theory: Gaussian beam and SHG efficiency

According to its definition given in Equation (2.12), the frequency-doubling efficiency increases with the intensity of the fundamental wave. The nonlinear crystal is placed where it is the highest: at waist. There are considerations regarding whether the waist should be centred in the middle or on the input face of the crystal [21]. In practice, the waist position can be adjusted during alignment and chosen to provide the highest efficiency.

Considering a TEM$_{00}$ Gaussian beam of radius $w(z)$, the relation between the power at any point $P(z)$ is related to the intensity $I(z)$ via:

$$P(z) = \frac{\pi w^2(z)}{2} I(z) \tag{7.18}$$

The assumption here is that the beam radius barely increases over the crystal length l_{cr} and remains close to its waist value w_0, typically over the Rayleigh range $z_0 = \pi w_0^2 n_{cr}/\lambda$ with n_{cr} the nonlinear crystal refractive index. From this, the efficiency at phase-matching can be rewritten (in the undepleted regime):

$$\eta_{SHG} = \frac{2\omega^2 d_{eff}^2}{n_1 n_2 n_3 \epsilon_0 c^3} \cdot \frac{2 l_{cr}^2}{\pi w_0^2} P_1(0) = \epsilon_{SHG} P_1(0) \tag{7.19}$$

where ϵ_{SHG} is expressed in %/W and is also sometimes encountered in literature as the "efficiency" of the frequency-doubling process.

In first instance, the beam radius around waist can be considered relatively constant for a length of crystal equal to twice the Rayleigh range (distance over which the beam expands by $\sqrt{2}$). In-depth studies considered a focusing parameter $\xi = l_{cr}/b$ linking the confocal parameter $b = 2z_0$ to the crystal optical path length [22]. It was calculated that, for a fundamental TEM$_{00}$ Gaussian mode focussed in the centre of a uniaxial nonlinear crystal, with no considerations for double-refraction, the maximum efficiency was obtained for $\xi = 2.84$.

Design considerations

The LBO crystal length was $l_{cr} = 15\text{mm}$. For an expansion limited to the Rayleigh range, i.e. $l_{cr} = 2z_0$, the waist radius was evaluated at 40µm over 1060-1080µm. For the theoretical optimum value given by the focussing parameter $\xi = l_{cr}/b = 2.84$ with confocal parameter $b = 2z_0$, the evaluated waist radius was 24µm.

Type I SHG occurs for a propagation in the (x, y) plane and a linear polarisation along the z axis so that $n_{cr} = n_z$. The value of $n_z = 1.62$ was calculated from the Sellmeier equations in the green spectrum [15].

The diameter size evolution of a free-space fundamental Gaussian beam focussed down to a waist was evaluated with and without an LBO crystal placed at this waist. Calculations showed that the variation of refractive index induces a waist position shift of 2.8mm along the propagation axis regardless of the waist diameter. Also the waist diameter was theoretically not affected by the change of medium. In practice, this means that the bow-tie arms length should be adjusted accordingly.

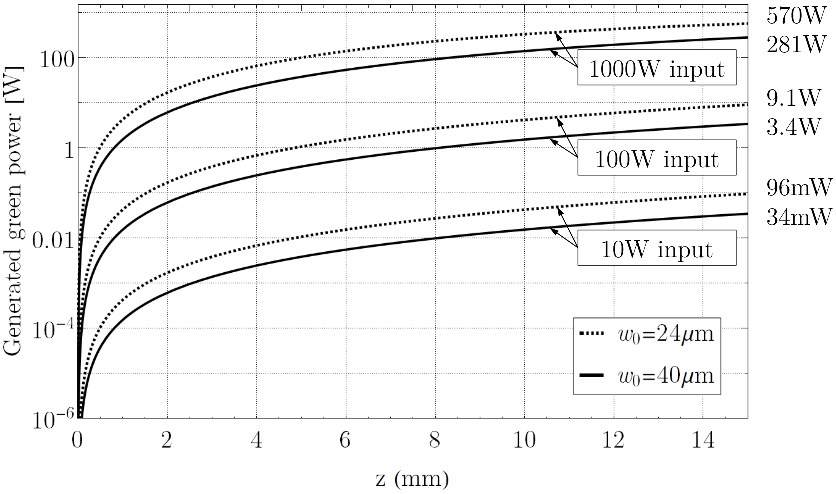

Figure 7.11: Theoretical generated green power inside a 15mm-long LBO crystal for various fundamental input powers and beam diameters

Figure 7.11 provides plots of the generated green power across the LBO crystal for the two waist values of 24µm and 40µm and three different fundamental powers: 10W, 100W and 1000W. These are plots from combined equations (2.11) and (7.18) as for a 1000W input the efficiency is such that the undepleted approximation Equation (7.19) is no longer valid. This simulation considers type-I phase-matching so that $n_1(\omega) = n_2(\omega) = n_3(2\omega) = n_z$, a constant and identical diameter for both the fundamental and the harmonic beams, and an effective nonlinear coefficient d_{eff} value of 1pm/V. The expected green output powers are also reported on the right-hand side.

These curves notably quantify the conversion efficiency dependence on both the input fundamental power and its intensity via the waist radius. In this figure, inputs between 100W and 1000W are not unreasonable: the enhancement-cavity circulating power is supposedly much higher than the ring-fibre-cavity circulating one.

In conclusion, a maximum conversion efficiency is expected for beams that are focussed tightly enough to ensure a high intensity but relatively collimated to remain within the angular phase-matching bandwidth of the LBO crystal. Theoretically, the optimum waist should be around 24µm and 40µm for which theoretical extracted green powers are reported. In the intended laser configuration, 100% extraction is not the target as the nonlinear crystal, and therefore the enhancement cavity, are designed to transmit enough feedback power to the fibre in the near-infrared spectrum.

7.3.2 Waist conversion in the bow-tie cavity

The bow-tie cavity achieves the waist size conversion between the triangular arm and the nonlinar crystal, respectively between the upper arm and the lower arm. The curved mirrors radius of curvature R_{curv}, the distance separating each mirror and the angle of incidence define the stable spatial modes of the cavity.

In first instance, the concave mirrors could be assimilated to plano-convex lenses and astigmatism was neglected. The study reduces to the beam size evolution from the upper waist to the lower waist through a $2l_{up} + l_{low}$ drift length, a lens of focal length $f_{curv} = R_{curv}/2$ and a second l_{low} drift length. Lengths l_{up} and l_{low} are represented in Figure 7.12 and are the distance between respectively the upper waist and an adjacent flat mirror and the lower arm waist with an adjacent curved mirror.

Figure 7.13 gives l_{up} and l_{low} as functions of lower arm waist radius w_{low} for an upper

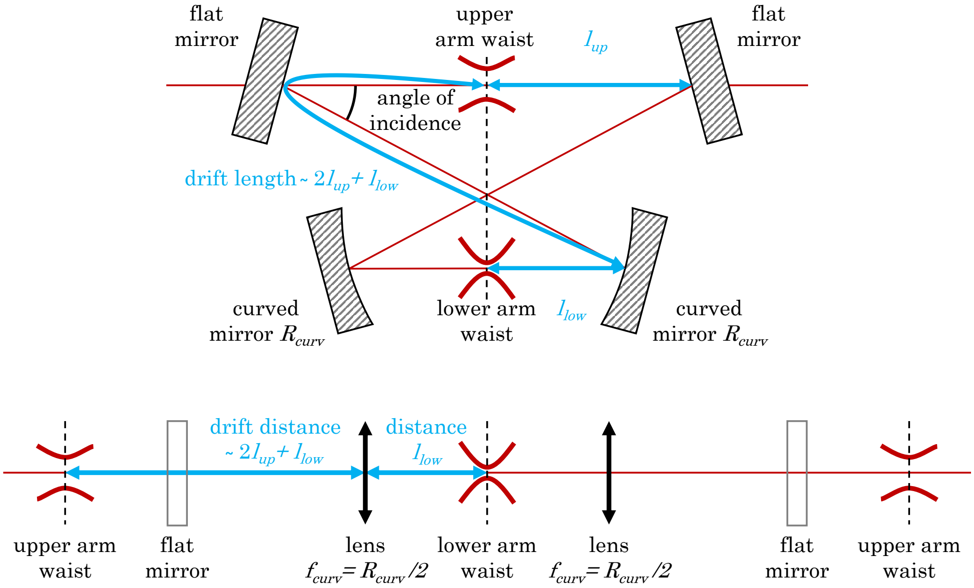

Figure 7.12: Lens system equivalent to the bow-tie cavity

arm length of $w_{up} = 162\mu\text{m}$ (see next section) and for six different curved mirror radii. For a targeted lower arm waist value, these graphs provide the appropriate arms length to implement. They also highlight the dependency of the waist stability relative to each arm's length.

For example, considering the case where $R_{curv} = 150\text{mm}$, a $24\mu\text{m}$ waist in the lower arm would be obtained for $l_{up} = 24\text{cm}$ and $l_{low} = 9\text{cm}$. It appears that any variation of the upper arm length would not have a direct impact on the waist size whereas variations of similar amplitude of the lower arm length would lead to a detrimental fluctuation of the waist size.

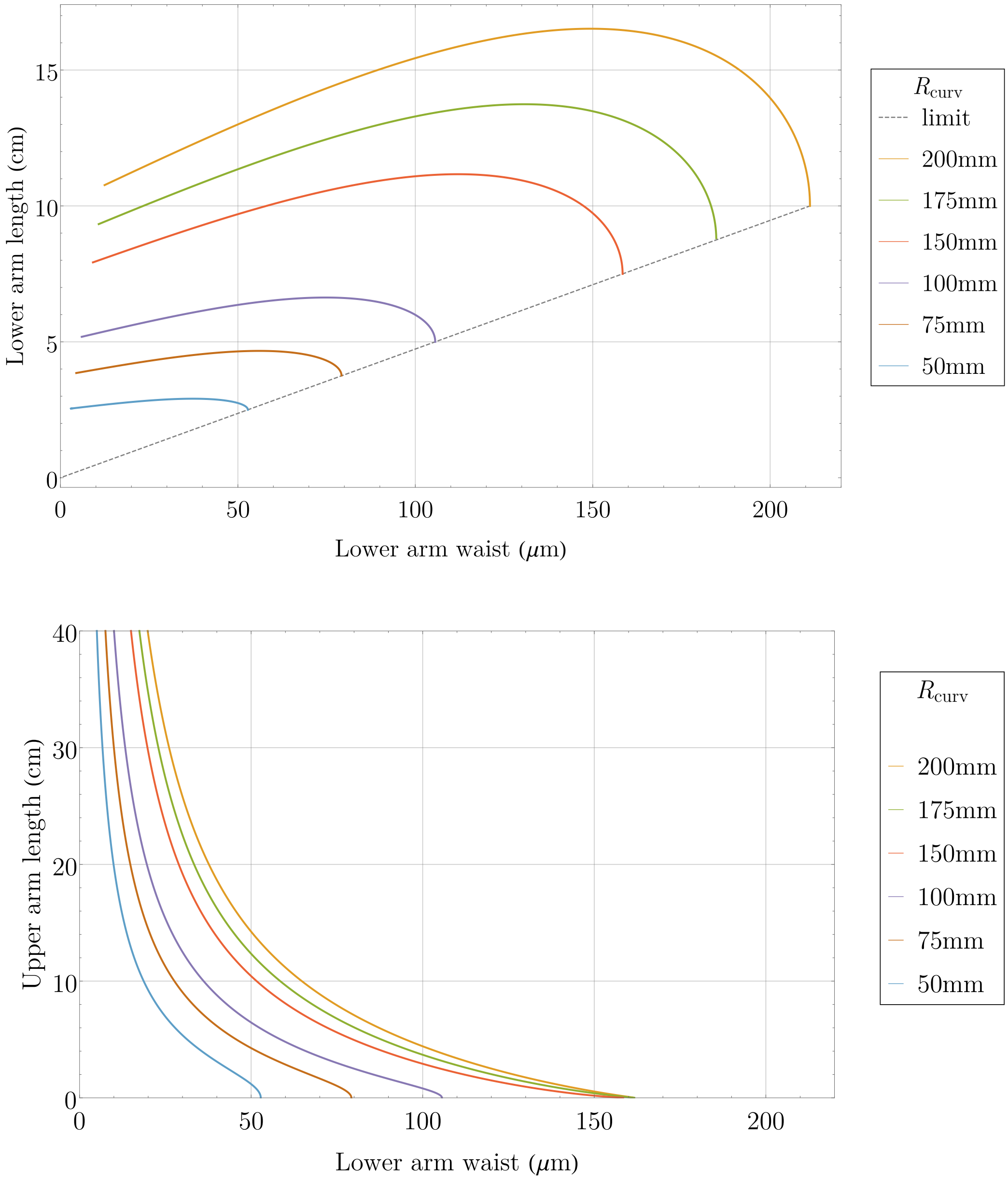

Figure 7.13: Upper and lower arms lengths as functions of the targeted lower arm waist for a fixed 162μm upper-arm waist and six available concave mirror radii of curvature

7.3.3 Beam radius in triangular ring arm

Theoretical calculations provided that the target waist size in the nonlinear crystal was around 24µm and 40µm. Previous section showed that for a target waist value, the set of curved mirror and bow-tie arm length provides a range of possible upper arm waist values. When designing the triangular ring arm of the overall ring fibre cavity, the choice of lenses was chosen accordingly.

The triangular arm is composed of two lenses which respectively collimate and focus the fibre output (and vice-versa on the returning path). The generated waist must overlap with the bow-tie upper-arm waist. Note that the waist is generated in the middle of the optical length and is therefore slightly offset from the physical middle point. This is due to the presence of transmission components with a higher refractive index on the returning path (Faraday isolator, spectrum-narrowing element).

The triangle waist radius was evaluated at 162µm at 1060nm wavelength for a 10µm-diameter fibre core, a 3mm-thick end-cap, collimating and focussing lenses of respectively 15mm and 500mm focal lengths and a 10cm separation between them.

However, in practice, the waist radius was 95µm and this difference finds its origin in the alignment process. Indeed, the collimating lens was introduced in the cavity at the empty triangular configuration stage. Rather than actually collimating, this lens probably focussed slightly to provide a maximum fibre recoupling efficiency. The focussing lens was eventually put in and focussed the beam even more down to 95µm radius, smaller than the theoretical 162µm.

7.4 Experimental results: triangular ring cavity with empty enhancement cavity

7.4.1 Introduction

The enhancement cavity in a bow-tie configuration without the nonlinear crystal is represented on Figure 7.14. The bow-tie was composed of two flat input and output couplers, respectively $\mathrm{M_{in}}$ and $\mathrm{M_{out}}$ with low transmission coefficients at 1060-1080nm and two curved dichroic mirrors, $\mathrm{M_{CD,1}}$ and $\mathrm{M_{CD,2}}$, HR-coated at 1060-1080nm and AR-coated in the green, as reported in Table 7.1. The other components are identical to previous chapter Configuration VII apart from the additional spectrum-narrowing element placed just before the Faraday isolator in the FSA returning loop. Mirrors $\mathrm{M_{FSA,1}}$ and $\mathrm{M_{FSA,2}}$ were interchanged so that the 70%-transmission mirror was placed after the enhancement cavity.

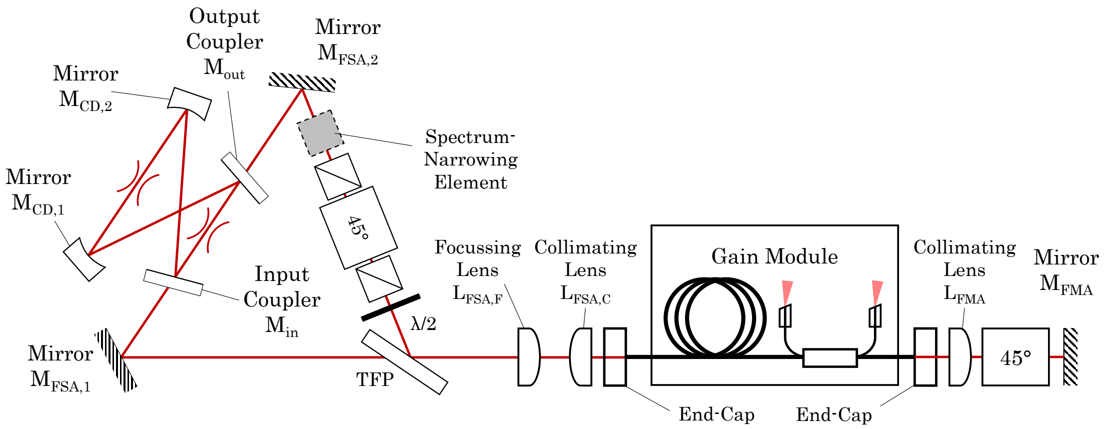

Figure 7.14: Ring fibre laser with empty enhancement cavity: schematic representation (configurations VIII and IX)

Theoretically, in the absence of nonlinear crystal, the impedance-matching condition given by Equation (7.13) becomes:

$$R(\mathrm{M_{in}}) = R(\mathrm{M_{out}})R(\mathrm{M_{CD,1}})R(\mathrm{M_{CD,2}}) \tag{7.20}$$

where $R(\mathrm{M})$ is the reflection coefficient of mirror M including losses (from scattering and imperfect coating transmissions). With the mirror specifications of $R(\mathrm{M_{in}}) = 5.5\%$, $R(\mathrm{M_{out}}) = 0.5\%$ and reflection coefficients of the curved dichroic mirrors close to 100%, the impedance-matching condition is not met. It is expected that a portion of power would be reflected, or rejected, from the input coupler. As the enhancement cavity input coupler is at an angle with the incident beam, there is no considerations regarding a residual backward propagating signal.

	Configuration	VIII	IX
FSA	$L_{FSA,C}$	LAS15	LAS15
	$L_{FSA,F}$	LTH500	LTH500
	$M_{FSA,1}$	M95FS	M95FS
	$M_{FSA,2}$	M70FS	M70FS
	Spectrum-Narrowing Element	F5NM	F5NM
	TFP	TFPNP	TFPLT
Bow-Tie	M_{in}	MIN55	MIN55
	M_{out}	MOUT10	MOUT05
	$M_{CD,1}$	MCDHR	MCDHR
	$M_{CD,2}$	MCDHR	MCDHR
FMA	L_{FMA}	LAS15	LAS15
	Faraday Rotator	FR1	FR2
	M_{FMA}	M95FS	M95FS
	End-Caps	Hybrid	Hybrid

Table 7.1: Ring fibre laser with empty enhancement cavity: list of components (configurations VIII and IX)

7.4.2 Polarisation maintenance

The set-up was operated at low pump power (14.9W) with one 5nm-bandwith central-wavelength-tuneable filter as a spectrum-narrowing element (F5NM). The initial power distribution in the FSA is given in Figure 7.15. The measured signals were: the transmitted powers from the pick-off mirrors $M_{FSA,1}$ and $M_{FSA,2}$, the leakages through the curved mirrors $M_{CD,1}$ and $M_{CD,2}$, the rejected power from the input coupler M_{in}, the rejection from the input and output cube polarisers of the Faraday isolator in the forward and backward directions, and finally the power leaking through the thin-film polariser after round-trip in the triangle. The internal powers were evaluated from the transmission coefficient of the mirrors.

The FSA and FMA recoupling efficiencies were respectively 76.3% and 69.7%. This is in agreement with the values obtained with previous configurations at low power.

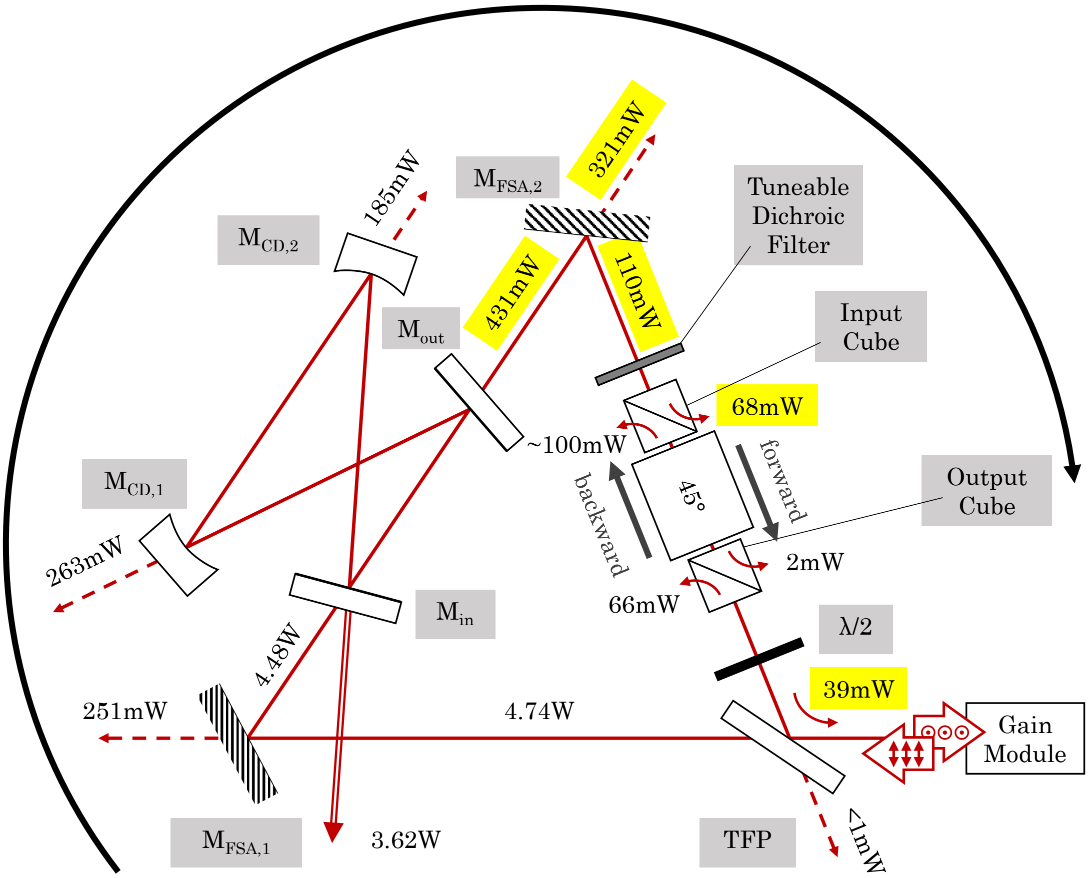

Figure 7.15: Configuration VIII: power distribution at low power above threshold

From the 321mW pick-off from mirror $\mathrm{M_{FSA,2}}$, it was measured that 110mW out of the 431mW transmitted by the enhancement cavity were reflected and fed back to the loop. However, the Faraday isolator input cube polariser beamed out 68mW (of the forward circulating signal). This portion was therefore vertically polarised (s-polarisation) as opposed to the incident horizontal polarisation (p-polarisation) onto the enhancement cavity. Roughly half of the transmitted signal was therefore in the wrong polarisation.

Mirror $\mathrm{M_{FSA,2}}$ output polarisation state was evaluated using a half-waveplate followed by a cube polariser. The waveplate angle rotated the output polarisation and the polariser separated the two orthogonal components.

The minimum transmission of the combined optics was 8% indicating that the signal is slightly elliptical. The polarisation ratio was $58(p)$:$42(s)$: the ellipse was at an angle close to 45°. Mirror $\mathrm{M}_{\mathrm{FSA},2}$ transmission coefficient is polarisation dependent (see Appendix A) so that the reflected signal onto the Faraday isolator had a $44(p)$:$56(s)$ power ratio. Calculations indicates that approximately 62mW should have been in the unwanted vertical polarisation, which is in good agreement with the experimental 68mW beamed out by the Faraday isolator input cube polariser. Likewise, the incident signal on the mirror was evaluated with a $55(p)$:$45(s)$ polarisation ratio.

Since the input polarisation on the bow-tie is linear horizontal, it was assumed that the cavity was rotating the polarisation. One possible explanation is the presence of a polarisation rotation element in the enhancement cavity. Even a small rotation contribution can have a considerable impact as light does multiple round-trips within the cavity before being coupled out.

A theoretical bow-tie cavity is considered with a single-pass polarisation rotation component θ. It is supposedly at resonance where the round-trip phase-shift ϕ_{rt} is a integer number of 2π. The following calculation borrows the rotation matrix $R_{rot}(\theta)$ from the Jones formalism and defined in Table 4.1. The incident electric field is horizontally polarised so that $\overrightarrow{E_{inc}} = E_{inc}\,\overrightarrow{u_x}$. The circulating electric field from Equation (7.2) is changed to:

$$\begin{aligned}\overrightarrow{E_{circ,1}} &= i\,t_{in}E_{inc}\,\overrightarrow{u_x} + i\,t_{in}E_{inc}r_m R_{rot}(\theta)\,\overrightarrow{u_x} + i\,t_{in}E_{inc}r_m^2 R_{rot}^2(\theta)\,\overrightarrow{u_x} + \dots \\ &= i\,t_{in}E_{inc}\sum_{n=0}^{\infty} r_m^n\Big(\cos(n\theta)\,\overrightarrow{u_x} + \sin(n\theta)\,\overrightarrow{u_y}\Big) \\ &= i\,t_{in}E_{inc}\left(\frac{1 - r_m\cos\theta}{1 - 2r_m\cos\theta + r_m^2}\,\overrightarrow{u_x} + \frac{r_m\sin\theta}{1 - 2r_m\cos\theta + r_m^2}\,\overrightarrow{u_y}\right) \qquad (7.21)\end{aligned}$$

And the transmitted electric field through the upper-arm of the cavity is:

$$\overrightarrow{E_{tr}} = -t_{in}t_{out}e^{i\phi_{up}}E_{inc}\left(\frac{1 - r_m\cos\theta}{1 - 2r_m\cos\theta + r_m^2}\,\overrightarrow{u_x} + \frac{r_m\sin\theta}{1 - 2r_m\cos\theta + r_m^2}\,\overrightarrow{u_y}\right) \qquad (7.22)$$

This is the expression of a linear polarisation at an angle $\arctan\left(r_m\sin\theta/(1 - r_m\cos\theta)\right)$ with the horizontal axis. And the cavity transmission at resonance is given by:

$$T_{cav|res} = \frac{t_{in}^2 t_{out}^2}{1 - 2r_m\cos\theta + r_m^2} \qquad (7.23)$$

It should be noted that for no rotation in the cavity, i.e. $\theta = 0$, this expression is identical to the one from Equation (7.9) and the transmitted electric field is horizontally polarised.

The previous results showed that the powers of the two orthogonal polarisations were approximately distributed according to a 55(p):45(s) ratio i.e. for $(1 - r_m \cos\theta)/r_m \sin\theta = 55/45$. For a reflectance parameter defined as $r_m = r_{in}\, r_{out}\, r_{HR}^2$ with values such that $T(\mathrm{M_{in}}) = 5.5\%$, $T(\mathrm{M_{out}}) = 0.5\%$ and $T(\mathrm{M_{CD,1}}) = T(\mathrm{M_{CD,2}}) = 0.37\%$, the single-pass rotation angle is evaluated at only 1.3mrad. This highlights that even a minimal single-pass rotation contribution θ can have considerable implications.

The origin of this polarisation rotation may be found in the bow-tie mirror birefringence. Each one of them four sits in the double-bored hole of a mirror mount and is held by a nylon-tipped screw. Opposite to the screw is a recess in the circular hole so that the optic is in contact with both edges of the recess plus the screw. Depending on how tightly the mirror is mounted, the stress applied at these three points can induce a non-negligible birefringence. Moreover, tens to hundreds of watts circulate inside the enhancement cavity and a portion is inevitably absorbed. It can induce differential expansion or contraction of the mirrors in their mounts providing an additional thermally-induced birefringence contribution.

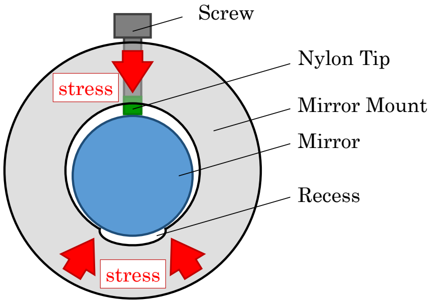

Figure 7.16: Mechanical stress points in mirror mounts

Decreasing the screw tension of the two mirrors working in transmission, i.e. the input and output couplers, improved the output polarisation ratio whereas no significant variations were observed for the curved mirrors working in reflection. The two transmission optics were glued to their mirror mount to suppress the three stress points on the round edge. Glue was applied at the corner between one optic surface and the mount bored hole edge while the other surface was against the mount counterbore.

Another possible contribution to the polarisation rotation can be an out-of-plane alignment of the bow-tie [23]. In theory, the bow-tie is composed of four mirrors whose respective normal of incidence all lay in a unique plane parallel to the optic bench, or more precisely parallel with the plane described by the triangular ring. However in practice any set of three mirrors defines a unique plan which is not necessarily parallel with the bench or the triangular ring. As an illustration, the triangular ring plane is defined by the normals of incidence of ($\mathrm{M_{FSA,1}}$, $\mathrm{M_{FSA,2}}$, TFP) and two planes of the bow-tie can be ($\mathrm{M_{in}}$, $\mathrm{M_{out}}$, $\mathrm{M_{CD,1}}$) and ($\mathrm{M_{in}}$, $\mathrm{M_{out}}$, $\mathrm{M_{CD,2}}$) for instance. An out-of-plane four-mirror cavity can induce a variation of the relative orientation of the s-polarisation and p-polarisation after one round-trip in the cavity.

Putting waveplates inside the bow-tie to counteract the effect of polarisation rotation was initially considered and implemented. However it proved itself unsuccessful due to the relatively low cavity single-pass rotation value of 1.3mrad. It would require the waveplates whose retardation is wavelength dependent to be extremely accurate and homogenous over the circulating signal linewidth (of the order of 1nm). This strategy would also not pay off since it would add a non-negligible loss in the enhancement cavity, and the waveplate might not be able to handle multiple hundreds of watts and more.

Reality is that a slightly out-of-plane configuration can actually be useful. Instead of trying to achieve an hypothetical perfect all-in-plane configuration, a slight induced polarisation rotation can be used to counteract the effects of the residual stress and temperature induced birefringence in the mirrors.

The bow-tie cavity was realigned and a few components were replaced giving configuration IX: the input coupler has a slightly higher design transmission, the thin-film polariser has a fused silica substrate and the FMA Faraday rotator has a higher power-handling to tackle the effects of thermal lensing (see Table 7.1). The power distribution obtained in the FSA is given in Figure 7.17.

The polarisation extinction ratio went down to a value better than $1(s)$:$75(p)$ which is reasonable to conclude that the enhancement cavity transmitted polarisation was mostly horizontal.

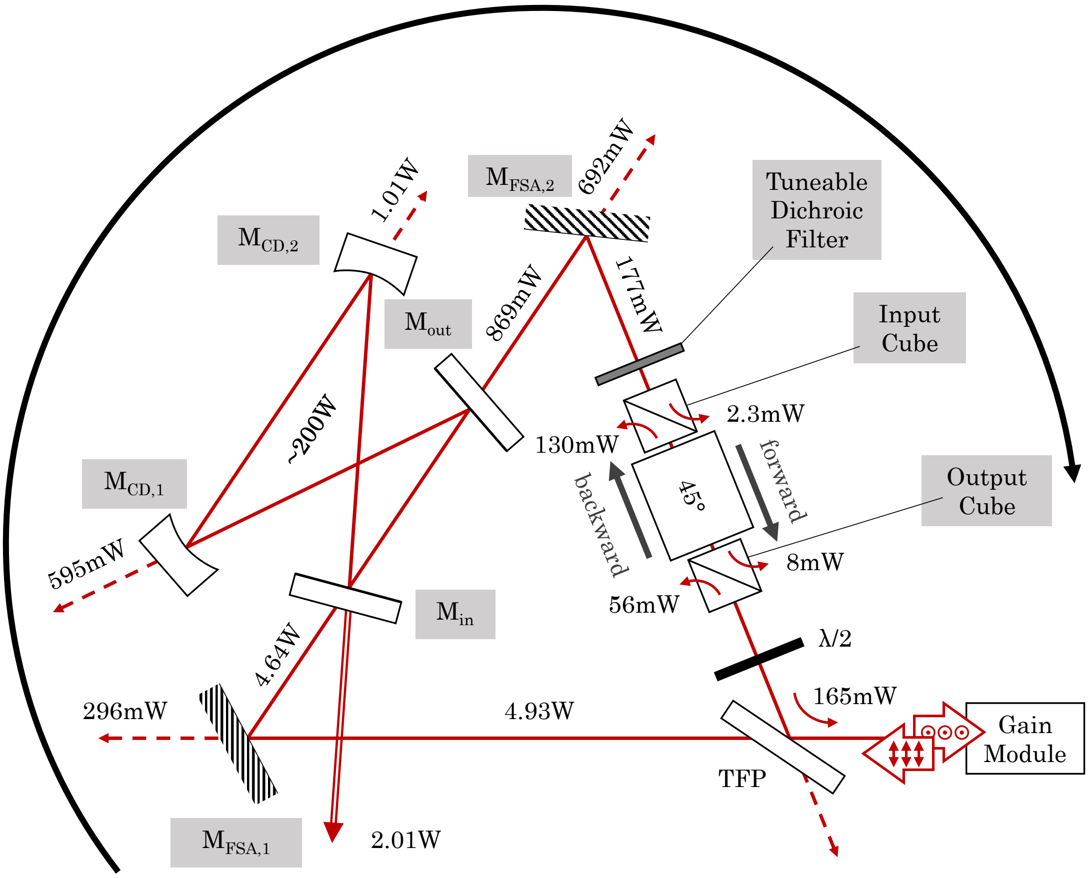

Figure 7.17: Configuration IX: power distribution at low power above threshold

7.4.3 Performance of the empty enhancement cavity

The gain module was run at 14.9W pump power. From the 4.64W incident on the enhancement cavity, 869mW were transmitted, giving a transmission coefficient $T_{cav|res} = 18.7\%$. For $T(\mathrm{M_{in}}) = 5.5\%$ and $T(\mathrm{M_{out}}) = 0.5\%$ and Equation (7.9), the experimental reflectance parameter is $r_m^{exp} = 0.9617$.

In order to take into account the round-trip loss in the bow-tie, a single-pass transmission coefficient $T_{r.t.} = t_{r.t.}^2$ can be defined. A contribution to a round-trip loss can be a transverse mode mismatch due to the astigmatism induced by the concave mirrors angle relative to the propagating beam. Imperfect mirror surface quality can also alter the phase-front quality. Consequently, the reflectance parameter can be redefined as $r_m = r_{in}\, r_{out}\, r_{HR}^2\, t_{r.t.}$ with $T(\mathrm{M_{CD,1}}) = 0.25\%$ and $T(\mathrm{M_{CD,2}}) = 0.5\%$ the transmission coefficient of both imperfect highly-reflective curved mirrors. The single-pas transmission coefficient was $T_{r.t} = 99.1\%$.

The curved mirrors leaked 595mW for $\mathrm{M_{CD,1}}$ and 1.01W for $\mathrm{M_{CD,2}}$. These powers are small in comparison to the intra-cavity power evaluated around 200W yet they are of the order of the 869mW transmitted through the output coupler. This comes from the imperfect coating of the curved mirrors whose transmission is comparable to the output mirror transmission.

These two leaks, of respectively 11.8% and 21.8% relative to the incident power, can be seen as a loss as they do not contribute to the ring operation. As mentioned previously, less feedback power in the FSA is not detrimental to the laser operation even though it means a higher fibre amplification gain value and therefore a fibre more prone to self-pulse. These two leaks are very low in comparison to the circulating power in the enhancement cavity but they have an impact on the impedance-matching condition, the circulating power, and the SHG efficiency. The curved mirrors should ideally be replaced but this is not a limiting element at this stage of development.

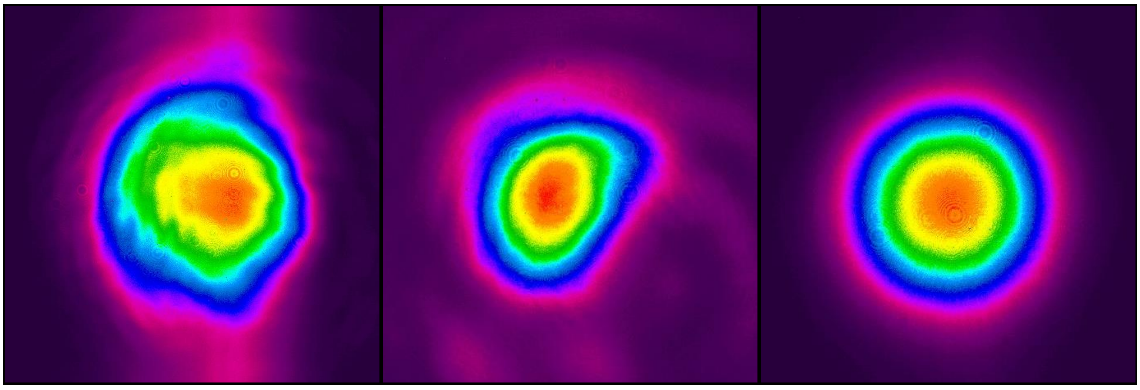

Figure 7.18: Beam profile of signal (left) transmitted through $\mathrm{M_{FSA,1}}$, (middle) rejected by $\mathrm{M_{in}}$ and (right) transmitted through $\mathrm{M_{FSA,2}}$

The transverse-mode selection achieved by the bow-tie cavity can be qualitatively evaluated. Figure 7.18 gives the beam profiles of the cavity incident, rejected and transmitted signals, respectively measured from the transmission through mirror $\mathrm{M_{FSA,1}}$, the reflection on the input coupler and the transmission through mirror $M_{FSA,2}$.

The incident beam profile is comparable to the far-field phase-front of the hybrid end-cap of Figure 6.18 although it differs with a slight distortion and some back-ground features induced by the number of optics crossed by the beam. These features are also predominant in the rejected signal phase-front whereas they are absent from the transmitted one. The latter is comparable to a nearly perfect TEM_{00} mode: it is the only eigen mode of the bow-tie cavity. The rejected signal is a combination of the fundamental mode circulating in the cavity and the uncoupled higher-order modes.

Quantitatively, the experimental reflectance parameter can be input in Equation 7.10 and predicts a rejected power of 0.93W below the 2.01W measured. If this 1.08W difference originates from uncoupled higher-order transverse modes, then it would mean that 23% of the incident signal is not purely TEM_{00}. Another contribution could be uncoupled longitudinal modes that are generated by the ring fibre laser but not resonant in the enhancement cavity. A glance at the rejected beam profile shows that the fundamental mode is not predominant and this second option is therefore less likely.

7.4.4 Power instabilities at high power operation

Oscilloscope traces

At 14.9W pump power, i.e. at low power above threshold, the total 186mW power rejected by the cube polarisers of the Faraday isolator in the backward direction is small in comparison to the 4.93W generated by the fibre and transmitted by the thin-film polariser (∼3.8%). This is still a concern as it can be the sign that the fibre gain module coupled to the Faraday mirror does not complete a total 90° polarisation rotation.

The temporal power stability was evaluated using photodiodes on various outputs of the set-up. Figure 7.19 gives the power over time for 14.9W and 112W pump powers. In first instance, considering the noise associated with the signal acquisition (both optical and electronic) and regarding the gain module stability as reported in Figure 7.7, the signal could be considered as stable.

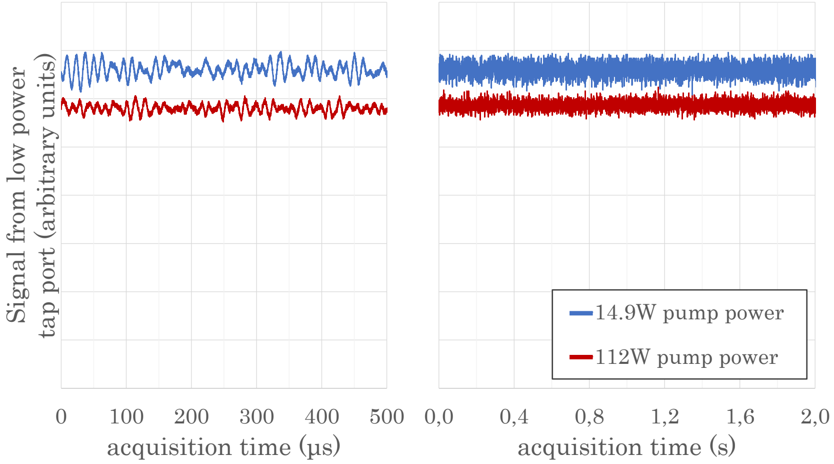

Figure 7.19: Configuration IX: temporal stability as from the tap coupler low-power port for 14.9W and 112W pump power, below instability threshold

When the pump power was increased to values above 112W, the signal stability significantly deteriorated and two features were observed as reported in Figure 7.20: first, a slow and arbitrary fluctuation of the power up and down with the time-scale of ∼1s, and secondly, high-speed high-peak power variations comparable to random self-pulsing behaviour.

How was the power lost? In the FSA, power was beamed out by the Faraday isolator input cube polariser in the backward direction (anti-clockwise). This is mostly unrotated vertical polarisation output from the fibre and reflected by the TFP. Just bellow the instability threshold, at 112W pump power, about 1W was beamed out. As the instability regime was entered, the thermal powermeter recorded rapid fluctuations with large amplitudes from a couple watts to a couple tens of watts.

Investigation of the slow variations

The slow-variation time-scale reported in Figure 7.20(a) is of the same order as of thermal effects such as thermal lensing. One possible explanation is that the FMA Faraday rotator birefringence is affected by thermal lensing and the Faraday mirror stops achieving a complete 90° rotation of the polarisation.

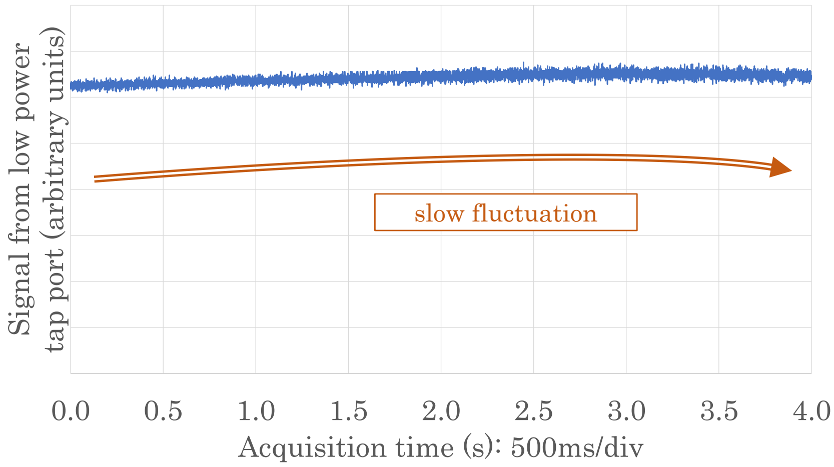

(a) Above instability threshold, at 135W pump power

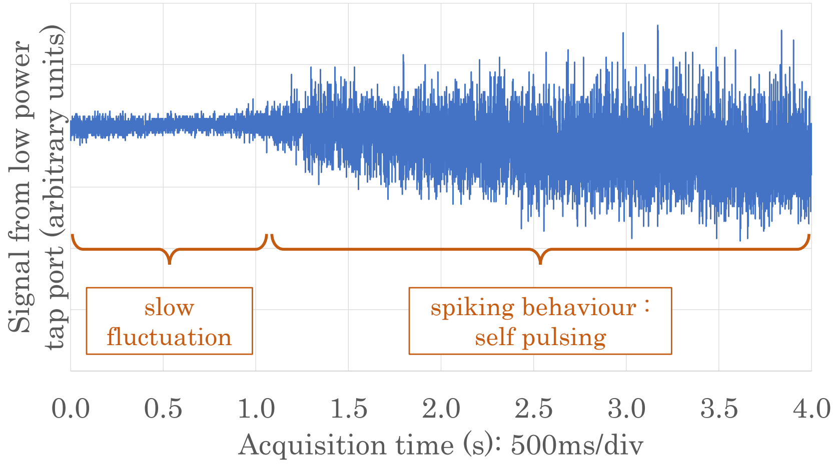

(b) Above instability threshold, at 161W pump power

Figure 7.20: Configuration IX: temporal behaviour as from the tap coupler low-power port at two arbitrarily-chosen times, above instability threshold

Another plausible explanation could be a third-order nonlinear response of the fibre to the propagating beam other than Brillouin and Raman scattering and known as optical Kerr effects. With optical fibres, the induced nonlinear birefringence manifests as a polarisation state rotation [24]. The Faraday mirror approach considering a linear birefringence may no longer be valid.

The optical Kerr effect is observed when the intensity of the light is sufficient to modify the refractive index of the dielectric it propagates in according to (in its simplest form):

$$n = n_0 + n_2 \frac{P}{A_{eff}} \tag{7.24}$$

with n_0 the dimensionless linear index, n_2 the nonlinear index expressed in $\mathrm{m}^2.\mathrm{W}^{-1}$, P the signal power and A_{eff} the effective fibre core area over which the fundamental transverse mode power distribution is equivalent to a top-hat distribution. It encompasses self-phase modulation (SPM), cross-phase modulation (XPM) and four-wave mixing.

A signal travelling alone will induce an index variation for itself and it corresponds to SPM. XPM occurs when a copropagating signal with either a different wavelength, direction of propagation or polarisation state gives an additional contribution to the refractive index as seen by the first considered wave. Therefore a signal propagating with two orthogonal components E_x and E_y experiences both SPM and XPM.

Considering the general case of an imperfect single-mode fibre with orthogonal fast and slow axes, and a input signal of power P_0 with phases ϕ_x and ϕ_y relative to respectively E_x and E_y, in the case where this input is linearly polarised at an angle θ with the slow axis, the nonlinear phase-shift $\Delta\phi_{NL} = \phi_x - \phi_y$ between its two orthogonal polarisations is given in continuous-wave operation by [25]:

$$\Delta\phi_{NL} = \frac{\gamma_{NL} \, P_0 \, l_{eff}}{3} \cos{(2\theta)} \tag{7.25}$$

where $l_{eff} = (1 - e^{-\alpha \, l_{fib}})/\alpha$ is the effective length of interactive region with α the propagation loss and l_{fib} the actual fibre length. It is the equivalent fibre length over which the power is constant and the propagation loss null. γ_{NL} is the nonlinear parameter defined as [25]:

$$\gamma_{NL} = \frac{2\pi n_2}{\lambda A_{eff}} \tag{7.26}$$

with signal wavelength λ.

For bulk silica glass, $n_2 = 2.7.10^{-20}\mathrm{m}^2.\mathrm{W}^{-1}$ at $\lambda = 1,06\mu\mathrm{m}$ [26]. The effective mode area can be roughly approximated to the core area so that $A_{eff} \simeq 79\mu\mathrm{m}^2$ for a 10µm-diameter core (alternatively it could be approximated to the mode-field diameter area but this would still not be fully accurate [27]). The calculated nonlinear parameter is $\gamma_{NL} = 2.0.10^{-3}\mathrm{W}^{-1}.\mathrm{m}^{-1}$.

Considering a single-pass signal through 20m of fibre with negligible propagation losses so that $l_{eff} \sim l_{fib}$, the amplitude of the nonlinear phase-shift $\Delta\phi_{NL}$ for a 50W signal is 0.67rad. Since the fast and slow axes position are subject to vibrations and temperature variations, the angle θ varies with time. This means that the phase-shift fluctuates within that ± 0.67rad window and the distribution of power between E_x and E_y varies accordingly.

This is a rough approximation as this considers a constant average power of 50W throughout the fibre despite the laser amplification gain. Also, it does not take into account the 90°-rotated returning signal from the Faraday mirror which adds an additional contribution to XPM. Nonetheless, these numbers highlight the potential contribution of the optical Kerr effects on the 90°-polarisation rotation loss and could explain the slow power fluctuations reported in Figure 7.20(a).

Investigation of the self-pulsing behaviour

The self-pulsing behaviour reported in Figure 7.20(b) could not be due to an insufficient fibre feedback: up to the instability threshold the recoupling efficiencies were relatively constant with an average 72.4% for the FMA and 71.5% for the FSA. However, the fibre gain ranged from ~10 at 14.9W pump up to ~20 just below the instability threshold. This higher gain could trigger certain self-pulsing mechanisms such as SBS. The same Configuration IX but without the enhancement cavity, i.e. an empty triangular ring configuration, was run and the instability power threshold remained unchanged despite the stronger feedback in the FSA. From that last observation, insufficient feedback can be ruled out of the causes of temporal instability.

A camera placed on $\mathrm{M}_{\mathrm{FSA},2}$ output highlighted small variations of the central position of the transmitted beam through the bow-tie at any power level (lateral displacement of 3-5% relative to the beam diameter as measured from a saturated signal). Such variations were not observed before the cavity on $\mathrm{M}_{\mathrm{FSA},1}$ output. Therefore the mechanical stability in the FSA should be improved.

The enhancement cavity can be seen as a transverse-mode filter. The output beam size and position depends on its mechanical stability and the stability of the input beam size and position too. The input waist in the bow-tie upper arm is the result of the alignment of

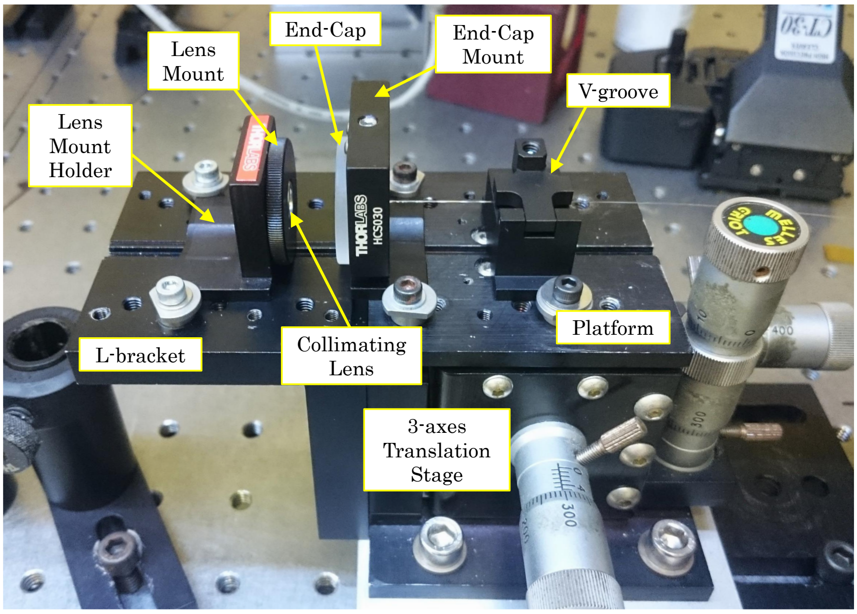

Figure 7.21: First optomechanical arrangement for the alignment of an end-capped fibre with a collimating lens

the fibre end and the collimating and focussing lenses $\mathrm{L}_{\mathrm{FSA,C}}$ and $\mathrm{L}_{\mathrm{FSA,F}}$. Any movement of the fibre end relative to the collimating lens can result in considerable variations of the waist position and size.

In practice, the fibre was originally held tight in a V-groove clamped to a three-axes translation stage. The collimating lens was held in a mount also clamped to a so-called L-bracket, itself screwed to the translation stage. Via the latter, the whole assembly was clamped to the optical table as shown on Figure 7.21. Each one of these intermediary components between the fibre and the lens induced a contribution to the mechanical arrangement unsteadiness.

Figure 7.22 reports a more stable arrangement which eliminates intermediate optomechanical components between the fibre end, the lens mount and the collimating lens. These components were glued to one another to reduce relative displacement. The end-cap and fibre mount was screwed to a pedestal clamped to the optical table. This sturdier mounting was implemented in the FSA but unfortunately this did not provide a noticeable change to the previous results.

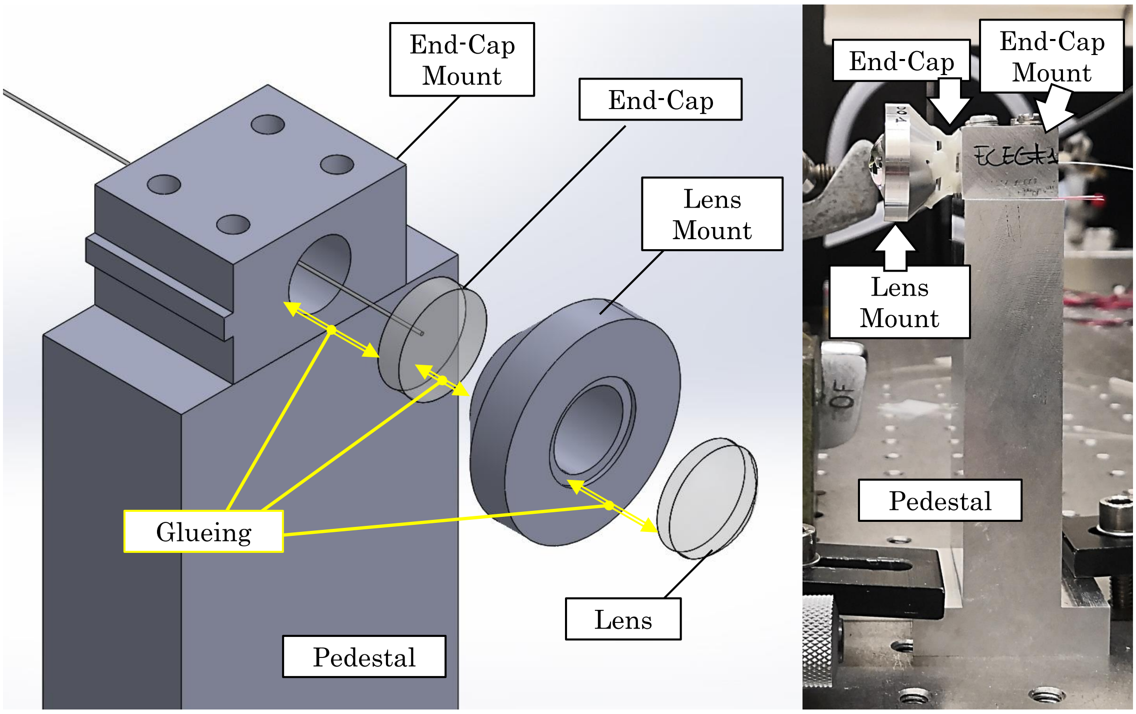

Figure 7.22: Robust mounting of the end-capped fibre with the collimating lens

Alternatively, signs of SRS were investigated (beside SRS critical power being theoretically above the SBS one) above the instability threshold. SRS would be responsible for the emission of a longer-wavelength signal with a shift from a couple nanometers to a few tens of nanometers from the spectrum-narrowing element central wavelength. The optical spectrum was observed at various outputs but such signal was not detected.

At last, it was observed that the temporal behaviour, with its sporadic instabilities, resembles relaxation oscillations. Relaxation oscillations have a characteristic frequency but unfortunately no oscilloscope traces were recorded in the instability region on a short timescale. Yet, the below-instability threshold traces given in Figure 7.19 show low-amplitude ∼13µs-period oscillations which could be due to relaxation oscillations and be the basis for the self-pulsing behaviour.

In theory, in steady-state operation above threshold, a laser upper-state population cannot exceed its threshold value and the round-trip gain (including losses) is equal to unity. However in practice, population inversion perturbations pushes the gain above unity and as a consequence, a series of bursts is generated. The phenomenon is referred to as spiking during a laser turn-on period and as relaxation oscillations when it is observed in continuous-wave operation with fluctuations around a steady-state value.

For a solid-state laser, whose upper-state lifetime τ_f ($\sim$ 1ms for an ytterbium-doped fibre) is usually much greater than the cavity round-trip time $t_{r.t.}$, the relaxation oscillation frequency (of either three-level or four-level energy system) can be approximated as [28]:

$$f_{RO} = \frac{1}{2\pi}\sqrt{\frac{\delta L_{tot} P_{avg}}{t_{r.t.}.E_{sat,l}}} \tag{7.27}$$

with $\delta L_{tot} = -\ln[(1 - L_{r.t.})(1 - T_{o.c.})]$ the overall round-trip loss coefficient function of the round-trip loss $L_{r.t.}$ and the output coupler transmission $T_{o.c.}$, P_{avg} the average power circulating in the cavity, and $E_{sat,l} = A_{core} h\nu_l/[\sigma_{abs}(\nu_l) + \sigma_{em}(\nu_l)]$ the saturation energy at the emission wavelength.

The round-trip time cavity composed of a double-passed 20m-long fibre module and 1.5m-long free-space portion is 0.20µs. The set-up has strong losses due to the two 75% fibre recoupling efficiencies, the ∼20% enhancement cavity transmission and the various output couplers. A rough round-trip loss coefficient estimation would be $\delta L_{tot} \simeq -\ln(1 - 90\%)$. For a 10µm-diameter fibre core, $\sigma_{abs}(\nu_l) = 1.10^{-27}\text{m}^2$ and $\sigma_{em}(\nu_l) = 2.10^{-25}\text{m}^2$, the saturation energy is $E_{sat,l} = 80\mu\text{J}$. Finally, for average circulating power of roughly 5W and 50W, the relaxation oscillation frequencies f_{RO} are respectively 0.14MHz and 0.45MHz with respective periods t_{RO} of 7.0µs and 2.2µs. These values are of the order of the experimental 13µs value.

Relaxation oscillations could therefore be the cause of these low-amplitude periodic power fluctuations but what could be their origin? Spatial hole burning was supposed negligible in first instance due to the large amount of longitudinal modes. In the case it is not, it could be responsible for low-amplitude gain variations locally in the fibre and distributed along its length, and therefore local variations of the population inversion.

Investigations were not longer conducted. In conclusion, above a certain pump power, the laser entered an instability regime with slow and fast power variations. The slow fluctuations were attributed to thermally induced mechanisms or the optical Kerr effect. Identifying heat-related issues and solving them was carried out in Chapter 6 but further investigation should be carried out, as well as investigating further nonlinear polarisation rotation in the fibre gain module.

Regarding the fast-oscillations, investigations highlighted that they were not due to SRS, were occurring with and without the enhancement cavity in i.e. regardless of the power returning to the gain module, and their threshold did not increase with a mechanical stability improvement. Yet, a possible highlighted origin could be relaxation oscillations due to, for instance, spatial hole burning. It could be interesting to carry out an analysis of this laser configuration in a single-frequency configuration as it would help identifying and quantifying spatial hole burning, and in the same time SBS.

Since considerable amount of power could nonetheless be generated by the gain module below the instability threshold, it was decided to carry on with the introduction of the LBO crystal in the enhancement cavity.

7.5 Configuration for green generation

Configuration X represented on Figure 7.23(a) has the same components as in Configuration IX with the addition of the LBO crystal in the lower arm of the bow-tie. The spectrum-narrowing is achieved by not one but two 5nm-bandwith central-wavelength-tuneable filters angled so that the transmission bandwidth is as narrow as 1nm and less. Two half-waveplates are also added before and after the enhancement cavity to provide it with a vertical polarisation and readjust it horizontally afterwards. The components are given in Table 7.23(b).

Regarding the beam size throughout the set-up, theory predicted a 162µm waist generated in the triangular arm however in practice the collimating lens slightly focussed the beam so that the measured waist had a 95µm radius. Graphics from Figure 7.13 were adjusted to this experimental value to appropriately dimension the bow-tie and target lower arm waists of 24µm or 40µm radius (the waist that should provide a maximum frequency-doubling efficiency).

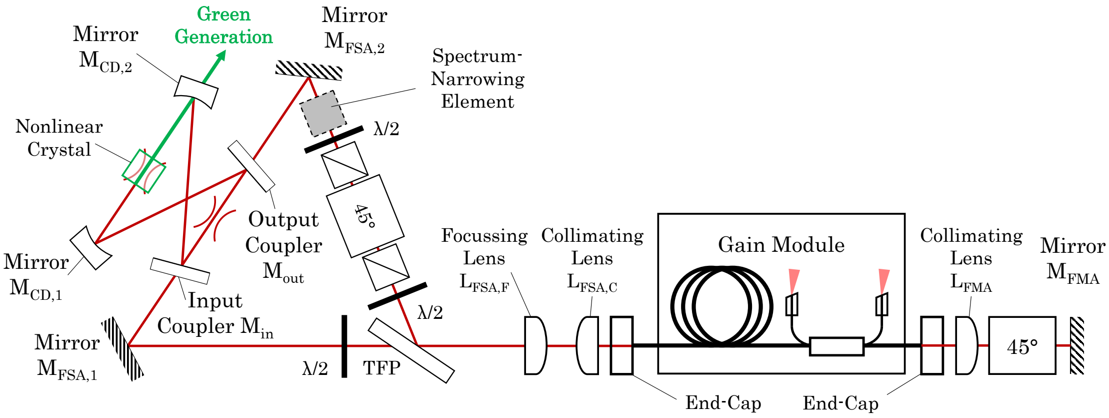

(a) Optical set-up

	Configuration	VIII
FSA	$L_{FSA,C}$	LAS15
	$L_{FSA,F}$	LTH500
	$M_{FSA,1}$	M95FS
	$M_{FSA,2}$	M70FS
	Spectrum-Narrowing Element	F5NM (×2)
	TFP	TFPNP
Bow-Tie	M_{in}	MIN55
	M_{out}	MOUT10
	$M_{CD,1}$	MCDHR
	$M_{CD,2}$	MCDHR
	Nonlinear Crystal	LBO
FMA	L_{FMA}	LAS15
	Faraday Rotator	FR1
	M_{FMA}	M95FS
	End-Caps	Hybrid

(b) List of components

Figure 7.23: Configuration X: triangular ring fibre laser with internal enhancement cavity for frequency-doubling to the green

Theoretically, the optimum waist radius for a maximum frequency-doubling efficiency ranges between 24µm and 40µm. However in practice these values were too small and the beam was too tightly focussed in the nonlinear crystal. As a consequence, the output beam profile showed side lobes as represented in Figure 7.24 which correspond to the side lobes of the phase-mismatch function reported in Figure 7.8. The portion of light within the phase-matching bandwidth contributed to the central lobe whereas the portion with a high divergence, on the edges on the crystal, were outside the nonlinear crystal angular acceptance. This pattern notably highlighted the direction of tightest angular acceptance corresponding to the φ angle.

The crystal was tested with increasing waist sizes in a single-pass configuration until the diffraction pattern was no longer obtained. This was achieved for a lower-arm waist of 71µm radius. It was achieved with mirrors of 200mm radius of curvature, a bow-tie angle of incidence of 7.8° and distances $l_{up} = 2$cm and $l_{low} = 14.3$cm.

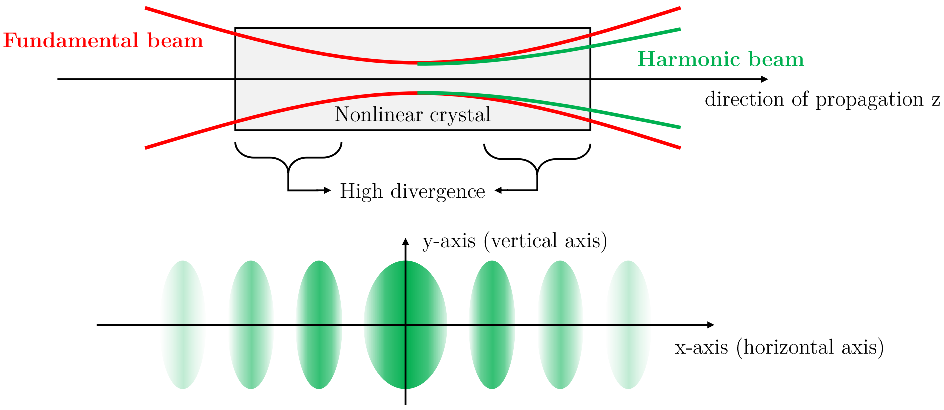

Figure 7.24: Second harmonic transverse profile in a nonlinear crystal pumped by a fundamental beam with a high beam divergence

The crystal alignment process consisted in tuning separately the φ angle, the crystal heater temperature and the lower-arm waist size to reach the highest frequency-doubling efficiency. The maximum efficiency was achieved when the crystal cut at $(\theta 90°, \varphi 11.36°)$ for type I critical phase-matching at 1064nm was slightly angled. This difference of angle can either be attributed to the wavelength of operation around 1071nm different from 1064nm or to the fact that non-critical phase-matching occurs at angle $(\theta = 90°, \varphi = 0°)$. The optimum heater temperature was close to 41°C. The crystal was run close to the critical phase-matching condition.

The two tuneable dichroic filters used in this set-up have a 5nm transmission window. This window central wavelength can be tuned by adjusting the angle of incidence with respect to the propagating beam. The two filters were set at different angles with therefore two offset transmission windows so that the resulting overlapping transmission bandwidth was lower than 5nm. On one hand, narrowing the bandwidth increases the frequency conversion efficiency. On the other hand the transmission window does not have perfect vertical edges (in the optical spectrum) and the overall transmission value reduces as the steep edges meet, which provide a lower limit on the achievable transmission bandwidth. During the alignment, the optimum angle-tuning was obtained for a signal of 0.55nm linewidth. Above this value less green power was generated, below this value the whole set-up circulating power would decrease.

The set-up was run at low pump power (14.9W) and the power distribution is given in Figure 7.25. From the 1.02W output from the second curved mirror $M_{CD,2}$, only 3.7mW were in the green spectrum. This value is well below the watt level expected from 225W circulating power and a 71µm fundamental waist in the crystal as according to calculations reported in Figure 7.11.

For the information of the reader, the introduction of the nonlinear crystal inside the enhancement cavity was carried out at the very end of the PhD project. If time allowed, a number of improvements would have been made.

First, the mechanical stability of the enhancement cavity would have been revisited. The 3-5% lateral displacement of the beam output from the empty bow-tie and recorded from the $M_{FSA,2}$ pick-off mirror with a camera indicates that the cavity did not maintain a stable TEM_{00} mode. Figure 7.26 is a set-up photography and it clearly appears that the curved mirrors mounting could be improved. A number of posts, translation stage and intermediate optomechanical pieces separate the mirror mounts from the optical bench and this number should be reduced to a minimum.

Secondly, the temperature of 41°C is far from the LBO NCPM temperature of ~130°C. The crystal was perhaps working in the angular phase-matching condition and the alignment of the cavity was achieved around a local maximum of the frequency-doubling effi-

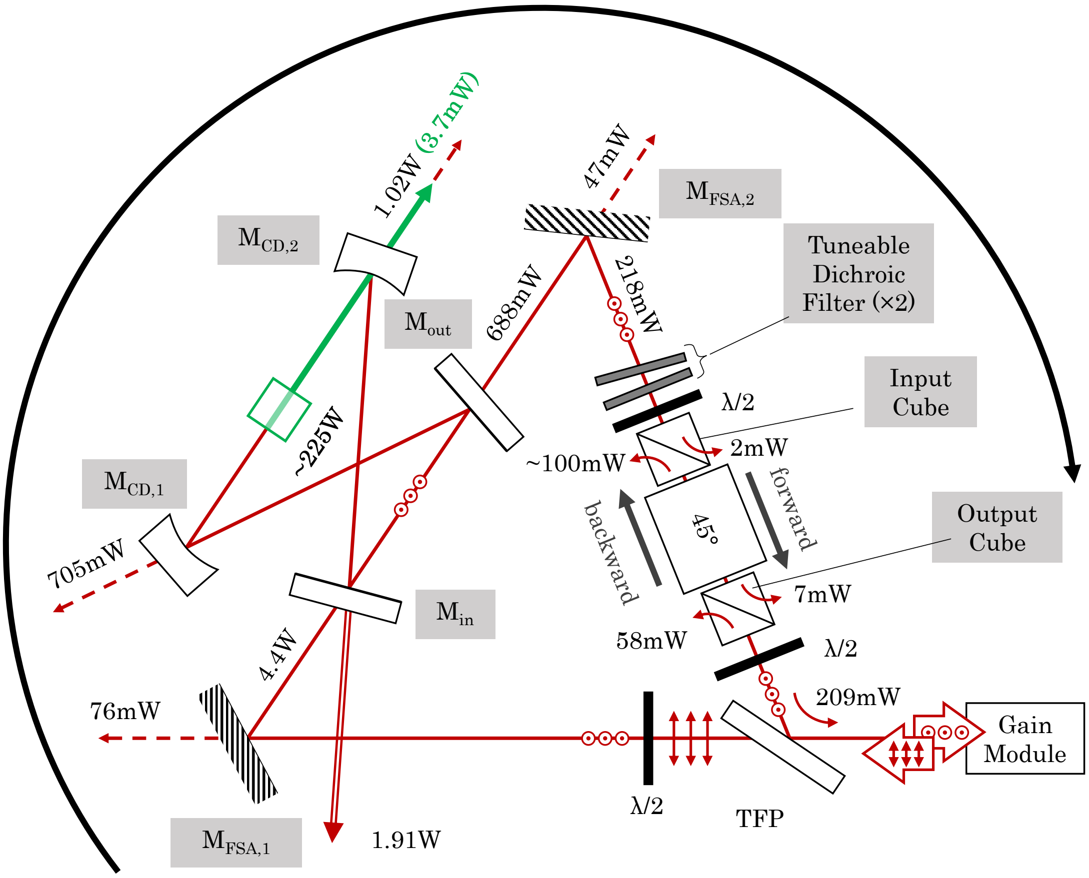

Figure 7.25: Configuration X: power distribution at low power above threshold

ciency. Starting to work at the NCPM temperature of 130°C rather than room temperature and then optimising the alignment should be tested.

Thirdly, the spectrum-narrowing filters reduced the near-infrared signal linewidth down to 0.55nm. Below this value, the filters would start to increase the losses of the overall setup. Changing the spectrum-narrowing element could allow to work with smaller linewidth which would bring a higher conversion efficiency.

As reported in Chapter 4, using an AOTF in a ring fibre laser can provide signal of FWHM as narrow as 0.4nm. This same AOTF was used as a spectrum-narrowing element, however it did not provide a substantial improvement. A diffraction grating could be considered but the losses associated with their reflection can be considerable. Volume Bragg gratings

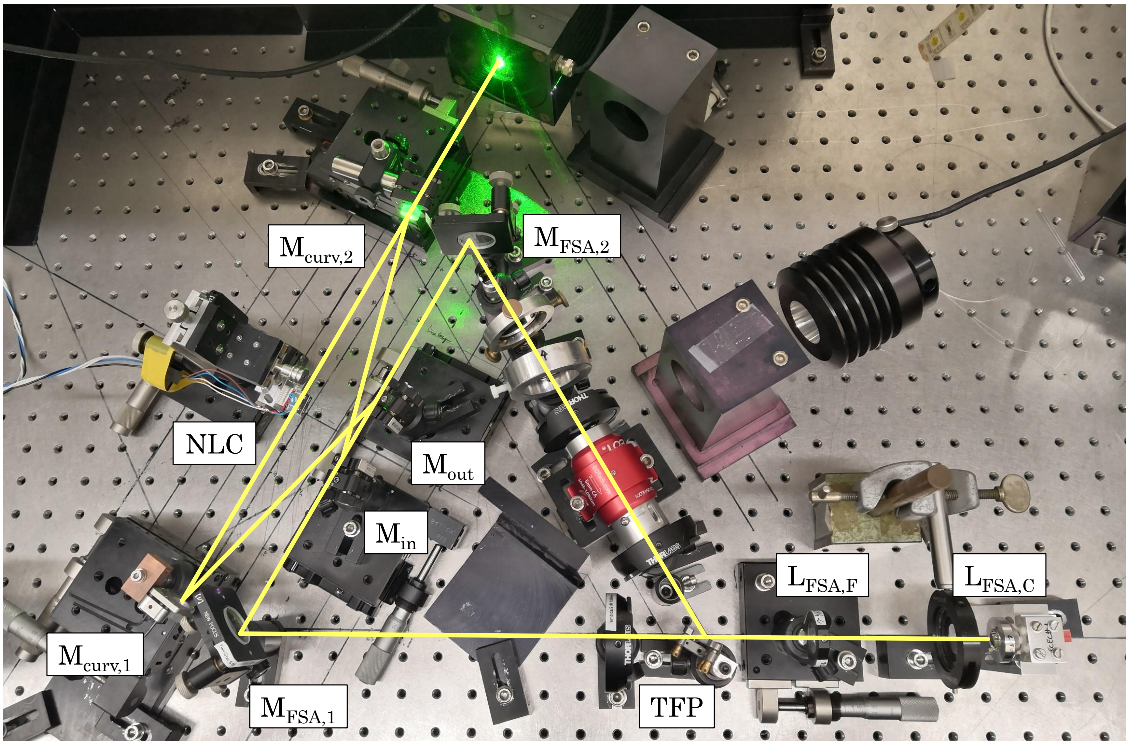

Figure 7.26: Configuration X: picture of the FSA in operation

are also an alternative as commercial ones can present a linewidth as short as a couple tens of picometers [29]. However they cannot be tuned during the alignment procedure as it can introduce a beam deviation, detrimental to the feedback to the fibre. It should also be reminded that a narrow linewidth also means lower power thresholds to nonlinear effects in fibres such as SBS and SRS.

7.6 Conclusion and discussion

The enhancement cavity with a bow-tie geometry was introduced in the triangular ring configuration. The whole set-up was studied without and with the nonlinear crystal in.

At low power operation (14.9W pump power), the enhancement cavity initially failed to maintain its input polarisation state. The output polarisation was slightly elliptical at an angle close to 45° relative to the input. The sources of this phase variation were identified to be stress-induced birefringence in the optics working in transmission and out-of-plane alignment. Mechanical constraint on the transmission optics was reduced by glueing them in their mounts rather than holding them tight by applying pressure on the side from a screw. Realignment of the bow-tie eventually readjusted the polarisation.

Above a certain pump power threshold (112W), the triangular ring configuration presented slow power fluctuations and periodic sections of high-power pulses despite reasonable fibre recoupling efficiencies (with or without the empty enhancement in). The slow variations were associated with a 90°-rotation polarisation loss from the fibre associated to the Faraday mirror. The highlighted possible causes were thermal effects in the Faraday rotator and optical Kerr effects in the fibre, contributing to additional nonlinear birefringence. The fast high-peak power variations were also investigated. SRS was ruled out but not SBS. Relaxation oscillations were shown to potentially be the mechanism responsible for these pulses.

Analysing the temporal behaviour of the fast oscillations could be the starting point of an in-depth study to prevent such effects. Another interesting experiment could be to power-scale the gain module coupled to a Faraday mirror alone as a double-pass amplifier and see whether the same instabilities are observed and if so, compare their power threshold.

Other than that, the empty enhancement cavity worked relatively well according to the theory of impedance-matching. The rejected power from the input coupler reasonably matched this theory therefore it could be concluded that only the modes resonant in both cavities were circulating otherwise the rejected power would have been significantly higher.

The introduction of the nonlinear crystal in the enhancement cavity was rather unsuccessful as it generated very little power and the conversion efficiency was well below predictions. This is attributed to a lack of time to make further progress on the alignment and improve the mechanical stability of the bow-tie cavity. Other than that, there is no reason why this set-up should not yield a higher conversion efficiency as achieved by previous students who worked in comparable set-ups before.

Bibliography

[1] A. Ashkin, G. Boyd, and J. Dziedzic, “Resonant optical second harmonic generation and mixing,” *IEEE Journal of Quantum Electronics*, vol. 2, no. 6, pp. 109–124, June 1966.

[2] N. Ismail, C. C. Kores, D. Geskus, and M. Pollnau, “Fabry-Pérot resonator: spectral line shapes, generic and related Airy distributions, linewidths, finesses, and performance at low or frequency-dependent reflectivity,” *Opt. Express*, vol. 24, no. 15, pp. 16 366–16 389, Jul 2016. [Online]. Available: http://www.opticsexpress.org/abstract.cfm?URI=oe-24-15-16366

[3] W. Sellmeier, “Zur erklärung der abnormen farbenfolge im spectrum einiger substanzen,” *Annalen der Physik*, vol. 219, no. 6, pp. 272–282, 1871. [Online]. Available: https://onlinelibrary.wiley.com/doi/abs/10.1002/andp.18712190612

[4] F. A. Jenkins and H. E. White, *Fundamentals of Optics 4th edition*, 1976.

[5] P. A. Cahill, K. D. Singer, and L. A. King, “Anomalous-dispersion phase-matched second-harmonic generation,” *Opt. Lett.*, vol. 14, no. 20, pp. 1137–1139, Oct 1989. [Online]. Available: http://ol.osa.org/abstract.cfm?URI=ol-14-20-1137

[6] A. M. Glazer and K. G. Cox, *Chapter 1.6. Classical linear crystal optics.* John Wiley & Sons, Inc., 2006, pp. 150–177.

[7] J. E. Midwinter and J. Warner, “The effects of phase matching method and of uniaxial crystal symmetry on the polar distribution of second-order non-linear optical polarization,” *British Journal of Applied Physics*, vol. 16, no. 8, pp. 1135–1142, aug 1965. [Online]. Available: https://doi.org/10.1088%2F0508-3443%2F16%2F8%2F312

[8] M. V. Hobden, “Phase matched second harmonic generation in biaxial crystals,” *Journal of Applied Physics*, vol. 38, no. 11, pp. 4365–4372, 1967. [Online]. Available: https://doi.org/10.1063/1.1709130

[9] F. Jonsson, “Lecture notes on nonlinear optics,” KTH, Physics, Tech. Rep. 2003:26, 2003, nR 20140804.

[10] N. P. Barnes and V. J. Corcoran, “Parametric generation processes: spectral bandwidth and acceptance angles,” *Appl. Opt.*, vol. 15, no. 3, pp. 696–699, Mar 1976. [Online]. Available: http://ao.osa.org/abstract.cfm?URI=ao-15-3-696

[11] J. Yao and Y. Wang, Eds., *Nonlinear optics and solid-state lasers: Advanced concepts, tuning-fundamentals and applications.* Heidelberg : Springer Verlag, 2012.

[12] M. Hobden and J. Warner, “The temperature dependence of the refractive indices of pure lithium niobate,” *Physics Letters*, vol. 22, no. 3, pp. 243 – 244, 1966. [Online]. Available: http://www.sciencedirect.com/science/article/pii/0031916366905919

[13] R. S. Weis and T. K. Gaylord, “Lithium niobate: Summary of physical properties and crystal structure,” *Applied Physics A*, vol. 37, no. 4, pp. 191–203, Aug 1985. [Online]. Available: https://doi.org/10.1007/BF00614817

[14] E. Luppi and V. Véniard, “A review of recent theoretical studies in nonlinear crystals: towards the design of new materials,” *Semiconductor Science and Technology*, vol. 31, no. 12, p. 123002, nov 2016. [Online]. Available: https://doi.org/10.1088%2F0268-1242%2F31%2F12%2F123002

[15] C. Chen, Y. Wu, A. Jiang, B. Wu, G. You, R. Li, and S. Lin, “New nonlinear-optical crystal: LiB_3O_5,” *J. Opt. Soc. Am. B*, vol. 6, no. 4, pp. 616–621, Apr 1989. [Online]. Available: http://josab.osa.org/abstract.cfm?URI=josab-6-4-616

[16] T. Ukachi, R. J. Lane, W. R. Bosenberg, and C. L. Tang, “Phase-matched second-harmonic generation and growth of a LiB_3O_5 crystal,” *J. Opt. Soc. Am. B*, vol. 9, no. 7, pp. 1128–1133, Jul 1992. [Online]. Available: http://josab.osa.org/abstract.cfm?URI=josab-9-7-1128

[17] S. Lin, Z. Sun, B. Wu, and C. Chen, “The nonlinear optical characteristics of a LiB_3O_5 crystal,” *Journal of Applied Physics*, vol. 67, no. 2, pp. 634–638, 1990. [Online]. Available: https://doi.org/10.1063/1.345765

[18] A. L Bondarenko, S. Grechin, D. Kochiev, A. Sharikov, and I. A Shcherbakov, “Temperature dependence of angular noncritical phase-matched second-harmonic generation of focused laser radiation,” *Laser Physics Letters*, vol. 15, p. 025402, 02 2018.

[19] S. Lin, B. Wu, F. Xie, and C. Chen, "Phase-matching retracing behavior: New features in LiB_3O_5," *Applied Physics Letters*, vol. 59, no. 13, pp. 1541–1543, 1991. [Online]. Available: https://doi.org/10.1063/1.106276

[20] H. Kogelnik and T. Li, "Laser beams and resonators," *Appl. Opt.*, vol. 5, no. 10, pp. 1550–1567, Oct 1966. [Online]. Available: http://ao.osa.org/abstract.cfm?URI=ao-5-10-1550

[21] S. Carrasco, B. E. A. Saleh, M. C. Teich, and J. T. Fourkas, "Second- and third-harmonic generation with vector gaussian beams," *J. Opt. Soc. Am. B*, vol. 23, no. 10, pp. 2134–2141, Oct 2006. [Online]. Available: http://josab.osa.org/abstract.cfm?URI=josab-23-10-2134

[22] G. D. Boyd and D. A. Kleinman, "Parametric interaction of focused gaussian light beams," *Journal of Applied Physics*, vol. 39, no. 8, pp. 3597–3639, 1968. [Online]. Available: https://doi.org/10.1063/1.1656831

[23] W. W. Chow, J. Gea-Banacloche, L. M. Pedrotti, V. E. Sanders, W. Schleich, and M. O. Scully, "The ring laser gyro," *Rev. Mod. Phys.*, vol. 57, pp. 61–104, Jan 1985. [Online]. Available: https://link.aps.org/doi/10.1103/RevModPhys.57.61

[24] P. D. Maker, R. W. Terhune, and C. M. Savage, "Intensity-dependent changes in the refractive index of liquids," *Phys. Rev. Lett.*, vol. 12, pp. 507–509, May 1964. [Online]. Available: https://link.aps.org/doi/10.1103/PhysRevLett.12.507

[25] G. Agrawal, "Chapter 6 - Polarization Effects," in *Nonlinear Fiber Optics (Third Edition)*, third edition ed., ser. Optics and Photonics, G. Agrawal, Ed. Academic Press, 2001, pp. 203 – 259.

[26] D. Milam and M. J. Weber, "Measurement of nonlinear refractive-index coefficients using time-resolved interferometry: Application to optical materials for high-power neodymium lasers," *Journal of Applied Physics*, vol. 47, no. 6, pp. 2497–2501, 1976. [Online]. Available: https://doi.org/10.1063/1.322965

[27] M. R. Vastag, "White paper: Mode field diameter and effective area," Corning Incorporated, One Riverfront Plaza, Corning, NY 14831U.S.A., Tech. Rep. WP7071, October 2001. [Online]. Available: www.corning.com/opticalfiber

[28] A. Schlatter, S. C. Zeller, R. Grange, R. Paschotta, and U. Keller, "Pulse-energy dynamics of passively mode-locked solid-state lasers above the Q-switching threshold," *J. Opt. Soc. Am. B*, vol. 21, no. 8, pp. 1469–1478, Aug 2004. [Online]. Available: http://josab.osa.org/abstract.cfm?URI=josab-21-8-1469

[29] OptiGrate Corp., "Volume Bragg gratings from OptiGrate," Brochure, p. 3, 2015. [Online]. Available: https://optigrate.com/OptiGrate%20Overview%20Brochure.pdf

Chapter 8

Conclusions and future prospects

8.1 Summary of thesis

The goal of this PhD project was the implementation of a high-power ring ytterbium-doped-fibre laser with an internal enhancement cavity for the generation of green radiation without using polarisation-maintaining fibres. This thesis presented a number of experiments that were carried out along the way and going in that direction.

One of the many challenges when aligning fibre lasers is self-pulsing. It lead to the creation of a seed source presented in Chapter 3 and was used throughout the PhD duration for the alignment of the diverse fibre laser configurations. During alignment when the cavities were open, the seeded fibre gain modules behaved as amplifiers and did not trigger self-pulsing mechanism which would have lead to their failure and deterioration.

The emission linewidth of the ASE source were dictated by the requirements for injection-locking of a fibre laser. The all-fibre source was composed of an SLED, multiple amplification stages and three consecutive bandwidth-slicing stages achieved with internally-developed and commercial FBGs. The ASE source output was centred at 1075.0nm with a 85pm-linewidth and a maximum 2.97W power. This power level was sufficient to save quite a number of gain stages from self-pulsing and test injection-locking.

The first implementation of a ring fibre laser with a Faraday mirror used to tackle the effects of the fibre birefringence on the polarisation was successful. Chapter 4 reported a wavelength-tuneable linearly-polarised ytterbium-doped fibre ring laser. The gain module developed for this experiment had absorption efficiencies of 75.9%, 81.1% and 90.3% as relative respectively to the laser diode power, the combined pump power and the absorbed pump power.

The spectrum covered ranged from 1047.1nm to 1085.8nm with a linewidth of 0.4nm and less (FWHM). The average output power was 32.0W corresponding to a 70.2% efficiency relative to the pump power. The polarisation extinction ratio measured for the evaluation of the 90°-rotation of the polarisation achieved by the fibre associated with the Faraday mirror was $\sim$100:1.

Injection-locking of a ring configuration with the Faraday mirror and without any spectrum-narrowing element was attempted in Chapter 5 with the ASE source developed in Chapter 3 as a seed source. Historically, injection-locking has often been achieved with single-frequency source as the master oscillator. Whether injection-locking by an ASE source is a success or not is not clear.

From the delivered power from the 1075nm see source, 1.86W were injected in the ring fibre laser whose maximum free-running power was 25.9W. The ring fibre laser emitted at 1075nm up to 17.4W output before parasitic lasing occurred around 1084 and 1088nm. However in what appeared a successful injection-locking power range below 17.4W, the output RF spectrum showed that such conclusion could not be drawn. Further analysis indicated that regenerative amplification likely happened partially if not entirely.

Power-scaling of the triangular ring fibre laser that would further house an enhancement cavity for green generation and its intermediate linear configurations was carried out in Chapter 6 using a gain module capable of generating powers in the 200W regime. The procedure highlighted that a number of optics were absorbing enough power at 1060-1080nm to trigger thermal lensing, alter the beam quality and reduce significantly the fibre recoupling efficiencies. This was corrected by using fused-silica substrate-based optics as it did not absorb at these power levels.

Throughout this PhD, an fibre end-capping set-up was developed as a collaborative effort within the research group. First, large bulk anti-reflection-coated end-caps were spliced to fibre ends and provided satisfying results. No feedback-related issues from the fibre terminations were detected. The phase-front quality of the output they deliver was evaluated for one of them and is reported in Chapter 4. The measured M^2 value was 1.08 which was not ideal and the beam profile presented some higher-order modes. Hybrid end-caps were produced and improved fibre recoupling efficiencies by 16%.

The enhancement cavity in the ring fibre laser was introduced in Chapter 7. While empty, it highlighted the tight dependence of the polarisation state on the out-of-plane alignment of the bow-tie and the stress-induced birefringence in the mirrors. Otherwise, at low powers, it showed good agreement with the impedance-matching theory which also confirms that the longitudinal mode-matching between the enhancement cavity and the ring fibre laser was occurring too. Unfortunately, this configuration showed limitations in terms of power stability when entering the 110W pump regime. Slow amplitude variations were observed and were attributed to thermal effects or nonlinear polarisation rotation in the fibre. Sporadic fast pulse-type instabilities were recorded that could be due to relaxation oscillations whose origin could be spatial hole burning but this theory would need further analysis.

At last, the nonlinear crystal was placed in the enhancement cavity but, due to a lack of time, the frequency-doubling efficiency it yielded was well bellow expectations.

8.2 Conclusions and future prospects

The work carried out during this thesis mostly revolved around the Faraday mirror approach. The concept was initially tested for an ytterbium-doped fibre pumped at ~50W in a resonator with the wavelength-tuneable linearly-polarised fibre ring laser experiment and it was successful. In that perspective, injection-locking was tested with a similar set-up, did not provide clear results on the nature of the spectrum output but this did not question the efficiency of the 90° polarisation rotation. Then only, power-scaling showed that for pumped power around 110W, the polarisation rotation is no longer ensured. Further investigations should be oriented in that direction. A potential experiment could be testing the high-power gain module coupled to the Faraday mirror outside the resonator, in a amplification configuration. Also, the resonator could be tested in single-mode operation to evaluate experimentally the SBS critical power and its manifestation, and compare it to the fast pulse-type instabilities recorded during the power-scaling of the triangular ring fibre.

Regarding the enhancement cavity, before introduction of the crystal, the observations were promising since impedance-matching and mode-matching conditions were verified. Regarding frequency-doubling, further alignment should provide immediate satisfying results. Changing the spectrum-narrowing element to reduce the laser linewidth is advised as well as improving the mechanical stability of the enhancement cavity.

Injection-locking requires a more thorough investigation both theoretically and experimentally. The seed source did manage to force the ring fibre to lase at its injected wavelength up to a certain power level. This could be of interest in the context of green fibre laser.

Appendix A: Optical components characteristics in chapters 6 and 7

This appendix presents some components used in the progressive construction of the green laser source with the relevant specification and characterisation data to the understanding of this thesis.

Mirrors

Name	Data
M70SH	off-the-shelf flat mirror, unknown substrate, T=70% at 1.0-1.1μm
M70FS	- flat mirror, fused silica substrate, T~70% at 1 micron - transmission at 1073nm at half Brewster's angle incidence: horizontal polarisation: 79.6%, vertical polarisation: 68.3%
M95FS	- specifications: flat mirror, fused silica substrate, T=95-98% at 1030-1100nm - transmission at 1073nm at half Brewster's angle incidence: horizontal polarisation: 3.63%, vertical polarisation: 1.09% - transmission at 1073nm at 0°-angle incidence: horizontal polarisation: 1.41%, vertical polarisation: 1.41%
MIN55	- specifications: flat mirror, fused silica substrate, T=5.5% at 1060-1080nm - transmission at 1073nm at 7°-angle incidence: horizontal polarisation: 4.07%, vertical polarisation: 3.63%

Name	Data
MOUT05	- specifications: flat mirror, fused silica substrate, T=0.5% at 1060-1080nm - transmission at 1073nm at 7°-angle incidence: horizontal polarisation: 0.28%, vertical polarisation: 0.24%
MOUT10	flat mirror, fused silica substrate, T=1% at 970-1190nm
MCDHR	- specifications: curved dichroic mirror, fused silica substrate, HR at 970-1150nm and HT at 485-635nm at 5-15° angle - transmission at 1073nm at 7°-angle incidence: horizontal polarisation: 0.38%, vertical polarisation: 0.34%

Lenses

Name	Specifications
LTH15	aspheric lens, f=15.29mm, NA=0.16, 1050-1620nm AR coating, H-LaK54 substrate
LTH18	aspheric lens, f=18.40mm, NA=0.15, 1050-1620nm AR coating, H-LaK54 substrate
LAS15	aspheric lens, f=15.0mm, NA=0.39, 1000-1600nm AR coating, fused silica substrate
LTH500	plano-convex lens, f=500mm, 1050-1700nm AR coating, fused silica substrate

Faraday rotators

Name	Specifications
FR1	rotating material: terbium gallium garnet (TGG) crystal (high absorption)
FR2	rotating material: terbium gallium garnet (TGG) crystal (low absorption)

Thin-film polariser

Name	Specifications
TFPNP	Brewster angle, $R_s > 99\%$ and $T_p > 95\%$ at 1064nm, BK7 substrate
TFPLT	Brewster angle, $R_s > 99.8\%$ and $R_p < 2\%$ at 1064nm, fused silica substrate

Spectrum-narrowing element

F5NM is a bandpass filter with a fixed transmission bandwidth and a angle-tuneable central wavelength. The filter bandwidth is 5.2nm and the central wavelength at 0° is 1071.2nm according to the specifications. The chart below gives the transmission windows at two different angles.

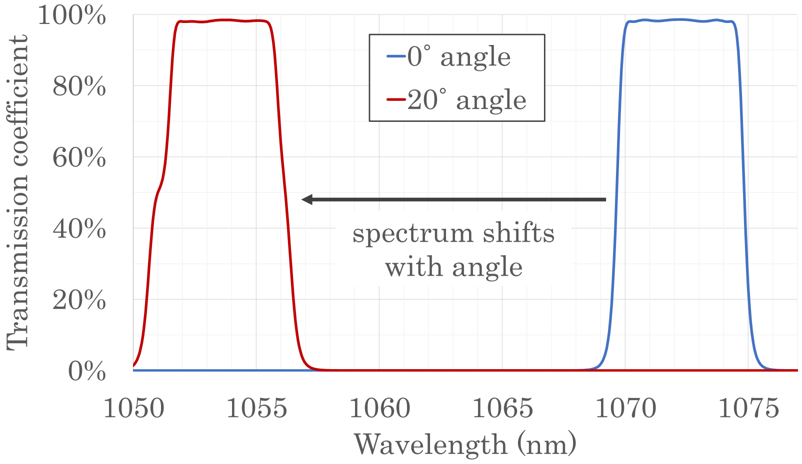

Waveplates

The half and quarter waveplates used were optically contacted zero order waveplates designed at 1064nm.